NASA/CR—1999-209404

Development of GENOA Progressive Failure Parallel Processing Software Systems

Frank Abdi
Alpha STAR Corporation, Long Beach, California

Levon Minnetyan
Clarkson University, Potsdam, New York

December 1999

The NASA STI Program Office . . . in Profile

Since its founding, NASA has been dedicated to the advancement of aeronautics and space science. The NASA Scientific and Technical Information (STI) Program Office plays a key part in helping NASA maintain this important role.

The NASA STI Program Office is operated by Langley Research Center, the Lead Center for NASA's scientific and technical information. The NASA STI Program Office provides access to the NASA STI Database, the largest collection of aeronautical and space science STI in the world. The Program Office is also NASA's institutional mechanism for disseminating the results of its research and development activities. These results are published by NASA in the NASA STI Report Series, which includes the following report types:

- TECHNICAL PUBLICATION. Reports of completed research or a major significant phase of research that present the results of NASA programs and include extensive data or theoretical analysis. Includes compilations of significant scientific and technical data and information deemed to be of continuing reference value. NASA's counterpart of peer-reviewed formal professional papers but has less stringent limitations on manuscript length and extent of graphic presentations.

- TECHNICAL MEMORANDUM. Scientific and technical findings that are preliminary or of specialized interest, e.g., quick release reports, working papers, and bibliographies that contain minimal annotation. Does not contain extensive analysis.

- CONTRACTOR REPORT. Scientific and technical findings by NASA-sponsored contractors and grantees.

- CONFERENCE PUBLICATION. Collected papers from scientific and technical conferences, symposia, seminars, or other meetings sponsored or cosponsored by NASA.

- SPECIAL PUBLICATION. Scientific, technical, or historical information from NASA programs, projects, and missions, often concerned with subjects having substantial public interest.

- TECHNICAL TRANSLATION. English-language translations of foreign scientific and technical material pertinent to NASA's mission.

Specialized services that complement the STI Program Office's diverse offerings include creating custom thesauri, building customized data bases, organizing and publishing research results . . . even providing videos.

For more information about the NASA STI Program Office, see the following:

- Access the NASA STI Program Home Page at ***http://www.sti.nasa.gov***

- E-mail your question via the Internet to help@sti.nasa.gov

- Fax your question to the NASA Access Help Desk at (301) 621-0134

- Telephone the NASA Access Help Desk at (301) 621-0390

- Write to:
  NASA Access Help Desk
  NASA Center for AeroSpace Information
  7121 Standard Drive
  Hanover, MD 21076

NASA/CR—1999-209404

Development of GENOA Progressive Failure Parallel Processing Software Systems

Frank Abdi
Alpha STAR Corporation, Long Beach, California

Levon Minnetyan
Clarkson University, Potsdam, New York

Prepared under Contract NAS3–97041

National Aeronautics and
Space Administration

Glenn Research Center

December 1999

Note that at the time of printing, the NASA Lewis Research Center
was undergoing a name change to the
NASA John H. Glenn Research Center at Lewis Field.
Both names appear in these proceedings.

Available from

NASA Center for Aerospace Information
7121 Standard Drive
Hanover, MD 21076
Price Code: A11

National Technical Information Service
5285 Port Royal Road
Springfield, VA 22100
Price Code: A11

Contents

Contents

Contents

Contents

Illustrations

Illustrations

Illustrations

Illustrations

Illustrations

Illustrations

Illustrations

Illustrations

Illustrations

Tables

Executive Summary

Polymer matrix composite (PMC) materials in the form of, braided, woven or stitched laminated are increasingly being used in critical aircraft structure that must be damage tolerant for reasons of safety, reliability, maintainability and supportability. This means that PMC structures must be durable and reliable under service conditions that can expose aircraft structure to many types of damage mechanisms. Basic to the evaluation of durability and reliability is the analysis of fracture initiation and progression under static or cyclic thermo-mechanical loading and impact loading in variable environments (e.g., humidity, engine exhaust, or sea air).

Fracture initiation is associated with defects such as voids, machining irregularities, stress concentrating design features, damage from impacts with tools or other objects resulting in discrete source damage (DSD), and nonuniform material properties stemming for example, from improper heat treatment. After a fracture initiates it can grow and progressively lower the residual strength of a structure to the point where it can no longer support design loads making global failure imminent. The processes of fracture initiation and subsequent progressive growth have large probabilistic elements stemming from the complexities introduced in PMC materials by the presence of multiple components and their interactions. Add to this the multiplicity of design options arising from the availability of numerous choices of fibers, fiber coatings, fiber orientation patterns, fiber preform variations, matrix materials, and constituent material combinations and there results a large array of design parameters to be considered making numerical analysis difficult. As a consequence, costly and time-consuming experimental testing has been primarily relied upon to evaluate design iterations of PMC structure.

NASA and aerospace industry recognized early on that design of PMC structure was becoming very expensive because of rapidly escalating experimental testing requirements for verification of structural designs for critical applications. As a consequence, the use of newer more advanced computers to perform numerical analysis simulations of composite structure is envisioned as a means of overcoming the difficulties imposed by the multiplicity of variables. Successful computerized simulations would offer a viable means of reducing experimental testing requirements and shortening design time. This vision has now been realized to a significant extent, under NASA-Lewis funding, by the development reported herein of GENOA progressive failure analysis (PFA), a commercial software with a parallel processing mode for rapid simulation of fracture initiation and progression in PMC structure.

Designing continuous fiber reinforced composites with optimum ability to arrest cracks and prevent self-similar crack propagation is a very complex task because of the existence of a multiplicity of design options arising from the availability of numerous choices of fibers, fiber coatings, fiber orientation patterns (Figure E-1), matrix materials, constituent material combinations, and hybridizations. The resulting large array of design parameter variables, that must be considered in order to predict durability and performance, presents a logistical problem that complicates and prolongs design optimization and certification processes and adds significantly to the cost of composite parts.

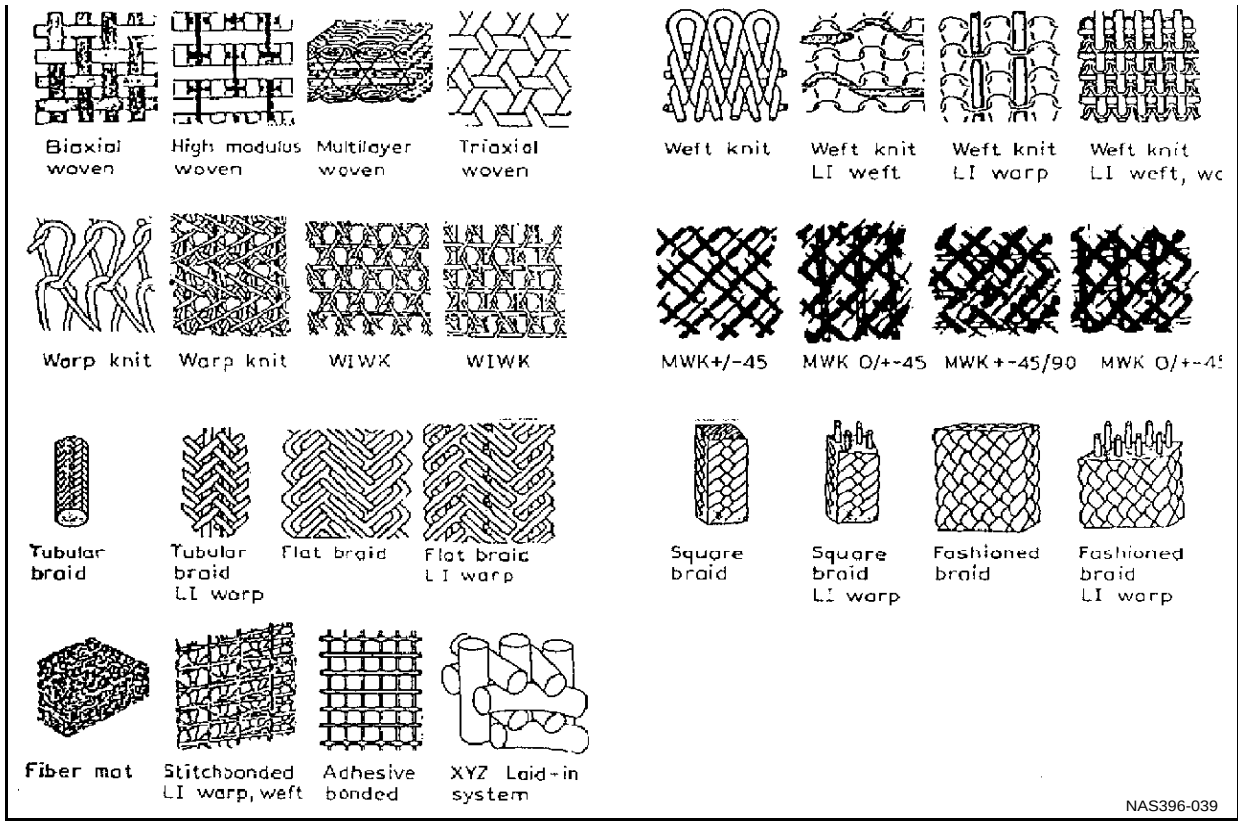

Figure E-1. Fiber Architecture Family Created By Different Preform Fabrication Techniques

Designing and fabricating with PMC materials in an engineering environment acquires highly sophisticated, analytical tools that integrates an array of specialized technologies. Due to the inherent complexity of the woven and braided PMC material system many of the specialized analysis techniques and mathematical models are computationally intense. Because they require multiple levels of iterative analysis utilizing time consuming convergence criteria. Recognizing this, the GENOA progressive failure analysis software tool was developed to make design and analysis of 3D braided PMC structure fast and significantly more cost effective.

A primary thrust of the effort was to identify and model the types of progressive failure expected to be encountered and then to develop a verified computer code to simulate progressive effects on the 2D/3D braided composite structure. The simulation code utilized mathematical computation employing finite element analysis (FEA) in combination with composite mechanics capabilities already existing in GENOA, with appropriate modifications to assure applicability to braided composite structure. A very important part of the effort was that of concurrent development of progressive damage simulation, and experimental testing of full scale sections of 3D composite structure.

1.1 PROGRESSIVE FAILURE SIMULATION SOFTWARE

A number of attempts have been made to computatively analyze durability and damage tolerance (D&DT) in fiber reinforced composite materials and structures. The resulting computer codes, as with Alpha STAR's GENOA-PFA code, generally utilize simplifying assumptions, semi-empirical relations derived from closed form approximate solutions correlated with test data. These codes are typically fast, cost effective, and easy to use but lack the capabilities of Alpha STAR's GENOA-PFA software to:

simulate: 1) dynamic loading responses, 2) 3D fiber geometries, 3) woven/braided fiber configurations, 4) through the thickness fiber stitching, 5) degradation of fiber and matrix mechanical/physical properties, 6) damage tracking, 7) creep, and 8) fatigue. Also, these codes do not have GENOA-PFA's adaptive mesh capability for automatically refining an FEM mesh at stress concentration locations to assure simulation accuracy, and the capability to incrementally integrate FEM with macro and micro mechanical basics. The uses of GENOA-PFA capabilities are presented in Table E-1. A comparison of GENOA-PFA's simulation capabilities with other available D&DT simulation software codes is presented in Table E-1. Table E-2 presents the advantages and disadvantages of D&DT prediction methods.

Table E-1. GENOA-PFA Vs. Other Durability and Damage Tolerance (D&DT) Solutions

Integrated GENOA D&DT Solution	Other D&DT Solutions
Damage initiation/growth and residual strength predictions Modeling of fiber orientation, matrix, and Stitching Manufacturing defects: voids, fiber waviness, fiber misalignment and cure residual stress) Degradation of material properties (stiffness, and strength) under service condition Detailed stress analysis, photo-elastic fringe pattern Automated adaptive FEM meshing, and crack growth monitoring Sensitivity analysis of design parameters to failure criteria Fatigue, impact and creep predictions	Provide for design (preliminary, and detailed) parametric studies and preliminary structural analysis of resulting designs, detailed designs Can be used for empirical prediction of damage growth and residual strength (semi-empirical) accuracy guarantee is at best limited to range of test variables)

Table E-2. Advantages and Disadvantages of D&DT Prediction Methods

NO.	Method	Advantages	Disadvantage	Ref
1	GENOA Progressive Fracture - A New Approach	a) Reduce experimental testing b) Reduce design time c) Reduce design cost d) Computer code available e) Verified accuracy f) Deemed most powerful of methods	Requires significant computer resources	NASA TM 105574
2	Simplified Equations	a) Rapid analysis b) Promotes design optimization	Accuracy is limited	NASA TM 103113
3	R-Curve	Well established method	a) Little predictive capability for fracture propagation in PMC b) Requires extensive testing c) R-curves are part specific	Poe, Harris, Coats & Walker
4	Linear Elastic Fracture Mechanics (LEFM)	Accurate prediction of tensile strength if matrix cracking and delamination are minimal	a) Not good for long damage cuts b) Not good if matrix cracking and/or delamination are significant	NASA ACT Publication
5	Damage Energy Release Rate (DERR)	a) Computational simulation method b) Indicates structural resistance to damage propagation.		AIAA-95-1463-CP
6	Non-Linear Response	Analytical study suggests accurate prediction of stiffened shell response to damage	a) Insufficient experimental verification b) Limited effort in this area	AIAA-95-1462-CP

Progressive Fracture Methodology

It is generally accepted that flawed structures fail when the flaws grow or coalesce to a critical dimension such that the structure no longer has an adequate safety margin to avoid catastrophic global fracture. This is true for structures made from either traditional homogenous materials or PMC materials. The difference between PMC materials and monolithic materials is that PMC materials have more fracture modes than monolithic materials. Any predictive approach for simulating structural fracture in PMC (e.g. S/RFI) materials needs to formally quantify (1) possible fracture modes, (2) the types of flaws (existing or generated by thermomechanical loading) that can initiate fracture modes, and (3) the coalescing and propagation of flaws to critical dimensions for imminent structural fracture.

The approach to determining the effects of DSD on D&DT in the framework of structural damage in PMC structure is characterized by five sequential stages: (1) initiation, (2) growth, (3) accumulation (i.e. coalescence of propagating flaws), (4) stable propagation (up to the critical amount), and (5) unstable or very rapid propagation (beyond the critical amount) to catastrophic failure. This fundamental concept is implemented by developing formal procedures to (1) identify the five different stages of damage, (2) quantify the amount of damage at each stage, and (3) relate the amount of damage at each stage of the degradation to global structural behavior. ASC's GENOA-PFA (Figure E-2) has the algorithms needed for simulating the effects of DSD on D&DT in PMC structure, including the effects of a through-the-thickness crack or hole-like DSD with edge, pocket, internal, or mixed-mode delaminations.

The modeling of PMC in GENOA-PFA considers the physics and mechanics of PMC materials and structure by integration of a hierarchical multilevel macro-scale (lamina, laminate, and structure) and micro scale (fiber, matrix, and interface) simulation analyses (Figure E-2). The modeling involves (1) ply layering methodology utilizing FEM elements with through-the-thickness representation, (2) simulation of effects of material defects and conditions (e.g., voids, fiber waviness, and residual stress) on global static and cyclic fatigue strengths, (3) including material nonlinearities (by updating properties periodically) and geometrical nonlinearities (by Lagrangian updating), (4) simulating crack initiation, and growth to failure under static, cyclic, creep, and impact loads, (5) progressive fracture analysis to determine durability and damage tolerance, (6) identifying the percent contribution of various possible composite failure modes involved in critical damage events, and (7) determining sensitivities of failure modes to design parameters (e.g., fiber volume fraction, ply thickness, fiber orientation, and adhesive-bond thickness).

GENOA-PFA progressive failure analysis is now ready for use to investigate the effects on structural responses to PMC material degradation from damage induced by static, cyclic (fatigue), creep, and impact loading in 2D/3D PMC structures subjected to hygrothermal environments. Its use will significantly facilitate targeting design parameter changes that will be most effective in reducing the probability of a given failure mode occurring.

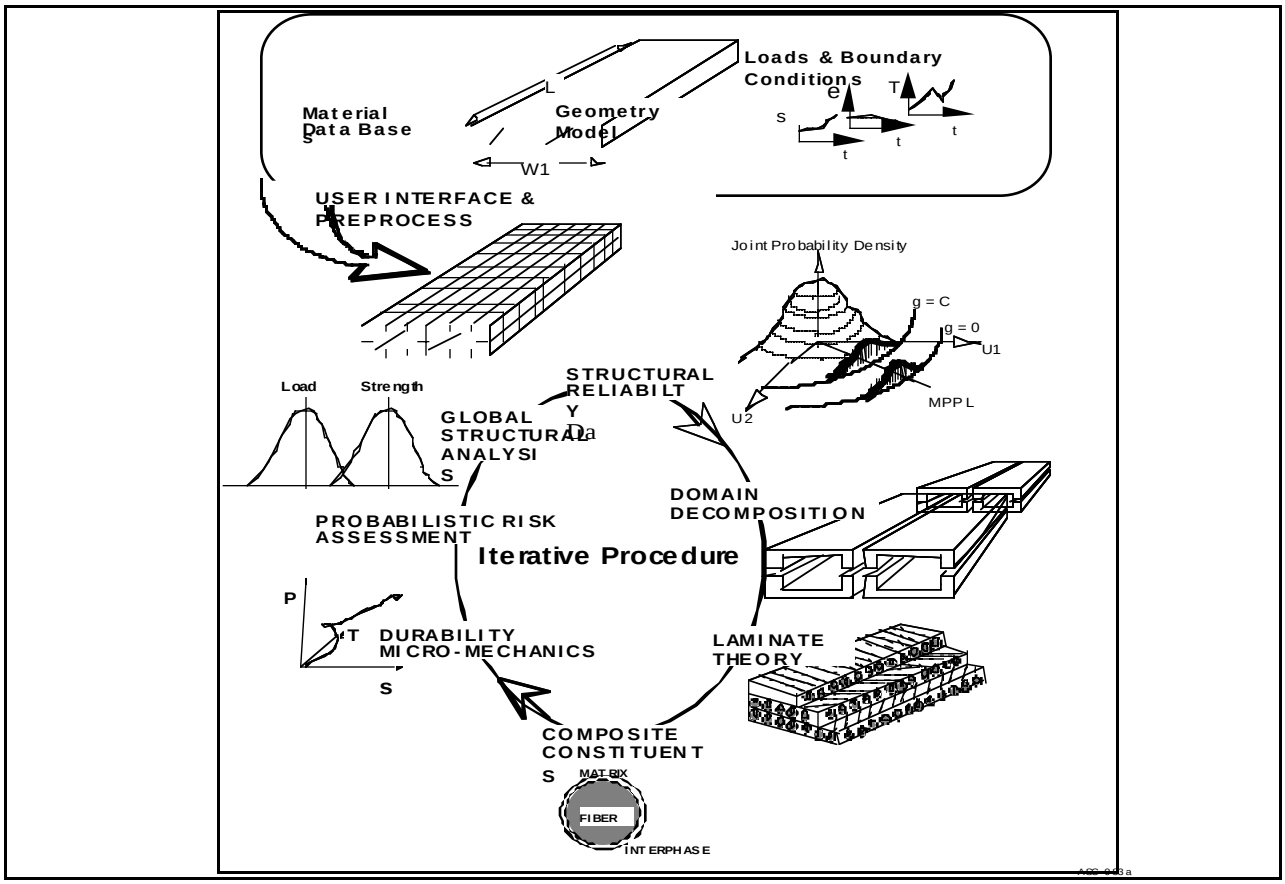

Figure E-2. GENOA, a Parallel Processing Software For Structural Analysis of Polymer Matrix Composites, Utilizes a Hierarchical Multi-Level Approach on Macro and Micro Scales

Development of 2D/3D PMC progressive failure analysis took into account requirements and verification criteria defined by key industry sources to help designers meet manufacturing and FAA requirements relative to:

1. Durability and Damage Tolerance – by providing accurate numerical simulation of a design structure subjected to thermal-mechanical service environments of static, fatigue, and impact damage.
2. Damage Initiation Location and Propagation Pattern – by showing designers where design strengthening might be needed or the effect of reducing structure thickness to save weight.
3. Probabilistic failure analysis – by providing designers with sensitivities of component durabilities (at critical failure events: crack initiation, crack propagation, final failure) with respect to design parameters (i.e. fiber volume fraction, fiber orientation, fiber strength, fiber stiffness, matrix strength).
4. Virtual Testing – by accurately simulating results of projected experimental testing approaches to optimize/minimize experimental testing requirements.
5. Manufacturing of Preform Composite Net Part Shape – by simulating reshaping to establish initial fiber preform braid, fiber orientation angle changes, buckling, and scissoring lock-up conditions.
6. Equivalent Laminate Properties of 2D/3D woven/braided/Stitched composites – by simulating: a) Equivalent laminate moduli, moisture property, thermal property, and heat conductivity, and

b) Degradation of material properties due to environmental (moisture, thermal), manufacturing (void, defects, residual strains), etc.

Key GENOA-PFA simulation applications shown in Table E-3. Demonstrated achievement of the overall goal of providing a validated commercial PFA tool that an analyst or designer can use to accurately and rapidly evaluate durability and damage tolerance by progressive failure analysis in design of PMC structure and thereby reduce design cost and time to market. Specific Phase II efforts were directed to modify an existing GENOA-PFA precursor (Phase I) software to:

1. Model a variety of 2D/3D woven/braided/stitched laminate fiber architectures
2. Improve flexibility and portability by modularization and standardization
3. Refine FEM meshing as necessary at any iteration
4. Simulate progressive fracture under static, cyclic fatigue, and impact loading
5. Simulate reshaping of braided fiber preforms to assist manufacturing
6. Perform probabilistic failure analyses
7. Generate equivalent woven/braided/stitched composite material properties
8. Perform virtual testing
9. Provide interface capability to commercially used software (i.e. NASTRAN, PATRAN)
10. Improve graphics for visualization of simulated results
11. Provide the capability to show results in animated graphics (movie) form
12. Update User's and Theoretical manual
13. Allow Porting of GENOA-PFA software to Unix (HP, SGI, IBM), and NT operating systems

Table E-3. PMC Progressive Failure simulation Key Multi-disciplinary Features

Features	PFA Loading Condition	Functionality
Durability And Damage Tolerance-	Static Static cycling Fatigue-harmonic loading Fatigue-random Impact (pseudo–static) Impact -dynamics)	• Damage initiation and location (fiber, matrix or interface) within a lamina, • Percent of contributing failure mechanisms • Failure location , and fracture path within lamina, and structure • Residual strength after damage • Prediction of life cycle • Prediction of s-n curves, da/dn, and fracture toughness • Stress intensity factor • Prediction of material property degradation cycle • Animated graphics of pfa process
Virtual Testing	Static Static cycling Fatigue-harmonic Impact (pseudo–static) Impact –dynamics)	• Contour plots of the global strain/stress fields at crack initiation, propagation, and failure • Plot of far-field applied load vs. Deflection (deflectometer) • Plot of applied load vs. Strain (strain gage) • Photo-elastic fringe simulation (isochromatic, and isoclinic) • Local and global energy release rates vs. Applied loads representing acoustic emissions • Plot of crack length vs. Applied load to show the fracture toughness • Plots of stress vs. Strain at selected locations • Predictions of static failure resulting from discrete source damage (dsd) • Prediction fatigue damage initiation at multiple sites • Prediction of required tests based on sensitivity of failure criteria • Movie play of virtual testing process
Probabilistic Failure Analysis	Static Static cycling Fatigue-harmonic Impact (pseudo–static) Impact - dynamics	• Uncertainty evaluation of material strength to material parameters • Sensitivities of design requirements to design parameters. • Predicting the degree to which design parameters contributed to failure • Generation of cumulative distribution functions (cdf) for failure strength evaluation • Probability of time to failure • Margin of safety predictions
Manufacturing of Preform Composite Net Part Shape	Static	• Fiber orientation and volume fraction changes • Attainable best fit to a shape, • Minimize occurrences of failure (buckling, fiber wrinkling) • Simulating multiple reshaped preforms of different sizes interleaved with woven sheet strips • Transferring fiber orientation data directly to design and manufacturing process software • Animated graphics of manufacturing process
Equivalent Laminate Properties	Laminated, 2D/3D woven/braided/Stitched	• Equivalent laminate moduli, moisture property, thermal property, , and heat conductivity • Degradation of material properties due to environmental factors (moisture, thermal), or manufacturing (voids, defects, residual strains) • Plot of ply strength vs. Ply stress

Realization of PFA required verification of the software system with experimental test results of fiber reinforced composite primary structures. This was recently accomplished by Alpha STAR with key industry partners in the major aerospace composite programs described in the following .

The Boeing Advanced Composite Technology (ACT) Wing Program under NASA sponsorship was aimed at analysis and experimental verification of DSD in S/RFI commercial aircraft. Alpha STAR supplied virtual testing predictions to Boeing in sealed envelopes prior to experimental testing of eight (four in tension and four in compression) stitched fiber reinforced-resin matrix composite three stringer test panels with variations in stringer heights and thicknesses. Predicted and experimental ultimate tension and compression loads for the wing panels agreed within -3.8% to 6.8%. Other simulation predictions supplied to Boeing in sealed envelopes and compared with experimental test results were: 1) fracture propagation patterns, 2) crack turning (Figure E-3) caused by a failure mode change in tension panels, 3) contour plots of global strain/stress fields at crack initiation, propagation, and failure, 4) plots of far-field

applied load vs. bend deflection, 5) plots of applied load vs. strain, 6) photo-elastic isochromatic and isoclinic fringe patterns, 7) plot of local and global energy release rates vs. applied loads, 8) crack length vs. applied load plots related to fracture toughness, and 9) plots of stress vs. strain at selected locations. Simulation and experimental results agreed well.

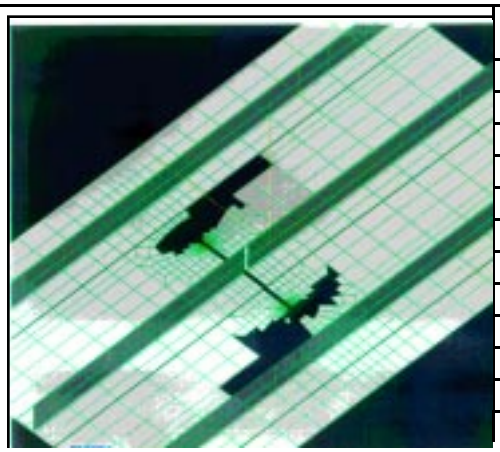

Failure Mechanism	% at Crack Initiation	% at Crack Turning	% at Final Fracture
Longitudinal tensile	14.3	32.5	32.6
Longitudinal Compressive	28.3	17.7	14.7
Transverse tensile	28.3	17.7	15.5
Transverse Compression	5.6	20.8	7.5
Normal tensile	0.0	0	0.0
Normal Compression	0.0	0	0.0
In Plane Shear (+)	11.6	5.56	13.2
In Plane Shear (-)	11.6	5.56	13.8
Transverse Normal Shear	0.0	0.0	0.0
Transverse Normal Shear (-)	0.0	0.0	1.0
Longitudinal Normal Shear	0.0	0.0	1.0
Longitudinal Normal Shear (-	0.0	0.0	1.0

Figure E-3. Contribution of Failure Modes at Damage Initiation, Crack Turning and Final Fracture Events

Figure E-4a shows a 3-stringer panel mounted in the load frame for a tension test. Generally, three-stringer tension panel failures were characterized by initiation of damage at the radii of the saw cuts. Increasing the applied load on the panels caused the tension failure damage to rapidly propagate transversely to the loading direction until it reached the inner flanges in the outer stringer regions. From this location the damage propagated in a vertically oriented translaminar shear failure mode parallel to the flanges in the loading direction in all four tension test articles. Stable propagation of the shear failure mode continued until the damage neared the loading tabs resulting in catastrophic panel failure (Figure E-4b).

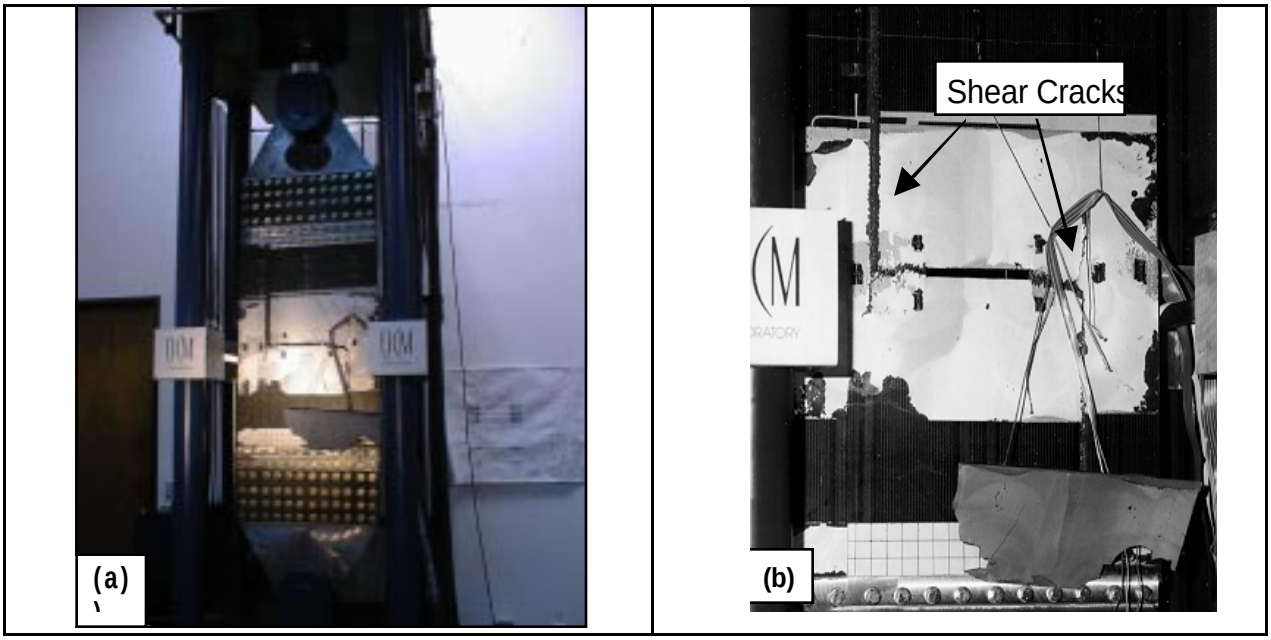

Figure E-4. (a) Tension Test Panel Mounted in the Load Frame, (b) Translaminar Shear Damage Zones in Tension Test Panel

Figure E-5a shows a 3-stringer panel mounted in the load frame for a compression test. A close-up view of one edge of a failed compression test article (Figure E-5b) shows a failure typical of those observed in the compression test articles. The compression failures displayed classic transverse shear surfaces typically observed in stitched composites. No stringers were pulled off of the panel skin.

Figure E-5a. Compression Test Panel After Failure

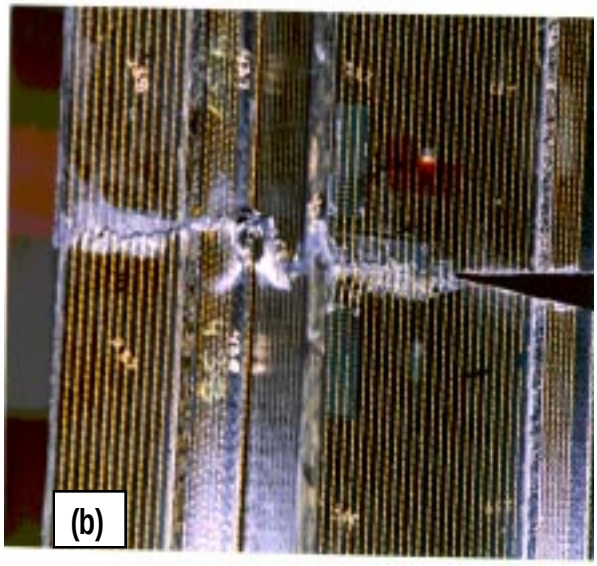

Figure E-5b. View Of Failure Zone Compression Test Panel

The Boeing Mini Space Plane Maneuverable Vehicle (SMV) under the Air Force SMV wing box and center fuselage demonstration program. The SMV was an all composite (fiber reinforced resin matrix) structure that included honeycomb construction. Simulations of the SMV center fuselage and wing box attachments were directed to predict the failure load and bracket the location of failure for a projected experimental test in which upward loads would be applied to the wing box attachment points while the fuselage front was subjected to rotational torque (Figure E-6). Virtual testing was conducted with a detailed FEM mesh (Figure E-7) and the results were presented prior to experimental testing. The predicted failure load was within 2.1% of the experimental failure load and the predicted failure location was in close agreement with the actual failure location.

The successful verification of the PFA analytical tool on key industry projects (Table E-4) reduced experimental testing requirements substantially thereby shortening the design time for future composite aircraft by:

- Reducing uncertainties in the understanding of damage formation in 2D/3D PMC structure
- Validating cost effective means for progressive failure analysis of 2D/3D PMC test articles
- Reducing uncertainties in analytical models
- Validating methods for analytical predictions of damage growth and residual strength in PMC structure
- Demonstrating the durability and robustness of composite primary PMC structures

Figure E-6. Anti Symmetric Test Limit Loading Applied To SMV Fuselage and wing box

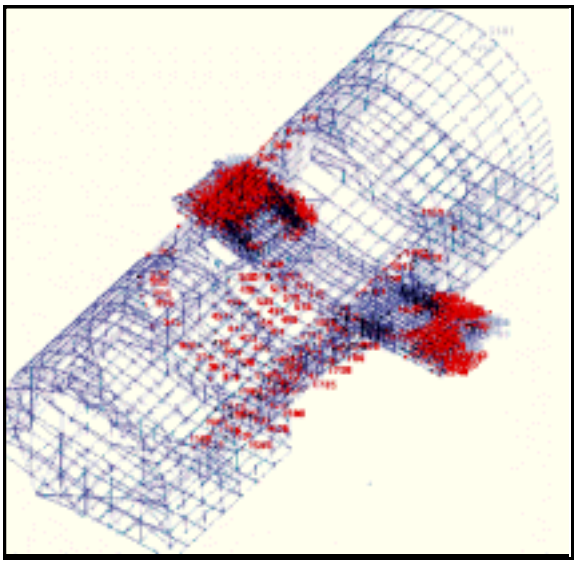

Figure E-5. Identification of Damaged Nodes Location

Table E-4. Demonstrated Progressive Failure Analysis (PFA) Capabilities

Verified PFA Simulation	Primary Methodology	Project	Company/Agency
Residual Strength, Fracture Pattern, Design Curves, DSD Effects, & Stress/Strain Distributions in S/RFI Composite Structure	PFA under static loading of Stitched/Resin Film Infusion	Analytical and Experimental Verification of DSD In S/RFI Commercial Aircraft	Boeing -AST/NASA-LaRC
Comparison with full scale X40 test article (Residual Strength, failure location)	PFA under static loading of laminated sandwich (tape, honeycomb, fabric) structure	X40 Structural Test Demonstrator	Boeing/NASA-LaRC
Support full scale design of laser reactor housing (crack initiation, residual Strength, and failure location)	PFA (under static loading) including, probabilistic analysis of laminated sandwich (honeycomb, fabric) structure	Air born Laser Reactor housing	DOD/Boeing/TRW/STI-Optronics
Acoustic fatigue failure from random vibration shake test	PFA (under acoustic random loading)	Lockheed F22 adhesively bonded airfoil coupon joints	Lockheed
Determining Changes in Orientation Angles, Sissoring Lock-up, and Preform Geometry on Reshaping Braided/Woven Fiber Preforms	Fiber Preform Reshaping in manufacturing	NASA/AST composite affordability	NASA-LeRC
		GE-90 Turbine Engine Blade	General Electric Aircraft Engine
		Windmill Generator Blade	Sandia National Laboratory/ Goldsworthy
Residual strength after projectile Impact on PMC component	PFA (under impact loading)	Verification for PMC component design	NASA-White sands
Probabilistic fatigue life analysis of Integrally assembled structure (IAS) panel lap joint in the presence of multi site damage (MSD)	PFA of riveted orthotropic aluminum structure (under static and fatigue loading) including, probabilistic analysis	Verification for 747 Crown Panel component redesign	Boeing (Long Beach) NASA-LaRC
Progressive and Probabilistic fatigue life analysis of composite reinforced structure	Laminate analogy for composite enhanced concrete structures	Simulation of composite reinforced Concrete arch, and panels for repair of infrastructure component redesign	National Institute of Standard (NIST)

1.0 Summary of Phase II

1.1 A NEW APPROACH TO PROGRESSIVE FAILURE SIMULATION

GENOA-PFA code is an commercial version of The CODSTRAN (COmposite Durability STRuctural ANalysis) computer code, [1] simulates damage initiation, damage growth, and fracture in PMC materials under various loading conditions, taking into account the effects of residual stresses and environmental conditions. The simulation of progressive fracture by CODSTRAN has been verified to be in reasonable agreement relative to experimental tensile test results [2]. CODSTRAN has enabled investigation of the effects of: (1) composite degradation on structural response [3], (2) global fracture toughness of composite structures [1], (3) effect of the hygrothermal environment on durability [4], (4) damage progression in composite shells subjected to internal pressure [5], (5) simulation of steel pressure vessel fracture [6], (6) and damage progression in a discontinuously stiffened composite panel subjected to compressive loading [7].

CODSTRAN's computational simulation approach bypasses traditional fracture mechanics and instead utilizes an alternative evaluation method. CODSTRAN can be used by the design engineer to obtain a detailed quantitative descriptions of damage initiation, growth, accumulation, and propagation up to ultimate fracture of a stitched PMC material.

When a composite structure undergoes progressive fracture, a significant amount of energy is expended. The cumulative Damage Energy Release Rate (DERR) per unit damage created is used as a measure of the overall resistance of the composite structure to damage propagation. The damage energy may be computed via computational simulation as the work done by the applied forces and pressures during the evolution of damage. The DERR is then defined as the ratio of the expended work to the amount of created damage. DERR exhibits a typical minimum value at a load level that signals an upper limit for damage tolerance. The levels of DERR during damage initiation and progression also indicate the structural resistance to damage propagation.

GENOA-PFA includes CODSTRAN modified for simulation of three dimensional composites (woven, brided, and stitched fiber orientations). The modular architecture of the GENOA software suite allows CODSTRAN to be supported by the other modules such as:1) GUI, post graphics, movie of damaged process, probability of failure due to damage, virtual testing, and 2D/3D equivalent material property generation, and degradation of material strength during the PFA.

1.1.1 Three Dimensional Composites

Three-dimensional composites are reinforced with three dimensional textile preforms, which are fully integrated continuous-fiber assemblies with multi-axial, in-plane and out-of-plane fiber orientations. These composites exhibit several distinct advantages, which are not realized in traditional laminates. First, because of the out-of-plane orientation of some fibers, three-dimensional composites provide enhanced stiffness and strength in the thickness direction. Second, the fully integrated nature of fiber arrangement in three-dimensional preforms eliminates the inter-laminar interface characteristic of laminated composites. Third, the suitability for application of textile preforming technology provides a unique opportunity for near-net-shape manufacturing of composite components with minimized cutting and joining of parts. Thereby reducing manufacturing costs.

Three-dimensional textile preforms can be categorized according to whether they are braided, woven, stitched. Braiding preforms are formed with three basic techniques, namely two-step, four-step and multi-step braiding. In the case of two step braiding (Florentine 1992), the axial yarns are stationary and the braider yarns move among the axial yarns. In four-step braiding, all yarn carriers change their positions in the braiding process and do not maintain a straight configuration. Multi-step braiding (Kostar and Chou

1994) is an extension to the four-step braiding. By allowing for both individual controls of a given track/column and the insertion of axial yarns, the range of attainable braid architecture is greatly broadened in multi-step braiding.

In woven preforms, there are two major categories. The first is the angle-interlock multi-layer weaving technique which requires interlacing the yarns in three dimensions. The warp yarn in this three-dimensional construction penetrates several weft layers in the thickness direction, and therefore the preform structure is highly integrated. The second is the orthogonal woven, for which the yarns assume three mutually perpendicular orientations in either a Cartesian coordinate system or a cylindrical coordinate system.

The process of stitching is mainly based upon an existing technology for converting two-dimensional preforms to three-dimensional ones. This process is relatively simple. The basic needs include a sewing machine, needle and stitching thread. Major concerns of the stitching operation include depth of penetration of the stitching yarns which limits, the thickness of two-dimensional preforms that can be stitch-bonded and reduces the in-plane properties by damaging in-plane yarns.

Three-dimensional knitted fabrics can be produced by either weft knitting or warp knitting processes. The technique of knitting is particularly desirable for producing preforms with complex shapes because the variability of the geometric forms is almost unlimited. The large extensibility and conformability of knitted preforms enable them to be designed and manufactured for reinforcing composites subject to complex loading conditions.

Even though three-dimensional (3-D) composites have attracted much interest due to their unique mechanical properties, such as enhanced transverse moduli and strength, improved shear resistance increased impact damage tolerance, the actual use of the 3-D composite material poses many problems in engineering design. The main problem comes from the complex geometry of 3-D composites. The fiber geometry is so complex that the geometric modeling itself is very difficult, much less accurate stress distributions. For example, in plain weave textile composites, there are many fiber tows (warp and fill) interlacing each other. There can be nesting of the fiber tows of one layer in adjacent layers. The existence of matrix pockets adds to the complexity of the geometry. Many research papers have been devoted to modeling the geometry of 3-D composites (Pierce 1987, Pastore and Ko 1990, Du and Chou 1991).

The inherent geometric complexity of 3-D composites makes a detailed stress analysis very formidable that most analytical and numerical techniques are restricted in predicting the stiffness properties. Only a few models have been developed for detailed stress analysisand strength prediction of textile composites (Woo and Whitcomb 1994, Yoshino et al 1981, Kriz 1989, Pastore et al 1993). To date, there is no information in the existing literature on simulating the entire procedure of damage propagation of 3-D composites.

1.1.2 Stiffness Properties of Three Dimensional Composites

The stiffness averaging method which was developed by Kregers et al (1978, 1979) is widely used to predict the deformation characteristics of a composite with three-dimensional reinforcement from the known mechanical properties of its components. The basic idea behind stiffness averaging method is to treat the fibers and matrix as a set of composite rods having various spatial orientations. The local stiffness tensor for each of these rods is calculated and rotated in space to fit the global composite axes. The global stiffness tensors of all the composite rods are then superimposed, with respect to their relative volume fraction, to form the composite stiffness tensor. This approach is also called the Fabric Geometry

Model (Pastore and Gowayed, 1994) or Orientation Averaging Method . The stiffness of the individual directions of reinforcement are averaged in accordance with the following expressions:

$$A_{jklm} = \frac{1}{V}\sum_{i=1}^{N} V_i A_{jklm}^{(i)}$$

$$V = \sum_{i=1}^{N} V_i$$

Where A_{jklm} represents the components of the stiffness tensor of the three-dimensionally reinforced composite: V_i is the calculated volume of the *i-th* direction of reinforcement; and N is the number of discrete directions of reinforcement ($N \geq 1.$)

Ko (1986) presented a geometric model for a three-dimensional braid composite using the concept of average cosine to evaluate the tensile strength and modulus. The three-dimensional braid composite was divided into a series of unit cells with yarn segments idealized as being straight in a unit cell (Figure 1-1).

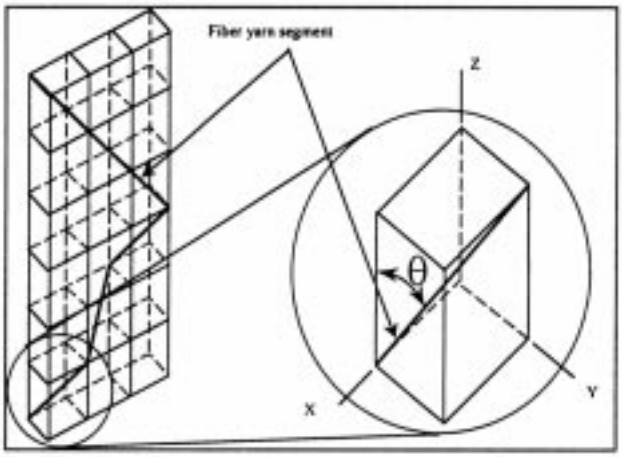

Figure 1-1. Idealized Fiber Yarn Segment in Unit Cell of 3D Braid Composites

An average representation of yarn orientation was obtained using the average cosine of yarn angles:

$$\cos\bar{\theta} = ND_y / D_f$$

Where N = number of yarns in the fabric, D_y = yarn linear density, D_f = fabric linear density. The predicted composite tensile strength and modulus in the longitudinal direction based on the average angle of yarn, in general, were within 20 percent of the experimental results.

1.2 GENOA-PFA Simulation Of 2D/3D Woven/Braided/Stitched PMC Structure

GENOA is an integrated structural analysis/design software suite that can be easily ported to any hardware platform using a UNIX and NT operating systems. It cost-effectively simulates aerospace structural components made of monolithic and 2D/3D braided/laminated/stitched/woven composite materials to predict their residual strengths, ultimate strengths, reliability, and durability. These predictions take into account degradation of material properties due to (1) initiation and growth of damage under static, dynamic, thermal, impact, creep, and low/high frequency cyclic fatigue loading

conditions, and (2) defects introduced by manufacturing and in-service operations and environments. GENOA simulations utilize finite element modeling with 3/D element finite element meshes to allow determination of (1) through-the-thickness responses, (2) effects of material properties and defects (voids, fiber weaviness, residual stress) on global static and cyclic fatigue strengths, (3) crack initiation, and growth to failure under static, cyclic, creep, and impact loads, (4) progressive fracture to determine durability and damage tolerance, (5) the contribution of the various composite failure modes involved in critical damage events, and (6) sensitivities of failure modes to design parameters (e.g. fiber volume fraction, ply thickness, fiber orientation, and adhesive bond thickness).

1.2.1 Executive Controller System (ECS) and Graphic User Interface (GUI)

The ECS and GUI are the main modules controlling GENOA. The ECS module is menu driven and serves the function of accessing and inter-connecting all of the GENOA modules. The GUI module is driven by icons and menus to provide convenient means of (1) visualizing results, (2) importing CAD models from PATRAN or NASTRAN, and (3) exporting data to other software systems such as NASTRAN and PATRAN. The GUI is written in the C language, employs a standard graphical library (X11 Motif and OPENGL) and has on-line help options (Figure 1-2) for preparation of input, contour plotting, and post processing plotting. The GUI provides visualization of updated (1) FEM meshes, (2) FEM stresses, strains, and photoelastic fringe patterns, (3) ply stresses, (4) micro-stresses, (5) damage locations, and (6) percent contribution of failure modes. It also provides plots showing the history of strain, TDERR, DERR, percent-damage, and strength degradation.

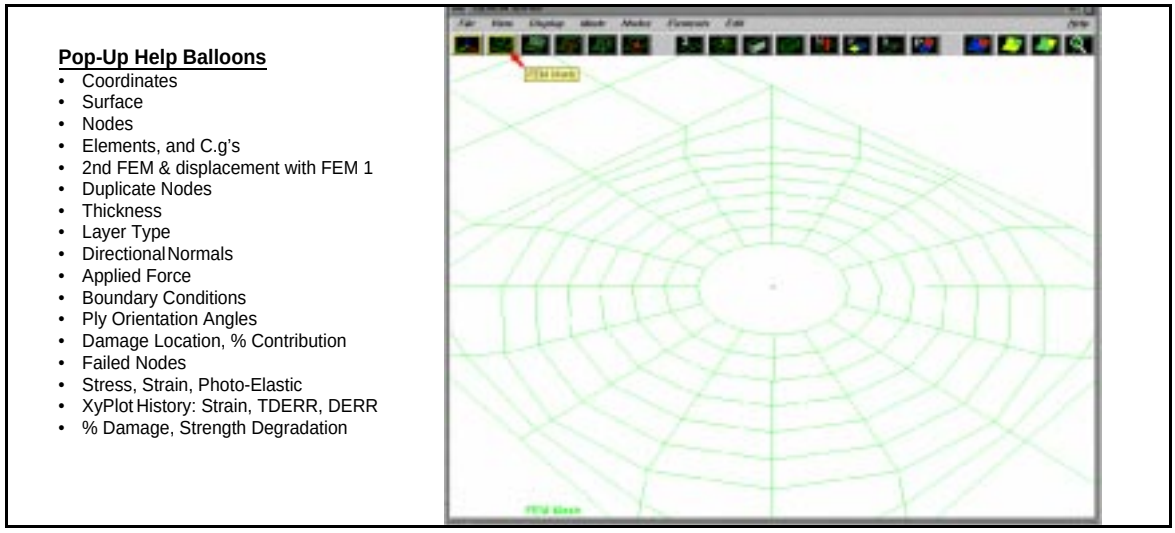

Figure 1-2. Pop-up Help Balloons Inform The User Reviewing Options Available In This Close-up View Of The Center Of A Model

The GENOA-PFA code, used for analyses in this program, is an integrated, open-ended, stand alone computer code utilizing (1) micro and macro composite mechanics analysis, (2) finite element method (FEM) analysis, and (3) damage evaluation methods. Calculated material stiffness values are input to the finite element analysis module that models composite materials with anisotropic brick and thin shell elements. As shown in Figure 1-3, GENOA-PFA utilizes an iterative analysis approach to simulate damage accumulation in a structure. The overall evaluation of composite structural durability is carried out in the damage-tracking module that incrementally evaluates composite material degradation in a structure subjected to a specified load spectrum. The composite damage-tracking module evaluates damage initiation/progression in a structure based on the FEM analysis results and failure criteria that guide the synthesis of structural stress redistribution due to material degradation. The damage-tracking

module also relies on a composite mechanics module (GEN-PMC) for material property data needed to characterize lamina and laminate micromechanical behavior.

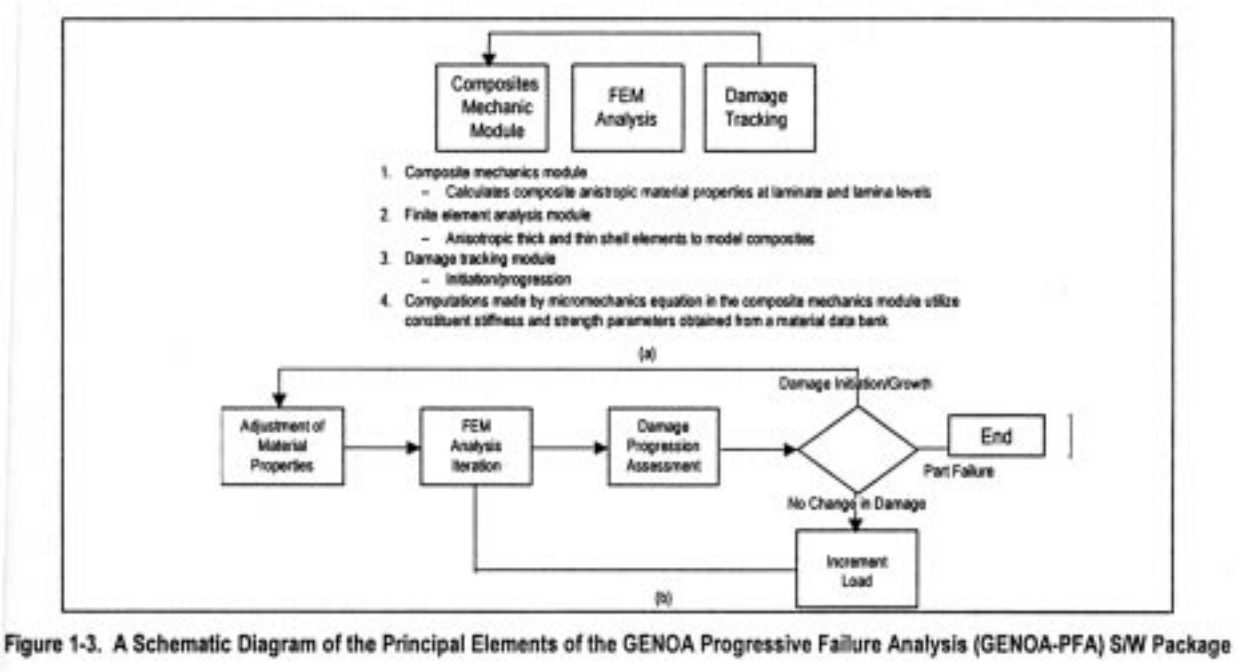

Figure 1-3. A Schematic Diagram of the Principal Elements of the GENOA Progressive Failure Analysis (GENOA-PFA) S/W Package

The FEM module used in GENOA-PFA was originally derived from the MARC analysis code developed over 20 years ago. This software development lineage results in GENOA-PFA being a nodal based finite element code. The FEM module library contains 4-node plate and 8-node brick elements suitable for use in structural analyses. The 4-node plate element is most suited for extended analysis since the use of Reissner-Mindlin theory in its formulation allows accounting for transverse shear deformations in a structure.

1.2.2 The Damage Tracking Process

Damage tracking is carried out in the damage progression module that keeps track of composite degradation for the entire structure. The damage progression module relies on the composite mechanics module for micromechanic and macromechanic analysis and uses the FEM analysis module to obtain generalized stresses and displacements in a composite structure.

Figure 1-4 shows an example of GENOA-PFAs damage tracking sequence as the load on a structure is increased. A damage equilibrium state is defined as existing when an incremental load increase does not either initiate or exacerbate damage. As the load is increased a point is reached (Location 1 in Figure 1-4) where there is an assessment of initial composite material damage based on the 14 failure criteria. According to the operative failure criteria, material properties are then degraded for use in FEM iterations to reevaluate the now damaged structure at the damage initiation load. The applied load at a given damage event is maintained and FEM iterations continued as damage accumulates (Locations 2, 3, and 4 in Figure 1-4) until an equilibrium damage state is again reached or until global structural failure occurs (Location 5 in Figure 1-4).

GEN-PMC is called before and after each FEM analysis to update composite properties based on the fiber and matrix constituent characteristics and the state of damage in the composite lay-up. Through-the-thickness laminate properties computed by GEN-PMC considers the elastic moduli of membrane

terms, bending terms, membrane-bending coupling terms, bending gradient terms, and shear terms. The finite element analysis module accepts the GEN-PMC generated properties for each node of a structural model under evaluation and then performs a structural analysis to determine the effect of a given load increment on the generalized nodal force resultants and deformations. The new values so determined are supplied back to the GEN-PMC module that evaluates the nature and amount of local damage, if any, in the plies of the composite laminate.

Failure Index Process/Description
1. Ply failure indicates initial damage • Properties are degraded • Reconstitute a new FEM reanalysis is conducted under the same load
2. Damage accumulation • More degradation, possible composite ply failure
3. Damage stabilization • No additional damage, with structure in equilibrium
4. Damage propagation
5. Analysis stops at nodal fracture

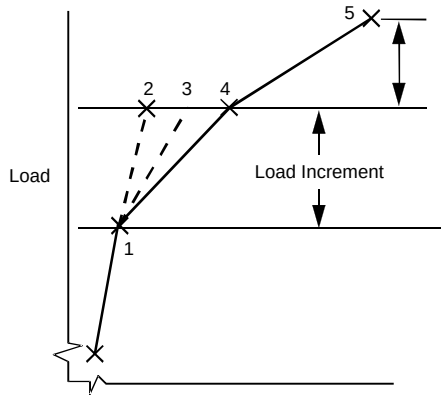

Figure 1-4. Damage Tracking Expressed in Terms of Load vs. Displacement

1.2.3 Failure Evaluation Approach

GENOA's approach to failure evaluation involves comparison of computed constituent properties with criteria of stress limits, distortion energies, degree of relative ply rotation, global scalar-damage, and global damage energy release rate (DERR). Of the 14 local failure criteria in Table 1-1 used by GEN-PMC to evaluate damage, the first 12 are stress limits computed by the micromechanical equations in GEN-PMC based on a material's constituent stiffness and strength values. (The equations used for ply stress limits are given in "ICAN User's and Programmer's Manual", NASA Technical Paper 2515, March 1986.) In addition to the 12 failure criteria based on stress limits, interply delamination due to relative rotation of plies and a modified distortion energy (MDE) failure criterion that takes into account combined stresses are included as failure criteria. If ply damage is predicted due to longitudinal tensile or compressive failure, ply stiffness is reduced to zero at the damaged node. On the other hand, if ply damage is predicted due to transverse tensile, compressive, or shear failures, only the matrix stiffness is degraded and the longitudinal tensile stiffness of fibers is retained.

Table 1-1. Fourteen Damaged Modes Considered In GENOA

Mode of Failure	Description
Longitudinal Tensile	Fiber tensile strength and the fiber volume ratio.
Longitudinal Compressive	Rule of mixtures based on fiber compressive strength and fiber volume ratio Fiber microbuckling based on matrix shear modulus and fiber volume ratio, and Compressive shear failure or kink band formation that is mainly based on ply intralaminar shear strength and matrix tensile strength.
Transverse Tensile	Matrix modulus, matrix tensile strength, and fiber volume ratio.
Transverse Compressive	Matrix compressive strength, matrix modulus, and fiber volume ratio.
Normal Tensile	Plies are separating due to normal tension
Normal Compressive	Due to very high surface pressure i.e. crushing of laminate
In Plane Shear (+)	Failure due to Positive in plane shear with reference to laminate coordinates
In Plane Shear (-)	Failure due to negative in plane shear with reference to laminate coordinates
Transverse Normal Shear (+)	Shear Failure due shear stress acting on transverse cross section that is taken on a transverse cross section oriented in a normal direction of the ply

Transverse Normal Shear (-)	Shear Failure due shear stress acting on transverse cross section that is taken on a negative transverse cross section oriented in a normal direction of the ply
Longitudinal Normal Shear (+)	Shear Failure due shear stress acting on longitudinal cross section that is taken on a positive longitudinal cross section oriented in a normal direction of the ply
Longitudinal Normal Shear (-)	Shear Failure due shear stress acting on longitudinal cross section that is taken on a negative longitudinal cross section oriented in a normal direction of the ply
Modified Distortion Energy Criterion	Modified from Distortion Energy combined stress failure criteria used for isotropic materials
Relative Rotation Criterion	Considers failure if the adjacent plies rotate excessively with respect to one another

Two global failure criteria, a scalar-damage variable, and a DERR, are incorporated in the FEM analysis module. The scalar damage variable is defined simply as the ratio of the volume of damage to the total volume of the composite material affected by the operative damage mechanisms. It is useful for assessing the overall degradation of a given structure under a prescribed loading condition and its rate of increase provides a measure of structural propensity for fracture. The DERR is defined as the rate of work done by external forces in producing incremental damage in a structure. It can be used to evaluate structural resistance to damage propagation at different stages of loading.

Stress limits, needed to establish stress failure criteria, are determined by GEN-PMC as follows:

- Ply longitudinal tensile strength is computed based on fiber tensile strength and the fiber volume ratio.
- Ply longitudinal compressive strength is taken as the minimum value found using: (1) rule of mixtures based on fiber compressive strength and fiber volume ratio, (2) fiber micro-buckling based on matrix shear modulus and fiber volume ratio, and (3) compressive shear failure or kink band formation that is mainly based on ply intralaminar shear strength and matrix tensile strength.
- Ply transverse tensile stress limits are computed from matrix modulus, matrix tensile strength, and fiber volume ratio. Similarly, the ply transverse compressive stress limits are computed from the matrix compressive strength, matrix modulus, and fiber volume ratio.
- Ply intralaminar shear strength limit is computed based on matrix shear strength, matrix shear modulus, and the fiber volume ratio.
- The interlaminar shear strength limit is computed based on matrix shear strength, matrix shear modulus, fiber volume ratio, and fiber transverse shear modulus.

Failure Evaluation Method

Progressive damage and fracture evaluations are carried out by imposing failure criteria locally within unit subvolumes with reference to the local coordinates of the composite materials. At each individual load step, stresses in stitching and in-plane subvolumes obtained through the composite microstress analysis are assessed according to distinct failure criteria (Table 1-1). The first twelve modes of failure are associated with the positive and negative limits of the six local stress components in the material directions as follows:

$$S_{\ell 11C} < \sigma_{\ell 11} < S_{\ell 11T}$$

$$S_{\ell 22C} < \sigma_{\ell 22} < S_{\ell 22T}$$

$$S_{\ell 33C} < \sigma_{\ell 33} < S_{\ell 33T}$$

$$S_{\ell 12(-)} < \sigma_{\ell 12} < S_{\ell 12(+)}$$

$$S_{\ell 23(-)} < \sigma_{\ell 23} < S_{\ell 23(+)}$$

$$S_{\ell 13(-)} < \sigma_{\ell 13} < S_{\ell 13(+)}$$

The thirteenth failure mode in Table 1-1 is a combined stress or modified distortion energy (MDE) failure criterion that is obtained by modifying the usual distortion energy failure criterion. The modification takes into account the significant differences in the stress limits of the longitudinal and transverse directions of an orthotropic composite ply. Each component of ply stress is normalized with respect to its limiting strength. No relationship is assumed between normal and shear strengths. The MDE failure criterion has been demonstrated to be a good predictor of combined stress failure in composites. It may be considered as a variation of the Tsai-Hill theory (Tsai 1968). The MDE failure criterion (C. Chamis 1969) can be expressed as:

$$\left(\frac{\sigma_{\ell 11\alpha}}{S_{\ell 11\alpha}}\right)^2+\left(\frac{\sigma_{\ell 22\beta}}{S_{\ell 22\beta}}\right)^2-K_{\ell 12\alpha\beta}\frac{\alpha_{\ell 11\alpha}}{S_{\ell 11\alpha}}\frac{\sigma_{l22\beta}}{S_{l22\beta}}+\left(\frac{\sigma_{\ell 12S}}{S_{\ell 12S}}\right)^2<1$$

Where α and β indicate tensile or compressive stresses, $S_{\ell 11\alpha}$ is the local longitudinal strength in tension or compression, $S_{\ell 22\alpha}$ is the transverse strength in tension or compression, and the directional interaction factor is defined as:

$$K_{\ell 12\alpha\beta}=K'_{\ell 12\alpha\beta}\frac{\left(1+4\upsilon_{12}-\upsilon_{13}\right)E_{22}+\left(1-\upsilon_{23}\right)E_{11}}{\left[E_{11}E_{22}\left(2+\upsilon_{12}+\upsilon_{13}\right)\left(2+\upsilon_{21}+\upsilon_{23}\right)\right]^{1/2}}$$

where $K'_{\ell 12\alpha\beta}$ is a theory-experiment correlation factor.

The directional interaction factor approaches to unity for homogeneous isotropic materials.

The fourteenth failure criterion concerns interply delamination for which the interply layer is governed by:

$\Delta\phi_j = 0.5(\varepsilon_{cyy}-\varepsilon_{cxx})(\sin2\theta_i-\sin2\theta_{i-1})+ 0.5\varepsilon_{cxy}\ (\cos2\theta_i-\cos2\theta_{i-1})$

where:

θ = ply angle

ε = strain

if $\Delta\phi_j$ <0 interply delamination is assumed to have taken place.

1.2.4 GENOA Finite Element Analysis

After the micromechanics analysis module generates the elastic properties for a composite, the finite element analysis module is called to analyze the structural response. In general, the type of finite element model used depends on the complexity of the structure and the availability of computer resources. There are two possible choices for the analysis of composite structures. One is using anisotropic three-dimensional solid elements such as hexahedral or brick elements that accept the computed three dimensional composite properties directly. However, the modeling of a practical composite structure with three-dimensional elements is usually incorporated because it requires huge computer resources. The second option is to use anisotropic shell elements that use the composite plate/shell element properties. The use of anisotropic plate or shell elements to represent through-the-thickness properties of the woven/braided/stitched composite is more efficient computationally than using three-dimensional elements. Therefore, implementation was focussed on the use of plate/shell elements for finite element modeling. The finite element module accepts the force-deformation relations computed by the composite macromechanics module, and carries out a stress analysis to generate the generalized stresses *Nx, Ny,*

Nxy, Mx, My, Mxy, Qxz, Qyz for each node. The generalized stresses are supplied back to the composite mechanics module for the computation of local ply/stitch stresses and failure analysis.

1.2.5 Simulation of Damage Progression

After each finite element stress analysis, failure criteria are used to evaluate possible failure within each sub-volume of each ply at each node of the composite structure. Once the damage modes at each node are determined they are submitted to a damage index created to record the damage information for each node. The damage index contains the node number, the ply number, and the list of damage criteria that have become activated. When a new failure occurs at a sub-volume, the damage index is updated accordingly. The properties of each node-domain are degraded according to the node damage index.

If there is no damage after a load increment, the structure is considered to be in equilibrium and an additional load increment is applied. If damage occurs or escalates, the composite properties affected by the damage are degraded, the computational model is reconstituted with an updated finite element mesh and material properties, and the structure is reanalyzed under the same load increment. After reanalyzing, if there is any additional damage, the properties are degraded further and the structure is reanalyzed. This cycle continues until no further damage occurs.

The damage progression module keeps a detailed account of composite degradation for the entire structure. It also acts as the master executive module that directs the composite mechanics module to perform micromechanics and macromechanics analysis/synthesis functions, and calls the finite element module with thick shell analysis capability to model woven/braided/stitched laminated composites for global structural response.

1.3 SUMMARY OF PHASE II PROGRESS

Alpha STAR Corporation (ASC) and Clarkson University (CU) team have developed and integrated GENOA-PFA (Composite Durability STRuctural Analysis) software package for 2D/3D laminated braided composite for the use in progressive failure analysis. The tasks were divided into code development (Clarkson University) and code integration (Alpha STAR Corporation). The software was organized into three main libraries: 1) Finite Element Solver (FEML_MHOST_4.0, NESSUS_6.0); 2) Polymer Matrix Composite (ICAN2D/3D); and 3) Damage Tracking Solver (COD2 - COD8). The software was written in : 1) modularized; and 2) stand-alone versions.

1.3.1 Improve Flexibility And Portability By Modularization And Standardization

In the modularized version of GENOA-PFA each module can be substituted by another equivalent code by use of a simple interface code. Modularization of the original tightly knit architecture of GENOA was accomplished to greatly improved the flexibility of porting it to facilities with code preferences different from some codes in GENOA-PFA modules. The purpose of the modularization in development of GENOA-CODSTRAN was to 1) reduce the computer memory needed to run the software and 2) provide the ability to use other code modules. Thus, for example, if an NESSUS (MHOST upgrade) code is preferred it can be readily installed by means of a simple code written to make the input and output features of MHOST compatible with GENOA-PFA.

1.3.2 Methodology of Mesh Refinement in Progressive Failure Analysis

Mesh refinement for CODSTRAN software was conducted to improve simulation accuracy. In order to avoid unduly increasing FEM computation time, a simulation was begun with a computation time-saving coarse FEM mesh that was subsequently refined in only those regions delineated by elements connected to damaged nodes. Thus, when nodes suffer damage according to the damage criteria, those mesh elements connected to the damaged nodes are refined by the refinement module generating smaller elements to represent the damage regions. When all modes of composite resistance fail at a node, that node is deleted and new detached nodes are created at the same point. The number of new nodes created in place of deleted node is equal to the number of elements that connected to the deleted node. This approach allows tracking crack growth without loss of accuracy due to improper meshing.

Two approaches to mesh refinement were used in modification of stand alone CODSTRAN. In one approach each element connected to a damaged node is divided into five elements in place of the original element. In the second approach each element connected to a damaged node is divided into three elements in place of the original element. In either approach if any node connected to newly generated elements is damaged, those elements are further refined. This process is continued until final fracture occurs.

Late in the program progressive fracture simulation with adaptive mesh refinement became available to provide a higher resolution fracture pattern for a 3-stringer panel than obtained without adaptive mesh refinement (Figure 1-5).

Figure 1-6 compares the TDERR versus load fracture pattern simulated using adaptive and non-adaptive mesh techniques. Figure 1-7 compares damage volume versus load with and without utilizing the adaptive mesh technique. It was concluded that adaptive mesh refinement would provide a more accurate residual strength. There also were changes (shifts to a lower value) in the DERR minimum and maximum values calculated with and without the adaptive mesh refinement technique (Figure 1-8).

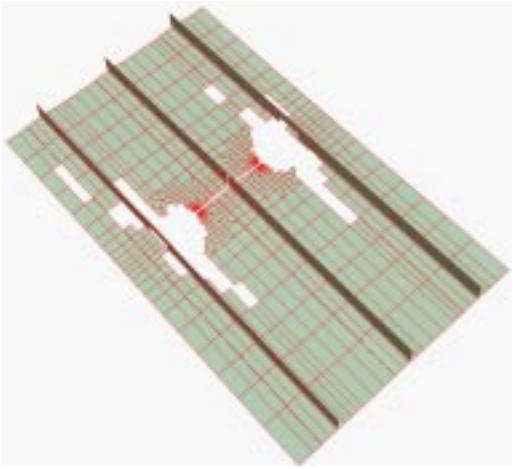

Figure 1-5a. Fracture Path and Damage Progression with no adaptive Meshing (1518 Nodes, 1208 Elements)

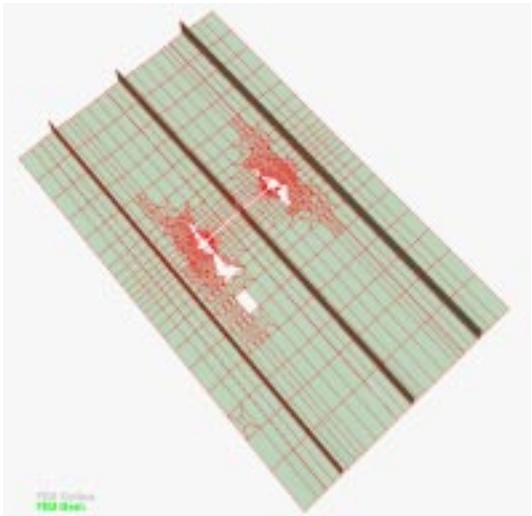

Figure 1-5b. Fracture Path and Damage Progression with adaptive Meshing (2148 nodes, 1707 Elements)

1.0 Summary of Phase II

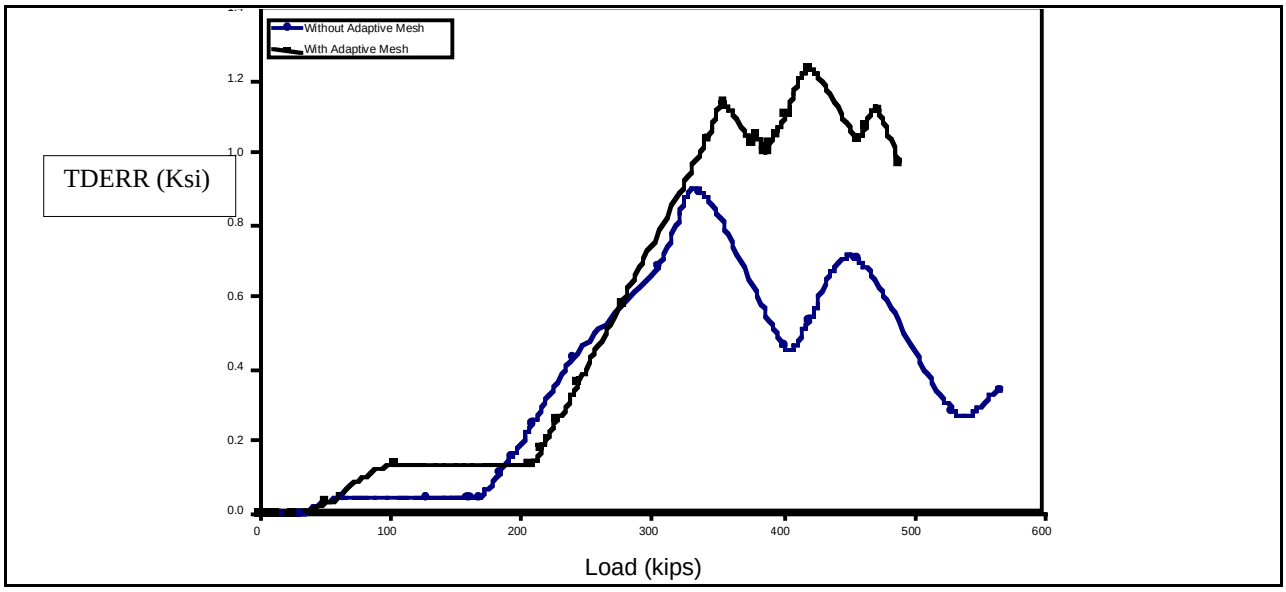

Figure 1-6. Total DERR versus Load Comparison of Adaptive Meshing and Non-Adaptive Meshing

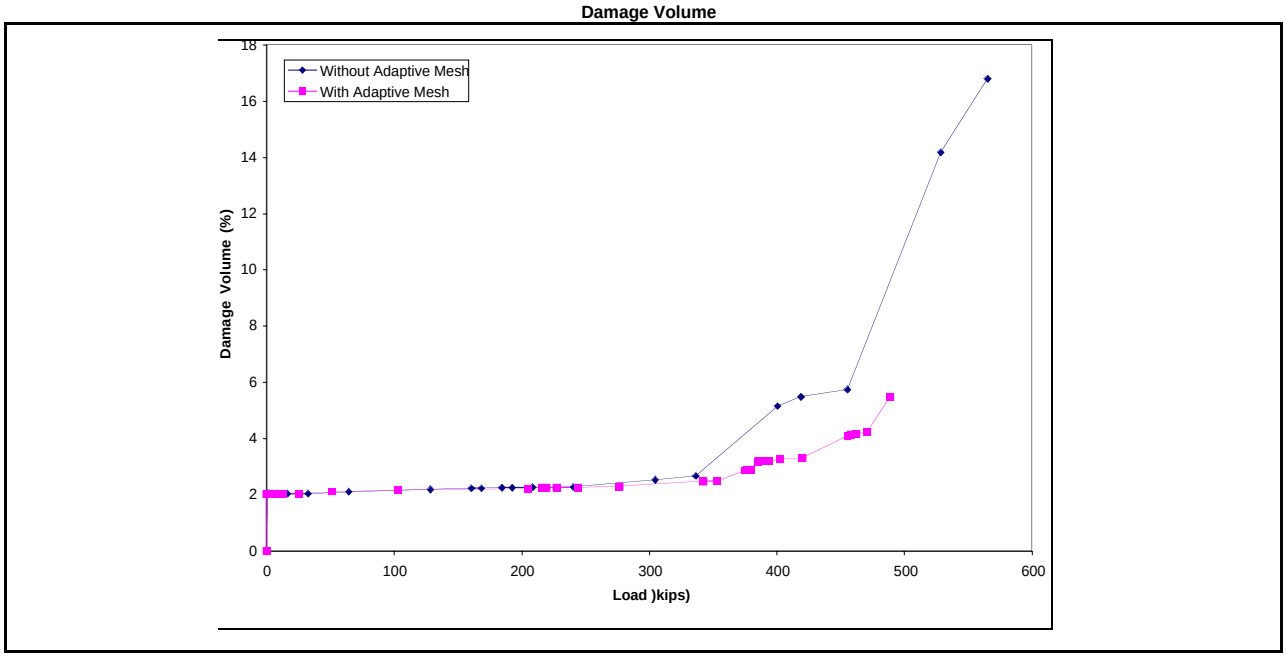

Figure 1-7. Percent Damage Versus Load Comparison of Adaptive Meshing and Non-Adaptive Meshing

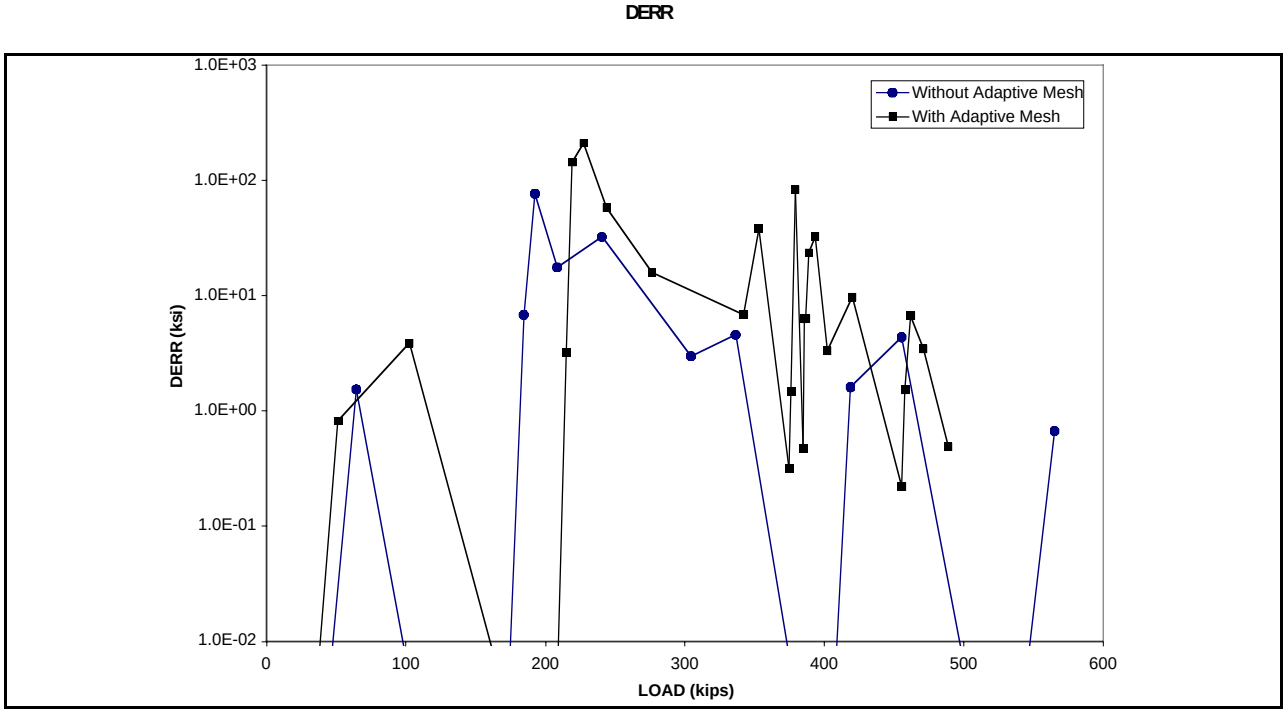

Figure 1-8. DERR Versus Load Comparison of Adaptive Meshing and Non-Adaptive Meshing

1.3.3 Re-evaluation with Restart

The Restart process allows a re-evaluation/re-analysis at a given progressive failure equilibrium point for which data from a previous simulation has been stored. The re-evaluation/re-analysis can be conducted with a modified (smaller) load increment thereby providing a commensurably more detailed and accurate rendition of critical damage events such as crack initiation, crack progression, and final failure. This reduces likelihood of missing a critical excursion of a parameter of interest. A helpful feature of GENOA-PFA is that of specifying the iterations at which critical events occurred that are of likely interest for more detailed study using Restart for re-evaluation.

The results of a restart simulation of the three stringer tension panel at 400 kips are presented in Figures 1-9, 1-10, and 1-11. Figure 1-9 compares the curves of original and restart TDERR values vs. load as derived from simulations of tension testing Panel. Figure 1-10 compares the curves of the original and restart DERR values Vs. load as derived from simulations of tension testing Panel. Figure 1-11 compares the curves of original and restart percent change in damage volume vs. load as derived from simulations of tension testing Panel. As shown by the increased number of data points the resolution of restart results is much greater than the original result because of the reduced size of the loading increments. This illustrates a very valuable aspect of the restart capability.

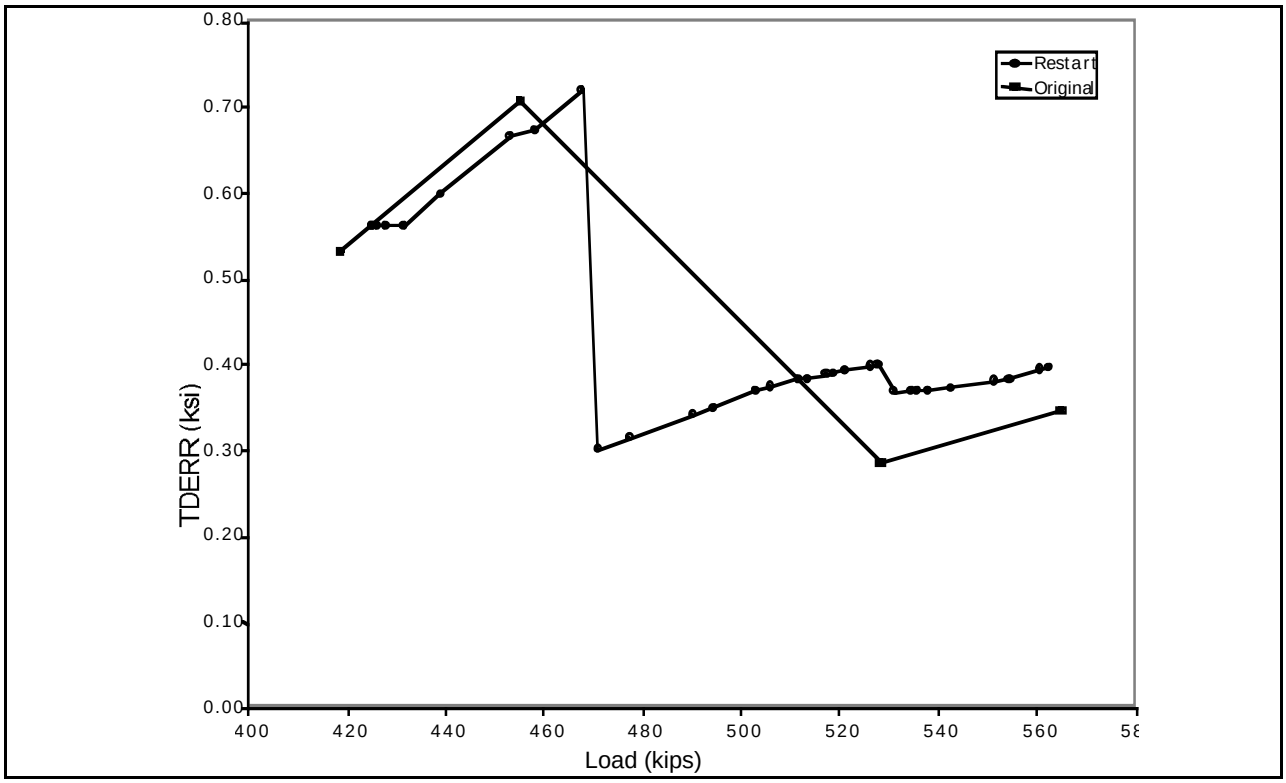

Figure 1-9. Comparison of Original Damage with Restart damage Versus Load from Simulation of Three Stringer Tension Panel

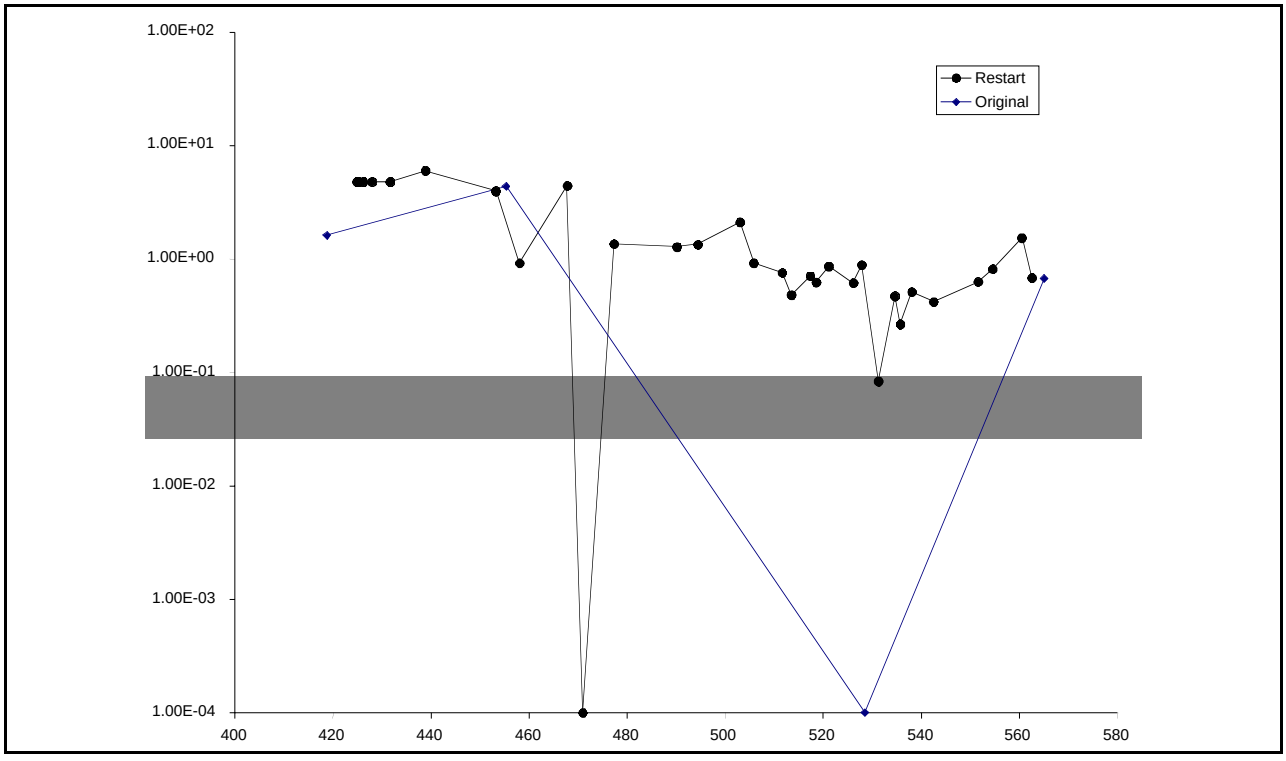

Figure 1-10. Comparison of Original DERR with Restart DERR Versus Load from Three Stringer Tension Panel

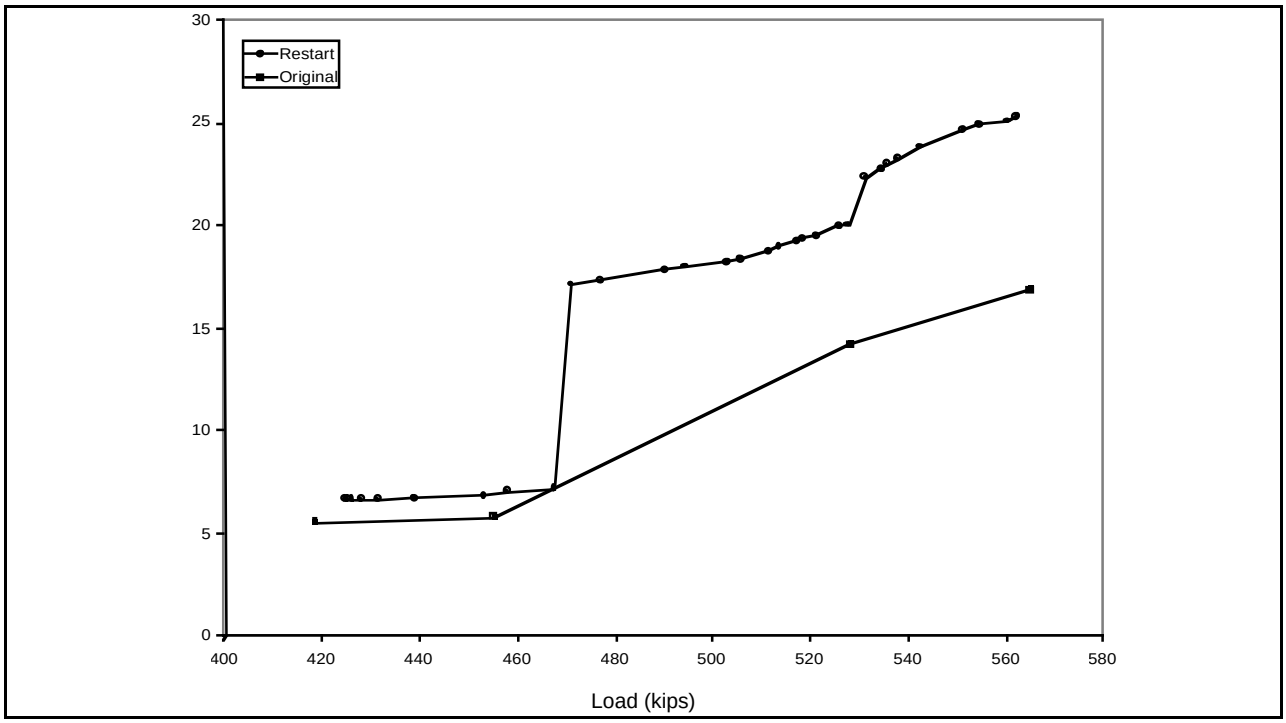

Figure 1-11. Comparison Of Original and Restart Percent Change In Damage Volume Vs. Load From Three Stringer Tension Panel

1.3.4 Modeling Of A Variety Of 2D/3D Woven/Braided/Stitched Laminate Fiber Architecture

Introduction of the methodology for analysis of composites with three dimensional weave patterns was accomplished by modifying the ICAN software. Figure 1-12 shows the three typical types of weave in woven 3D composites, namely, (a) layer to layer, (b) through the thickness angle interlock, (c) orthogonal interlock weaves.

In 3D woven composites, the stuffers and fillers alternate in layers through the thickness. The stuffers and fillers form a coarse 0°/90° array as shown in Figure 1-12 for most woven composites. The developed method allows the arbitrary orientation of stuffers and fillers in the X-Y plane. Through the thickness reinforcement, or warp weavers, may be oriented in any direction with reference to the 3D composite coordinate axes. Stitched composites may be modeled by weaver or stitch fibers that are oriented perpendicular to the X-Y plane and parallel to the Z-axis of the composite.

The developed 3D analysis software was verified by comparing failure predictions with experimental test data from 3D PMC structures: 1) Rockwell lightly and heavily compacted 3D woven PMC coupons, and 2) Boeing/NASA-LaRC ACT 3D coupon data.

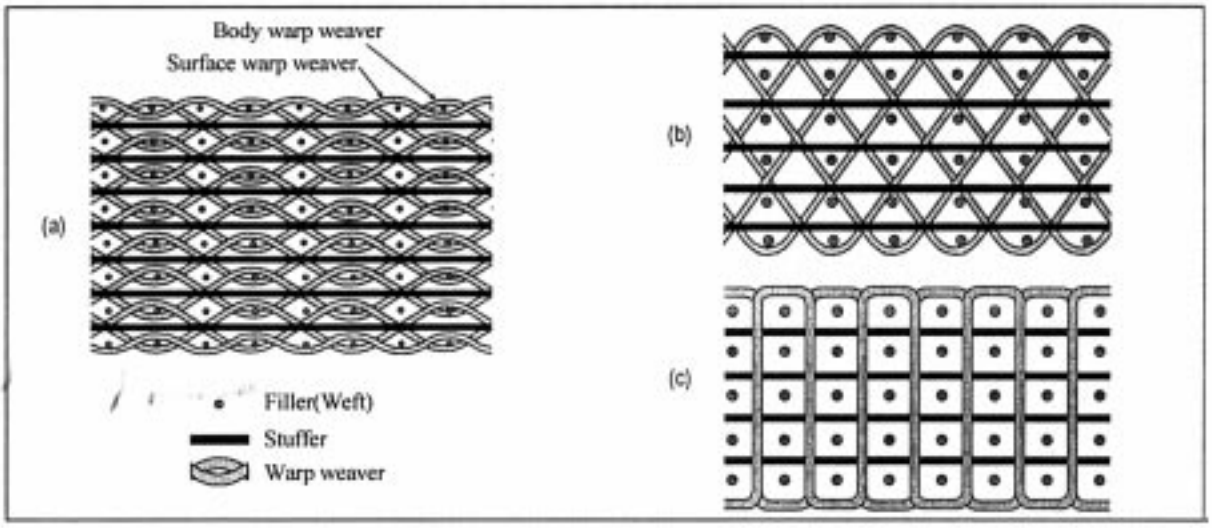

Figure 1-12. Schematics of (A) Layer-to-layer Angle Interlock, (B) Through-the- Thickness Angle Interlock, and (C) Orthogonal Interlock Weaves

1.3.5 Generate Equivalent Woven/Braided/Stitched Composite Material Properties

GENOA-PFA can predict the equivalent laminate moduli (Figure 1-13), moisture response, thermal properties, and heat conductivity of various composite systems. The ICAN module provides important design information (e.g., margin of safety) needed to optimize composite material systems, and facilitates designers in understanding fiber and matrix stress distributions in a composite system under load (Figures 1-14, and 1-15). Figure 1-16 shows an example of the ultimate strength prediction versus the applied stress to determine the margin of safety, and provide information relative to failed layers in a composite.

Alpha STAR Corporation has made available commercially PMC3, a part of GENOA-PFA. The PMC3 software incorporates the enhanced ICAN with a graphics user interface (GUI). This user-friendly software has already been acquired by The Boeing Company. ICAN is planned to be used to predict composite properties and response in a Future X X40 program, in a follow-on program to the Airborne Laser (by the NASA White Sand testing facility) and by the National Institute of Standards.

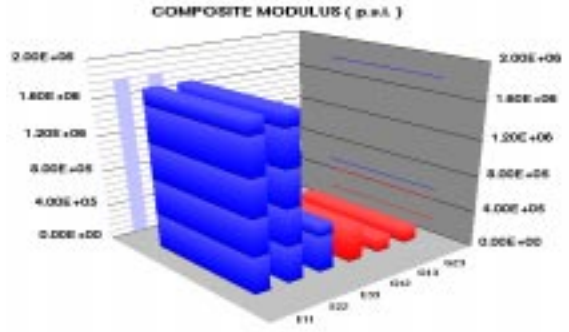

Figure 1-13. Equivalent Laminate Moduli for Graphite Design

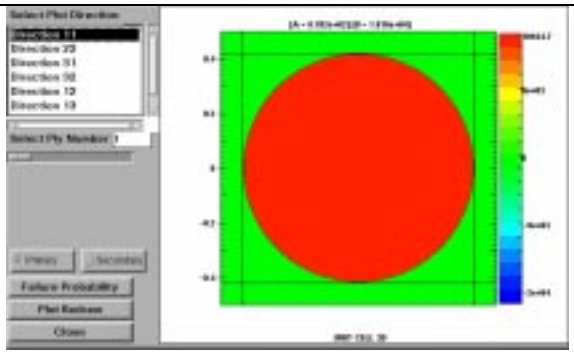

Figure 1-14. Fiber And Matrix Stress Distributions In Composite System

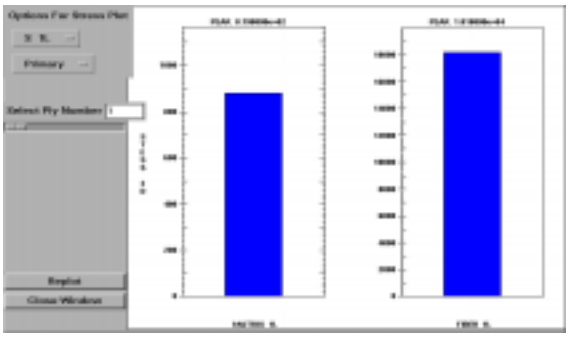

Figure 1-15. Distribution Of Stress To Fiber And Matrix

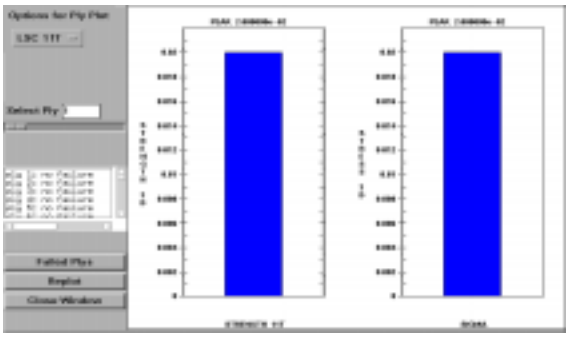

Figure 1-16. Composite Strength Vs. Applied Stress (Right), & Failed Layers In Composite Due To Environmental Loading

1.4 SIMULATION OF PROGRESSIVE FRACTURE IN TIME DOMAIN

1.4.1 Low cycle Fatigue Loading

GENOA-PFA was enhanced to perform progressive analysis of Boeing IAS and Crown panels. The skin and stringers were of T7475-T7351 aluminum alloy and the rivets were of 2017 aluminum alloy The frames were of 7050-T7451 aluminum alloy (Figures 1-17 and 1-18).

The enhancement was based on: 1) modification of the load increment to allow for pressure cycling, and 2) logarithmic degradation of material properties vs. pressure cycles. Cyclic fatigue and static simulation analyses were conducted on NASA coupons and the Boeing Crown Panel to determine in detail the effects of multi-site damage on ultimate loads and cycles to failure and calibrate the software. Damage initiation and progression were determined as functions of cyclic loading. Deterministic accomplishments of this effort were: 1) PFA verification with data from five NASA coupon tests and the Boeing crown panel static cyclic test, and 2) analysis of the fatigue lap joint model (extracted from the Boeing crown panel model), using 5 percent variation of lap joint thicknesses. A comparison of simulation and experimental test results is shown in Table 1-2.

Table 1-2. Summary of Results (NASA Coupon and Crown Panel) From Testing and Deterministic Simulation Analyses

Specimen	Loading condition	Maximum stress	Simulation	Testing
NASA Coupon	Static Loading (ultimate load)		14060 LB	13500 LB
	Cyclic Loading (cycle to failure)	22KSI	84,000	81,541
		18KSI	204,800	153,951 (test 1) 239,361 (test 2) 154,142 (test 3)
		16KSI	324,100	313,138
Crown Panel	Static Loading (ultimate load)		10.48 PSI	~10.3 PSI
	Cyclic Loading (cycle to failure)		10,720	10,333

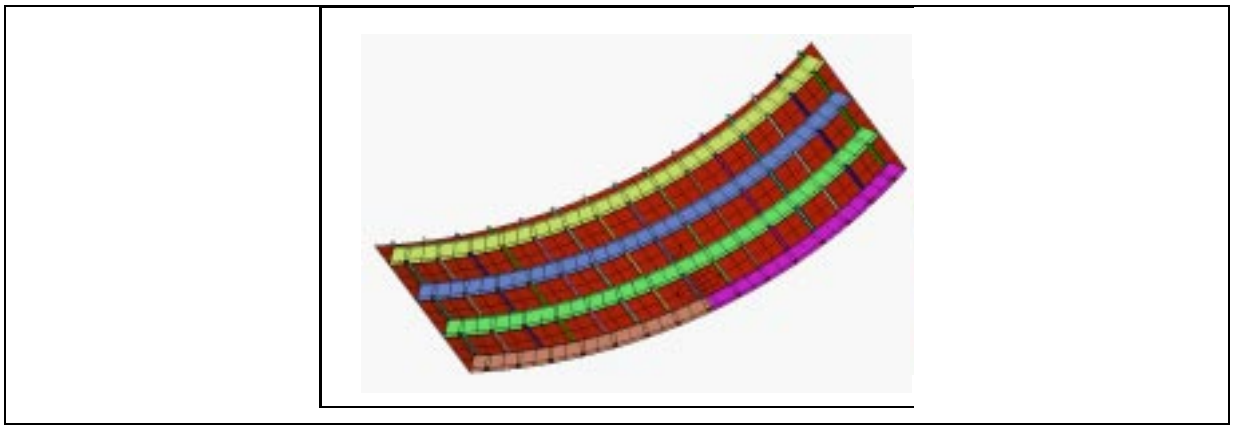

Figure 1-17. Boeing 747 Aluminum Crown Panel Finite Element Model

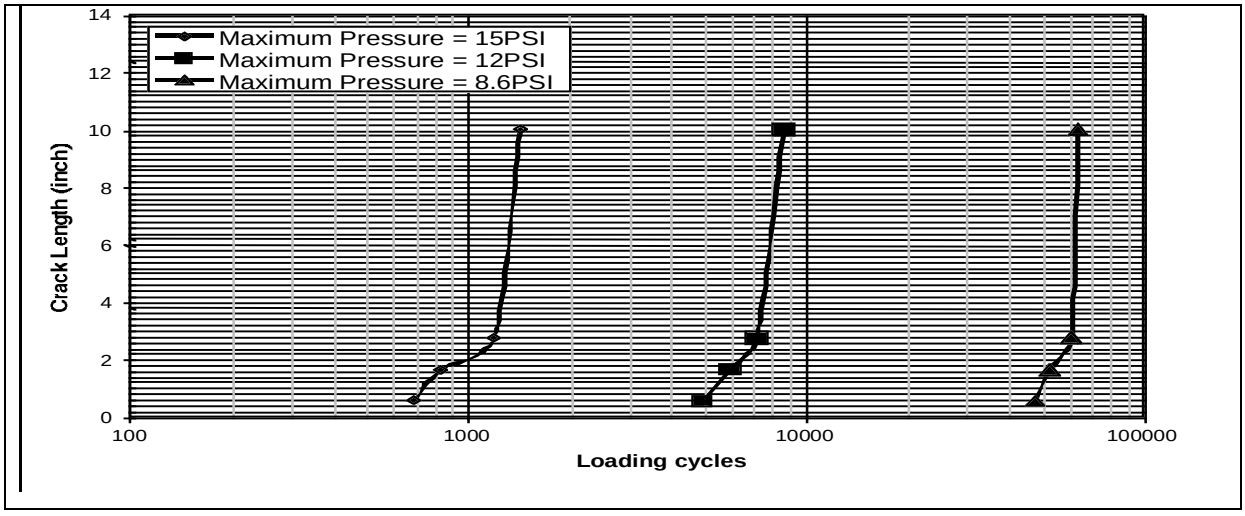

Figure 1-18. Crack Length Growth With Loading Cycles

1.4.2 Simulate Progressive Fracture in PMC Structure Under Time Domain High Cyclic Fatigue Loading

The GENOA-PFA software as modified to predict durability and damage tolerance under cyclic fatigue (time domain) loading in PMC structures was used to simulate progressive fracture and critical damage location in a Lockheed F-22 PMC (16 ply AS-4/HMHS [±45/0/90/±45/90/0]) airfoil structure subjected to 50 HZ acoustic cyclic excitation based on constituent material properties, part geometry, stress limits and strain limits. Preliminary results of a GENOA asymmetric loading fatigue simulation of the Lockheed PMC rotary wing airfoil test coupon are shown in Figures 1-19 through 1-22. Excitation was by application of a sinusoidal harmonic load with an amplitude of 13.0 lbs and a frequency of 8 cycles/sec. A damping ratio of 0.005 was used for the damage mode. Structural adhesive bond material (R976) thickness was 0.005 in. After 93 GENOA iterations (the equivalent of 8×10^6 Cycles) complete fracture occurred at the junction of the vertical support and the air foil (Figure 1-19) while bond damage was approximately fifty percent (green and yellow colors in bond area of Figure 1-20). Figure 1-21 shows the most dominant mode of damage to be matrix failure in transverse tension. There also were longitudinal fiber and in plane shear matrix damage modes.

Figure 1-22 shows the stress concentration causing the failure at the junction of the vertical support and the air foil. Initial conversation with Lockheed confirmed that this is where the PMC rotary wing

airfoil test coupon actually failed. Figure 1-21 shows the most dominant mode of damage to be matrix failure in transverse tension. There also were longitudinal fiber and in plane shear matrix damage modes. Since the failure occurred in the test support at its junction with the airfoil member bond strength could not be determined. However, even though this would seem indicate the adhesive bond to be strong, simulation showed approximately 50% damage volume in the adhesive bond.

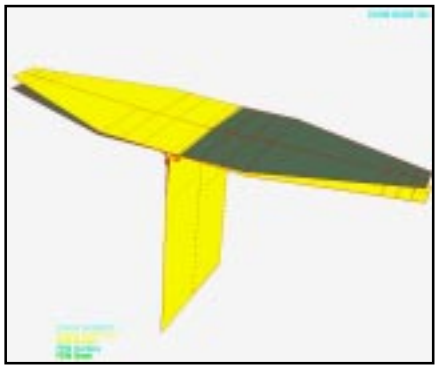

Figure 1-19. After GENOA Iterations (The Equivalent of 8 x 106 Cycles) Complete Fracture Occurred at the Junction of the Vertical Support and the Air Foil

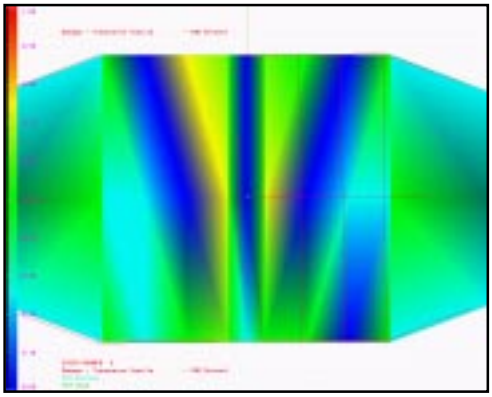

Figure 1-20. Percent of Bond Failure (~50%) is Identified as Green-Yellow Contours

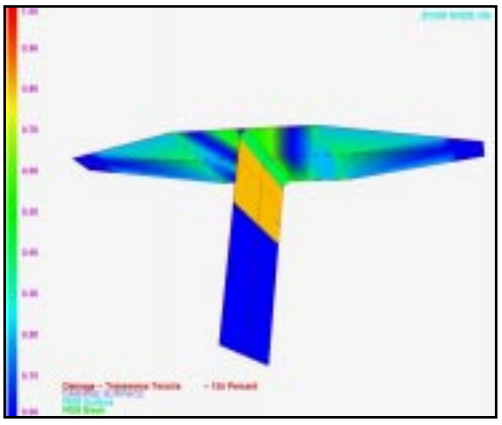

Figure 1-21. The Most Dominant Mode of Damage was Identified as Matrix Failure in Transverse Tension

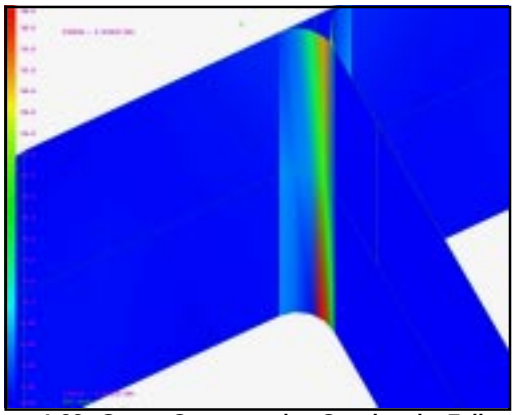

Figure 1-22. Stress Concentration Causing the Failure at the Junction of the Vertical Support and the Air Foil

1.4.3 Simulate Progressive Fracture Under Impact Loading

Simulation of impact loading of woven/braided/stitched composite structure was achieved by: 1) modification of PFA to perform pseudo-dynamic (including inertia, and acceleration) analysis, and 2) post processing of PFA static analysis to generate pseudo static (excluding inertia, and acceleration) impact. The NASA-White Sands facility is verifying this capability for verification against test data.

1.4.4 Simulate Reshaping Of Braided Fiber Preforms To Assist Manufacturing

Simulation of novel, emerging manufacturing method of reshaping braided tubular “sock” preform, was developed as extension to PFA to provide a link between the computer generated knowledge base, analysis software and automated machine tools. The method is based on a braided “sock” preform of commingled thermoplastic yarns in a form of a “sock” that is made to conform to a net shaped mandrel. This very promising, economical process of generating shaped fiber preforms for composites involves

three steps: 1) braiding a simple, commingled fiber tubular preform, 2) reshaping the preform over a mandrel of a desired shape (Figure 1-23), and 3) processing (heating) the reshaped preform to flow the resin matrix fiber material around the high strength fibers. For a rational design, it is necessary to predict 1) fiber orientations and volume fraction changes, 2) the necessary forces/strain to best fit onto a shaped mandrel, and 3) occurrences of failure (buckling, fiber wrinkling) in the preform after shaping. A durability and damage tolerance analysis was conducted to demonstrate the importance of the fiber angle change tracking.

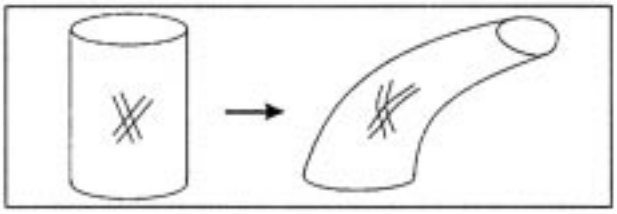

Figure 1-23. Initial and Reshaped Textile Preform

Since the reshaping operation can significantly change fiber orientations, it becomes critical to evaluate the extent of this change, its effect on composite performance, and the extent to which the changes can be negated by adjusting the braid angles of the tubular textile preform. The software allows attainment of the best preform net fit to a desired shape without occurrences of buckling and fiber wrinkling/crimping by: 1) iterative FEM analysis utilizing resin matrix composite micromechanics; 2) prediction of the effects of changes of braid/weave angle on resin matrix composite micromechanical properties; and 3) use of an iterative contact algorithm for analysis of sock conformance to a shaped tool. The preform reshaping simulation tool was developed by Alpha STAR in support of the NASA funded AST GE project and verified against experimental GE results of reshaping preforms for conical bent and elliptical components.

State of Software Verification. The GENOA code has provided the needed capabilities for the fiber preform reshaping process for large, complex, PMC components. This effort has been verified to simulate reshaping of tubular fiber textile preforms (e.g, GE90 Turbine blade, bent cone, cylinder, bent cylinder) in a cooperative exploratory effort with General Electric Aircraft Engine. Figure 1-24 (a-c) shows the Sandia National Laboratory 26 ft long and 4 ft wide Wind-Mil best fit simulation that has been verified against actual hardware developed by Goldsworthy to be within 4% of the actual measured data by simulating use of multiple reshaped preforms of different sizes with commingled fibers.

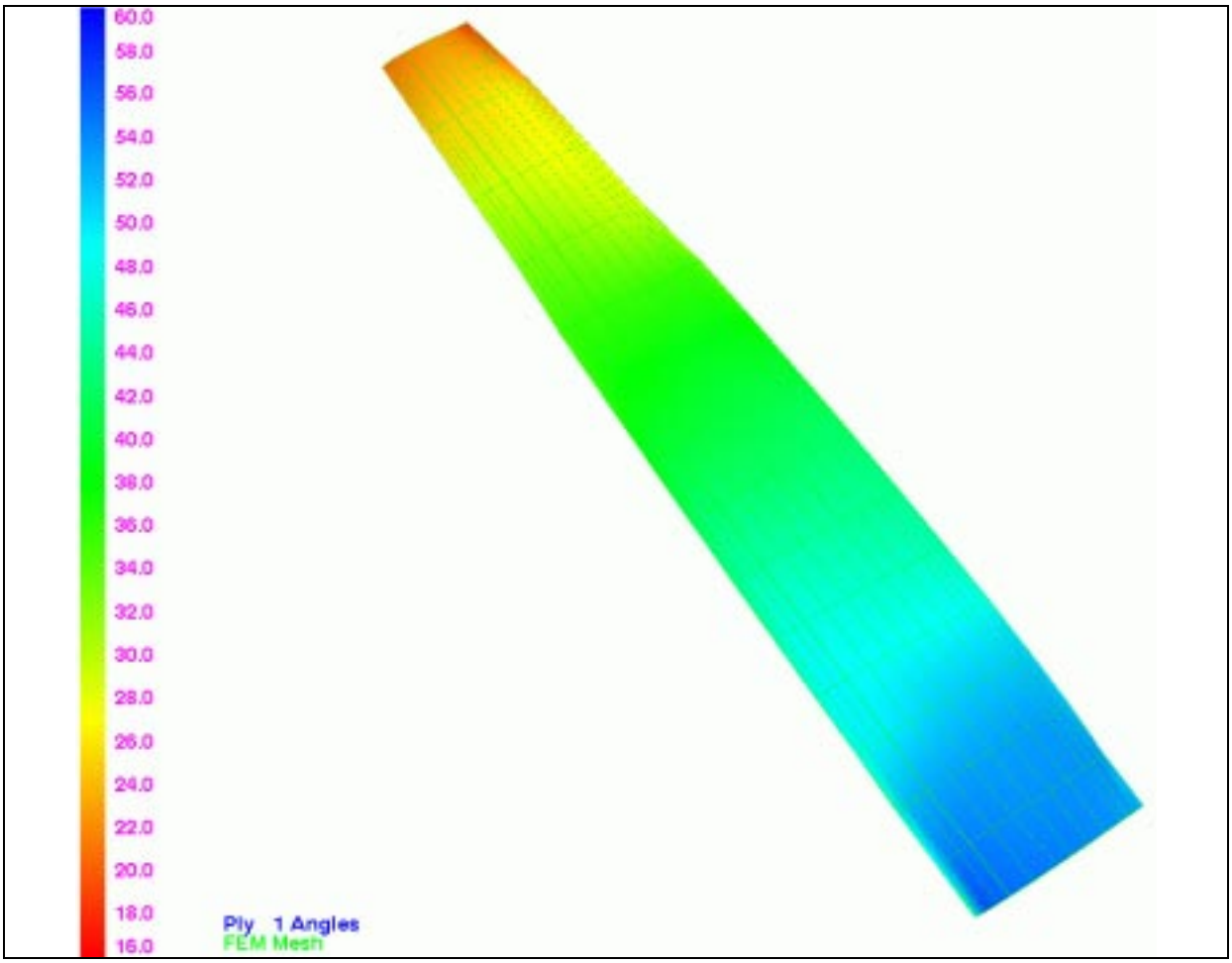

Figure 1-24(a). As received Preform Sock of ±45 orientation was fitted on a Wind Mil mandrel

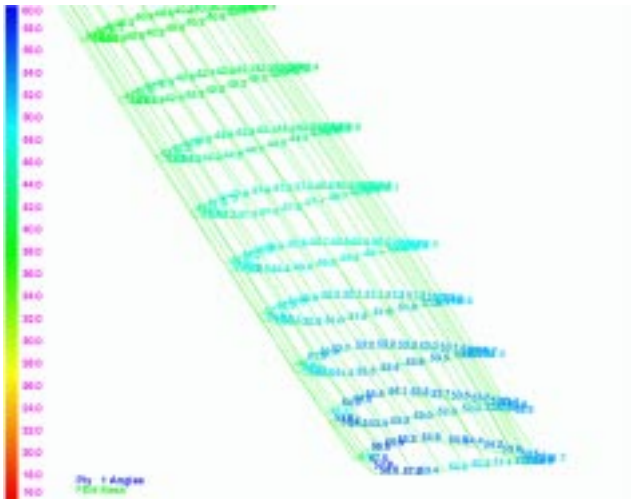

Figure 1-24(b). As Received Preform Sock of ±45 Orientation was Fitted on a Tip of Wind Mil Mandrel

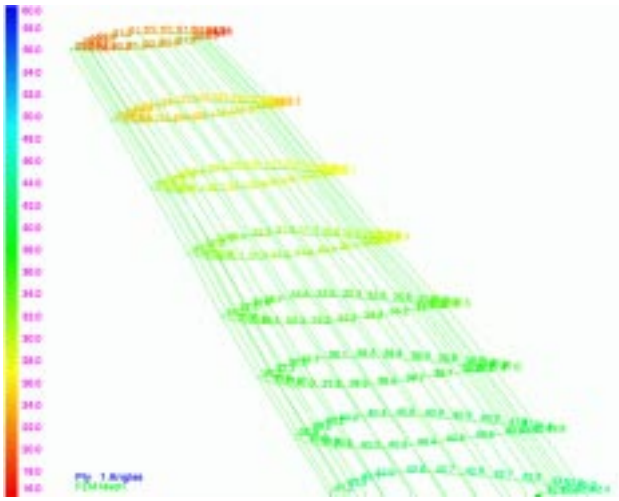

Figure 1-24(c). As Received Preform Sock of ±45 Orientation was Fitted on a Root of Wind Mil Mandrel

1.4.5 Perform Virtual Testing analyses

Figure 1-25 compares ACT three stringer S/RFI Compression panel simulated strains vs. test strains as function of applied load. Agreement is very close.

Figure 1-26 shows simulations of photoelastic fringe patterns of three stringer S/RFI tension panel at prescribed load levels of 25 Kips. Experimental fringe patterns (Figure 1-26a) (NASA/LaRC provided polariscope camera) and the GENOA- predicted fringe patterns (Figure 1-26b) are in good agreement as verified by team member, Applied material Technology (AMT).

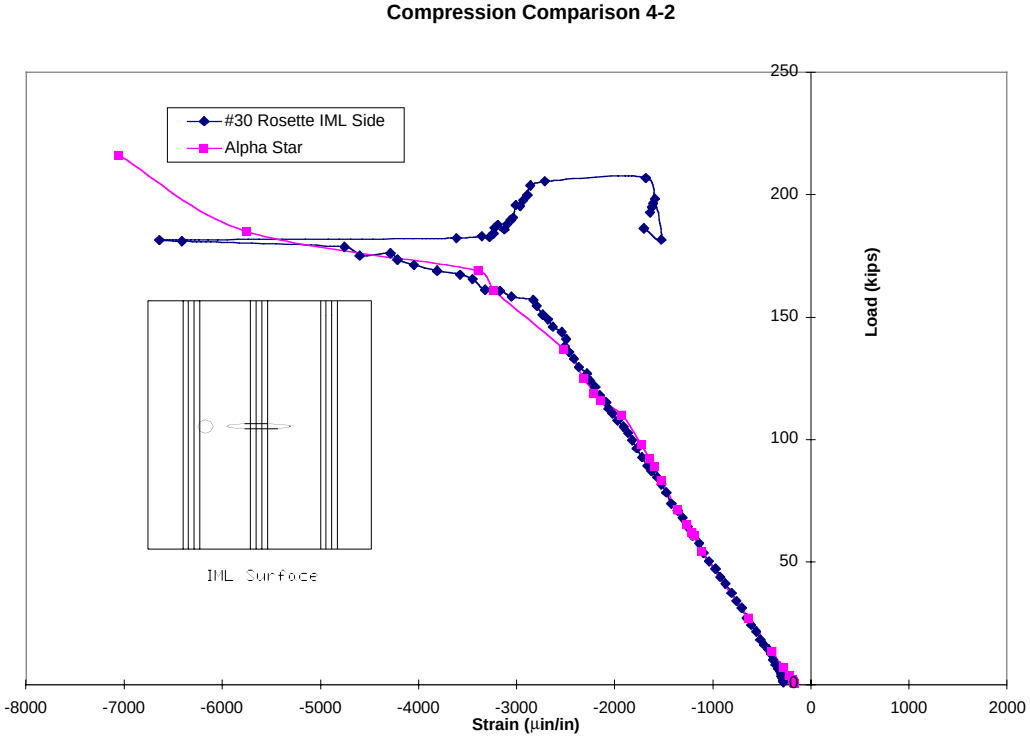

Figure 2-5 Comparison of Analytical vs Test Strains for Compression Panel Ahead of Crack Tip

Figure 1-25. Comparison of Analytical vs Test Strains Ahead of Crack Tip for Compression Panel

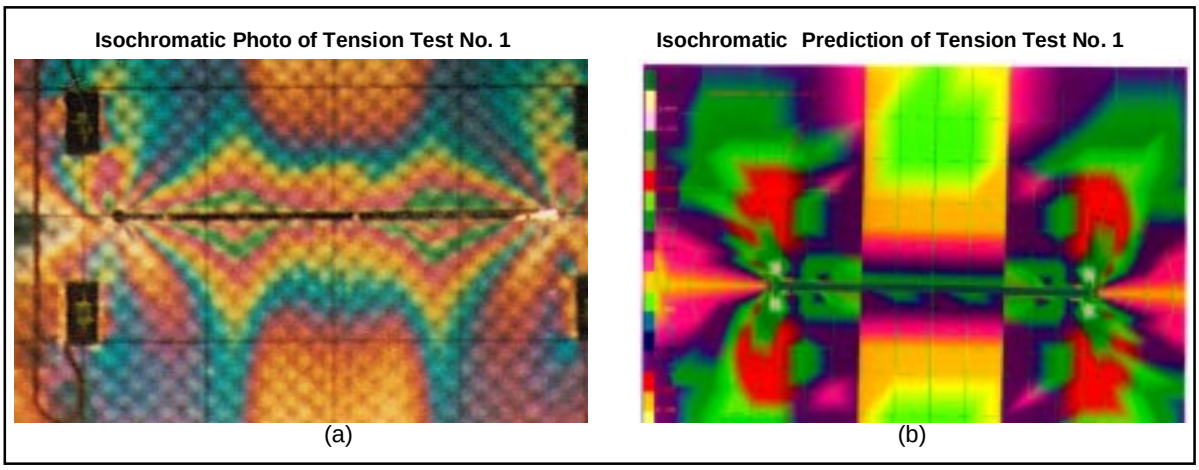

Figure 1-26. Photoelastic Prediction Provides a Visual Check of Color Contours for Comparison of Test and Simulation Results

1.4.6 Probabilistic Failure Analyses

Alpha STAR has developed GENPAM, a computer software for probabilistic composite structural analysis that integrates probabilistic methods, finite element methods, and composite mechanics. The software has been integrated as part of the GENOA suite of codes The available probabilistic methods include: 1) Monte Carlo Simulation (MCS), 2) advanced reliability algorithms and 3) importance sampling methods. MCS, traditionally used for reliability assessment, is deemed computationally too expensive for large structures or structures with complex behaviors. Extensive effort has been devoted to development of new, more computationally economic probabilistic algorithms for advanced reliability and importance sampling methods in the GENPAM program are a direct result of ten years of probabilistic structural analysis research funded by NASA.

The GENPAM code is constructed such that any real value in the input file of the progressive failure deterministic analysis can be selected as a random variable. An interface module was developed that can interface with any deterministic code as long as the uncertainties are one of the real values shown on the original deterministic input file. Integration with many commercial or in-house computer codes becomes transparent. Thus, integration effort is minimized and simplified. Various responses can be selected to be analyzed probabilistically, CDF/PDF functions and sensitivities to design random variables. The types of responses that can be specified are:

Type 1: Displacement responses specified by setting node numbers and the three transition degrees-of-freedom.

Type 2: Material responses specified by setting node number, layer number, and the 20 material properties and their combinations. The 20 material properties/responses that can be extracted for each ply node are the following:

1. Longitudinal strain
2. In plane shear strain
3. Transverse stress
4. Longitudinal tensile strength
5. Transverse tensile strength
6. In plane shear strength
7. Hoffman's failure criterion
8. Fiber crushing criterion (compressive strength)
9. Fiber microbuckling criterion (compressive strength)
10. Transverse normal shear stress
11. Transverse strain
12. Longitudinal stress
13. In plane shear stress
14. Longitudinal compressive strength
15. Transverse compressive strength
16. MDE failure criterion
17. Interply delamination failure criterion
18. Delamination criterion (compressive strength)
19. Longitudinal normal shear stress
20. Transverse normal shear strength

1.4.7 Improved Graphics User Interface (GUI) For Visualization (Including Animation) of Simulated Results

GENOA Graphics User Interface (GUI) can be utilized to execute all other GUI's capabilities such as:1) communication with other modules "GENEX", extract critical damage events "Post Cycle", view and animate the damage events and the resultant attributes "3D Plot", 2D/3D PMC equivalent property generation "Xgenoa2D". (Figure 1-27). Figure 1-28 shows the GUI post cycle tool bar used to extract the desired file for post analysis viewing. Figure 1-29 Shows 3D Plot GUI with visualization icons.

1.0 Summary of Phase II

1-27. GENOA Graphics User Interface : GENEX, Post Cycle, 3D Plot, Xgenoa 2D

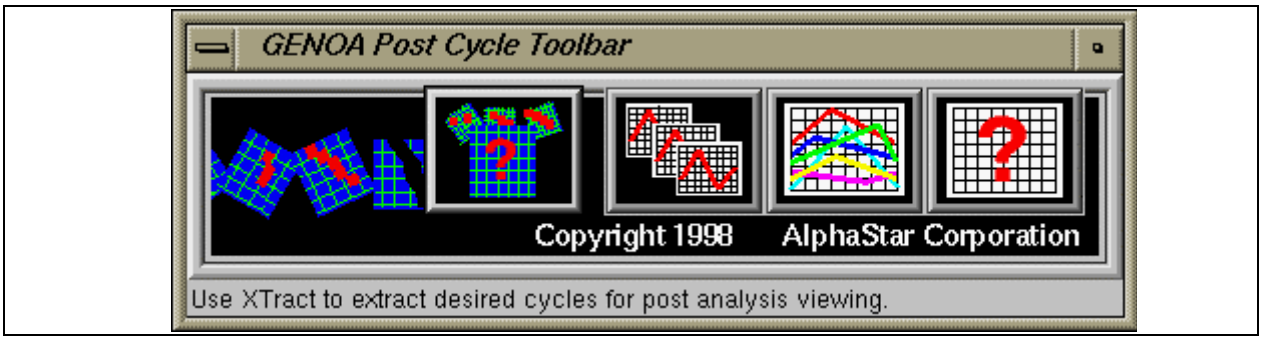

1-28. GENOA Post Cycle Tool Bar

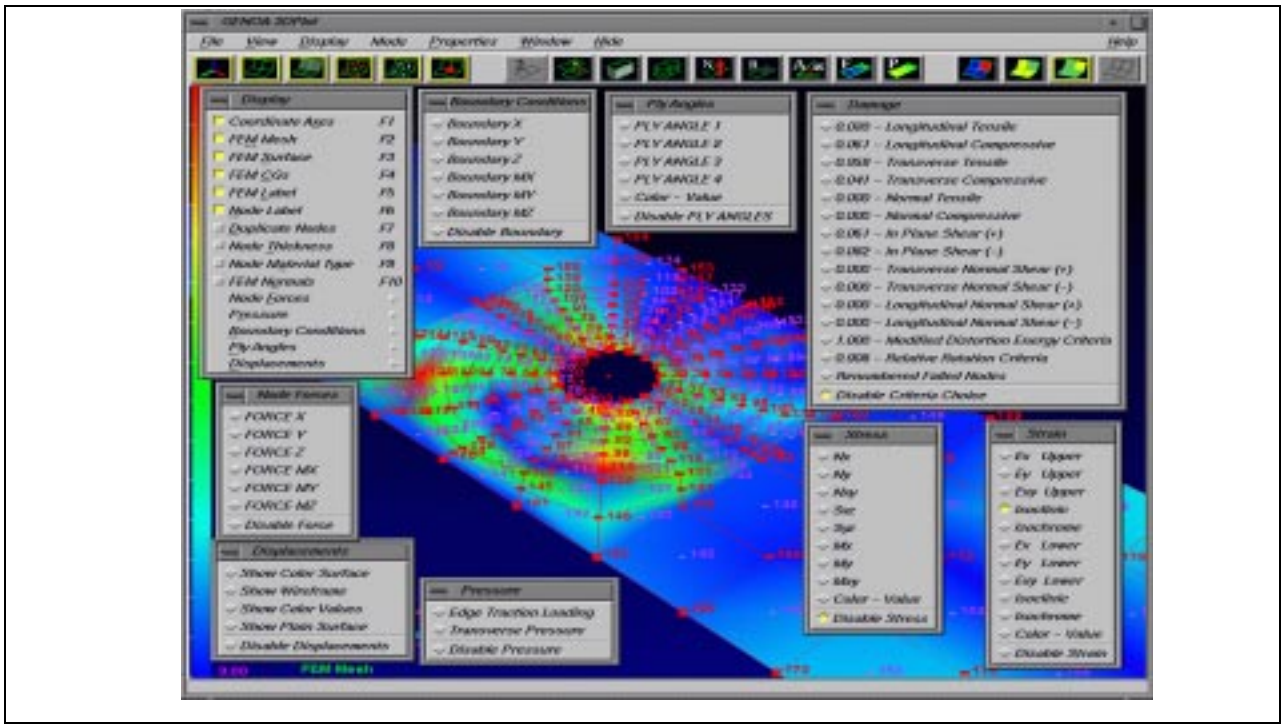

Figure 1-29. An Up-Close View of Default Display Properties Initiated from a Pull-Down Menu

1.4.8 Porting GENOA-PFA Software to Unix (HP, SGI, IBM), and NT Operating Systems

Porting To Other UNIX Workstations

Porting to any other UNIX workstation requires minimal changes due to the compatable nature of UNIX platforms. Since GENOA utilizes the Graphic User Interface package of Viewkit by Integrated Computer Solutions, an installation of Viewkit and a recompilation of the GENOA code is necessary for potting to another platform. Only minimal changes to compiling GENOA would be necessary if there were differences in compilers used or libraries of the operating system such as OpenGL support.

Porting To NT-

Porting to the NT platform requires the additional software of a UNIX toolkit called NutCracker Nutcracker is a UNIX operating system emulator that can run X11 and Motif applications, along with traditional UNIX commands. Since portions of GENOA utilizes the Graphic User Interface of Viewkit by Integrated Computer Solutions, compatibility was easily achieved since Viewkit is written in Motif. In addition to the operating system emulator, an X Server software was also required for the necessary OpenGL graphic rendering of GENOA called Reflection WRQ Server. Once the entire code of GENOA is successfully emulated on an NT platform, the last step is to compile and package the GENOA executables with a stand alone operating system version of Nutcracker that allows the package code to run on any desired NT workstation.

1.5 REFERENCES

1. Minnetyan L., Murthy P.L.N., and Chamis C.C., “Composite Structure Global Fracture Toughness via Computational Simulation,” Computers & Structures}, Vol. 37, No. 2, pp.175-180, November 1990}
2. Irvine T. B. and Ginty C.A., “Progressive Fracture of Fiber Composites,” {\em Journal of Composite Materials}, Vol. 20, March 1986, pp. 166-184.
3. Minnetyan L., Chamis C.C., and Murthy P.L.N., “Structural Behavior of Composites with Progressive Fracture,” Journal of Reinforced Plastics and Composites}, Vol. 11, No. 4, April 1992, pp. 413-442
4. Minnetyan L., Murthy P.L.N., and Chamis C.C., “Progressive Fracture in Composites Subjected to Hygrothermal Environment,” International Journal of Damage Mechanics}, Vol. 1, No. 1, January 1992, pp. 60-79
5. Minnetyan, L., Chamis, C. C., and Murthy, P. L. N., “Structural Durability of a Composite Pressure Vessel,” Journal of Reinforced Plastics and Composites}, Vol. 11, No. 11, November 1992, pp. 1251-1269}
6. Minnetyan, L., and Chamis, C.C., “Pressure Vessel Fracture Simulation,” Presented at the ASTM 25th National Symposium on Fracture Mechanics, Lehigh University, Bethlehem, Pennsylvania, June 28-July 1, 1993, Published in ASTM STP 1220, Fracture Mechanics: 25th Volume}, August 1995, pp. 671-684.}
7. Minnetyan, L., Rivers, J. M., Chamis, C. C., and Murthy, P. L. N., “Discontinuously Stiffened Composite Panel under Compressive Loading,” Journal of Reinforced Plastics and Composites}, Vol. 14, No. 1, January 1995, pp. 85-98.}
8. Minnetyan, L., and Chamis, C. C. 1997. "Progressive fracture of composite cylindrical shells subjected to external pressure." ASTM J. Compos. Technol. and Res., 1 9(2), 65-71.
9. Chamis, C.C. (1969) “Failure Criteria for Filamentary Composites,’’ Composite Materials Testing and Design: ASTM STP 460, American Society for Testing and Materials, Philadelphia, pp 336-351
10. Minnetyan, L., Murthy, P.L.N. and Chamis, C. C. 1992. “Progressive Fracture in Composites Subjected to Hygrothermal Environment,” International Journal of Damage Mechanics, Vol. 1, No. 1, pp 69-70.
11. Minnetyan, L., Rivers, 3. M., Chamis, C. C., and Murthy, P. L. N. 1995. "Discontinuously stiffened composite panel under compressive loading." J. Reinforced Plastics and Compos., 14(1), 85-98.
12. Minnetyan, L., Rivers. J.M., Chamis, C. C. and Murthy, P.L.N. 1992. “Structural Durability of Stiffened Composite Shells,” Proceedings of the 33rd SDM Conference, Dallas, April, pp2879-2886.
13. Jara-Alamonte, C and Knight, C. 1988. "The Specified Boundary Stiffness/Force SBSF Method for Finite Element Subregion Analysis," International Journal for Numerical Methods in Engineering, Vol. 26, pp 1567-1578.

2.0 Modularization of CODSTRAN

The CODSTRAN code with three-dimensional woven composite simulation capability (Figure 2-1) was upgraded and streamlined to consist of three independent modules. These modules were named as (1) COD6, (2) ICAN, and (3) FEML. The COD6 module contains the CODSTRAN executive code as well as the subroutines that assess the composite local failure modes after each analysis cycle and keep track of damage progression. The ICAN module contains the new ICAN code as recently updated with subroutines to analyze three-dimensional woven and braided composites. The FENL module contains the MHOST finite element analysis code. The modularization was accomplished by eliminating the common blocks to facilitate passing information between the modules by writing the interfacing information to external files.

2.1 IMPLEMENTATION OF MODULAR FINITE ELEMENT ANALYSIS

The difference between the Modular version of CODSTARN and semi modular COD6.is illustrated in Figures 2-2 and 2-3. As shown both flow diagrams utilize the same scratch files but with different module utilization except for File No. 83. Scratch File No. 83 in Figure 2-3 was replaced by a modified and modular info 1-MIR2 program which has a nodal normal vector calculation. (info1, presently a routine within MHOST program, creates the necessary CODSTRAN functional output files such as nodal stress, generalized force, total nodal and radial displacement for the next iteration in the sequential version of CODSTRAN.

INFO1-mir2, presently a stand alone program, contains: 1) a post processor for listing FEM output and input text files, preparation of the necessary CODSTRAN functional output files as described above and calculation: of normal nodal vectors tensor preparation (ETRANS), and radial displacement. This allows to assignment of internal pressure for the next step of CODSTRAN. The file communication is described in Table 2-1.

Table 2-1. MHOST FEM Scratch File Utilization

File Name	Function	Generated	Used By	Format
SCRA 36	MHOST Listing	MHOST	N/A	Text
SCRA 44	Argument list	Damage Track	MHOST	Text
SCRA 55	New input	Damage Track	MHOST	Text
SCRA 61	Nodal Stress	MHOST	Damage Track, CAN	Text
SCRA 78	Nodal Disp	MHOST	Damage Track	Binary
SCRA 80	Failure Index	MHOST	Damage Track	Binary
SCRA 83	Intermediate Output	MHOST	CODSTRAN, + HOST	Binary
SCRA 93	General Force	MHOST	Damage Track	Text

2.0 Modularization of CODSTRAN

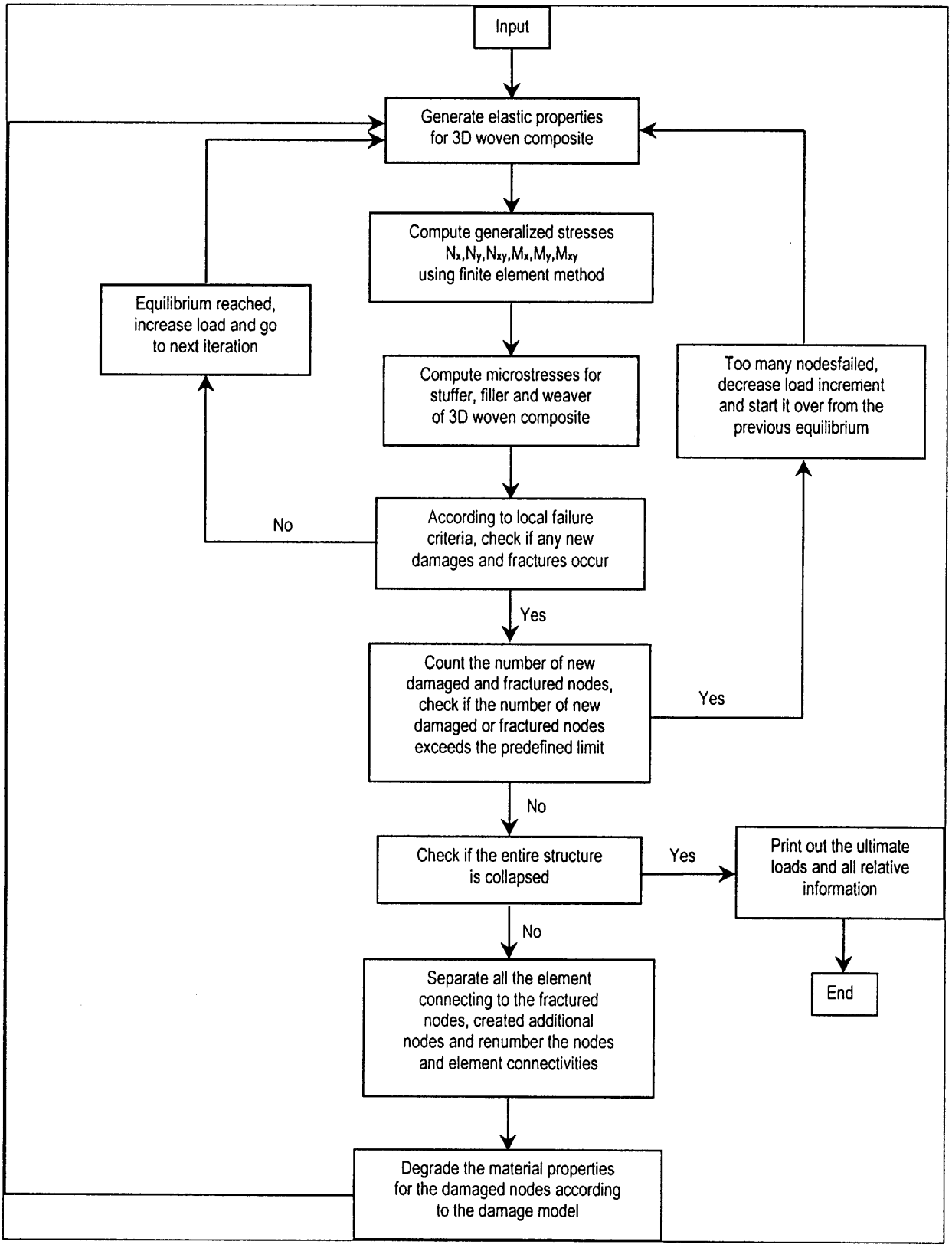

Figure 2-1. Integrated Computer Code For Simulating Damage Propagation Of 3D Woven Composites

2.0 Modularization of CODSTRAN

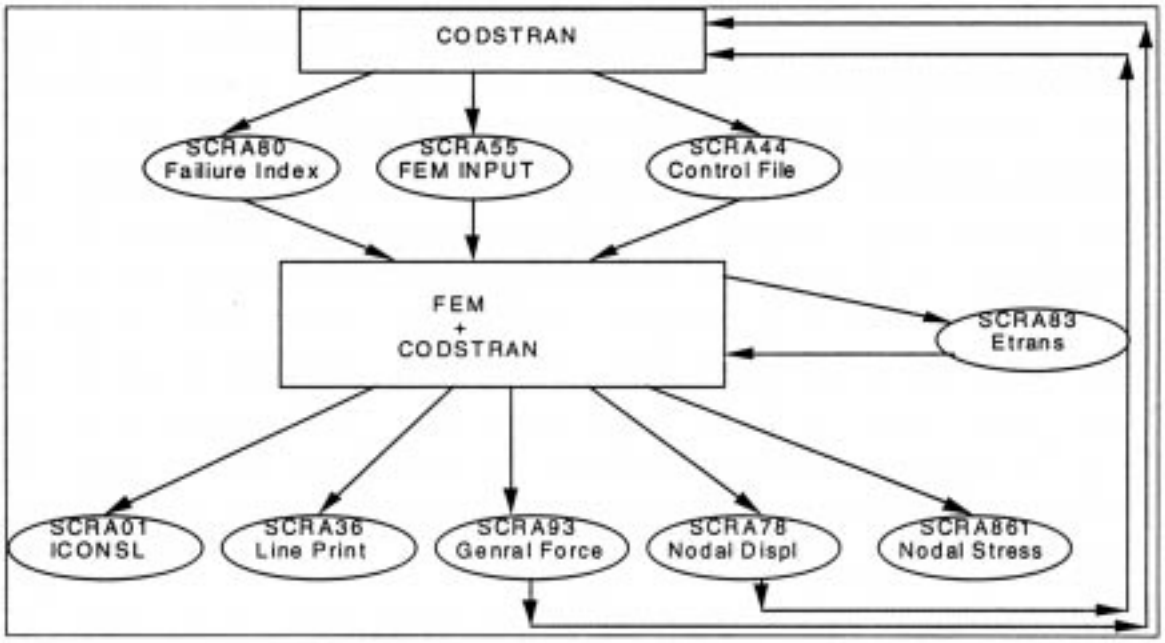

Figure 2-2. CODSTRAN Sequential Software Flow Diagram

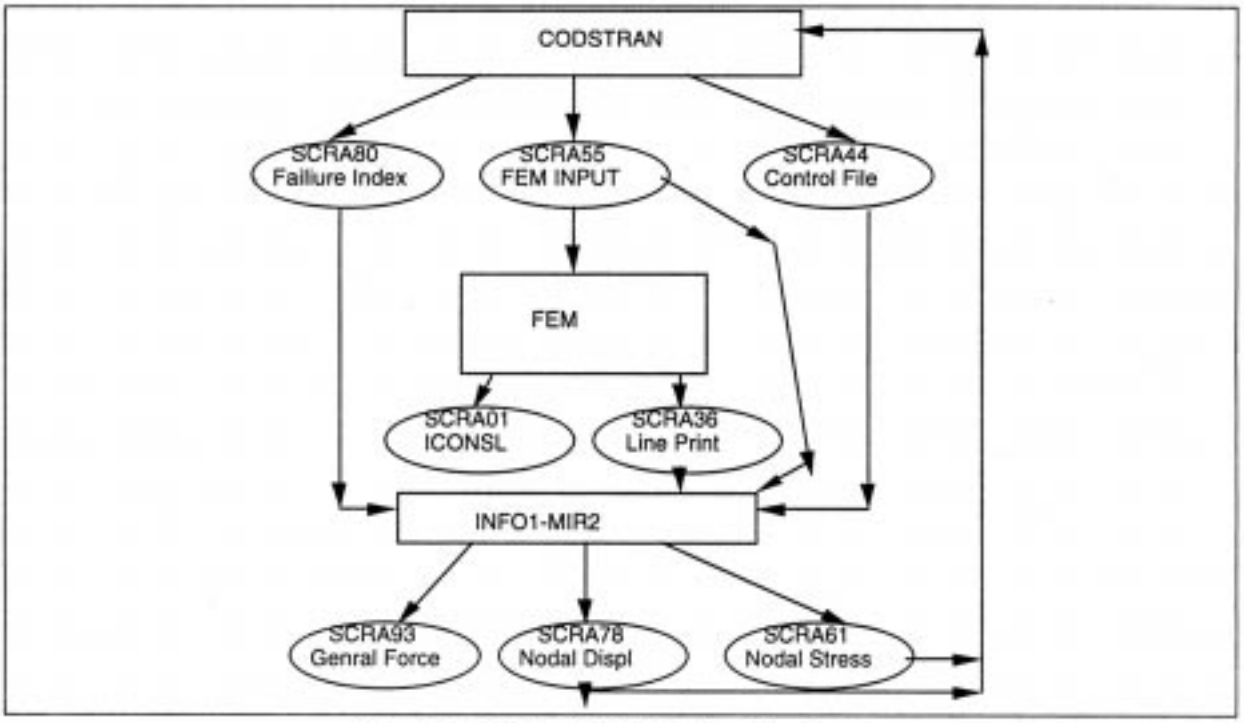

Figure 2-3. CODSTRAN Modular Software Flow Diagram

2.1.1 Modular Files Structure

The modular version of CODSTRAN code utilizes scratch files in binary and text format written by MHOST 4.2 (Table 2-2). The file communication is being re-directed to only process general finite element outputs. NESSUS 6.0 and FEM parallel will adopt the same file structure as in Table 2-2.

Table 2-2. Files Generated by MHOST FEM Module

File Name	Function	Generated	Used By	Format
SCRA 01	Log	MHOST	N/A	Text
SCRA 36	MHOST Listing	MHOST	N/A	Text
SCRA 44	Argument list	Damage Track	MHOST	Text
SCRA 55	New input	Damage Track	MHOST	Text
SCRA61	Nodal Stress	MHOST	Damage Track, CAN	Text
SCRA 78	Nodal Disp	MHOST	Damage Track	Binary
SCRA 80	Failure Index	MHOST	Damage Track	Binary
SCRA83	Intermediate Output	MHOST	N/A	Binary
SCRA85	New input	Damage Track	MHOST	Text
SCRA93	General Force	MHOST	Damage Track	Text

The modular version of CODSTRAN was further tested, augmented, and updated to COD7 which is now consistent with COD5. COD7 results were virtually identical with those of COD5 when the cure temperature was the same as the use temperature. The only difference between the results computed by COD5 and those computed by COD7 was in the computation of residual stresses. When the cure temperature was different than the use temperature, the residual stresses computed by COD7 were higher. This is because COD7 is based on the second generation ICAN composite mechanics module (Murthy et al 1993), that has improved thermal equations. For the cases studied, residual stresses computed by the second generation ICAN module were higher than those computed by the original ICAN (Murthy and Chamis 1986) with COD5.

The units of thermal conductivity have been changed. In COD5 the fiber and matrix thermal conductivities are input in BTU-in/hr/ft**2/F. In COD7 thermal conductivities are input in BTU-in/hr/in**2/F units. Therefore, to convert fiber and matrix material properties from the old to the new ICAN databank, all thermal conductivity values should be divided by 144. For example, the longitudinal thermal conductivity of AS-4 fibers in the old databank is 580 BTU-in/hr/ft**2/F; whereas, in the new databank it is 4.03 BTU-in/hr/in**2/F.

COD7 also has improved input and additional output for the through-the-thickness ply stresses and micro stresses for nodes selected by the user. COD7 prints out the micro stresses and ply stresses for each layer of a selected number of nodes. Ply stresses are printed to unit 7 (SCRA07) and the micro stresses are printed to unit 8 (SCRA08). Print outs of all ply stresses and micro stresses may be selected for up to 50 nodes. The node numbers selected for print out are modified by COD7, as needed, during node renumbering due to deleted nodes. Additionally, COD7 prints out (to unit 88) top and bottom laminate surface strains in the laminate (x,y) coordinates.

2.1.2 Modularization Of The CODSTRAN

Further Modularization of COD7 entails upgrading of finite element analysis for parallel processing, and utilization of general purpose FEM software. An attempt made to use the stand alone MHOST version 4.0 within the context of COD7 resulted in the following:

1. Investigation of the necessary MHOST parameters for translation between the FEM results and CODSTRAN damage tracking module.
2. Development of a routine "get_rec_sub.f" for text strings analysis by prototype words.
3. Integration of the shell element calculation from CODSTRAN info1 routine with the new interface program under final development
4. File structure allocation for the general purpose translation program was organized and debugged

Changes to input data - The node numbers for which ply stresses and micro stresses are to be printed out need to be specified by the user. Immediately before the ICAN statement, one line using (24X,i8) format gives the number of nodes where ply stresses and micro stresses are to be printed out. Subsequent lines give the specific node numbers using (10i8) formats.

Another change was made to eliminate unnecessary data lines when simulating 3D reinforced woven or braided composites. The LTYP, PLY, and MATCRD statements are the same as in the previous COD6 version. However, the STUFFER, FILLER, and WEAVER statements have been eliminated. For each fiber orientation that has an out-of-plane component a BRAID card is needed to specify the braid number, the fiber/matrix constituents, the three directional angles (degrees) of the fiber orientation with respect to the laminate x, y, z coordinates, and the ratio of braid fiber volume to the total fiber volume. The BRAID card uses (a8,i8,2a4,3f8.2,f8.0) format.

The last braid parameter (viz. the ratio of braid fiber volume to the total fiber volume) is computed from the weight of stitching thread, ws, as well as the pitch and row-spacing of the stitch, ps and rs. For example, for a laminate with a fiber volume ratio 0.555 (including the stitch fibers), using 1600 denier kevlar thread with ps=1/8 in., and rs=1/5 in., the last BRAID parameter is computed as follows: 1600 denier is equivalent to 9.95E-06 lbs/in. The thread cross sectional area, A thread, is obtained by dividing the weight per unit length by the weight density. Therefore, A thread = 9.95E-06 lbs/in / 0.053 lbs/in^3 = 0.00018783 in^2. Each stitch contains two threads, therefore the stitch area is As = 2*Athread = 0.00037566 in^2. Stitch fiber volume ratio = As/(ps*rs) = 0.00037566/0.025 = 0.01503. The BRAID fiber ratio is the fraction of stitch fiber volume ratio to overall (total) fiber volume ratio. If the in plane fiber volume ratio is, for example, 0.540, then the total fiber volume ratio is 0.540+0.01503=0.55503. Therefore, the ratio of BRAID fiber to the total fiber volume is 0.01503/0.55503 = 0.02708. This last number is the last parameter of the BRAID card.

COD7 was verified with simulations of laminated, stitched, and woven composites. A novel composite macromechanics approach that considers the alternating spatial configurations of the in-plane fiber orientations and the effects of out-of-plane fiber orientations was implemented via COD7 for the simulation of woven fabric composites.

2.1.3 Review Of Data Communication In Modular CODSTRAN

The implemented data communication methods among the COD7 modules were subject to review for the purpose of designing the optimal means of inter-modular communication structures for the parallelization of COD7 modules. This section summarizes the present implementation of modular CODSTRAN procedures and the data communication structures for clarification.

CODSTRAN consists of three modules: COD7, FEML and ICAN. COD7 controls the other two modules ICAN and FEML. COD7 calls ICAN and FEML via the function system() when necessary.

All data communication in the previous non-modular version was passed through subroutine arguments or COMMON blocks among subroutines. For the modular version, data transfer is still through subroutine arguments or COMMON blocks within each module. However, data cannot pass from one module to another in this way. Therefore all communication between modules is transmitted in files. That is, data that was originally passed by arguments and COMMON blocks is written to files in one module, to be read by files in another module.

The subroutines used by COD7 for calling external modules are ICANMN used to call ICAN and HOSTEX used to call FEML (MHOST). Inter-modular data transfer of common blocks and arguments in these subroutines is as follows:

Subroutine ICANMN - The following common blocks that are shared by COD7 and ICAN are written to unit 45 (SCRA45).

- COMMON /CODELM/
- COMMON /LECHNC/
- COMMON / PRTMCRNODE/

The following arguments that are passed from COD7 to ICAN are also written to unit 45 (SCRA45)- POST, NPLYMX, INODE, MAXBRAID, NL, NBRAID, IPASS, IFAIL, ILOCW, WOVEN

All the files that may be used by ICAN are closed before calling the ICAN module. These files are opened on calling ICAN.

Subroutine ICNPRE in COD7 is used to prepare input data for the ICAN module to compute composite properties: ICAN input data is generated in unit IO95 (ICAINP).

Subroutine NODFAL is called to check if there is any damage in a regular layer. (e.g. stuffer or filler, as in the previous version.)

Subroutine check-weaver-fail is called to check if any damage has developed in a weaver or braider. If there is weaver/braider damage, IOCW returns an integer value that gives the position of the nodal damage index in the damage index array IPLFO_W. If there is no damage in weaver/braider plies, IOCW returns zero.

If any damage occurs in a regular in-plane ply, the corresponding damage index is written to unit IO79 (SCRA79), and then subroutine REPINP is called to rearrange the laminate data so that each ply will have a corresponding material card. If any damage occurs in the weaver, the corresponding damage index is written to unit IO23 (SCRA23).

Subroutine ICANMN is called to activate ICAN to compute the laminate properties. After FEM analysis, subroutine ICNPOS is used to prepare data for the ICAN module to compute the ply stresses for composite: Laminate configuration data is read from IO85 (CODINP) and results from FEML analysis through unit IO93 (SCRA93). SCRA93 are created by INFO1 in the FEML module. Input data file for ICAN is prepared and written to IO95 (ICAINP).

Subroutine NODFAL is called to check if any damage has occurred in regular plies.

Subroutine check-weave-fail is called to check if any damage has developed in weavers.

Subroutine ICANMN is called to activate ICAN to compute stresses for each ply. The stress data file for regular plies (stuffer and filler) is copied from IO46 (SCRA46) to IO94 (SCRA94). SCRA46 is created by subroutine PLYCHK in ICAN module. Note that SCRA46 corresponds to unit IO94 rather than IO46 in the ICAN module. The ply stress data file for weavers is copied from IO47 (SCRA47) to IO94(SCRA22). SCRA47 is created by subroutine PLYCHK in the ICAN module. Note that SCRA47 is corresponds to unit IO22 rather than IO47 in ICAN module.

Communication files between modulus:

ICAINP(IO95): is an input file for ICAN, created by subroutine ICNPRE and ICNPOS in COD7 module.

FEMINP(IO55): is an input file for MHOST, created by subroutine PREHST in COD7 module.

SCRA22(IO22): stores the microstresses, strengths and modulus for weavers. It is copied from SCRA47 by subroutine ICNPOS in the COD7 module. SCRA47 is created by subroutine PLYCHK in ICAN module.

SCRA94(IO94): stores the ply stresses, strengths and modulus for regular plies. It is copied from SCRA46 by subroutine ICNPOS in the COD7 module. SCRA46 is created by subroutine PLYCHK in the ICAN module.

SCRA23(IO23): stores the weaver damage index array. It is created by subroutine ICNPOS in the COD7 module. The weaver damage index array is assigned by subroutine W_PFM in COD7.

SCRA79(IO79): stores the damage index array for regular in-plane plies. It is created by subroutine ICNPOS in the COD7 module. The damaged index array is assigned by subroutine PFM in COD7.

SCRA46(IO94): stores the ply stresses, strengths and moduli for regular plies in the ICAN module. It corresponds to SCRA94 in COD7 and is created by subroutine PLYCHK in the ICAN module.

SCRA47(IO22): stores the stresses, strengths and elastic moduli for weavers. It corresponds to SCRA22 in COD7 and is created by subroutine PLYCHK in the ICAN module.

SCRA93(IO93): is used to pass analysis results from MHOST to COD7. It is created by subroutine INFO1 in the FEML module. Its information is transmitted to ICAN by subroutine ICNPOS.

2.1.4 Modularization Enhancement of CODSTRAN-FEM

Effort was dedicated to: 1) implementation of the MCOD to FEM code within FEA and CODSTRAN damage progression analysis codes, 2) the FE program code which can work separately from CODSTRAN, and 3) debugging of the modular version of CODSTRAN-FEM. MCOD to FEM code is a separate FEM post - processor module that provides the interface for a the particular FEM software to the CODSTRAN module. The capacity of the MCOD to FEM code was extended to allow system calls from the CODSTRAN driver of MCOD to FEM for testing of an intermediate example (1000 DOF), as well as testing of stand alone five element programs. Currently implementation of MHOST version 4.2 (the old version) and a sequential version of NESSUS 6.0 are being explored. Evaluations and debugging of existing problems are discussed in the following sections.

Contrary to the previous modular version of COD7, the current version is incompatible with the modified version of MHOST included in CODSTRAN relative to such subroutines as info1, prnshl , etc. MCOD to FEM can be utilized in three ways: 1) Excluding FEM CODSTRAN (MHOST based) module, 2) to handle an intermediate test case (about 1000 D.O.F.) and perform required file operations for common disk file sharing, and 3) to provide dual capability to interface with NESSUS and MHOST input/output information.

Stand Alone MCOD to FEM Connection Program for FEM-CODSTRAN

Figure 2-4a through 2-4e show the flow charts for tracing the major nodal normal calculations in the FEM (MHOST) module of CODSTRAN. Basically, MHOST calculates the normal vectors through the ASSEMI route at the stage of assembling the stiffness matrices. This requires excessive (expensive) algorithm operations (i.e., using the entire MHOST preprocessor, blocks of logical flag settings, global-local coordinate transformations etc). This approach and one in which only needed routines are extracted both require reassembly of routines, fixing pointers, workspace memory redistribution, and cleaning up common blocks which are not longer needed. Because these features are very time consuming. It was decided to rewrite the procedure of nodal normal vector calculations to give coverage results and recalculate the ETRANS tensors in a stand-alone module. This procedure is shown in the flow charts of Figure 2-5a and 2-5b. The revised procedure will take any FEM output and produce a SCRA93 generalize force file.

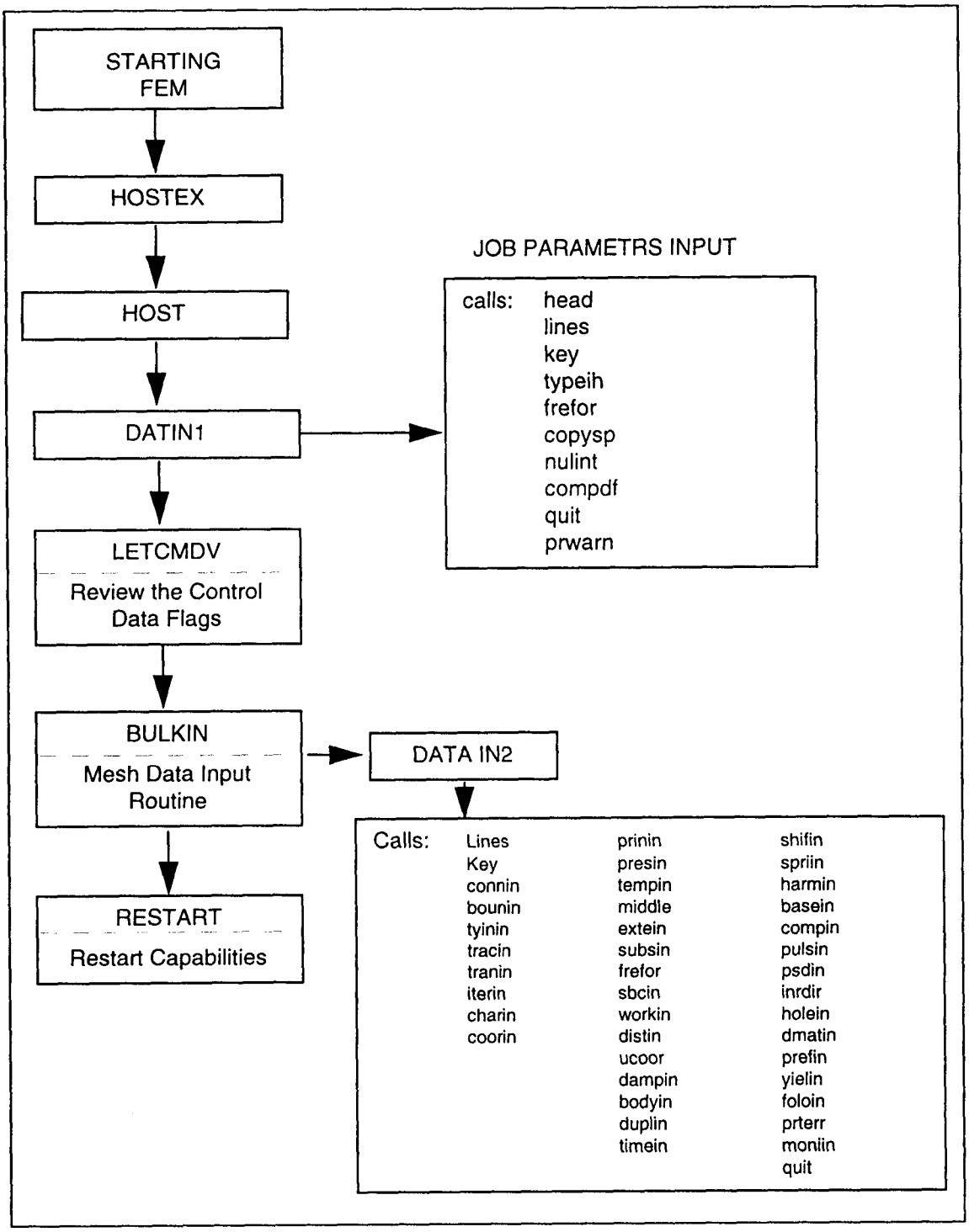

Figure 2-4a. Tracing of the Nodal Normal Calculations in the FEM (MHOST) CODSTRAN ROUTINE

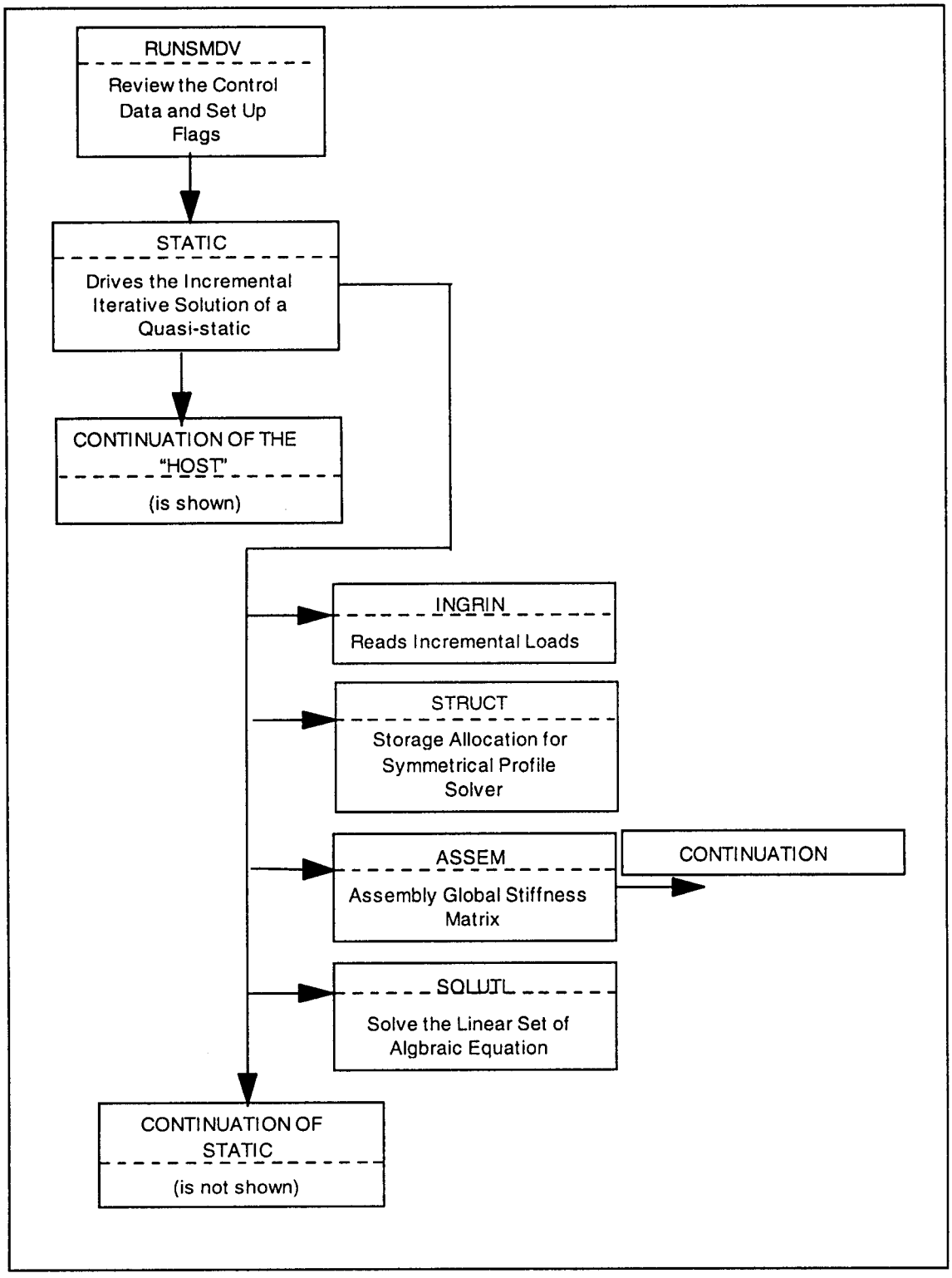

Figure 2-4b. Tracing of the Nodal Normal Calculations in the FEM (MHOST) CODSTRAN ROUTINE (Continued)

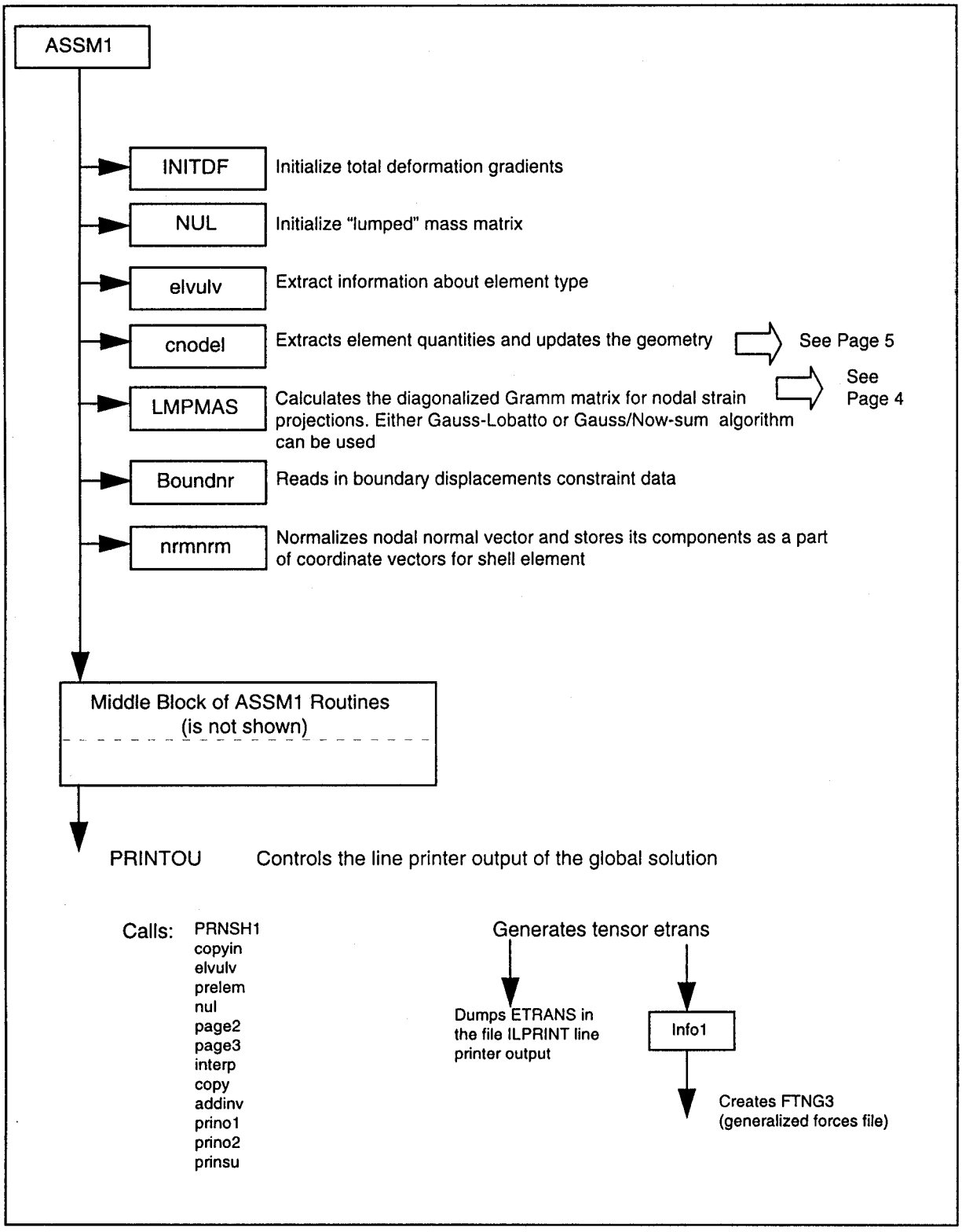

Figure 2-4c. Tracing of the Nodal Normal Calculations in the FEM (MHOST) CODSTRAN ROUTINE (Continued)

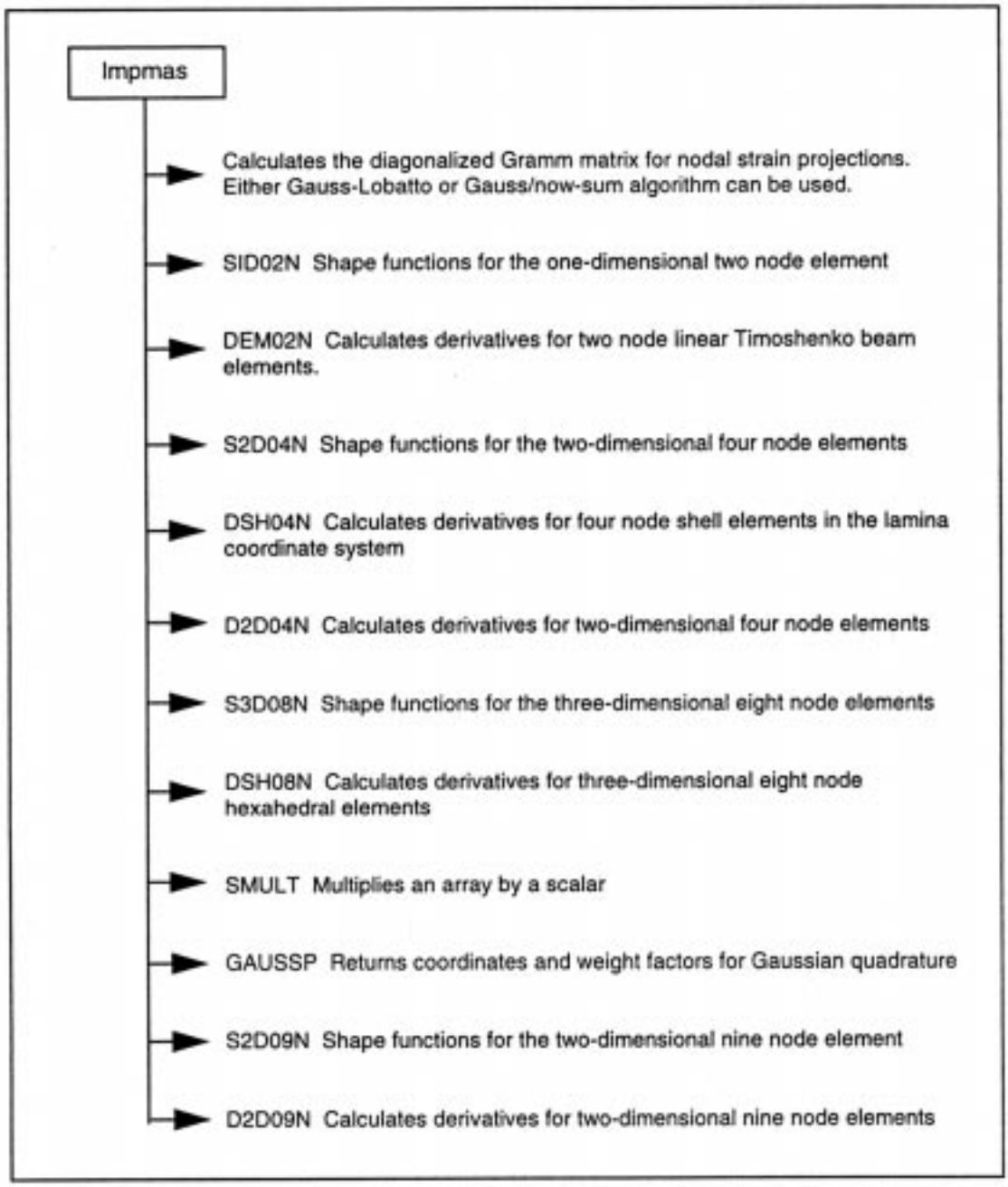

Figure 2-4d. Tracing of the Nodal Normal Calculations in the FEM (MHOST) CODSTRAN ROUTINE (Continued)

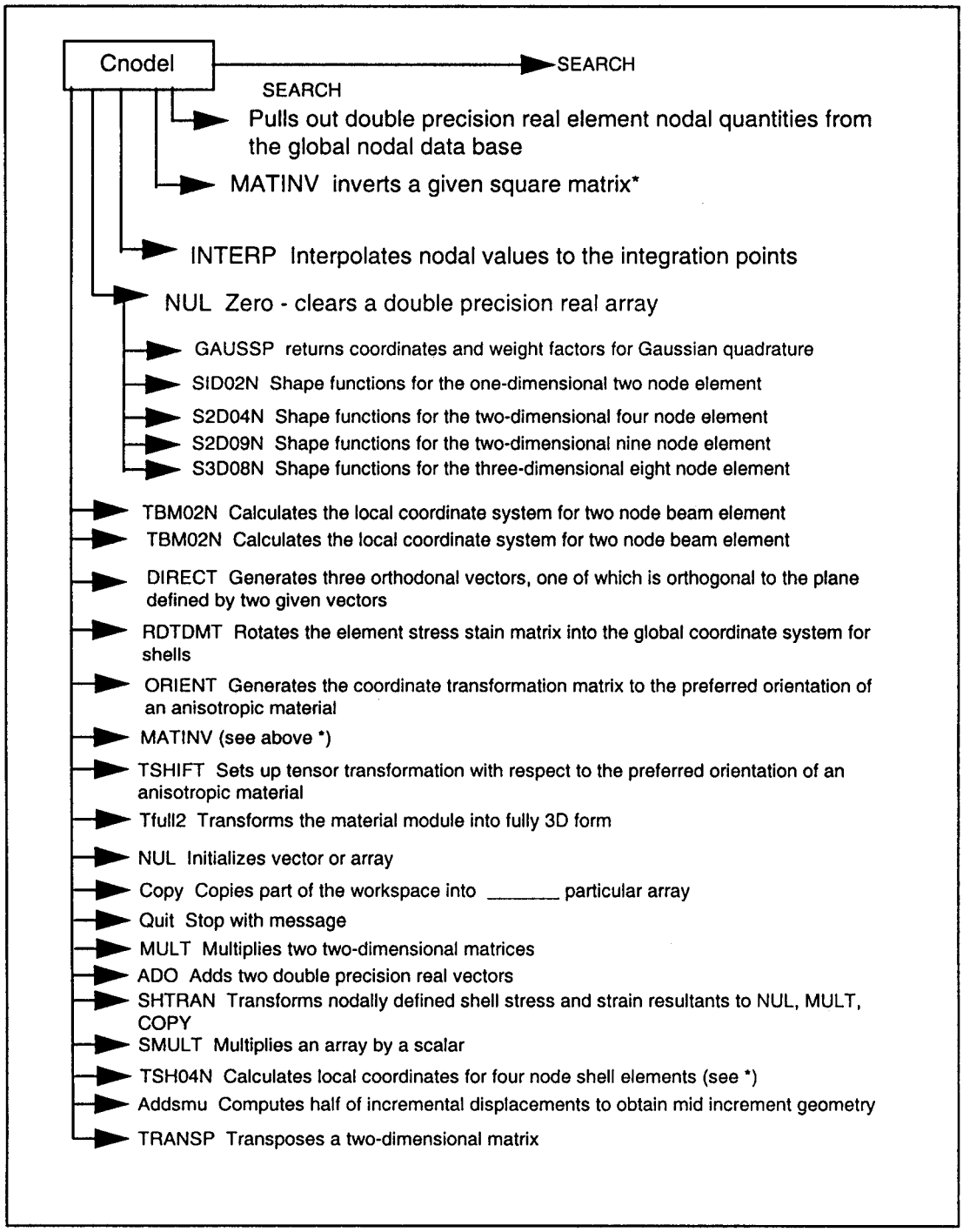

Figure 2-4e. Tracing of the Nodal Normal Calculations in the FEM (MHOST) CODSTRAN ROUTINE (Continued)

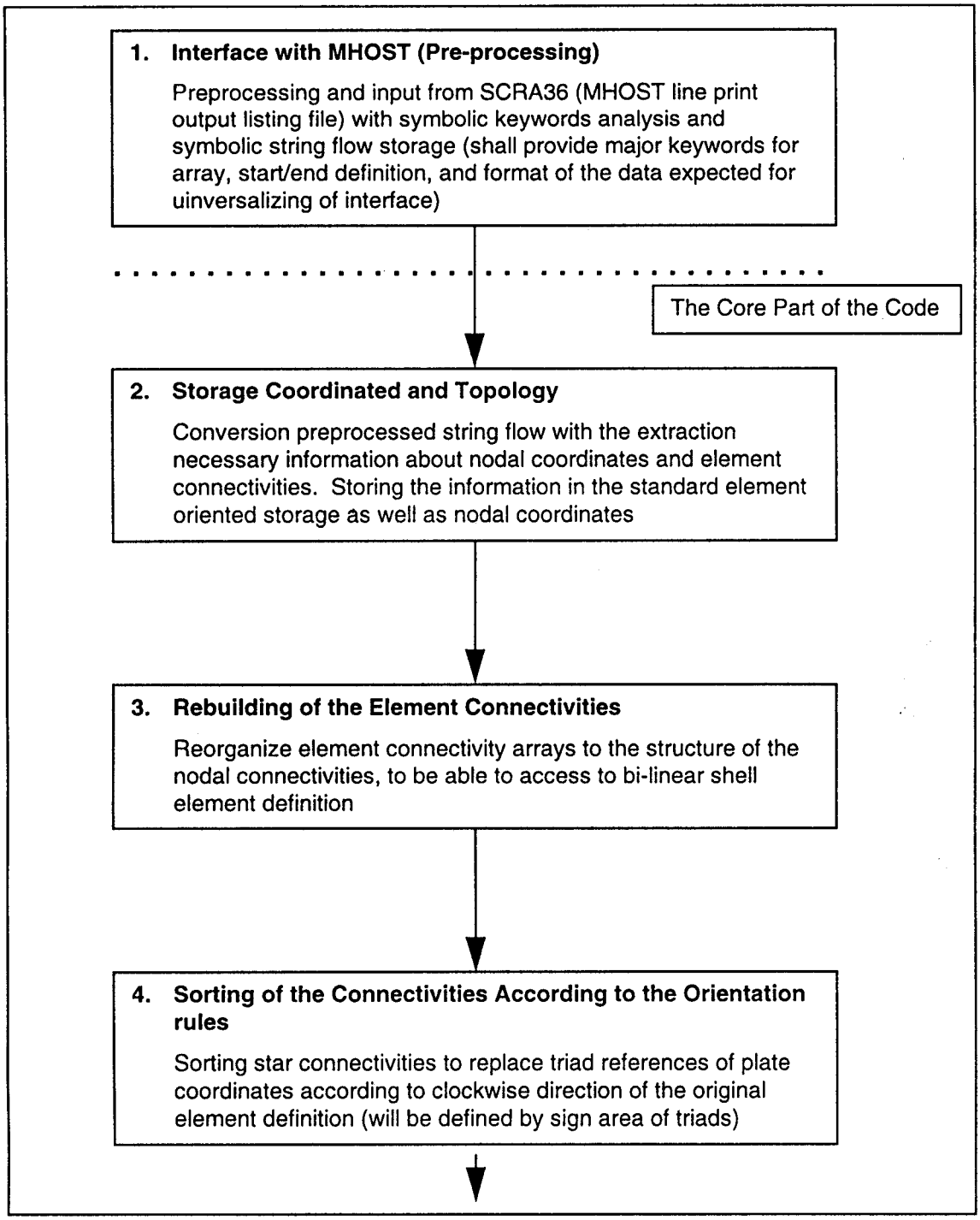

Figure 2-5a. Proposed Preliminary Functional Flow Chart within Respect of External Pressure Loads

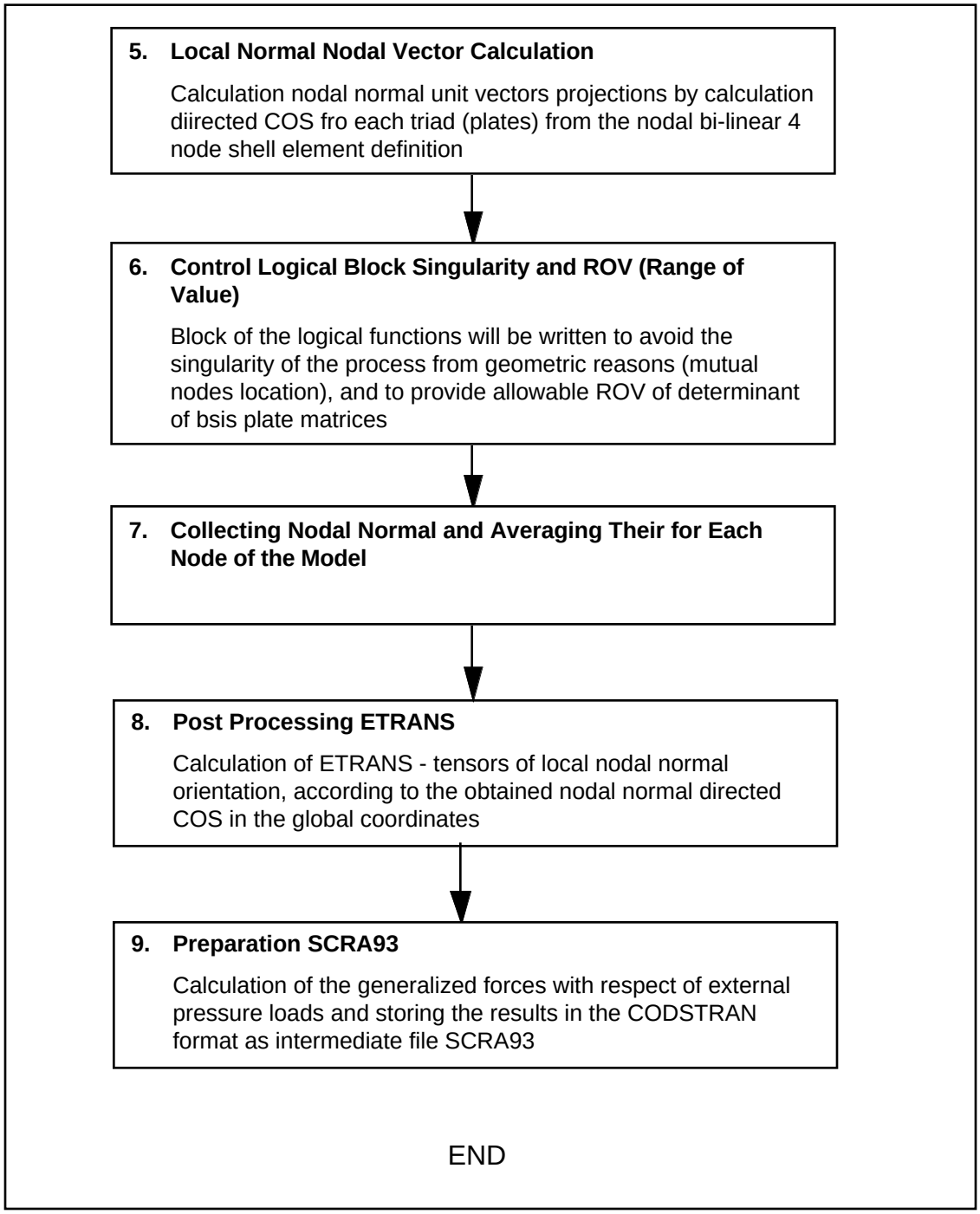

Figure 2-5b. Proposed Preliminary Functional Flow Chart within Respect of External Pressure Loads (Continued)

2.1.5 Implementation of Algorithm

The interface between **MCOD to FEM** and FEM output is not considered as a core part of the source code. The interface routine is to be rewritten for different FEM output format. Pre-processing is organized for input from 2 files: 1) SCRA55 - FEM input file, and 2) SCRA36 - main line print out protocol. The file SCRA55 is used for pre-processing model geometry and connectivity. The file SCRA36 contains results of FEM calculations such as running loads, displacements, etc.

Two generic pre-processor (interface) routines have been written named **io_nd_cn** and **io_str_dsp** to: 1) read symbolic information, 2) convert character strings for double precision real data storage, and 3) pass information to the core set of routines

The storage of nodes and element connectivities were organized as static 2D arrays that can be utilized up to a 15000-node shell element model. The current approach may not be the most rational, but, it is a fast way considering CODSTRAN restrictions. Stored elements and connectivity data are transferred for nodal local normal calculations to modules normals_1 and loc_nrm, respectively.

In the process of developing the modularized code, it was possible to avoid complete rebuilding of the element connectivity algorithm, by considering 2 neighboring nodes for each vertexes during the calculations. Local normal calculation is based on bi-linear shell element representation. Thus, after the local normal calculation for each element, an algorithm allows obtaining normals at each node that is connected to that element.

The local normal averaging algorithm was developed and considered the length of adjacent sides of elements as a weight factor in the calculations.

All of the results are passed to the post-processing output files **info1_mirv3.f** main program of **MCOD to FEM.** These results are needed by CODSTRAN for damage progression analysis.

2.1.6 MCOD to FEM Source Code Structure

The **MCOD to FEM** source code structure is shown in Table 2-3, along with the description of each module of the code.

Table 2-3. MCOD to FEM source code structure

info1_mirv3.f	The main module of MCOD to FEM. This module is calling input blocks, preprocessing of data, normal and ETRANS calculations, post- processing **info1** and preparing necessary files for transferring to CODSTRAN analyzer on the next loop of damage tracking
opfeml	Opening system channels for integration between MHOST, MCOD to FEM and CODSTRAN analyzer
get_record	Obtaining record number from the particular sequential text input file, according to given symbolic prototype. Moving pointer on the prototype matching record.
io_nd_cn	Generic input of the nodes and connectivity from SCRA55 FEM input file. It is not so advanced routine as MHOST preprocessor yet, but it will include at least GENEX capabilities on the stage of integration with GENEX
io_str_dsp	An input of the stress and displacements from SCRA36 - FEM output file. Interface. Has to be rewritten for the particular FEM output format
normals_1	This routine contains generic algorithm of the averaging local normal directed cosines, based on the weight distribution between local normalized vector in each vertexes within respect of adjacent side lengthens.
loc_nrm	Subroutine-function of the local (element defined) directed cosines
anorma	Based on pre-calculated coefficients of the plane of bi-linear shell element definition this routine calculates normalizing multiplier of local normal component
coeff	Calculates polynomial coefficients of arbitrary plane definition based on 3 given vertexes coordinates
alength	Function for calculations distance between vertexes defining local plane
info1	Post-processing of FEM results. The routine is preparing

2.1.7 Verification of the Modular Version Of CODSTRAN (COD6)

The COD versions 5, 6, and 7 for 3D stitched/braided composites as developed by Dr. Minnetyan were integrated with GENOA software system and debugged. One feature of the new code is the restart capability which is combined with start-stop-continue code execution at selected times. This allows execution of long jobs to take place at desired time segments (when there is no competition for computer resources).

The verification of the modular version of CODSTRAN (COD6) that had been installed on IBM, HP, and SGI workstations was conducted via simulations of built up stiffened composite panels with blade stiffeners and a diamond shape cutouts. The built-up panels were made of stitched composites with stacks of 7-Ply AS4/3501-6 [+45/-45/0_2/90]s Saerbeck Laminate [44%/44%/12%] stitched with 1600 denier kevlar thread with stitch spacing of 0.2 in. and a pitch of 0.125 in. Structural models with two different finite element mesh refinements were considered. The coarser model had 540 elements and 786 nodes. The more refined model had 1636 elements and 1638 nodes. Both models were simulated under axial compression using COD6 and the previous version COD5. The simulation of the refined model under COD6 proceeded up to the damage initiation stage but then encountered difficulties associated with memory allocation. The simulation of the coarser model gave exactly the same loads for damage initiation and progression under both COD5and COD6 simulations. However, the amount of damage computed by COD6 was greater than that computed by COD5 and the number of finite element structural analyses required by COD6 was greater than the number of analyses required by COD5to reach the same load. The displacements computed by cod6 were approximately two percent larger than the displacements computed by COD5before damage initiation. After substantial damage progression, COD6 displacements became five percent greater than the COD5displacements under the same load. Investigation of reasons for the differences between COD5and COD6 are still in progress.

2.2 TESTING AND VALIDATION

2.2.1 Model Definition (For Test Example)

A rectangular flat panel was considered for a test example to validate the modularized code. The model mesh had 2x3, 4 node shell elements of type 75 with 6 DOF per node and a total of 12 node and 6 elements. Two intermediate rows where 0.9 inches in Z direction, in order to check nodal normal calculations. The model had 18 boundaries, with the DOF fixed at one edge, and external nodal forces are applied in the X direction from another free edge. The composite consisted, of 4 plies, with 0 degree fiber orientation.

Comparison of the coordinates and nodal averaged normal components from the COD6 - MHOST and MCOD to FEM (Intermediate output).

The coordinates and the nodal normal components are listed in Tables 2-4 and 2-5 from MHOST and MCOD to FEM codes, respectively.

Table 2-4. Coordinate And Nodal Averaged Normal Components From MHOST

	X	Y	Z	cosα	cosβ	cosγ	Δ
1.	.00	.00	.00	-.66	.00	.75	.33
2.	.00	1.00	.00	-.66	.00	.75	.33
3.	.00	2.00	.00	-.66	.00	.75	.33
4.	1.02	.00	.90	-.40	.00	.92	.33
5.	1.02	1.00	.90	-.40	.00	.91	.33
6.	1.02	2.00	.90	-.40	.00	.92	.33
7.	2.05	.00	.90	.40	.01	.92	.33
8.	2.03	1.00	.90	.41	.00	.91	.33
9.	2.05	2.00	.90	.40	-.01	.92	.33
10.	3.08	.00	.00	.66	.02	.75	.33
11.	3.05	1.00	.00	.66	.00	.75	.33
12.	3.08	2.00	.00	.66	-.02	.75	.33

Table 2-5. Coordinate And Nodal Averaged Normal Components From MCOD To FEM

	X	Y	Z	cosα	cosβ	cosγ	Δ
1.	.00	.00	.00	-.66	.00	.75	.33
2.	.00	1.00	.00	-.66	.00	.75	.33
3.	.00	2.00	.00	-.66	.00	.75	.33
4.	1.02	.00	.90	-.38	.00	.93	.33
5.	1.02	1.00	.90	-.38	.00	.92	.33
6.	1.02	2.00	.90	-.38	.00	.93	.33
7.	2.05	.00	.90	.38	.01	.93	.33
8.	2.03	1.00	.90	.38	.00	.92	.33
9.	2.05	2.00	.90	.38	-.01	.93	.33
10.	3.08	.00	.00	.66	.02	.75	.33
11.	3.05	1.00	.00	.66	.00	.75	.33
12.	3.08	2.00	.00	.66	-.02	.75	.33

Comparison of the components of nodal running loads from the COD6-MHOST and MCOD to FEM (SCRA61).

The results of nodal running loads are listed in Tables 2-6 and 2-7 from MHOST and MCOD to FEM codes, respectively.

Table 2-6. Output of nodal running loads from the COD6-MHOST (SCRA61).

No.	Nx	Ny	Nxy	Q1	Q2	Mx	My	Myx
1.	.444049E-01	.756702E-03	-.106099E-02	.263657E-01	.448849E-03	-.162072E-04	-.395424E-01	.120904E-02
2.	.427889E-01	.723994E-03	.608107E-12	.265037E-01	.451097E-03	.264833E-11	-.395153E-01	.515064E-11
3.	.444049E-01	.756702E-03	.106099E-02	.263657E-01	.448849E-03	.162072E-04	-.395424E-01	-.120904E-02
4.	.158518E-01	.578358E-02	-.418313E-02	.150713E-01	.341761E-03	.724311E-05	-.218028E-01	.568331E-03
5.	.375709E-01	.613820E-02	.143576E-10	.151819E-01	.343575E-03	.312078E-11	-.218630E-01	.149137E-11
6.	.158518E-01	.578358E-02	.418313E-02	.150713E-01	.341761E-03	-.724310E-05	-.218028E-01	-.568331E-03
7.	-.134355E-01	-.753096E-02	-.355526E-02	-.340828E-04	-.711631E-04	.906664E-05	-.335956E-06	-.939671E-04
8.	.906555E-02	-.716736E-02	.184308E-10	.127539E-04	-.703492E-04	.309960E-11	.682565E-06	-.273999E-11
9.	-.134354E-01	-.753096E-02	.355526E-02	-.340828E-04	-.711631E-04	-.906664E-05	-.335944E-06	.939671E-04
10.	-.149089E-03	.323702E-02	-.148445E-03	-.466253E-04	.200806E-04	-.133774E-04	-.267497E-04	.116552E-04
11.	.106000E-02	.335050E-02	-.805363E-10	.669486E-04	.227273E-04	.225789E-11	.245598E-04	-.296972E-11
12.	-.149087E-03	.323702E-02	.148445E-03	-.466252E-04	.200806E-04	.133774E-04	-.267497E-04	-.116552E-04

Table 2-7. Output Of Nodal Running Loads From The MCOD To FEM (SCRA61).

No.	Nx	Ny	Nxy	Q1	Q2	Mx	My	Myx
1.	.444050E-01	.756700E-03	-.106100E-02	.263660E-01	.448850E-03	-.162070E-04	-.395420E-01	.120900E-02
2.	.427890E-01	.723990E-03	.608110E-12	.265040E-01	.451100E-03	.264830E-11	-.395150E-01	.515060E-11
3.	.444050E-01	.756700E-03	.106100E-02	.263660E-01	.448850E-03	.162070E-04	-.395420E-01	-.120900E-02
4.	.158520E-01	.578360E-02	-.418310E-02	.150710E-01	.341760E-03	.724310E-05	-.218030E-01	.568330E-03
5.	.375710E-01	.613820E-02	.143580E-10	.151820E-01	.343570E-03	.312080E-11	-.218630E-01	.149140E-11
6.	.158520E-01	.578360E-02	.418310E-02	.150710E-01	.341760E-03	-.724310E-05	-.218030E-01	-.568330E-03
7.	-.134350E-01	-.753100E-02	-.355530E-02	-.340830E-04	-.711630E-04	.906660E-05	-.335960E-06	-.939670E-04
8.	.906560E-02	-.716740E-02	.184310E-10	.127540E-04	-.703490E-04	.309960E-11	.682560E-06	-.274000E-11
9.	-.134350E-01	-.753100E-02	.355530E-02	-.340830E-04	-.711630E-04	-.906660E-05	-.335940E-06	.939670E-04
10.	-.149090E-03	.323700E-02	-.148440E-03	-.466250E-04	.200810E-04	-.133770E-04	-.267500E-04	.116550E-04
11.	.106000E-02	.335050E-02	-.805360E-10	.669490E-04	.227270E-04	.225790E-11	.245600E-04	-.296970E-11
12.	-.149090E-03	.323700E-02	.148440E-03	-.466250E-04	.200810E-04	.133770E-04	-.267500E-04	-.116550E-04

Comparison of the components of general forces from COD6-MHOST and MCOD to FEM (SCRA93).

The results of general forces are listed in Tables 2-8 and 2-9 from MHOST and MCOD to FEM codes, respectively.

Table 2-8. Output Of General Forces From COD6-MHOST (SCRA93).

	Nx	Ny	Nxy	Q1	Q2	Mx	My	Myx
1.	.444049E-01	.756702E-03	-.106099E-02	.263657E-01	.448849E-03	-.162072E-04	-.395424E-01	.120904E-02
2.	.427889E-01	.723994E-03	.608107E-12	.265037E-01	.451097E-03	.264833E-11	-.395153E-01	.515064E-11
3.	.444049E-01	.756702E-03	.106099E-02	.263657E-01	.448849E-03	.162072E-04	-.395424E-01	-.120904E-02
4.	.158518E-01	.578358E-02	-.418313E-02	.150713E-01	.341761E-03	.724311E-05	-.218028E-01	.568331E-03
5.	.375709E-01	.613820E-02	.143576E-10	.151819E-01	.343575E-03	.312078E-11	-.218630E-01	.149137E-11
6.	.158518E-01	.578358E-02	.418313E-02	.150713E-01	.341761E-03	-.724310E-05	-.218028E-01	-.568331E-03
7.	-.134355E-01	-.753096E-02	-.355526E-02	-.340828E-04	-.711631E-04	.906664E-05	-.335956E-06	-.939671E-04
8.	.906555E-02	-.716736E-02	.184308E-10	.127539E-04	-.703492E-04	.309960E-11	.682565E-06	-.273999E-11
9.	-.134354E-01	-.753096E-02	.355526E-02	-.340828E-04	-.711631E-04	-.906664E-05	-.335944E-06	.939671E-04
10.	-.149089E-03	.323702E-02	-.148445E-03	-.466253E-04	.200806E-04	-.133774E-04	-.267497E-04	.116552E-04
11.	.106000E-02	.335050E-02	-.805363E-10	.669486E-04	.227273E-04	.225789E-11	.245598E-04	-.296972E-11
12.	-.149087E-03	.323702E-02	.148445E-03	-.466252E-04	.200806E-04	.133774E-04	-.267497E-04	-.116552E-04

Table 2-9. Output of general forces from COD to FEM (SCRA93).

	Nx	Ny	Nxy	Q1	Q2	Mx	My	Myx
1.	.444050E-01	.756700E-03	-.106100E-02	.263660E-01	.448850E-03	-.162070E-04	-.395420E-01	.120900E-02
2.	.427890E-01	.723990E-03	.608110E-12	.265040E-01	.451100E-03	.264830E-11	-.395150E-01	.515060E-11
3.	.444050E-01	.756700E-03	.106100E-02	.263660E-01	.448850E-03	.162070E-04	-.395420E-01	-.120900E-02
4.	.158520E-01	.578360E-02	-.418310E-02	.150710E-01	.341760E-03	.724310E-05	-.218030E-01	.568330E-03
5.	.375710E-01	.613820E-02	.143580E-10	.151820E-01	.343570E-03	.312080E-11	-.218630E-01	.149140E-11
6.	.158520E-01	.578360E-02	.418310E-02	.150710E-01	.341760E-03	-.724310E-05	-.218030E-01	-.568330E-03
7.	-.134350E-01	-.753100E-02	-.355530E-02	-.340830E-04	-.711630E-04	.906660E-05	-.335960E-06	-.939670E-04
8.	.906560E-02	-.716740E-02	.184310E-10	.127540E-04	-.703490E-04	.309960E-11	.682560E-06	-.274000E-11
9.	-.134350E-01	-.753100E-02	.355530E-02	-.340830E-04	-.711630E-04	-.906660E-05	-.335940E-06	.939670E-04
10.	-.149090E-03	.323700E-02	-.148440E-03	-.466250E-04	.200810E-04	-.133770E-04	-.267500E-04	.116550E-04
11.	.106000E-02	.335050E-02	-.805360E-10	.669490E-04	.227270E-04	.225790E-11	.245600E-04	-.296970E-11
12.	-.149090E-03	.323700E-02	.148440E-03	-.466250E-04	.200810E-04	.133770E-04	-.267500E-04	-.116550E-04

Comparison Of Components Of Displacements And Displacements In Averaged Nodal Normal Direction From The COD6-MHOST And MCOD To FEM.

The results of displacements are listed in Tables 2-10 and 2-11 for MHOST and MCOD to FEM codes, respectively.

Table 2-10. Intermediate Output From COD6-MHOST (Stored In SCRA78).

	δx	δy	δz	‖δ‖
1	.2833223E-31	.1209083E-32	.2546441E-33	-.1851198E-31
2	.6067466E-31	-.1142886E-40	-.5092882E-33	-.4058061E-31
3	.2833223E-31	-.1209083E-32	.2546441E-33	-.1851198E-31
4	.3796913E-05	-.3096136E-07	-.4286469E-05	-.5451225E-05
5	.3659259E-05	-.1779857E-16	-.4104648E-05	-.5234383E-05
6	.3796913E-05	.3096136E-07	-.4286469E-05	-.5451225E-05
7	.3787142E-05	.4328028E-07	-.1171077E-04	-.9206727E-05
8	.3669303E-05	-.7439862E-14	-.1176150E-04	-.9262503E-05
9	.3787142E-05	-.4328029E-07	-.1171077E-04	-.9206727E-05
10	-.2975447E-05	-.2247131E-07	-.1944384E-04	-.1659171E-04
11	-.2867477E-05	-.3346390E-13	-.1911327E-04	-.1618926E-04
12	-.2975447E-05	.2247124E-07	-.1944384E-04	-.1659171E-04

Table 2-11. Intermediate Output From MCOD To FEM (Stored In SCRA78).

	δx	δy	δz	‖δ‖
1	.2833200E-31	.1209100E-32	.2546400E-33	-.1851183E-31
2	.6067500E-31	-.1142900E-40	-.5092900E-33	-.4058084E-31
3	.2833200E-31	-.1209100E-32	.2546400E-33	-.1851183E-31
4	.3796900E-05	-.3096100E-07	-.4286500E-05	-.5404840E-05
5	.3659300E-05	-.1779900E-16	-.4104600E-05	-.5188463E-05
6	.3796900E-05	.3096100E-07	-.4286500E-05	-.5404840E-05
7	.3787100E-05	.4328000E-07	-.1171100E-04	-.9413325E-05
8	.3669300E-05	-.7439900E-14	-.1176100E-04	-.9470786E-05
9	.3787100E-05	-.4328000E-07	-.1171100E-04	-.9413325E-05
10	-.2975400E-05	-.2247100E-07	-.1944400E-04	-.1659180E-04
11	-.2867500E-05	-.3346400E-13	-.1911300E-04	-.1618908E-04
12	-.2975400E-05	.2247100E-07	-.1944400E-04	-.1659180E-04

2.2.2 Comments MCOD to FEM

- MCOD to FEM is designed only for 4 node shell element concept.
- Validation and debugging for real pressure loads case has to be provided.
- Validation for stay alone MHOST module has to be provided.
- Real model size example (about 6000 DOF) has to be tested.
- System call from COD6 (CODSTRAN part) for FEM should be chosen.
- File SCRA83 is not needed any more. This file can be eliminated.
- Program should be checked with SCRA80 (failure index file) after integration with
- CODSTRAN through system call.
- Provide parametric dimensioning of the arrays according to the memory distribution concept.

2.2.3 Validation of COD7MM With an Intermediate Example (1000 DOF)

The validation process included running of the previous version of COD7 that agreed with the sequential version of CODSTRAN. Simulation results (generalized nodal stresses, damage history and progression characteristics files) were in good agreement from both code versions.

Definition of the Model for Validation

A flat panel (10.8x1 inches) was used for validation of the codes. The finite element mesh used contained 140 shell elements of type 75 and 165 nodes with 6 DOF per node (Figure 2-6). The panel was subjected to tension with 0 initial Z coordinates and a regular non- uniform 10x7 mesh. The FEM with 20 duplicate nodes (10 on each edge) in the direction of prolongation to give uniform boundary displacements. The panel was made from composite material having 36 fiber reinforced plies of various compositions (1AS4T3601 and 2IM-73601 with 1KEVL3601).

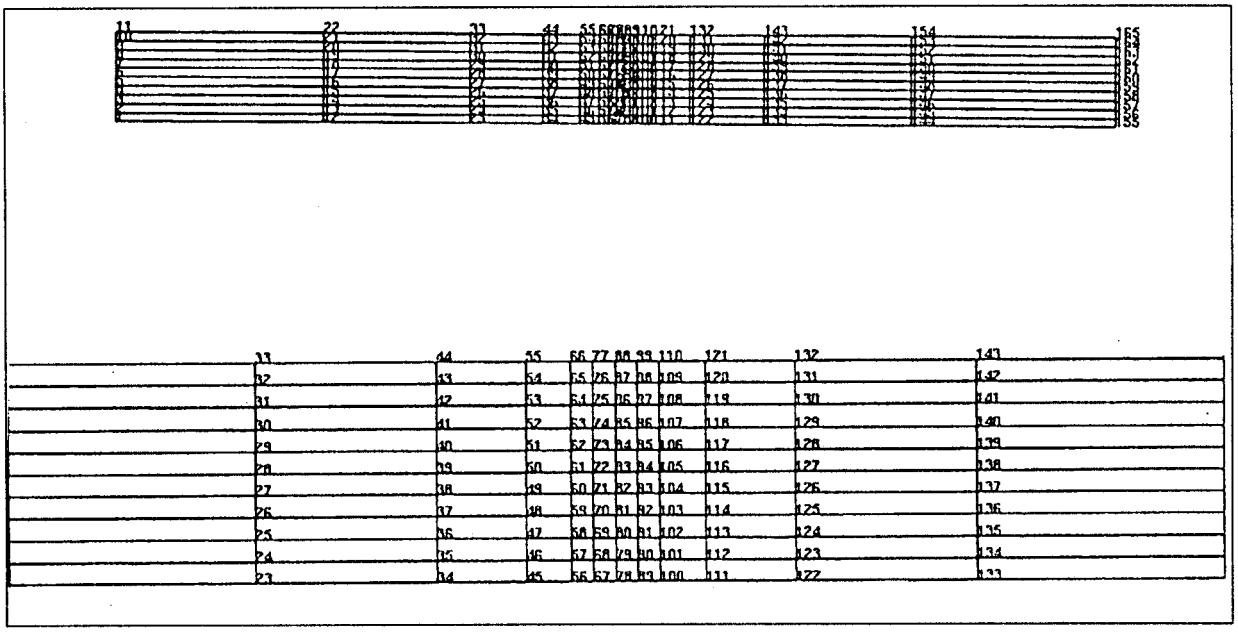

Figure 2-6. Finite Element Mesh

The boundary conditions consist of 79 constraints that restricted displacement in the out-of-plane direction for 3 rows of nodes on each side of the model, and fixed DOF in the longitudinal direction for all 11 nodes from one edge, and 2 nodes on the edges in Y direction. The initial profile of the loads applied to the free edge of all the 11 nodes was 1, 2, 3, 3, 3, 3, 3, 3, 3, 3, 3, 2, 1 pounds.

Validation of MHOST 4.2 Based Modularization

Comparison of the COD7MM and COD7 intermediate generalized nodal force results (between iterations) shows partial agreement at the initial stage of simulation as shown in Table 2-12.

Table 2-12. Generalized Nodal Forces From Files SCRA88 After 21 CODSTRAN Interactions

FEM ANALYSIS NO. 1

	COD7			COD7 + MHOST		
Node No.	NX	NY	NXY	NX	NY	NXY
1	.2856500E+02	.4740600E+01	.1698600E+00	.2856500E+02	.4740600E+01	.1698600E+00
2	.2836500E+02	.4707300E+01	.2000300E+00	.2836500E+02	.4707300E+01	.2000300E+00
3	.2825700E+02	.4689500E+01	.2098600E+00	.2825700E+02	.4689500E+01	.2098600E+00
4	.2819300E+02	.4678800E+01	.1555300E+00	.2819300E+02	.4678800E+01	.1555300E+00
5	.2815800E+02	.4673100E+01	.8156900E-01	.2815800E+02	.4673100E+01	.8156900E-01
6	.2814700E+02	.4671300E+01	-.5802400E-07	.2814700E+02	.4671300E+01	-.5802400E-07
7	.2815800E+02	.4673100E+01	-.8156900E-01	.2815800E+02	.4673100E+01	-.8156900E-01

• • •

	COD7			COD7 + MHOST		
Node	NX	NY	NXY	NX	NY	NXY
77	.2697200E+02	.1381200E-02	-.8034700E-03	.2697200E+02	.1381200E-02	-.8034700E-03
78	.2697000E+02	-.4265300E-02	.6336400E-09	.2697000E+02	-.4265300E-02	.6336300E-09
79	.2698700E+02	-.1132700E-03	.1091400E-08	.2698700E+02	-.1132700E-03	.1091400E-08
80	.2697100E+02	-.6095800E-02	.2061700E-08	.2697100E+02	-.6095800E-02	.2061700E-08
81	.2700300E+02	-.1086600E-01	.3325100E-08	.2700300E+02	-.1086600E-01	.3325100E-08
82	.2703400E+02	-.1673200E-01	.4623800E-08	.2703400E+02	-.1673200E-01	.4623900E-08
83	.2704000E+02	-.2157000E-01	.5166100E-08	.2704000E+02	-.2157000E-01	.5166100E-08
84	.2703400E+02	-.1673200E-01	.4623800E-08	.2703400E+02	-.1673200E-01	.4623800E-08
85	.2700300E+02	-.1086600E-01	.3325100E-08	.2700300E+02	-.1086600E-01	.3325000E-08

	COD7			COD7 + MHOST		
Node	NX	NY	NXY	NX	NY	NXY
..157	.2825700E+02	.4689500E+01	-.2098600E+00	.2825700E+02	.4689500E+01	-.2098600E+00
.158	.2819300E+02	.4678800E+01	-.1555300E+00	.2819300E+02	.4678800E+01	-.1555300E+00
159	.2815800E+02	.4673100E+01	-.8156900E-01	.2815800E+02	.4673100E+01	-.8156900E-01
160	.2814700E+02	.4671300E+01	-.3459300E-07	.2814700E+02	.4671300E+01	-.3459300E-07
161	.2815800E+02	.4673100E+01	.8156900E-01	.2815800E+02	.4673100E+01	.8156900E-01
162	.2819300E+02	.4678800E+01	.1555300E+00	.2819300E+02	.4678800E+01	.1555300E+00
163	.2825700E+02	.4689500E+01	.2098600E+00	.2825700E+02	.4689500E+01	.2098600E+00
164	.2836500E+02	.4707300E+01	.2000300E+00	.2836500E+02	.4707300E+01	.2000300E+00
165	.2856500E+02	.4740600E+01	.1698600E+00	.2856500E+02	.4740600E+01	.1698600E+00

FEM ANALYSIS NO. 5

	COD7			COD7 + MHOST		
Node	NX	NY	NXY	NX	NY	NXY
..1	.1285470E+03	.2133340E+02	.7606730E+00	.1285450E+03	.2133310E+02	.7606510E+00
2	.1276440E+03	.2118330E+02	.8971240E+00	.1276410E+03	.2118310E+02	.8970380E+00
3	.1271580E+03	.2110290E+02	.9427500E+00	.1271570E+03	.2110260E+02	.9425400E+00
4	.1268680E+03	.2105470E+02	.6992520E+00	.1268670E+03	.2105460E+02	.6989850E+00
5	.1267120E+03	.2102890E+02	.3668610E+00	.1267110E+03	.2102880E+02	.3665620E+00
6	.1266630E+03	.2102080E+02	-.3545010E-06	.1266620E+03	.2102060E+02	-.3140540E-03
7	.1267120E+03	.2102890E+02	-.3668610E+00	.1267110E+03	.2102880E+02	-.3671760E+00

• • •

..77	.1213860E+03	.7021630E-02	-.4106590E-02	.1213840E+03	.7046040E-02	-.4191330E-02
78	.1213750E+03	-.1835080E-01	.5048760E-07	.1213750E+03	-.1834210E-01	.2980910E-04
79	.1214460E+03	.9523300E-04	-.1066810E-06	.1214460E+03	.9628900E-04	.5599640E-04
80	.1213740E+03	-.2540590E-01	-.2368090E-06	.1213730E+03	-.2540440E-01	.9931130E-04
81	.1215130E+03	-.4525560E-01	-.8958620E-07	.1215130E+03	-.4525180E-01	.1265360E-03
82	.1216460E+03	-.7004310E-01	.1607450E-06	.1216460E+03	-.7004000E-01	.1413030E-03
83	.1216700E+03	-.9077220E-01	.2354820E-07	.1216690E+03	-.9076910E-01	.1476790E-03
84	.1216460E+03	-.7004400E-01	-.1185590E-06	.1216460E+03	-.7003800E-01	.1587060E-03
85	.1215130E+03	-.4525650E-01	.1199930E-06	.1215120E+03	-.4524460E-01	.1495280E-03

• • •

157	.1271580E+03	.2110290E+02	-.9427400E+00	.1271570E+03	.2110270E+02	-.9428700E+00
158	.1268680E+03	.2105470E+02	-.6992640E+00	.1268680E+03	.2105460E+02	-.6994150E+00
159	.1267120E+03	.2102890E+02	-.3668680E+00	.1267110E+03	.2102880E+02	-.3670800E+00
160	.1266630E+03	.2102080E+02	-.6181300E-07	.1266630E+03	.2102070E+02	-.2541380E-03
161	.1267120E+03	.2102890E+02	.3668680E+00	.1267120E+03	.2102880E+02	.3665940E+00
162	.1268680E+03	.2105470E+02	.6992640E+00	.1268680E+03	.2105460E+02	.6989330E+00
163	.1271580E+03	.2110290E+02	.9427400E+00	.1271570E+03	.2110270E+02	.9423600E+00
164	.1276440E+03	.2118330E+02	.8971240E+00	.1276430E+03	.2118320E+02	.8989970E+00
165	.1285470E+03	.2133340E+02	.7606780E+00	.1285450E+03	.2133300E+02	.7648000E+00

FEM ANALYSIS NO. 8

	COD7			COD7 + MHOST		
Node	NX	NY	NXY	NX	NY	NXY
1	.9284270E+03	.1540780E+03	.5487830E+01	.9283150E+03	.1540620E+03	.5486400E+01
2	.9218940E+03	.1529940E+03	.6474730E+01	.9218110E+03	.1529800E+03	.6469900E+01
3	.9183880E+03	.1524130E+03	.6806440E+01	.9183170E+03	.1524010E+03	.6796550E+01
4	.9162980E+03	.1520650E+03	.5049360E+01	.9162370E+03	.1520560E+03	.5036340E+01
5	.9151620E+03	.1518810E+03	.2649440E+01	.9151110E+03	.1518710E+03	.2634300E+01
6	.9148130E+03	.1518210E+03	-.1650330E-05	.9147820E+03	.1518140E+03	-.1610440E-01
7	.9151620E+03	.1518810E+03	-.2649450E+01	.9151310E+03	.1518730E+03	-.2665570E+01

• • •

77	.8767260E+03	.5177380E-01	-.3042380E-01	.8766640E+03	.5271970E-01	-.3450980E-01
78	.8766550E+03	-.1311010E+00	.1727260E-05	.8766350E+03	-.1306650E+00	.1496700E-02
79	.8771460E+03	.1823630E-02	.9788890E-06	.8771260E+03	.1862330E-02	.2862820E-02
80	.8766340E+03	-.1798420E+00	-.2290690E-05	.8766030E+03	-.1797830E+00	.5088090E-02
81	.8776230E+03	-.3202290E+00	-.2064840E-05	.8775930E+03	-.3201590E+00	.6446060E-02
82	.8785760E+03	-.4963530E+00	-.2640750E-06	.8785460E+03	-.4962360E+00	.7206170E-02
83	.8787400E+03	-.6442120E+00	.1705710E-06	.8786990E+03	-.6441380E+00	.7554160E-02
84	.8785760E+03	-.4963440E+00	.5697210E-06	.8785260E+03	-.4961610E+00	.8107910E-02
85	.8776230E+03	-.3202350E+00	.2285190E-05	.8775720E+03	-.3199010E+00	.7626350E-02

• • •

157	.9183880E+03	.1524130E+03	-.6806530E+01	.9183570E+03	.1524080E+03	-.6812460E+01
158	.9162980E+03	.1520650E+03	-.5049380E+01	.9162580E+03	.1520600E+03	-.5058370E+01
159	.9151620E+03	.1518810E+03	-.2649390E+01	.9151410E+03	.1518740E+03	-.2660550E+01
160	.9148130E+03	.1518210E+03	-.1355650E-05	.9147830E+03	.1518160E+03	-.1276620E-01
161	.9151620E+03	.1518810E+03	.2649390E+01	.9151420E+03	.1518750E+03	.2635120E+01
162	.9162980E+03	.1520650E+03	.5049380E+01	.9162680E+03	.1520620E+03	.5033450E+01
163	.9183880E+03	.1524130E+03	.6806530E+01	.9183670E+03	.1524090E+03	.6787190E+01
164	.9218940E+03	.1529940E+03	.6474730E+01	.9218730E+03	.1529900E+03	.6569700E+01
165	.9284270E+03	.1540780E+03	.5487830E+01	.9283350E+03	.1540580E+03	.5698890E+01

Comparison of Damage Progression History In Files SCRA73 After 21 CODSTRAN Interaction

The damage progression results of COD7 and COD7MM+MHOSTare in good agreement.

Comparison of Damage Progression History In Files SCRA28 After 14 CODSTRAN Interaction

After 14 CODSTRAN interactions the SCRA28 files were in good agreement relative to incremental loads, elastic energy, percentage of the damage, and damage energy. There was significant disagreement in energy release rate making it necessary to correct this situation. However, the DERR change appearing during Iteration No. 12, show that the processes in both runs were very similar (Tables 2-13 and 2-14)

Table 2-13. COD7 Volume Of Structure Is Computed As: .2430864E+01

Iter #	NEL	NODES	FORCE (kip)	PRESS (ksi)	ELA_ ENERGY	DAMAG (/100)	DERR (ksi)	TTL_DERR(ksi)	DMGE_ ENRGY
1	140	165	.2700E-01	.0000E+00	.4673E+02	0	0	0	0
3	140	165	.4050E-01	.0000E+00	.4648E+02	.1975E+01	.3871E-04	.3871E-04	.1456E+01
4	140	165	.6750E-01	.0000E+00	.4651E+02	.1975E+01	.3871E-04	.3871E-04	.1456E+01
5	140	165	.1215E+00	.0000E+00	.4659E+02	.1975E+01	.3871E-04	.3871E-04	.1456E+01
6	140	165	.2295E+00	.0000E+00	.4678E+02	.1975E+01	.3871E-04	.3871E-04	.1456E+01
7	140	165	.4455E+00	.0000E+00	.4730E+02	.1975E+01	.3871E-04	.3871E-04	.1456E+01
8	140	165	.8775E+00	.0000E+00	.4895E+02	.1975E+01	.3871E-04	.3871E-04	.1456E+01
9	140	165	.1742E+01	.0000E+00	.5461E+02	.1975E+01	.3871E-04	.3871E-04	.1456E+01
10	140	165	.3470E+01	.0000E+00	.7542E+02	.1975E+01	.3871E-04	.3871E-04	.1456E+01
12	140	165	.6926E+01	.0000E+00	.1541E+03	.9879E+01	.3821E+00	.3057E+00	.6799E+01
13	140	165	.1384E+02	.0000E+00	.4671E+03	.9879E+01	.3821E+00	.3057E+00	.6799E+01
14	140	165	.2766E+02	.0000E+00	.1706E+04	.9879E+01	.3821E+00	.3057E+00	.6799E+01

Table 2-14. COD7MM+MHOST Volume Of Structure Is Computed As: .2430864E+01

Iter #	NEL	NODES	FORCE (kip)	PRESS (ksi)	ELA_ENERGY	DAMAG(/100)	DERR(ksi)	TOTAL_DERR (ksi)	DMGE_ ENRGY
1	140	165	.2700E-01	.0000E+00	.4673E+02	0	0	0	0
3	140	165	.4050E-01	.0000E+00	.4648E+02	.1975E+01	.3093E-04	.3093E-04	.1456E+01
4	140	165	.6750E-01	.0000E+00	.4651E+02	.1975E+01	.3093E-04	.3093E-04	.1456E+01
5	140	165	.1215E+00	.0000E+00	.4659E+02	.1975E+01	.3093E-04	.3093E-04	.1456E+01
6	140	165	.2295E+00	.0000E+00	.4678E+02	.1975E+01	.3093E-04	.3093E-04	.1456E+01
7	140	165	.4455E+00	.0000E+00	.4730E+02	.1975E+01	.3093E-04	.3093E-04	.1456E+01
8	140	165	.8775E+00	.0000E+00	.4895E+02	.1975E+01	.3093E-04	.3093E-04	.1456E+01
9	140	165	.1742E+01	.0000E+00	.5461E+02	.1975E+01	.3093E-04	.3093E-04	.1456E+01
10	140	165	.3470E+01	.0000E+00	.7541E+02	.1975E+01	.3093E-04	.3093E-04	.1456E+01
12	140	165	.6926E+01	.0000E+00	.1541E+03	.9886E+01	.3048E+00	.2439E+00	.6799E+01
13	140	165	.1384E+02	.0000E+00	.4666E+03	.9886E+01	.3048E+00	.2439E+00	.6799E+01
14	140	165	.2766E+02	.0000E+00	.1702E+04	.9886E+01	.3048E+00	.2439E+00	.6799E+01

2.2.4 Validation of NESSUS based COD7MM Modularization

After 21 NESSUS iterations the results in the SCRA28 and SCRA73 files agree with those of the MHOST based COD7MM code. The SCRA88 files are in good agreement indicating that the main integration is satisfactorily provided by the FEM modules.

2.3 CONCLUSION, PROBLEMS, AND FUTURE DEVELOPMENT AND VALIDATION

Validation of the COD7MM demonstrated the ability of the enhanced modular version of CODSTRAN to communicate with different finite element programs by interfacing with input/output files only. This achievement allows use of different FE codes for the static analysis of damage progression by the CODSTRAN analyzer without code integration. COD7MM also has been integrated with the standard GENOA (GENEX) file management system.

Validation has shown the need to resolve some problems as follows:

- Several runs of COD7MM have shown a necessity to remove all SCRA* files before an iteration in order to obtain stable results. Apparently, some member of the CODSTRAN file system does not open properly.
- File SCRA28 has an unacceptable of DERR error which has to be corrected.
- CODSTRAN code interaction shows a significant Nxy error that may be connected with the DERR calculation.
- COD7MM code has to be verified on larger examples with about 6000-10000 DOF.
- COD7MM code needs to be tested with pressure loads.

3.0 Methodology of Adaptive Mesh Refinement in Progressive Failure Analysis

Conventional CODSTRAN updates a finite element model utilizing a Lagrangian updating technique. Presently during re-iterative re-analysis CODSTRAN eliminates or adds new nodes to the FEM mesh. When all modes of composite resistance fail at a node, that node is deleted and new detached nodes are created at the same point for the remaining adjacent finite elements. The number of new nodes created in place of deleted node is equal to the number of elements that had connectivity to the deleted node. For example, in a composite structure modeled via quadrilateral shell elements, if a deleted node was shared by four elements, then four new nodes would replace the deleted node. On the other hand, if the composite structure was represented by eight-node solid elements, and a deleted node was shared by eight elements then eight new solid element nodes would be created in place of the deleted node. In the three dimensional solid element version of CODSTRAN currently, the removal of an element due to the deletion of all nodes on one surface is made user selectable to enable investigation of the element deletion aspect in progressive fracture modeling.

This CODSTRASN approach was enhanced by adding adaptive mesh refinement to the CODSTRAN version in PFA to more precisely represent the fracture pattern during damage initiation and growth than does a simple coarse mesh. After a structure experiences ply damage, stress concentrations may develop around damage nodes. In order to characterize this situation accurately, adaptive mesh refinement must take place as damage occurs in structure.

Adaptive mesh refinement was introduced to reduce computational time that is spent on finite element analysis using a complete fine mesh throughout the PFA simulation. Instead PFA computation time is reduced by starting an analysis with a coarse finite element model and subsequently refining only those elements in the damaged areas. Thus, if the damage criteria are met at a node, more nodes and elements are generated at that loaction. This process is continued until the final fracture of the specimen. The methodology of adaptive mesh refinement has so far been only exercised for four node shell element meshes.

3.1 MODIFICATION OF CONVENTIONAL CODSTRAN MESH REFINEMENT MODULE

Two mesh refinement approaches were used in modifying the conventional CODSTRAN. In one approach the elements connected to a damaged node are divided into five new elements as illustrated in Figure 3-1.

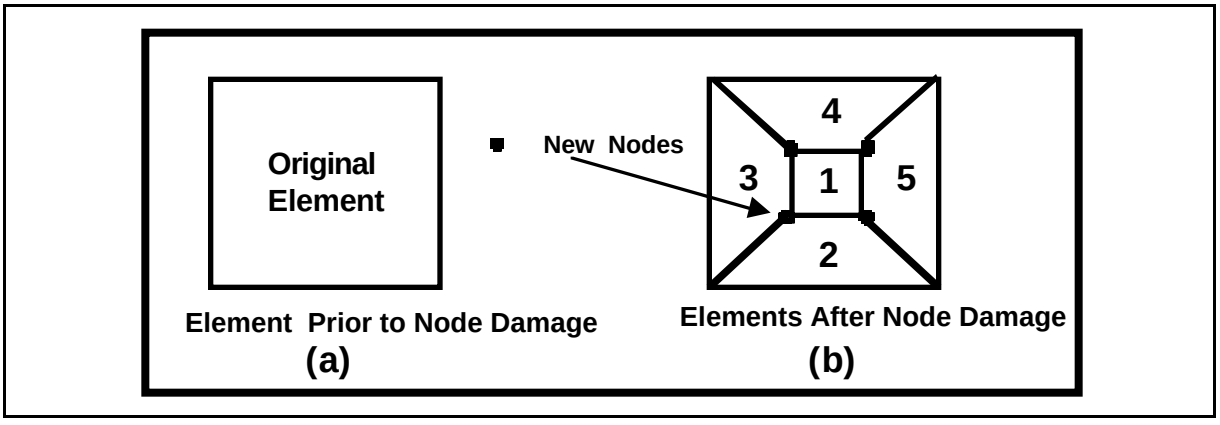

Figure 3-1. Schematic Of Mesh Refinement In The First Approach. (a) Original Element With Damaged Node, (b) Element Divided Into Five New Elements

In the second approach an element connected to a damaged node is divided into three elements (Figure 3-2). If any node within newly generated elements is damaged, more refinement will take place

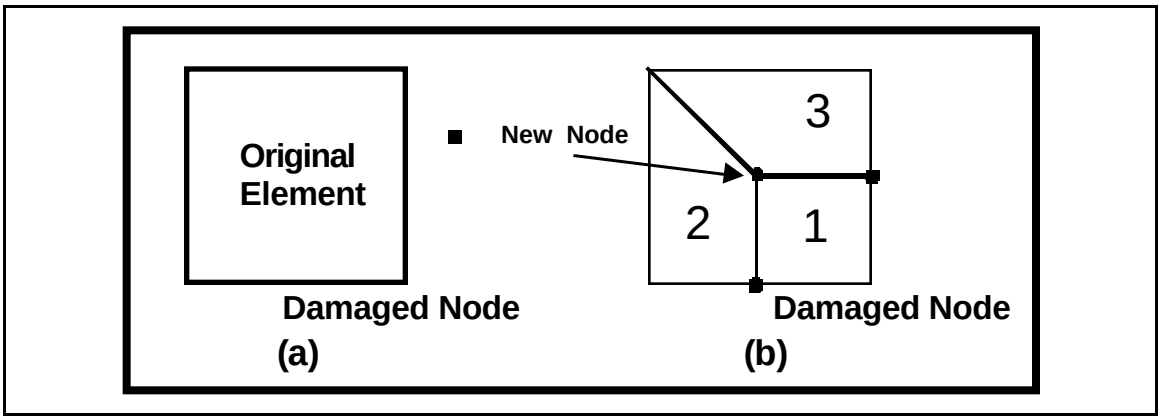

Figure 3-2. Schematic Of Mesh Refinement In The Second Approach. (a) Original Element With Damaged Node, (b) Element Divided Into Three New Elements.

3.2 VERIFICATION OF ADAPTIVE MESH REFINEMENT

Three models were considered for verification and validation of adaptive mesh refinement.

3.2.1 Test Specimen No 1 Flat Panel

A rectangular stitched laminated composite (9 plies with the orientation of 45/-45/0_2/90/0_2/-45/45) panel was the first test specimen for validation of mesh refinement methodology in progressive failure analysis (PFA). The panel was 4 inches long and 1 inches wide and had a total thickness of 0.054 inch. The panel was simulated under tensile loading. The FEM was coarse consisting of 96 shell elements (QUAD) and 120 nodes (Figure 3-3). The first adaptive mesh refinement approach was used in this PFA simulation.

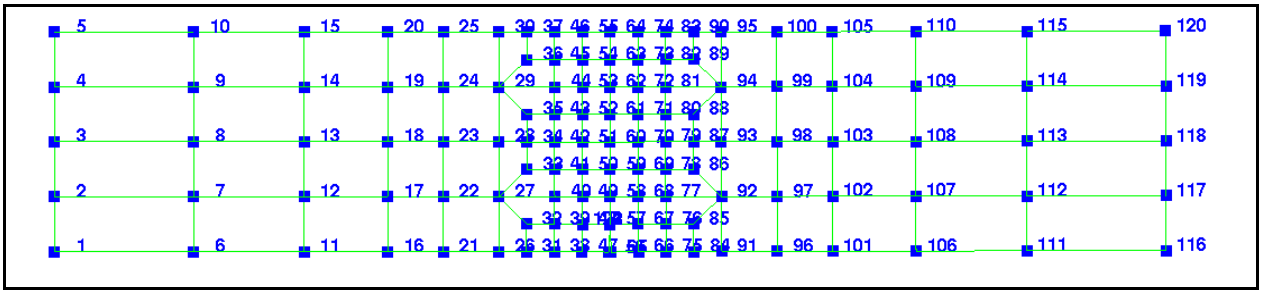

Figure 3-3. Validation of Adaptive mesh refinement in PFA Simulation of Test specimen No. 1.

Crack initiation was represented by two unconnected nodes (No. 56 and 65) located at the same coordinate position. Runs were performed with and without adaptive mesh refinement. Figures 3-4a, 3-4b, and 3-4c show a sequence of three FEM iterations (No. 83, 84, and 85) without adaptive mesh leading to global fracture.

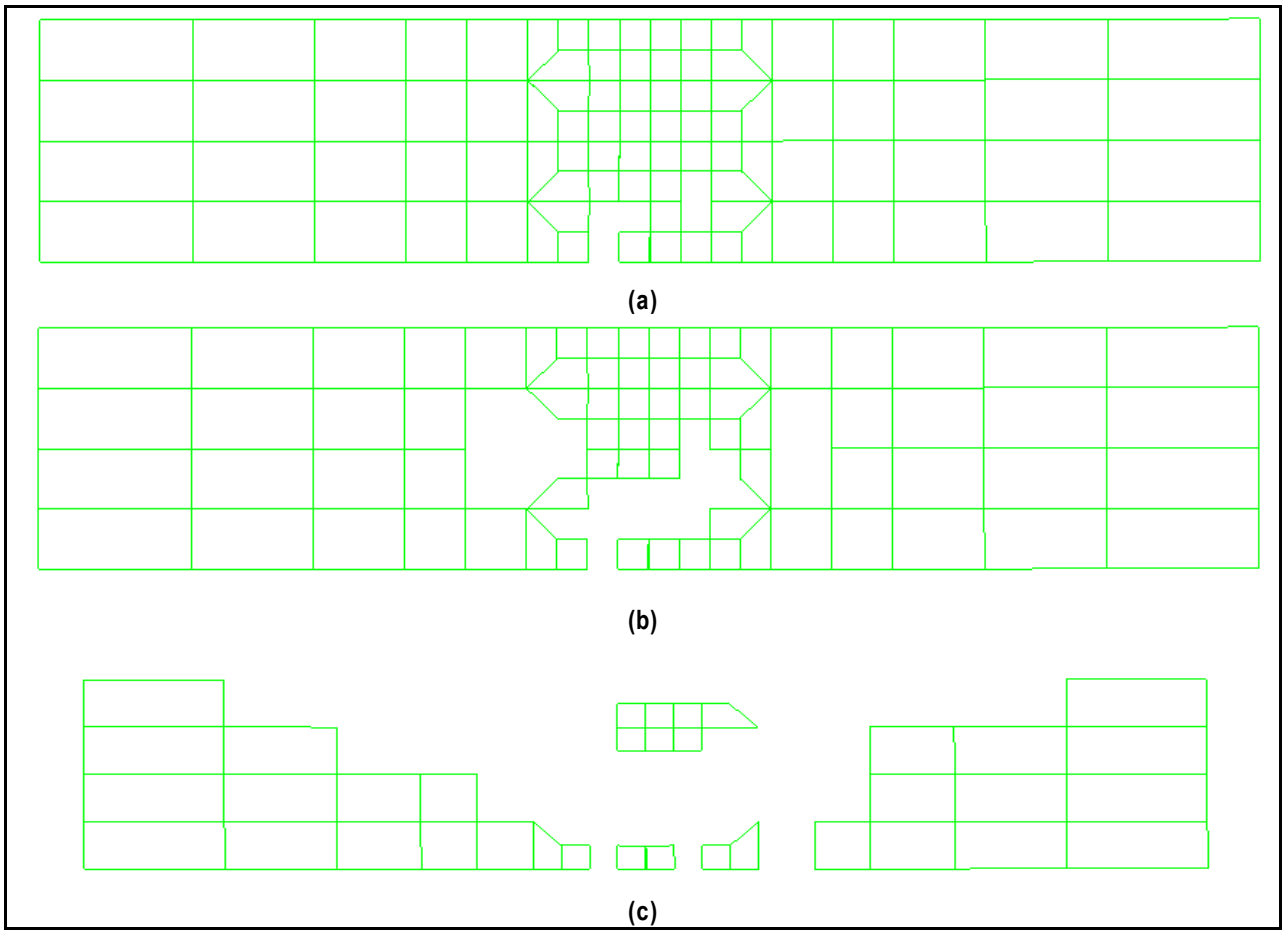

Figure 3-4 Meshes Generated Without Adaptive Mesh Refinement During FEM Analyses Of Test Specimen No. 1. At Iteration No. (a) 83, (b) 84, And (c) 85 Or Final Fracture.

Simulations made with adaptive mesh refinement (Figures 3-5a, 3-5b, and 3-5c) show the initiation of the crack (at the notch location at node No. 57) and its progression at FEM iterations No. 78, 79, and 80 (at final fracture)

The simulation made with adaptive mesh refinement has better resolution (i.e., more detail) than that without adaptive mesh refinement.

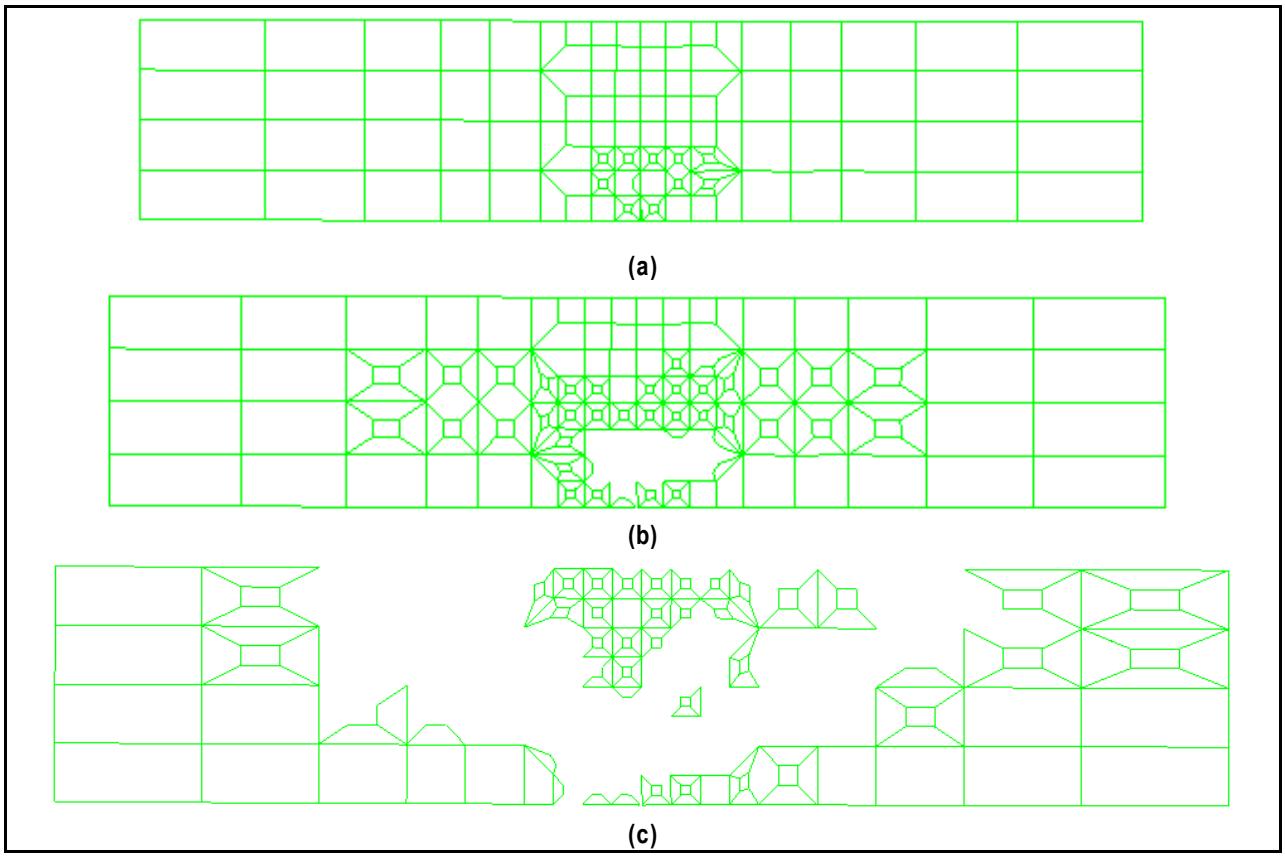

Figure 3-5. Meshes Generated With Adaptive Mesh Refinement During FEM Analyses Of Test Specimen No. 1 At Iteration No. (a) 78, (b). 79, And (c) 80 Or Final Fracture.

3.0 Methodology of Adaptive Mesh Refinement in Progressive Failure Analysis

Without adaptive mesh refinement, simulated stress distributions (in the x-direction) were obtained as shown in Figures 3-6a and 3-6b for FEM iteration No. 83 and 84.

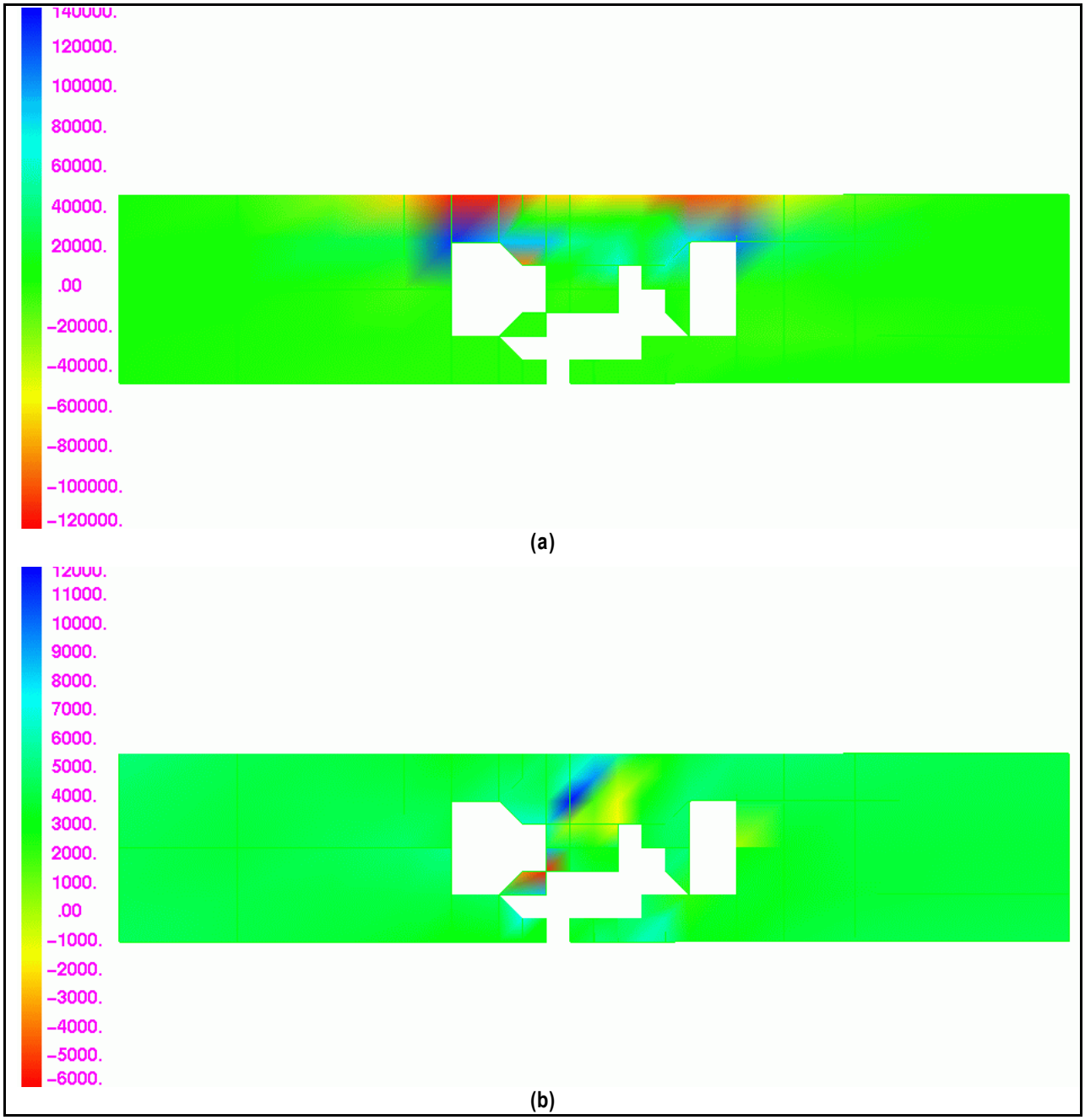

Figure 3-6. Normal Stress Distribution In The X-(Longitudinal) Direction Under Tensile Loading As Simulated Without Adaptive Mesh Refinement For FEM Iteration No. (a) 83, And (b) 84

The stress distributions obtained from simulations of Test Specimen No. 1 using adaptive mesh refinement are shown in Figures 3-7a and 3-7b for FEM Iteration No. 78 and 79. These stress distributions have significantly higher resolutions than those made without adaptive mesh refinement (Figure 3-6).

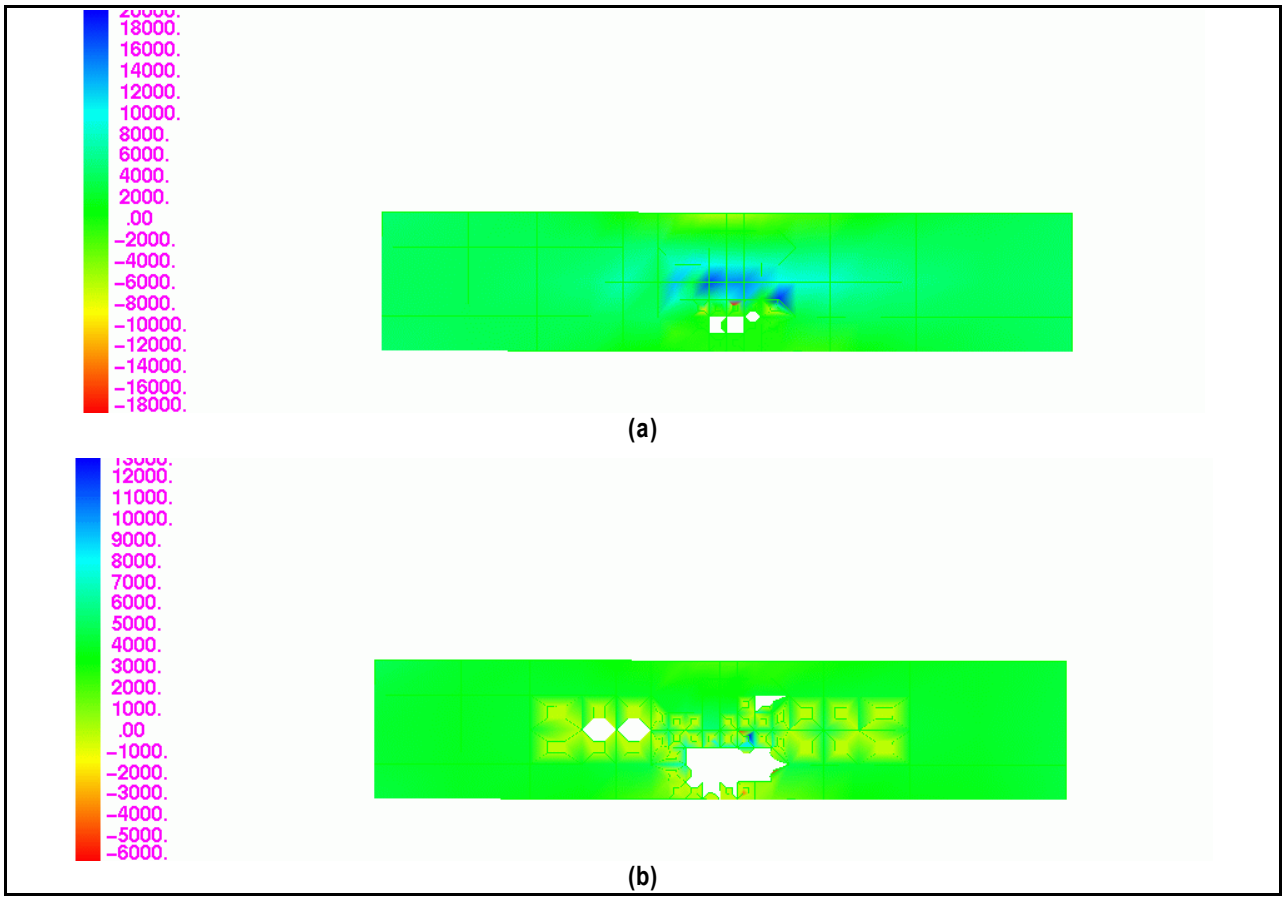

Figure 3-7. Distribution of Normal stress distribution in the x-(longitudinal) direction under tensile loading as simulated with adaptive mesh refinement at FEM Iteration No. (a) 78, and (b) 79

3.2.2 Flat Panel Model Definition for Test Specimen No. 2

The second test specimen was a rectangular panel made of stitched laminated composite consisting of 9 plies oriented in the 45/-45/0_2/90/0_2/-45/45 directions. The panel was simulated under tension loading for validation of the PFA mesh refinement methodology. The panel mesh was coarse consisting of 70 shell elements (QUAD) and 90 nodes (Figure 3-8). Simulations with and without the use of adaptive mesh refinement showed crack initiation to occur at node No. 43.

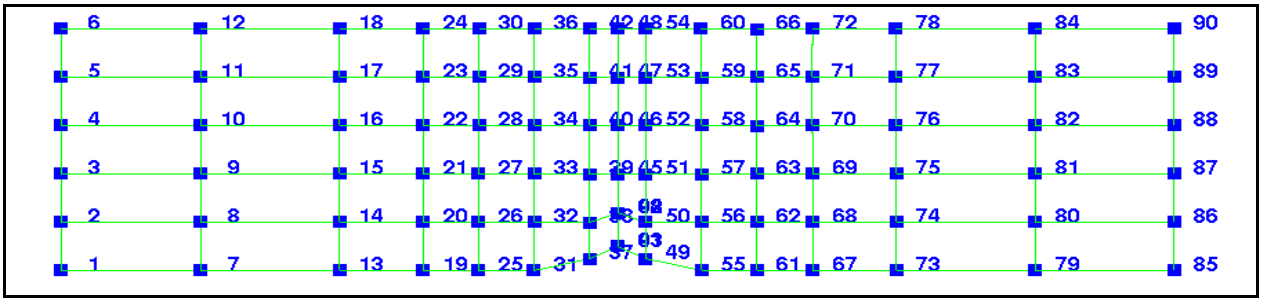

Figure 3-8. FEM mesh used for Test specimen No. 2 in validation of adaptive mesh refinement in PFA.

Crack patterns simulated without adaptive mesh refinement are shown at Iteration No. 50, 51, and 52 in Figures 3-9a, 3-9b, and 3-9c.

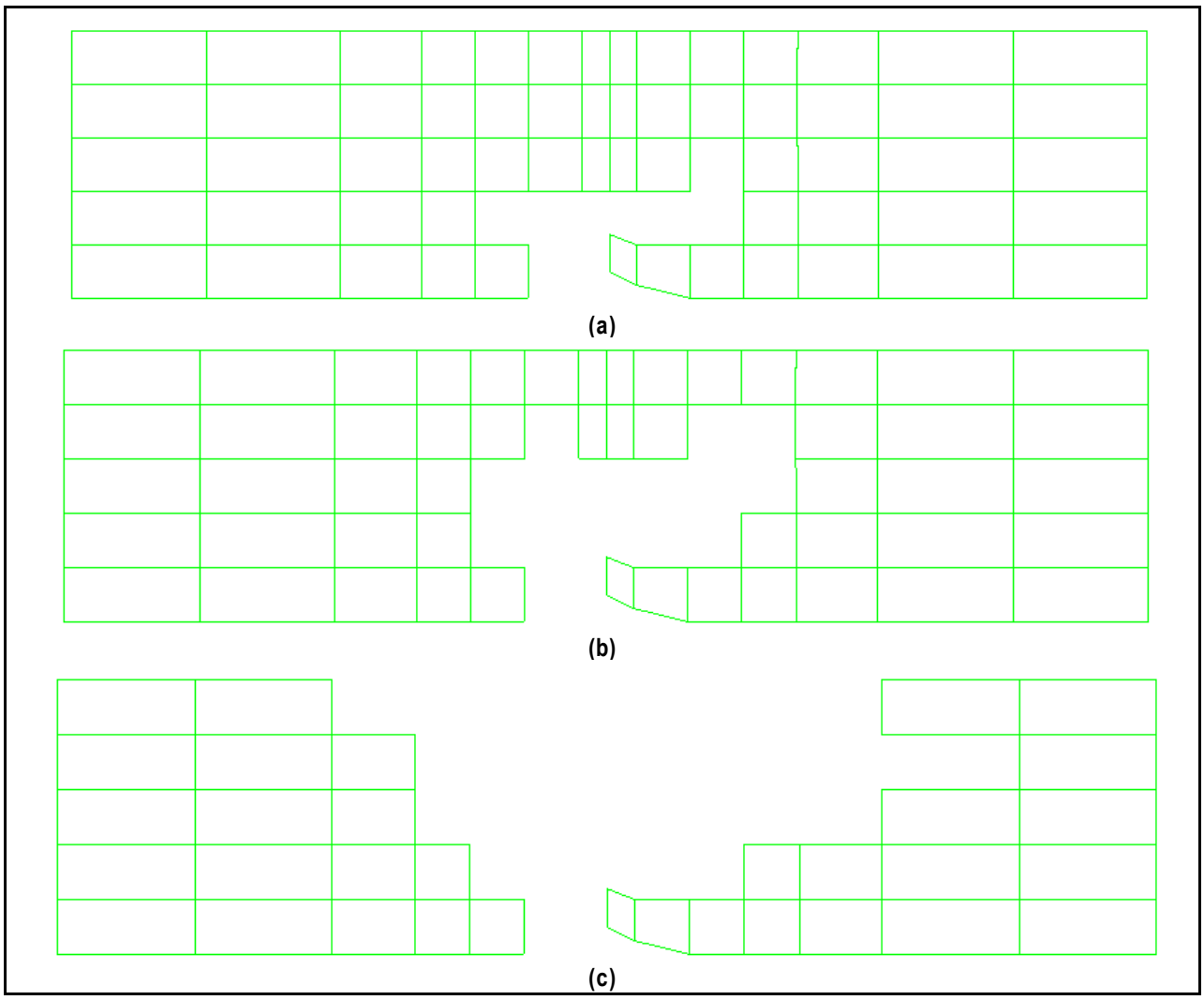

Figure 3-9. Meshes Generated Without Adaptive Mesh Refinement During FEM Analyses Of Test Specimen No. 2 At Iteration No. (a) 50, (b). 51, And (c) 52 At Final Fracture.

Simulations made with adaptive mesh refinement gave crack patterns shown in Figures 3-10a, 3-10b, and 3-10c at FEM iteration No. 39, 40, and 41 (at final fracture). As with Specimen No. 1 simulations, the resolution of the crack patterns obtained with adaptive mesh refinement is significantly greater than the resolution without adaptive mesh refinement.

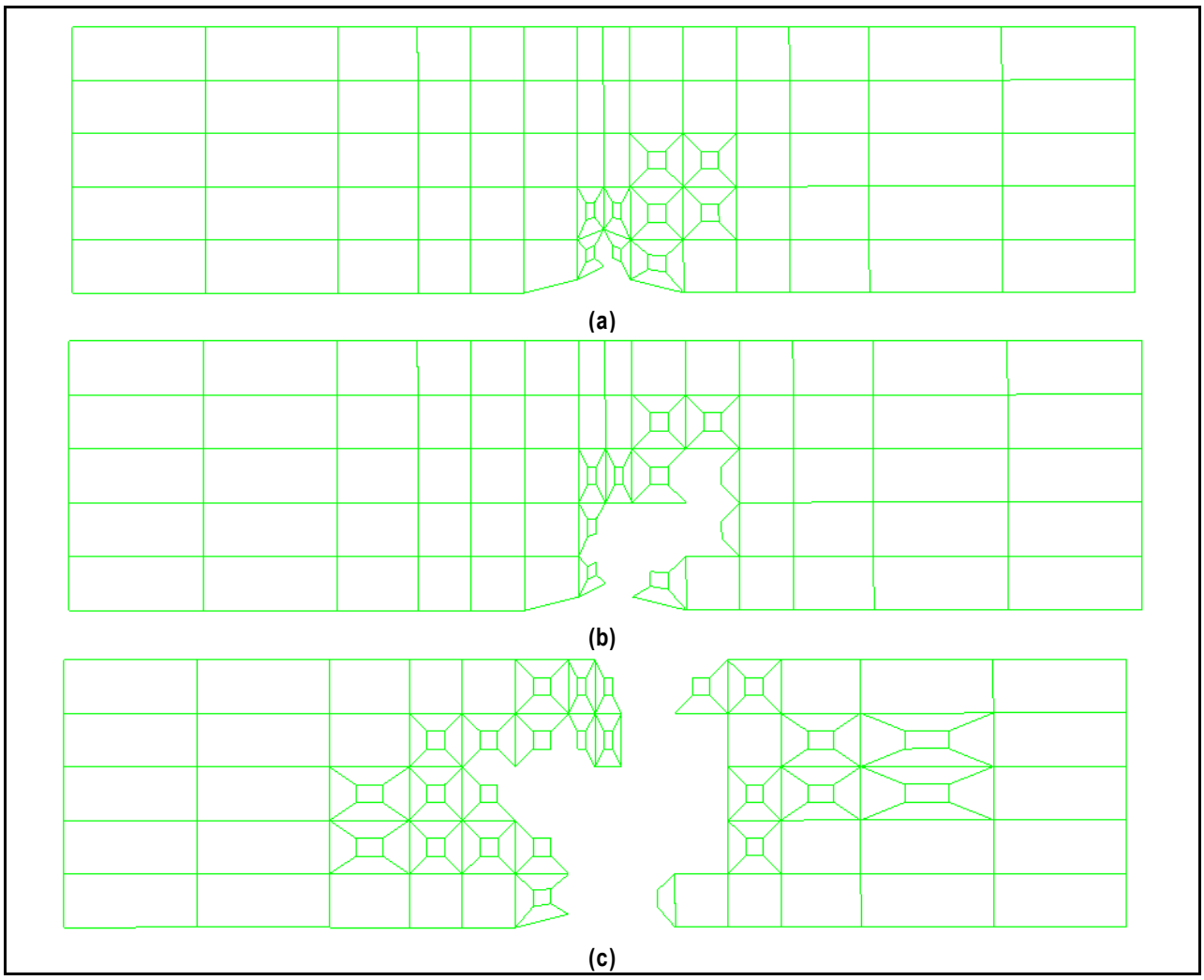

Figure 3-10. Meshes Generated With Adaptive Mesh Refinement During FEM Analyses Of Test Specimen No. 2 At Iteration No. (a) 39, (b). 40, And (c) 41 Or Final Fracture.

The x-direction stress distributions at iteration No. 50 and 51 from simulations without use of adaptive mesh refinement are presented in Figures 3-11a and 3-11b.

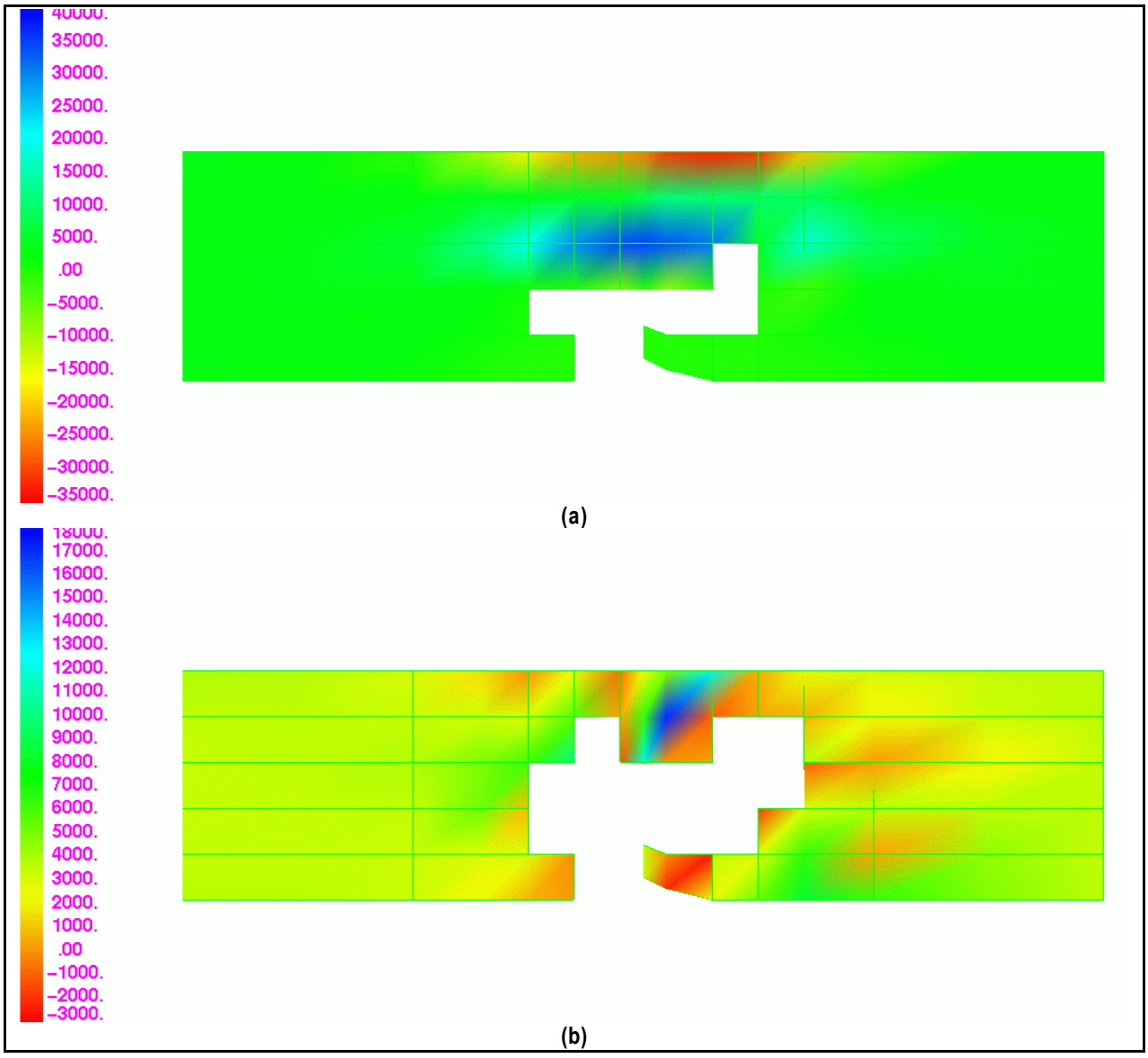

Figure 3-11. Distribution Of Normal Stresses In The X (Longitudinal) Direction For Test Specimen No.2 Under Tensile Loading As Simulated Without Adaptive Mesh Refinement At FEM Iteration No. (a) 50, And (b) 51

Similar results are found for stress distribution for the test specimen no. 1, but with adaptive mesh refinement. These are shown in Figures 3-12a and 3-12b, respectively for finite element No. of 39 and 40.

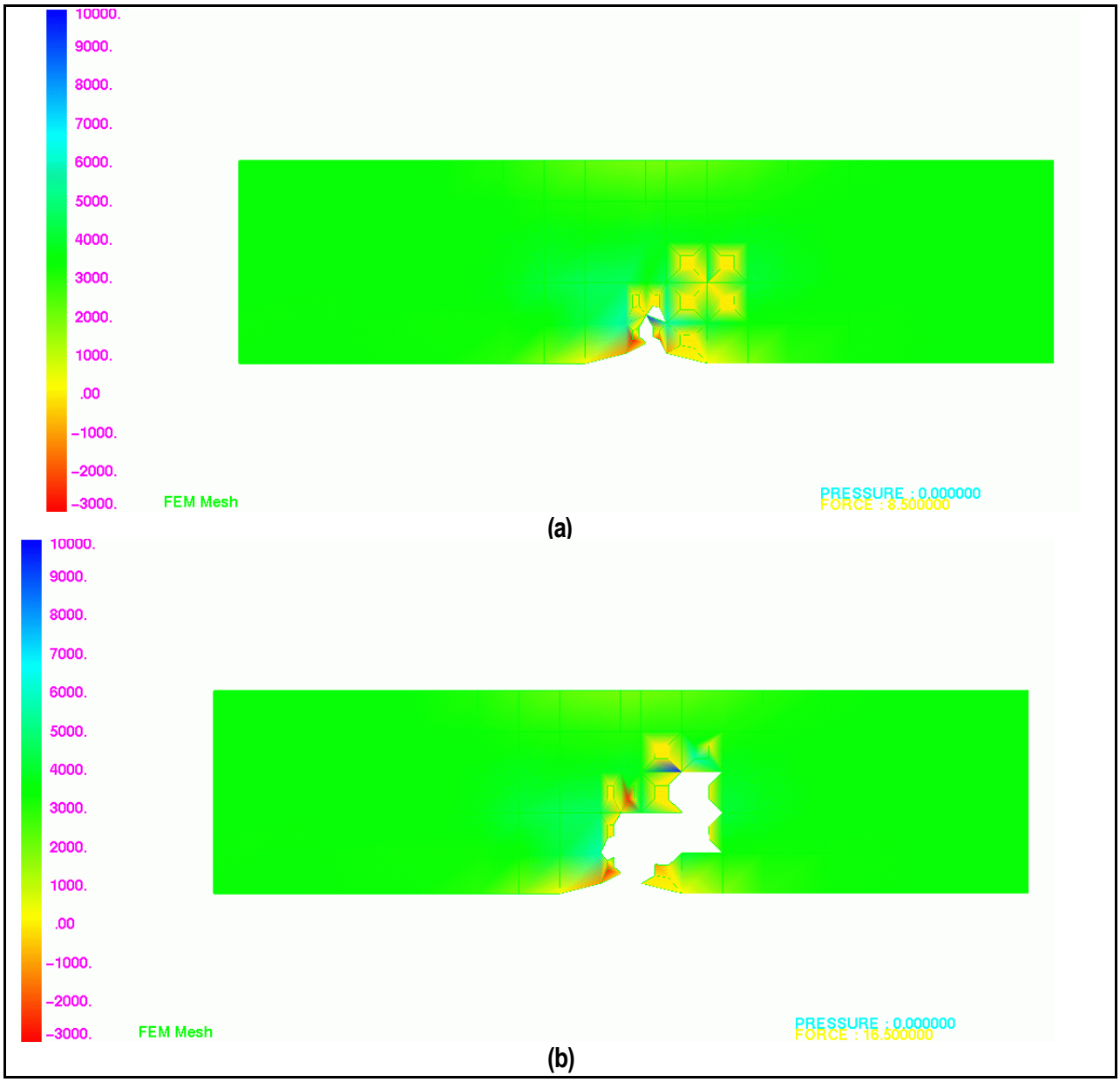

Figure 3-12. Distribution Of Normal Stresses In The X (Longitudinal) Direction For Test Specimen No.2 Under Tensile Loading As Simulated With Adaptive Mesh Refinement At FEM Iteration No. (a) 39, And (b) 40

The damage energy release rate (DERR) and the total damage energy released rate (TDERR) as simulated with adaptive mesh refinement for Specimen No. 1 are plotted in Figures 3-13a and 3-13b. The final fracture loads were 3.376 and 3.452 kip with and without adaptive mesh refinement, respectively. The results show that there is a difference in the ultimate loading for the complete fracture when the adaptive mesh refinement is used. The final DERR and TDERR are found to be 0.649 and 0.7.58 ksi, and 0.052 and 1.07, respectively, with or without adaptive mesh refinement.

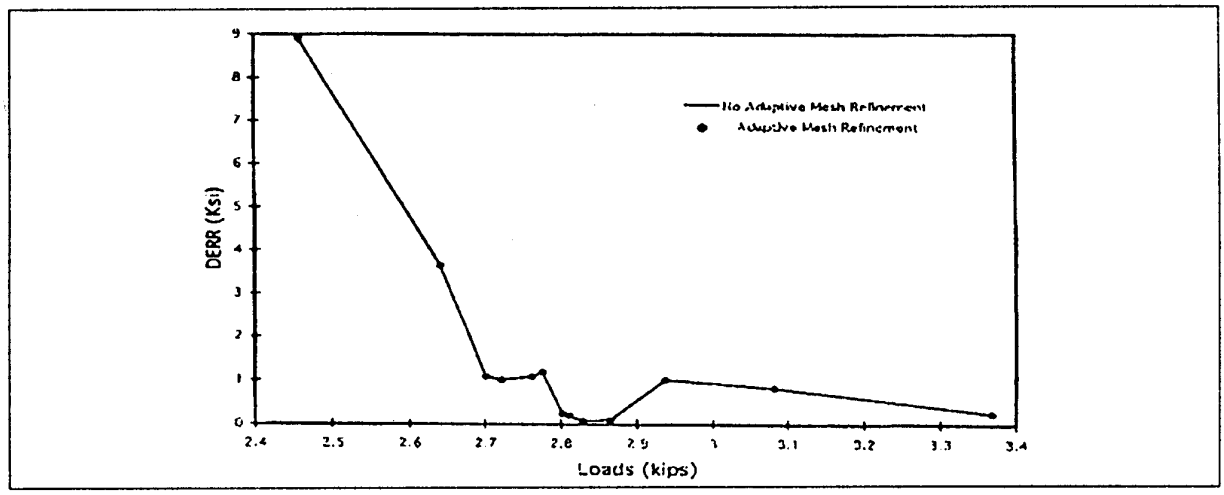

Figure 3-13a. Damage Energy Rate Versus Applied Load for Specimen No. 1 With and Without Using Adaptive Mesh Refinement.

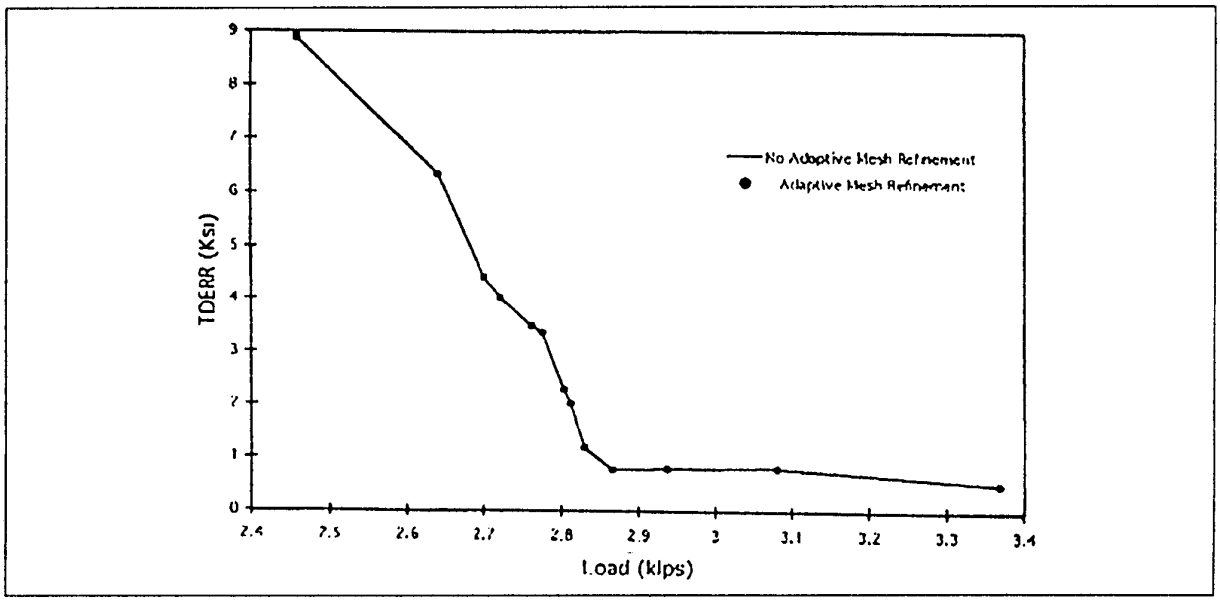

Figure 3-13b. Total Damage Energy Rate Versus Applied Load for Specimen No. 1 With and Without Using Adaptive Mesh Refinement.

Similarly, the damage energy released rate (DERR) and the total damage energy released rate (TDERR) are plotted for Specimen No. 2, in Figures 3-14a and 3-14b, respectively. The adaptive mesh is also applied. The final fracture load was 3.368 kip with or without adaptive mesh refinement. The results show that there is no differences in the ultimate loading for the complete fracture. The final DERR and TDERR are found to be 0.253 an 0.511 ksi, respectively, with or without adaptive mesh refinement.

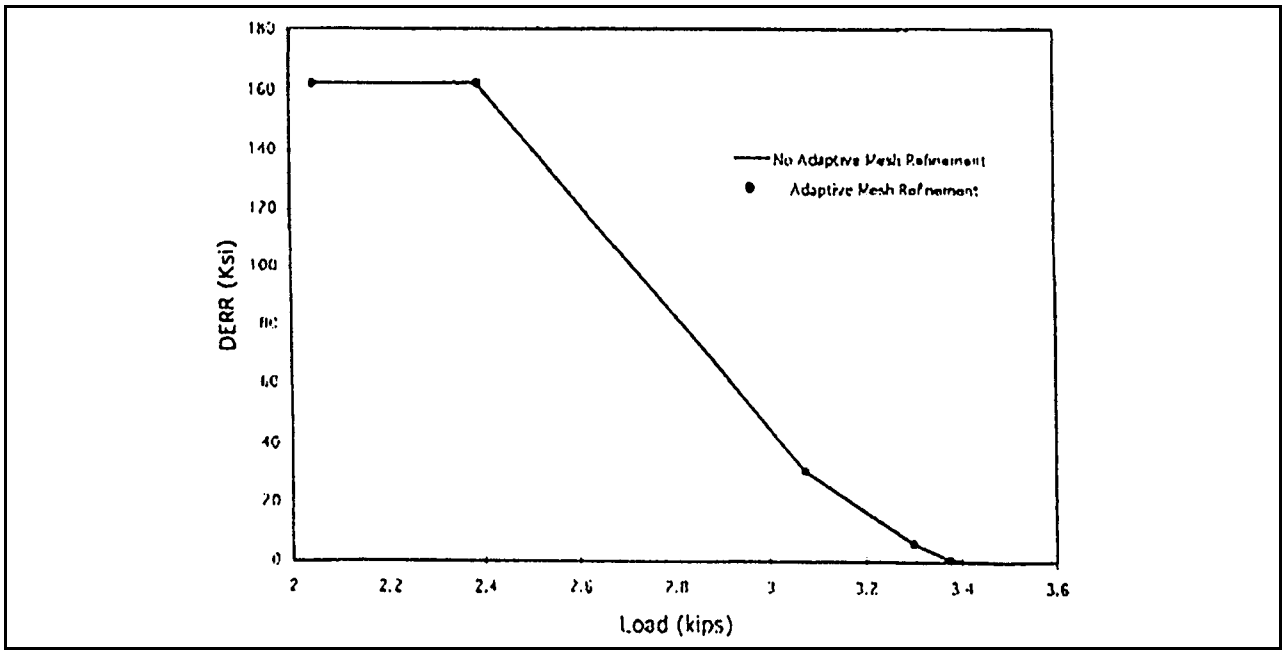

Figure 3-14a. Damage Energy Rate Versus Applied Load for Specimen No. 2 With and Without Using Adaptive Mesh Refinement.

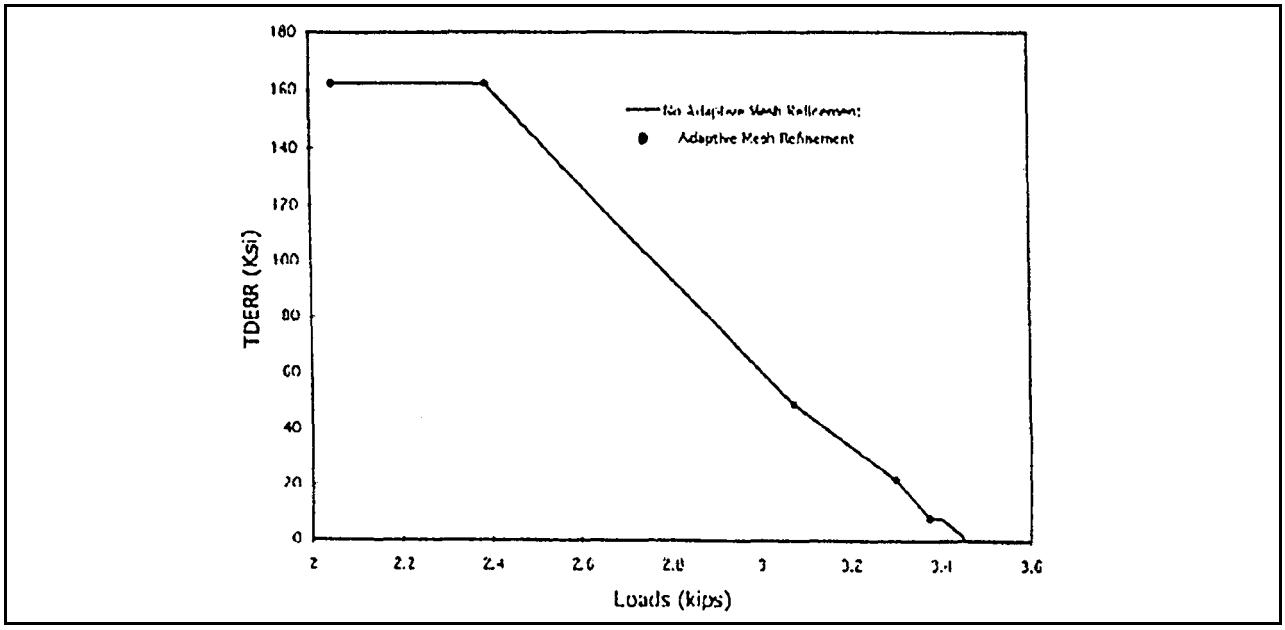

Figure 3-14b. Total Damage Energy Rate Versus Applied Load for Specimen No. 2 With and Without Using Adaptive Mesh Refinement.

3.2.3 Flat Model Test Specimen No. 3

In this approach if a node of an element is damaged, three node will be generated. One of the new generated node is located in the center of gravity of that element. The other two new nodes are located in the middle of the lines connected the adjacent nodes to the damaged node. Test specimen No. 3 was a rectangular flat panel plate is 4 inches long and 1 inches wide. The total thickness of the panel is 0.015 inches. The panel is stitched laminated composite. Total of 30 layers are used with the orientation of $0_{10}/90_{10}/0_{10}$. The indeces 10 in orientation refer to the number of ply used for each orientation. The

specimen is studied under tensile loading. The panel is partitioned into 200 shell elements (QUAD) with total of 231 nodes that is considered as coarse mesh and is shown in Figure 3-15.

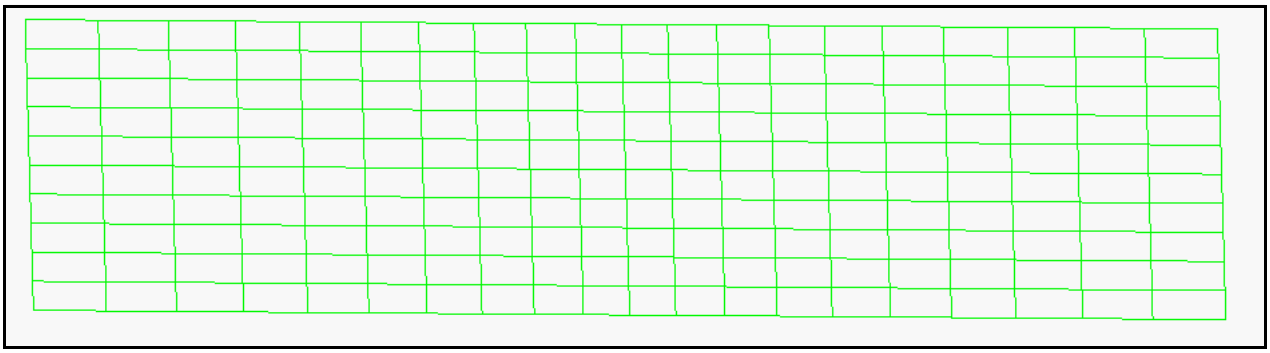

Figure 3-15. Test Specimen No. 3 Without Adaptive Mesh Refinement, Original Model

All nodes at the left side of the model are fixed. The right side is free and the uniform load is applied to all nodes at the right side. In this example no adaptive mesh refinement has been employed. The damage is initiated at node 220 and 210, respectively. This is shown in Figure 3-16.

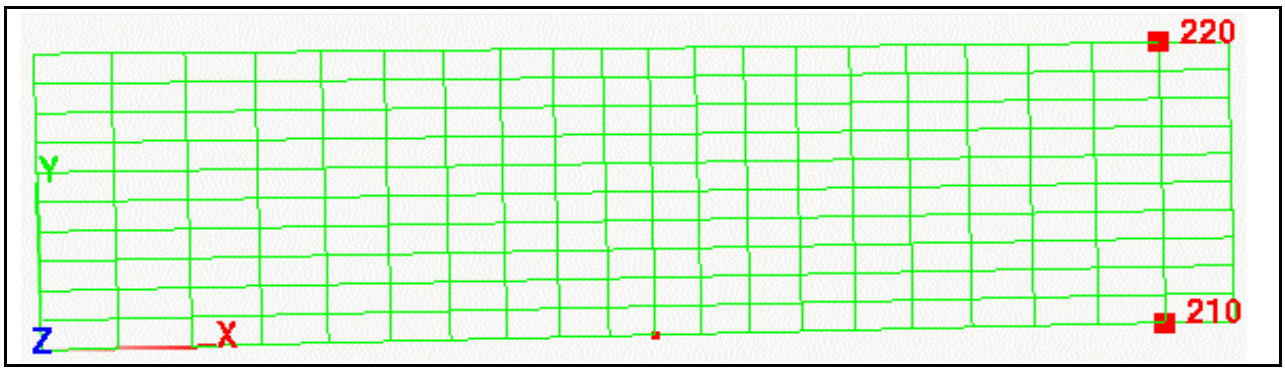

Figure 3-16. Test Specimen No. 3 Without Adaptive Mesh Refinement, Damage Initiation

Figures 3-17 shows the crack propagation at finite element no. 75 for Test Specimen No. 3.

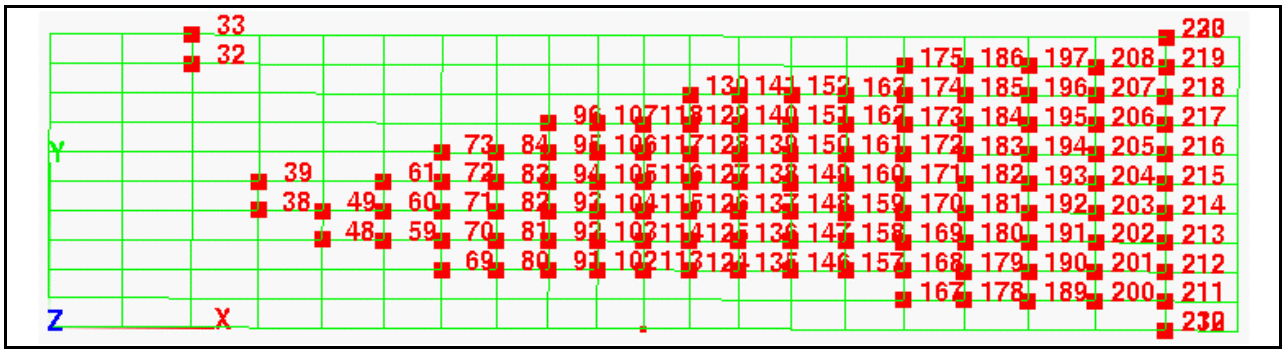

Figure 3-17. Test Specimen No. 3 Without Adaptive Mesh Refinement Damage Propagation, Finite Element No. 75

Figure 3-18 shows the final stage of the PFA crack propagation before the final fracture.

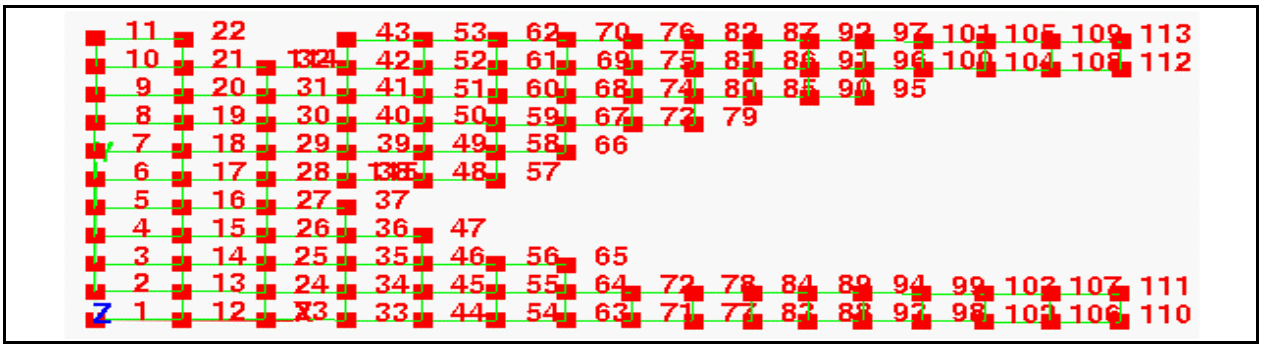

Figure 3-18. Test Specimen No. 3 Without Adaptive Mesh Refinement Damage Propagation, Finite Element No. 76

In the second example, Test Specimen No. 3 is used but using the second approach in adaptive mesh refinement. For this case the damages are initiated at node no. 61, 63, 65, and 194, respectively. This is shown in Figure 3-19. Note that the red numbers are damaged nodes in the test specimen.

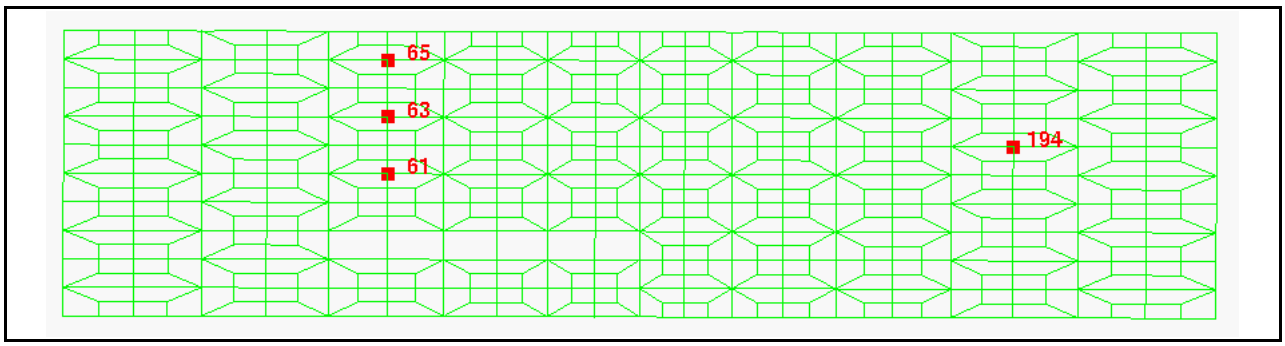

Figure 3-19. Test Specimen No. 3 With Adaptive Mesh Refinement Damage Initiation, Finite Element No. 75

Figures 3-20 and 3-21 show the evolution of the crack in PFA, for finite element numbers 76 and 77 until the final fracture.

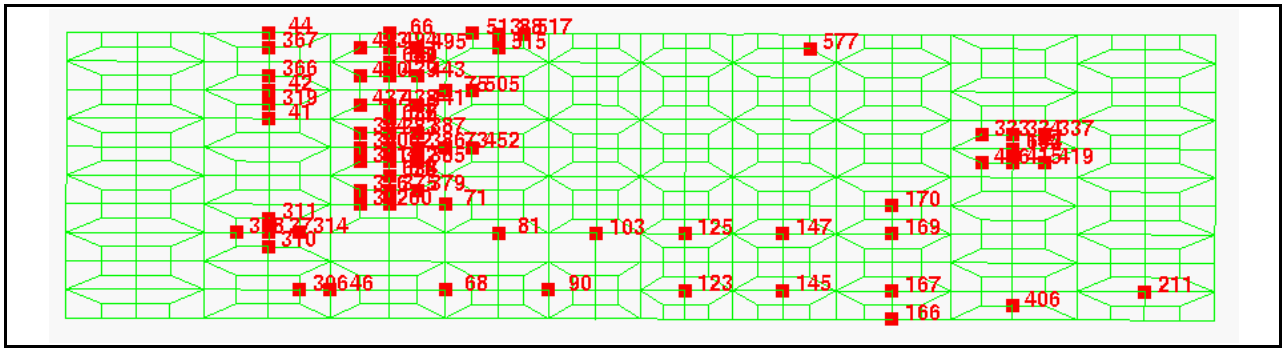

Figure 3-20. Test Specimen No. 3 With Adaptive Mesh Refinement Damage Propagation, Finite Element No. 76

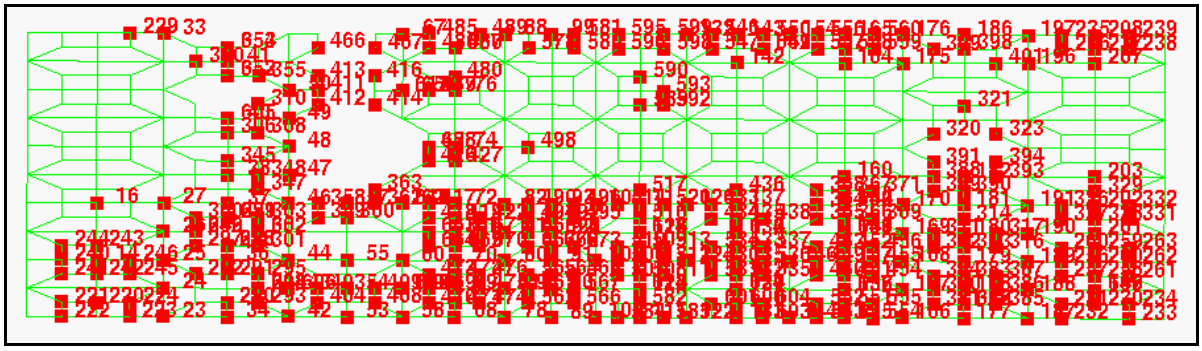

Figure 3-21. Test Specimen No. 3 With Adaptive Mesh Refinement Damage Propagation, Finite Element No. 77

The stress distribution (x-direction) for finite element No. 75 and 76 are presented in Figures 3-22a and 3-22b, respectively, without adaptive mesh refinement.

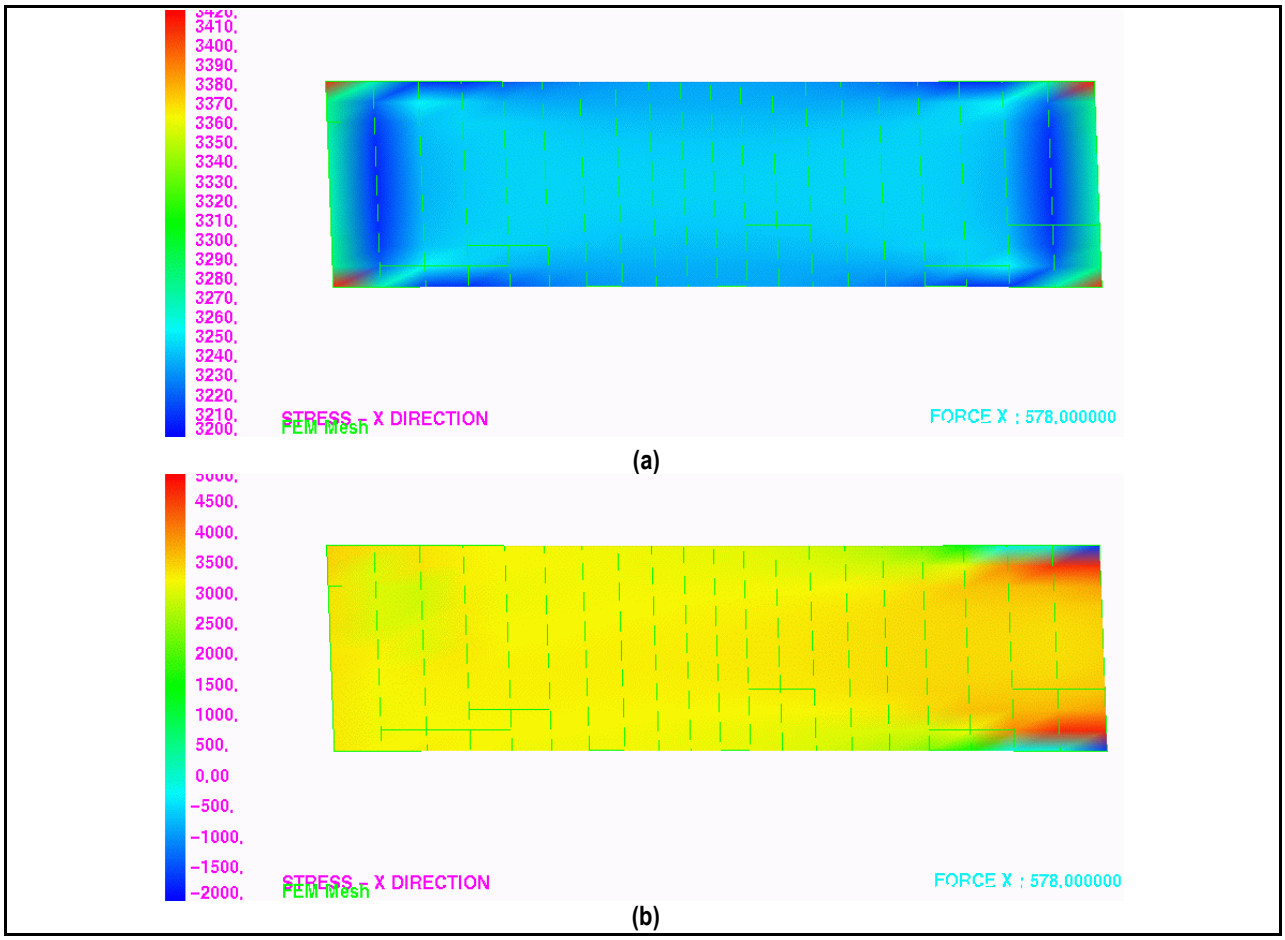

Figure 3-22. Normal Stress In X-Direction (Longitudinal Direction) σ_x Distribution Under Tensile Loading Condition Without Adaptive Mesh Refinement For Two Sequences Of Finite Element Runs. (a) Finite Element No. 75, (b) Finite Element No. 76

Similarly, the stress distribution (x-direction) for Finite Element No. 75, 76, and 77 are presented in Figures 3-23a, 3-23b, and 3-23c, respectively, with adaptive mesh refinement.

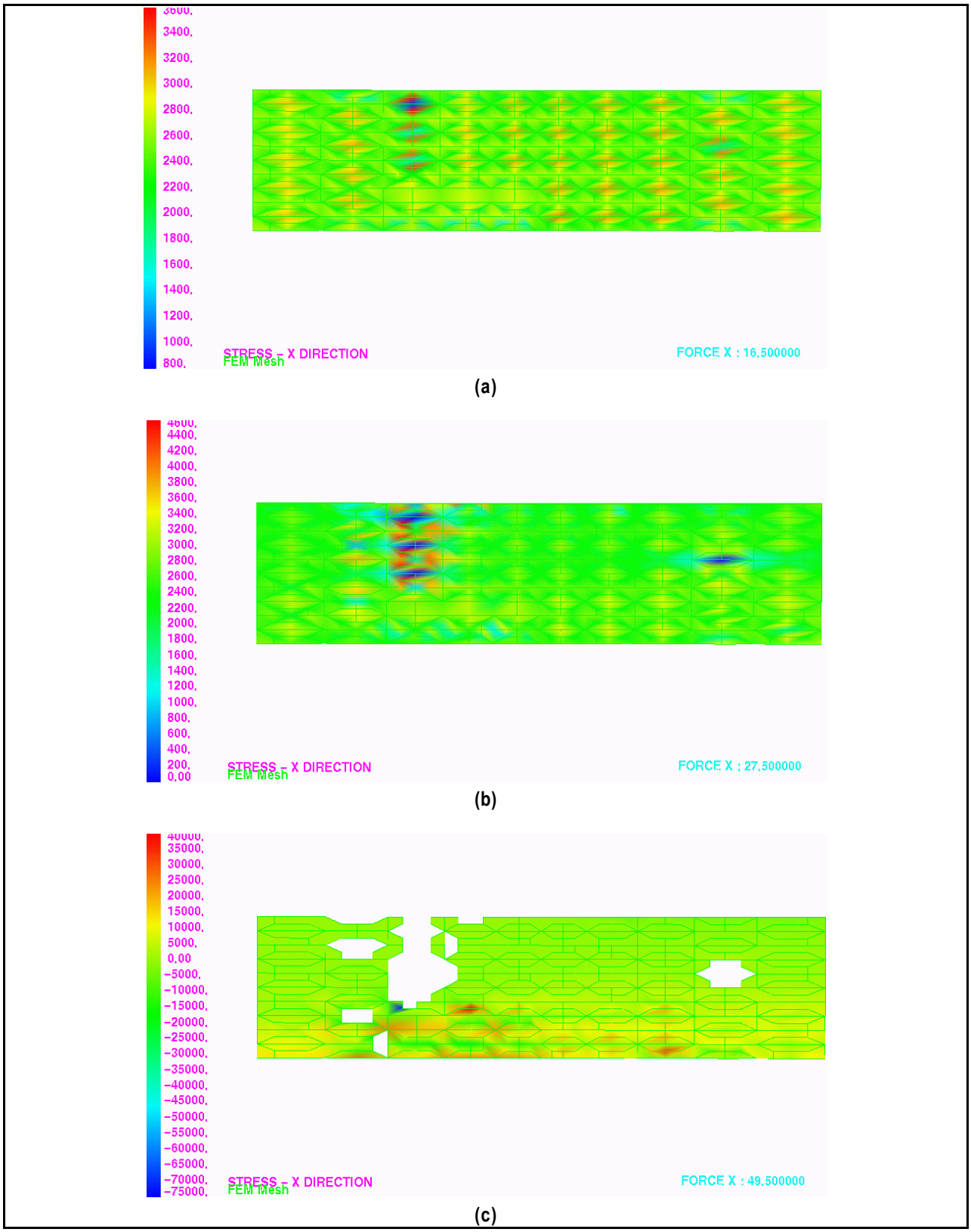

Figure 3-23. Normal Stress In X-Direction (Longitudinal Direction) σ_x Distribution Under Tensile Loading Condition Without Adaptive Mesh Refinement For Two Sequences Of Finite Element Runs. (a) Finite Element No. 75, (b) Finite Element No. 76, And (c) Finite Element No. 77

The results of adaptive mesh refinement were compared with those without any refinement. Figures 3-14a and 3-14b show that for Specimen No 2. there is no gain if the adaptive mesh refinement is used. On the other hand in Specimen No. 1 some benefit can be gained if the adaptive mesh refinement is used. The later is shown in Figures 3-13a and 3-13b for DERR and TDERR.

In the third example of specimen No. 3, the final loads found were 3.2 kips and 2.6 kips, respectively, without and with adaptive mesh. The differences in this case is about 18 percent can be explained in that adaptive mesh many elements with a bad shape that the finite element solver were not able to handle.

3.2.4 Verification Of Boeing Crown Panel with 38 inches Saw Cut

The Boeing Integral Airframe structure (IAS) crown panel with a 38-inch saw cut is used for validation of mesh refinement methodology in PFA. The finite element model used is shown in Figure 3-24. The specimen was simulated under the internal pressure loading. The FEM mesh was partitioned into a coarse mesh of 2300 shell elements (QUAD) with total of 3257 nodes (Figure 3-24).

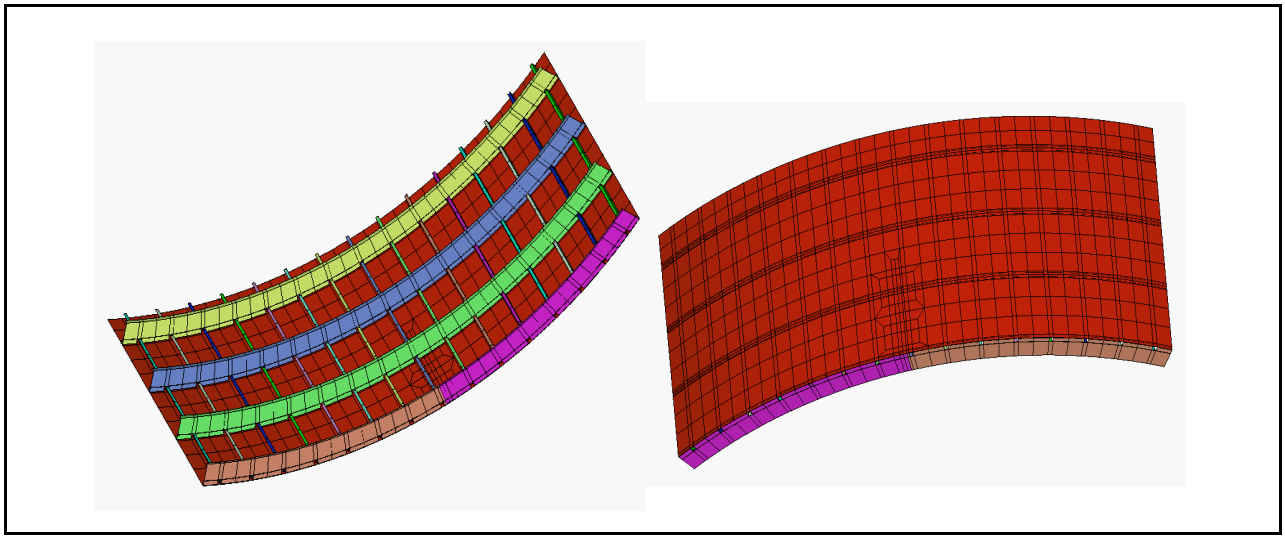

Figure 3-24. IAS Boeing Panel Finite Element Model

The skin and the stringers were made of T7475-T7351 aluminum alloy and the frames of 7050-T7451-aluminum alloy and the rivets of 2017 aluminum alloy. Thick shell elements (the thickness of the panel) were used to model the entire structure. Since skin, stringer, and frame thickness change with location, the thickness of elements was also changed with location.

The static progressive damage analysis with adaptive meshing was performed on the IAS panel. The starting finite element mesh is shown in Figure 3-24. Computational simulation was also started with an internal pressure of 1.0 psi. Fracture initiated at the tip of the saw cut at pressure of 8.5 psi. Figures 3-25 to 3-32 show the mesh sequences for various damage stages. Figure 3-29 shows the crack turning when it reached the second frame.

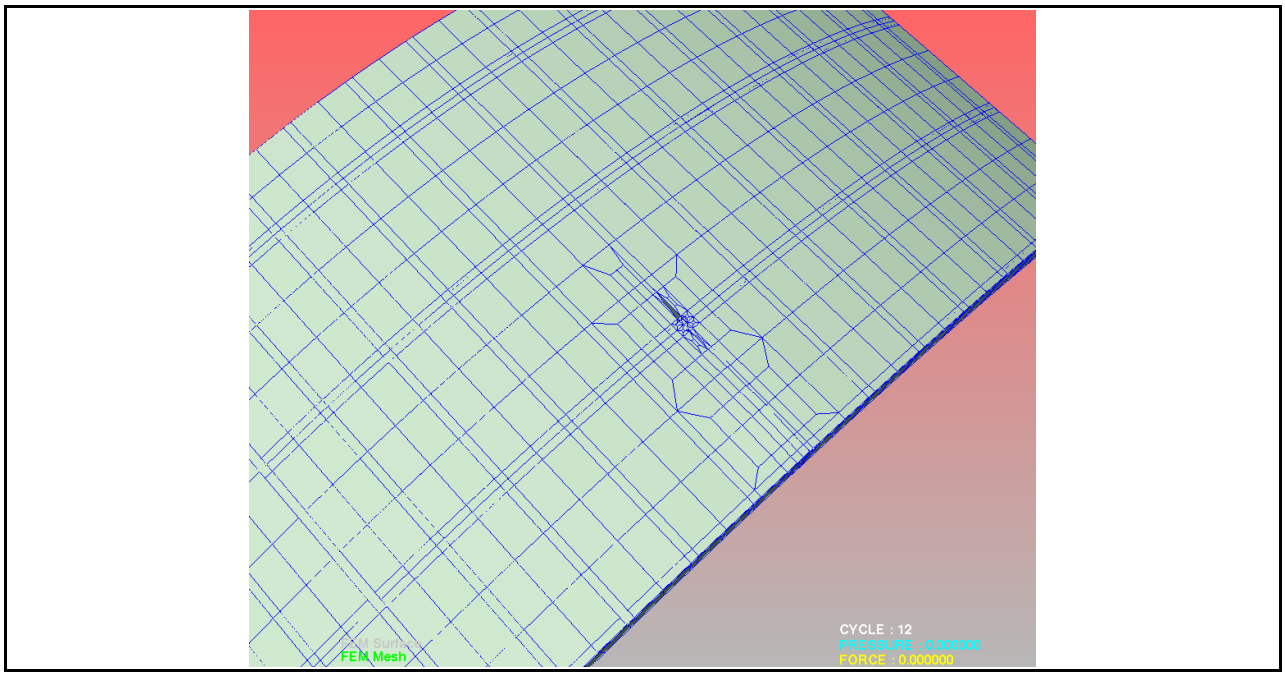

Figure 3-25. Adaptive Mesh Refinement at Damage Initiation Under Internal Pressure of 8.5 Psi

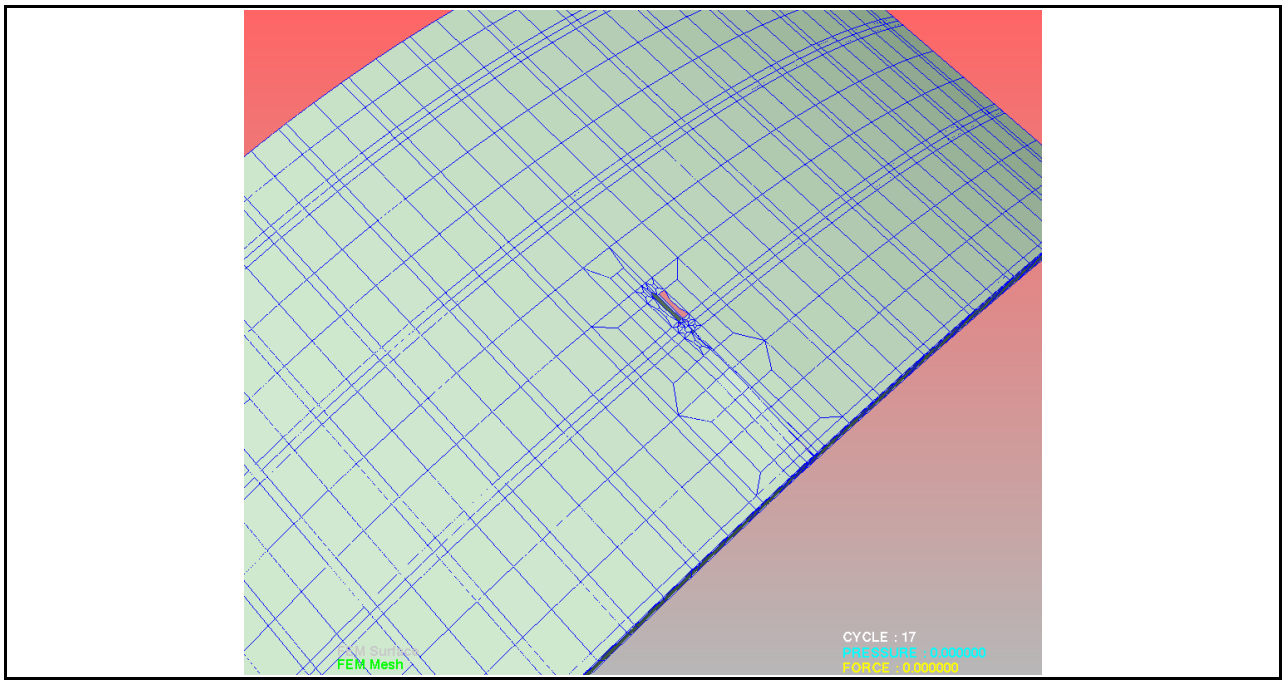

Figure 3-26. Adaptive Meshing At Damage Propagation Under Internal Pressure Of 8.67 Psi

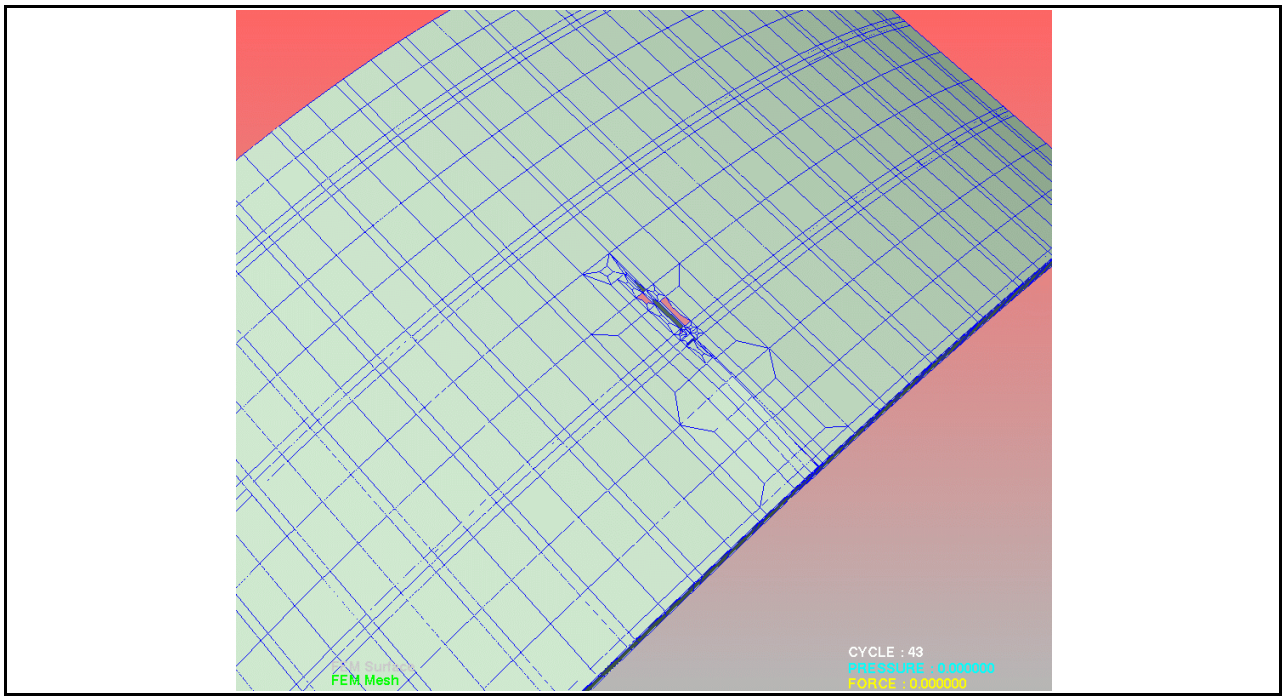

Figure 3-27. Adaptive Meshing At Damage Propagation Under Internal Pressure Of 8.97 Psi (Stage 1)

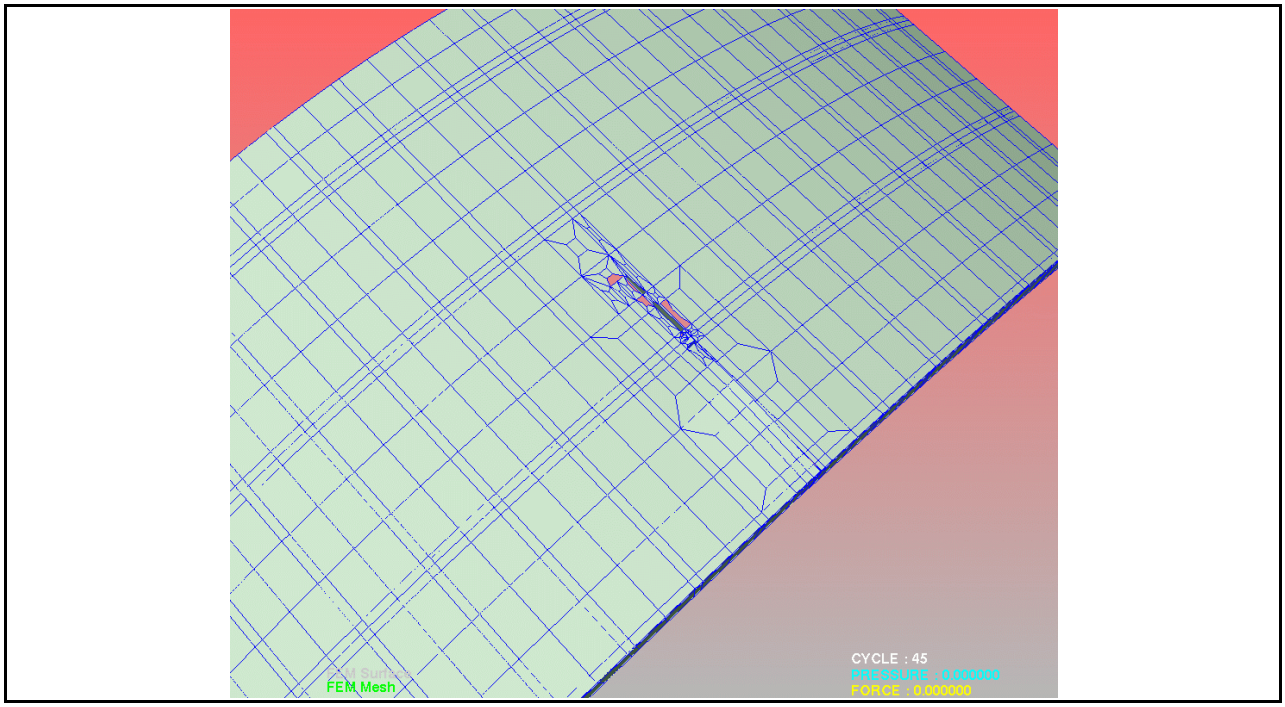

Figure 3-28. Adaptive Meshing At Damage Propagation Under Internal Pressure Of 8.97 Psi (Stage 2)

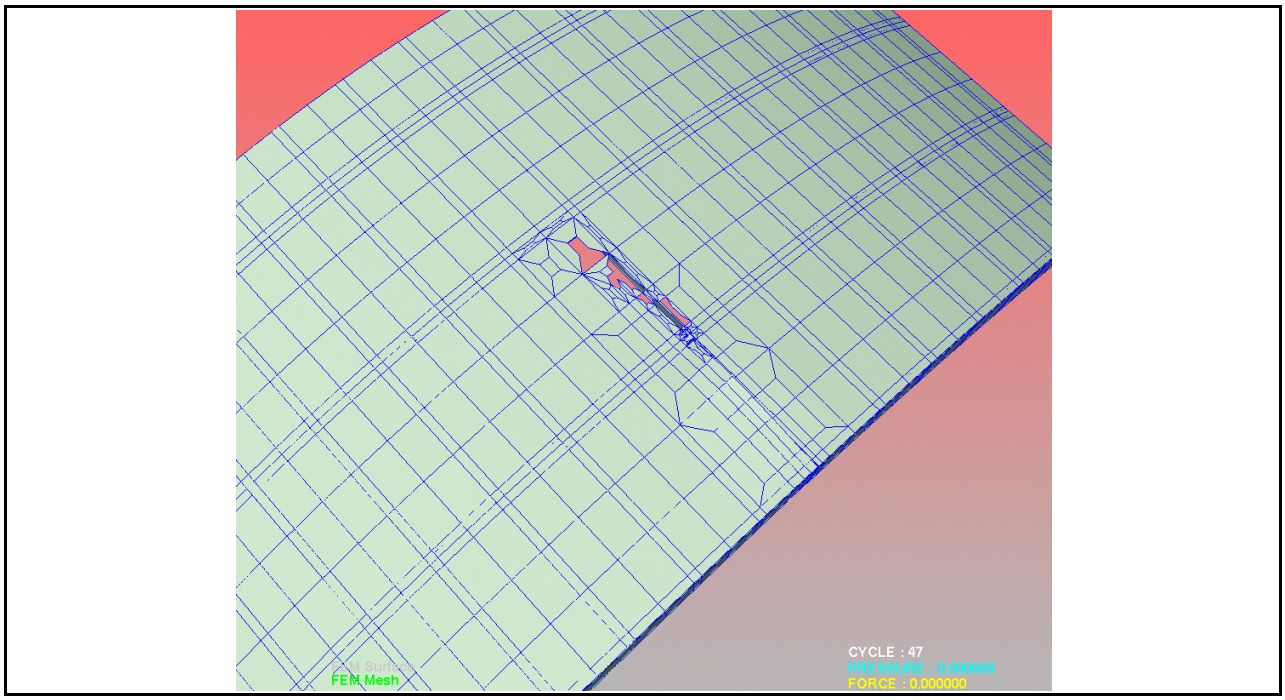

Figure 3-29 Adaptive Meshing At Damage Propagation Under Internal Pressure Of 8.97 Psi (Stage 3)

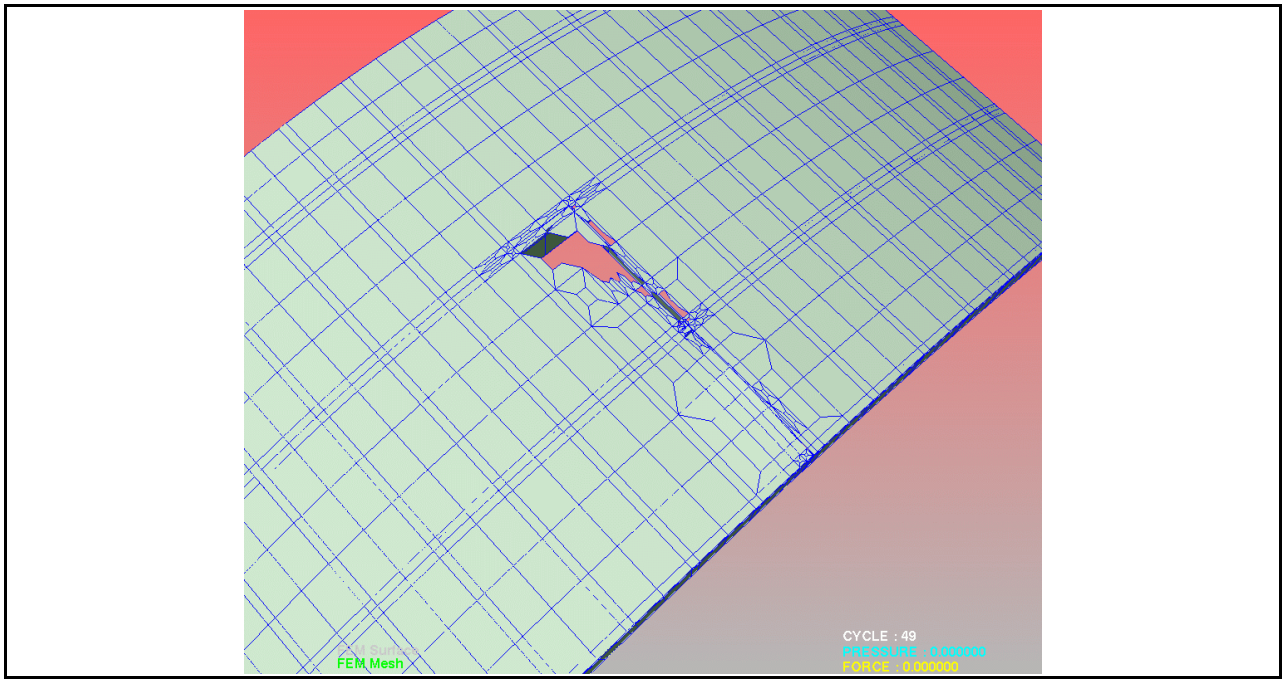

Figure 3-30. Adaptive Meshing At Damage Propagation Under Internal Pressure Of 8.97 Psi (Stage 4)

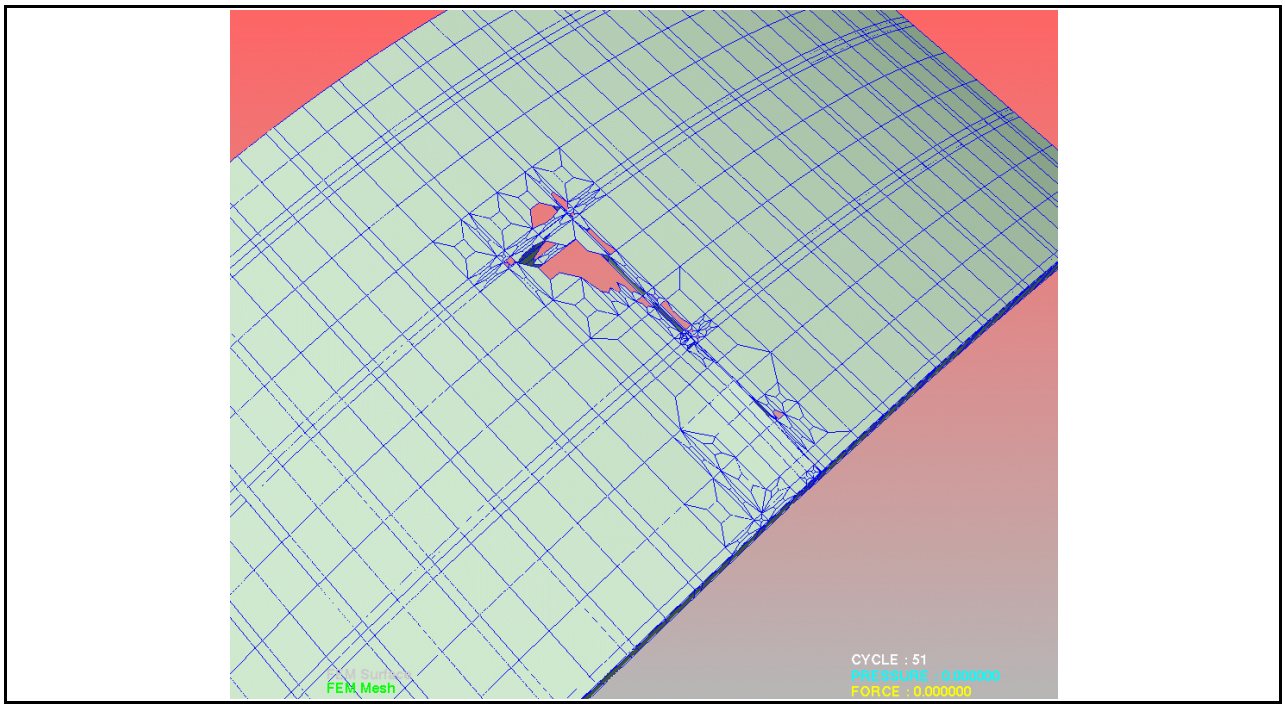

Figure 3-31. Adaptive Meshing At Damage Propagation Under Internal Pressure Of 8.96 Psi (Stage 5)

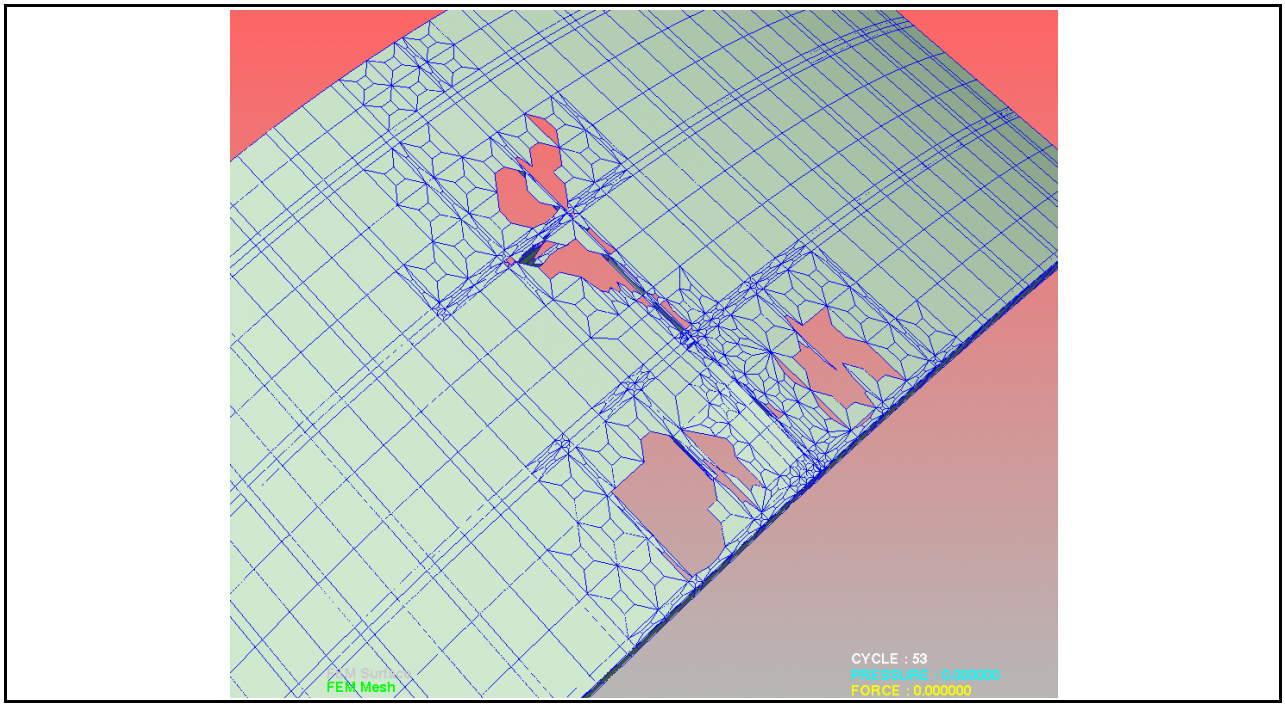

Figure 3-32. Adaptive Meshing At Damag E Propagation Under Internal Pressure Of 8.96 Psi (Stage 6)

4.0 Progressive Fracture of Composite Structures Under Cyclic Fatigue

Progressive fracture in polymer matrix composite (PMC) structures subjected to cyclic fatigue loading was evaluated by computational simulation to assess structural responses relative to damage initiation, damage growth, damage accumulation, damage propagation to fracture, defect/damage tolerance, and identification of critical locations at which damage initiates. The purpose of the simulations was to facilitate evaluation and optimization of PMC design iterations by providing an accurate numerical computative means of rapidly and cost effectively assessing the effects of on PMC aircraft structures under cyclic fatigue loads caused by structural vibrations and fluctuating surface pressures. An important aspect of the developed software is the capability of using constituent material properties obtained from experimental coupon testing at the structural level to evaluate the overall damage and fracture propagation in composites.

4.1 LOW CYCLE FATIGUE

The GENOA-PFA code was modified to account for the effects of low cyclic loading on PMC structure, as shown in the flow chart of Figure 4-1. Prior to each finite element analysis, the composite mechanics module computes the composite properties from the fiber and matrix constituent characteristics and the composite lay-up. The finite element analysis module accepts the composite properties that are computed for each node by the composite mechanics code and performs the global structural analysis at each load increment.

It is well known that cyclic loads can degrade materials properties over time. This is indicated by the typical stress vs. number of load cycles (S/N) curve of Figure 4-1, in which the ratio of residual to initial ultimate stress decreases markedly as the material strength degrades with an increasing number of stress cycles.

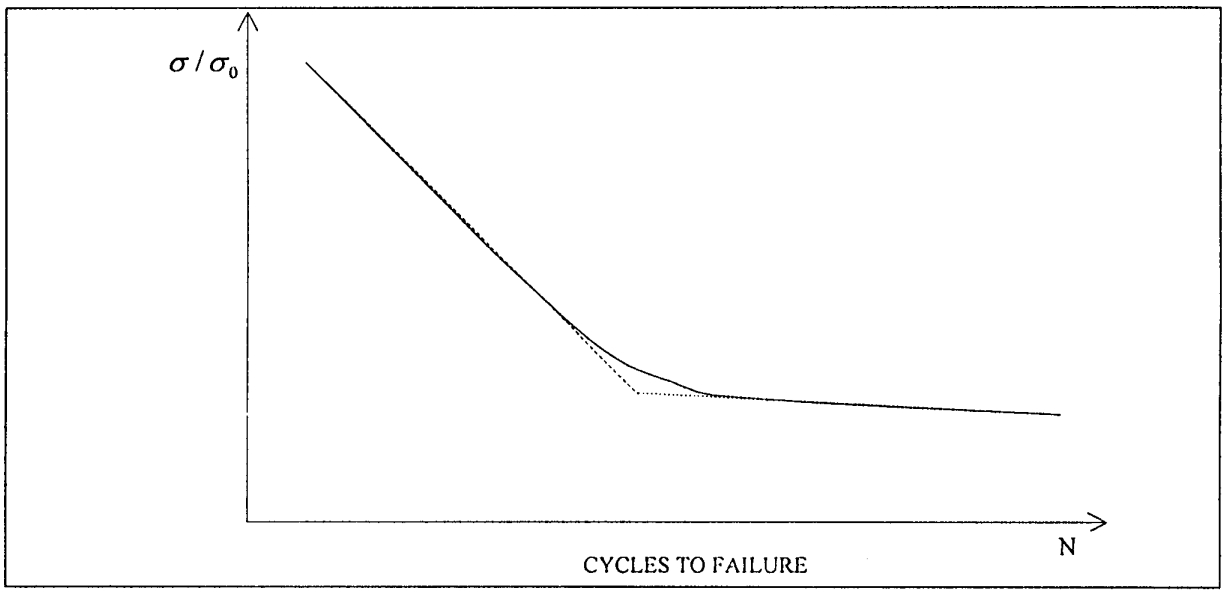

Figure 4-1. S/N Curve for Aluminum

The amplitude and duration of stress cycles are predominantly responsible for material property degradation. Therefore, the total degradation should be a function of stress and loading cycles. The GENOA software suite uses the slopes (β_1 and β) of the two segments of the curve in Figure 4-1 and the cycle number, N_C, in, the following formulas to determined a property degradation factor as follows

$$f = f_1(N)\, f_2(\sigma)$$

$$f_1(N) = \begin{cases} \max(1.0,\ f_0 - \beta_1 \log N) & (if\ \ N < N_C\ ) \\ f_0 - (\beta_1 - \beta_2)\log N_C - \log N & (if\ \ N \geq N_C\ ) \end{cases}$$

$$f_2 = \left(1.0 - \frac{\sigma}{\sigma_0} \right)^{\alpha}$$

Where f – property degradation factor.

f_1 – property degradation factor due to cycling

f_2 – property degradation factor due to stress

σ – stress component due to maximum loading

σ_0 – strength component corresponding to σ.

f_0, β_1, β_2, α – coefficients which can be calibrated with experimental results.

N_C – loading cycle number in which the β coefficient changes, which can be determined experimentally

N – loading cycle number.

4.1.1 NASA Test Coupon Simulation

The test coupon was 4 inches wide and approximately 20 inches long. It was made of two T7475-T7351 aluminum alloy panels lap joined with twelve 2017-aluminum alloy rivets as shown in Figure 4-2.

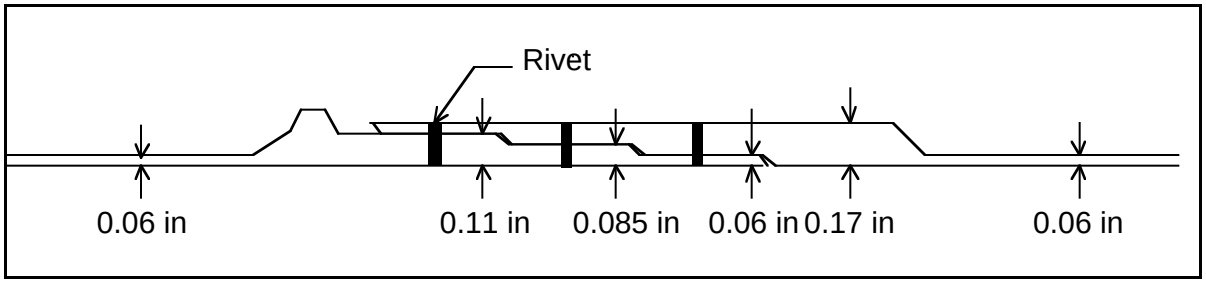

Figure 4-2. Schematic of the NASA Lap Joint Test Coupon

Shell elements reflecting the different thicknesses were used to separately model each half of the test coupon. The FEM mesh created (Figure 4-3) had 980 (QUAD) elements and 120 nodes.

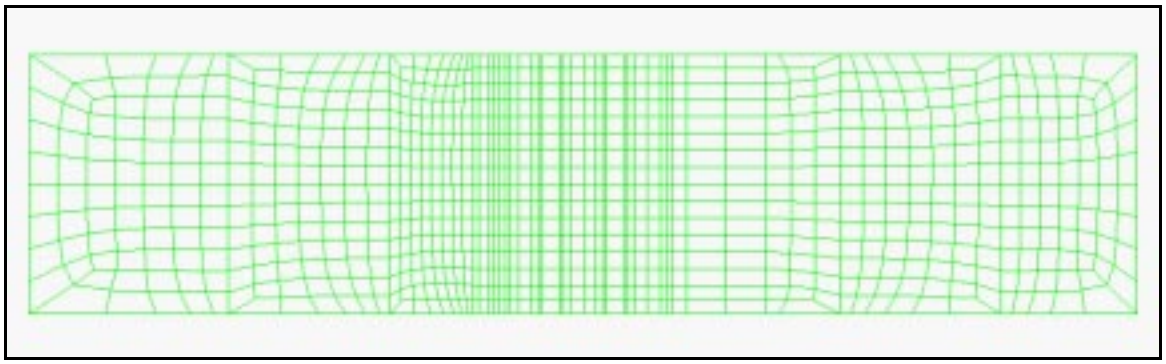

Figure 4-3. FEM Mesh of the NASA Test Coupon

The riveted lap joint was modeled with pairs of duplicated nodes that moved and rotated identically. The response of a node pair was terminated if one of the nodes broke. If a rivet is broke, the pair of duplicate nodes that represented the rivet were separated automatically by the GENOA-PFA software.

For the cyclic loading analysis, one end of the coupon was fixed while a tensile load was uniformly applied to on the other end. The coupon properties degraded as the number of cycles increased until the coupon failed. The degradation coefficient β was calibrated based on experimental results. Table 4-1 shows the NASA coupon results and the GENOA predicted coupon test results. The maximum stress vs. cycles to failure curve shown in Figure 4-4 is in good agreement with the limited number of NASA test results.

Table 4-1. Test and Predicted Cycles to Failure vs. Maximum Stress

Maximum Stress (ksi)	Cycles to Failure	
	NASA Test	GENOA Simulation
24	not available	50,000
22	81,541	84,000
18	153,951/239,361/154,142	204,800
16	313,138	324,100
14	not available	505,000
12	not available	830,700
11	not available	2,500,000
10	not available	29,100,000

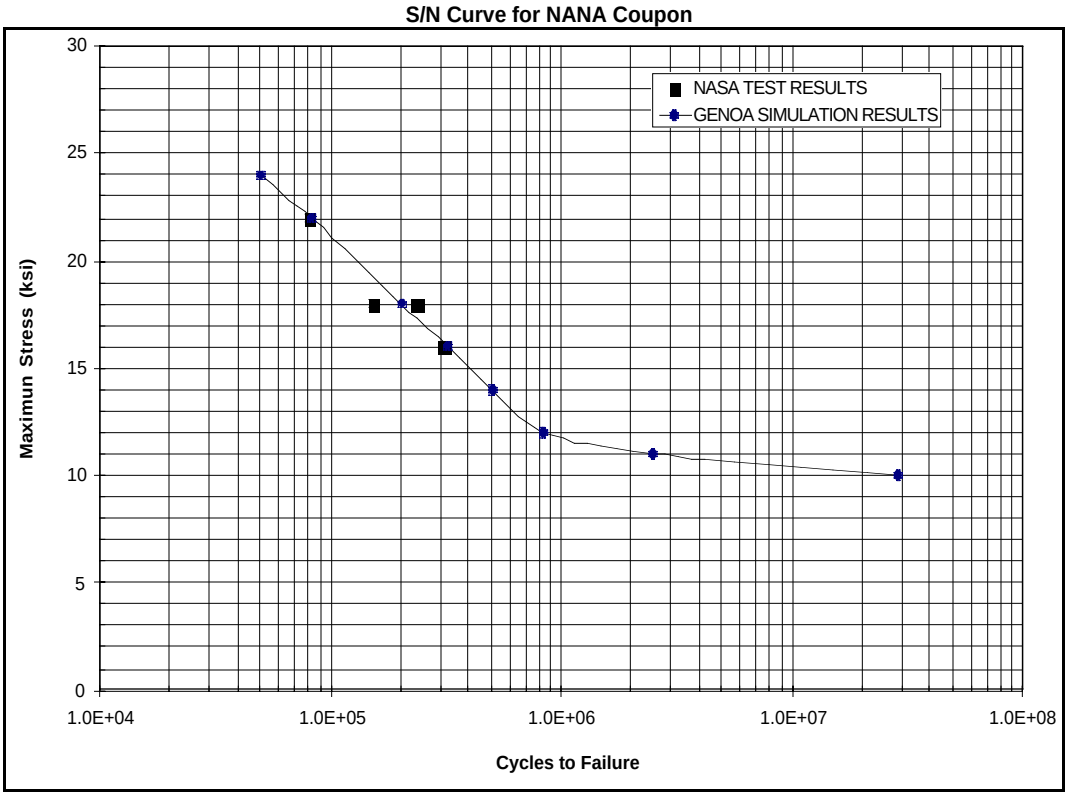

Figure 4-4. S/N Curve From Simulation of NASA Test Coupon

4.1.2 Crown Panel Simulation

The IAS crown panel was simulated using coefficients calibrated with NASA coupon test results except for β_2 which was based on test results from Mill Hand Book 5G, Figure 4-5 (7050 Aluminum plate: Kt = 1.0, Stress Ratio = -1.0) NASA because coupon test in the β_2 range was not available. The coefficient values used in the simulation were as follows:

$\beta_1 = 0.168$

$\beta_1 = 0.0127$

$f_0 = 1.196$

$\alpha = 1.15$

$N_C = 10^6$

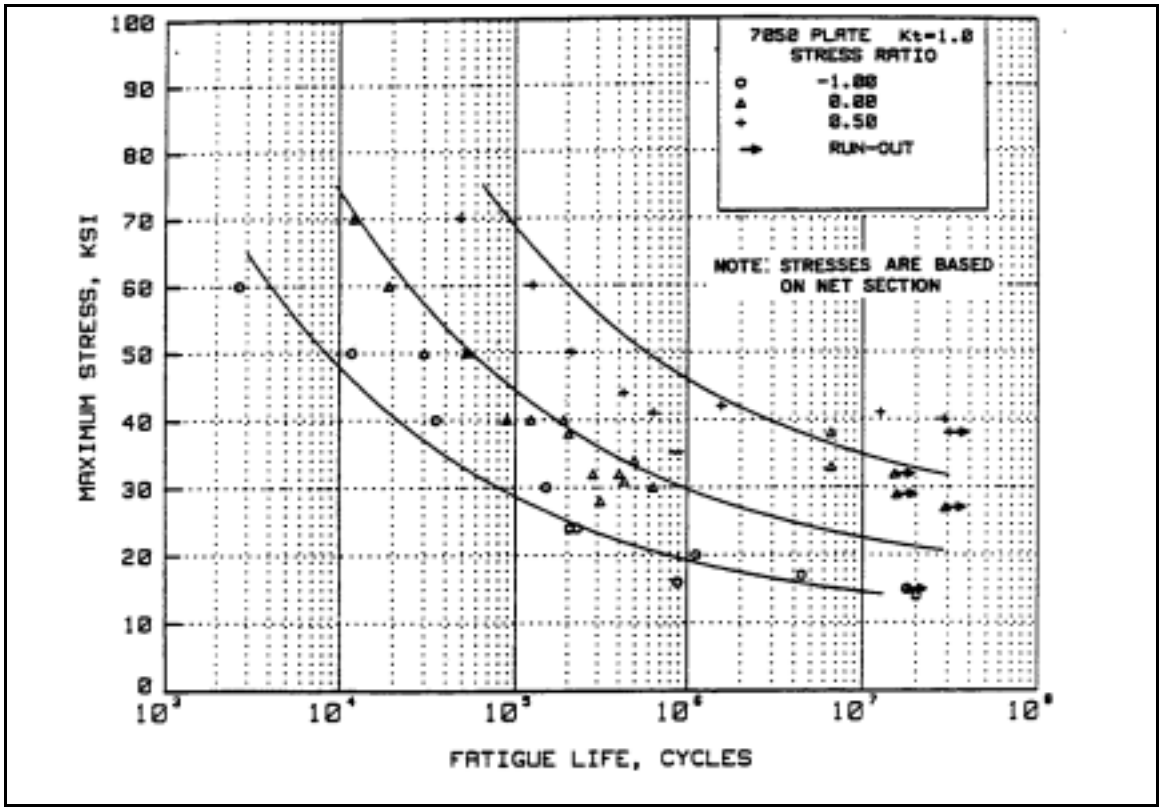

Figure 4-5. Material Property Degradation For 7050 Aluminum Plate (Max Stress Vs. Life Cycle)

Fracture patterns were very similar for all stress levels. Once damage occurred to a rivet node, it soon propagated to adjacent rivet nodes. Figures 4-6 through 4-12 show the damage propagation sequence for a maximum stress amplitude of 22 ksi, as the stress cycles were increased from 84,000 cycles by small increments.

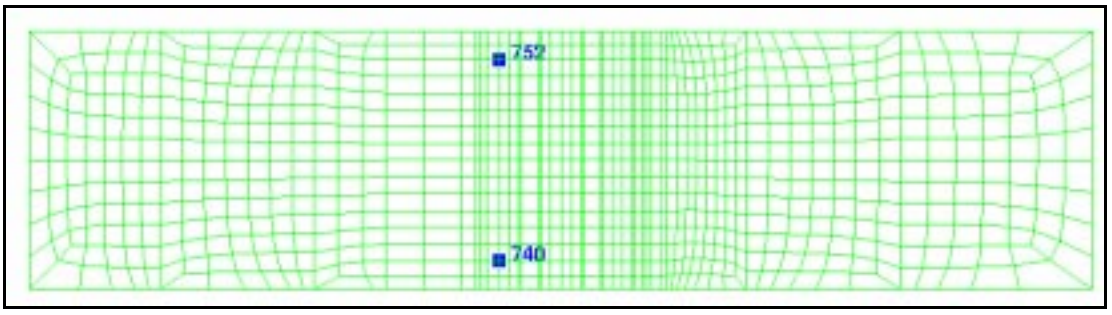

Figure 4-6. Damage Initiation Under Cyclic Loading at the Stress Amplitude of 22 ksi and 84,000 Cycles

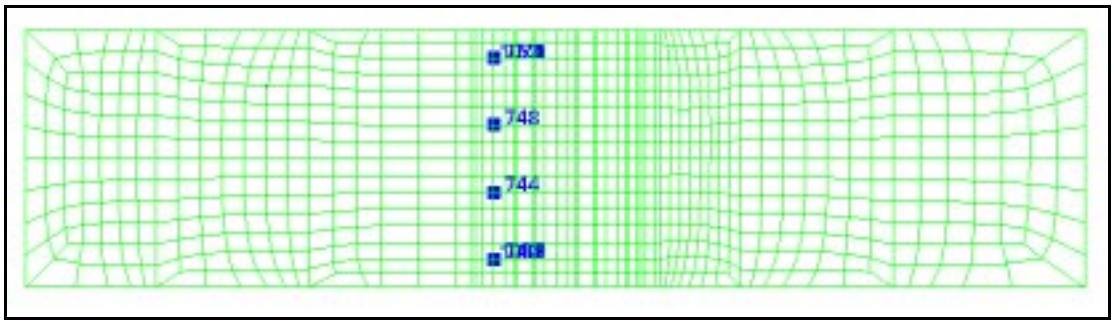

Figure 4-7. Damage Propagation (Stage 1) Under Cyclic Loading With Maximum Stress of 22 ksi at 84,000 $+\Delta_1$ Cycles.

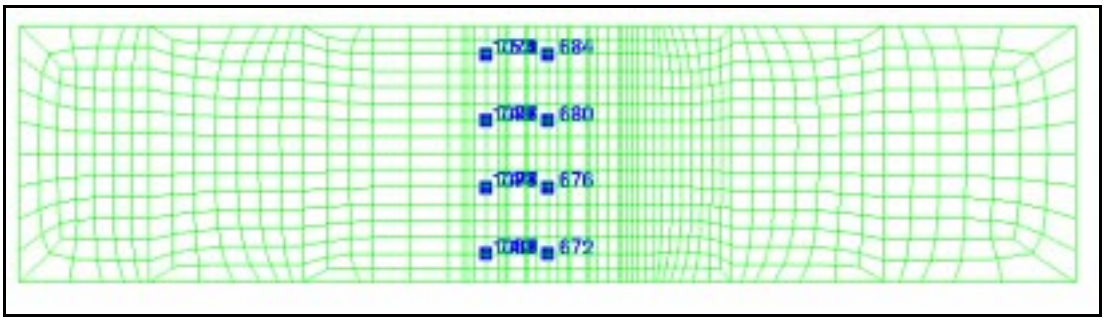

Figure 4-8. Damage Propagation (Stage2) Under Cyclic Loading With Maximum Stress of 22 ksi at 84,000 $+\Delta_2$ Cycles.

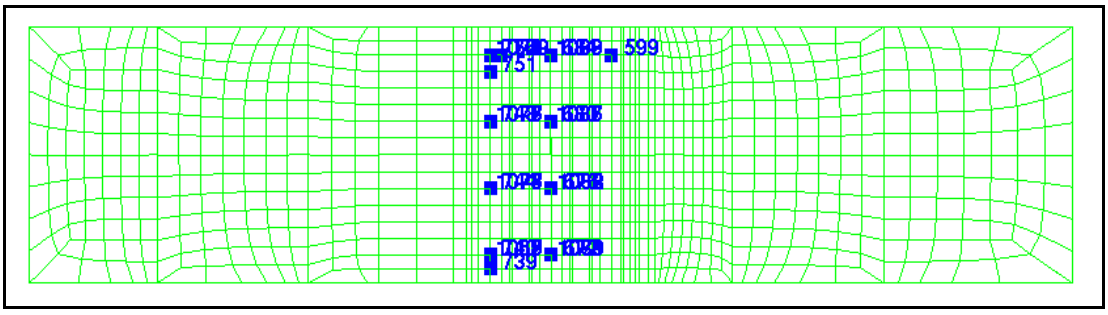

Figure 4-9. Damage Propagation (Stage 3) Under Cyclic Loading With Maximum Stress of 22 ksi at 84000 $+\Delta_3$ Cycles.

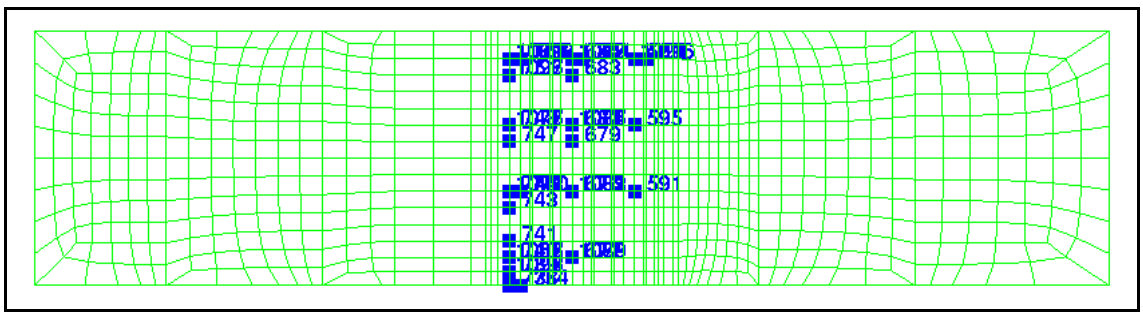

Figure 4-10. Damage Propagation (Stage 4) Under Cyclic Loading With Maximum Stress of 22 ksi at 84,000 $+\Delta_4$ Cycles.

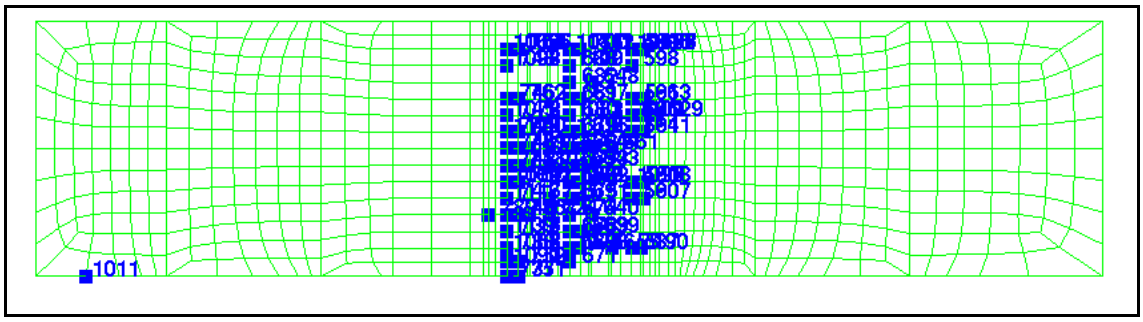

Figure 4-11. Damage propagation (stage 5) under cyclic loading with maximum stress of 22 ksi at 84,000 +Δ_5 Cycles.

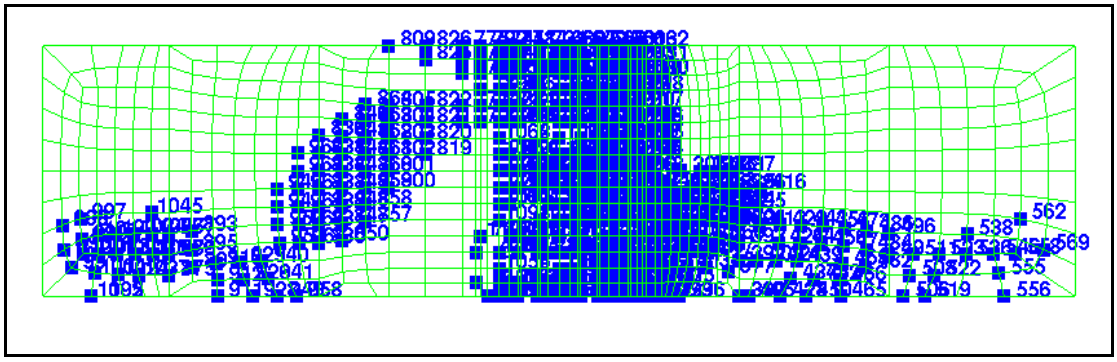

Figure 4-12. Damage Propagation (Stage 6) Under Cyclic Loading With Maximum Stress of 22 ksi at 84,000 +Δ_6 Cycles.

4.1.3 Verification of Boeing 747 Crown Panel Simulation

The Boeing panel had skin and stringers made of T7475-T7351 aluminum alloy and the frames of 7050-T7451-aluminum alloy. The finite element model used is shown in Figure 4-13. Thick shell elements were used to model the entire structure. The thicknesses of the elements was governed by the panel thickness as it changed with location. A comparison of simulation and experimental test results is shown in Table 4-2.

Table 4-2. Summary of Results From Testing and Deterministic Simulation Analyses

Specimen	Loading condition	Maximum stress	Simulation	Testing
Crown Panel	Static Loading (ultimate load)	Available	10.48 Psi	~10.3 Psi
	Cyclic Loading (cycle to failure)	Not Reported	10,720 Psi	10,333 Psi

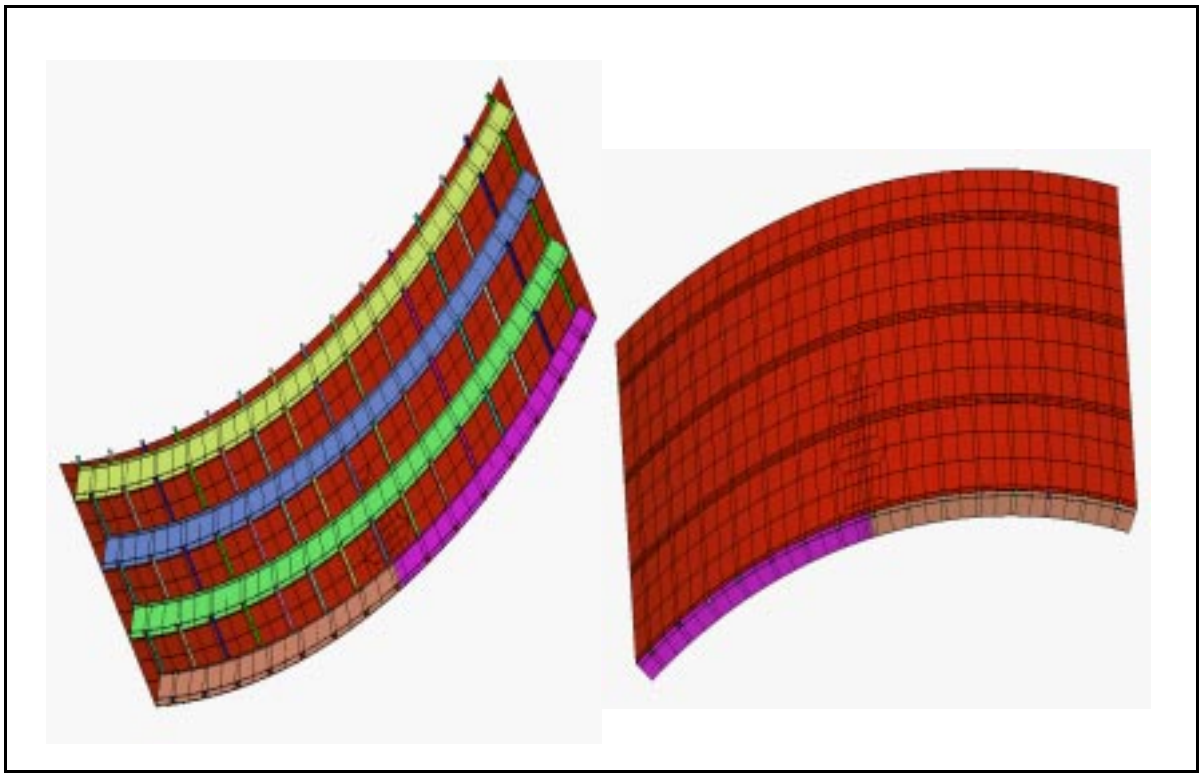

Figure 4-13. IAS Boeing Panel Finite Element Model

The cyclic loading analysis of the Boeing panel was conducted with a symmetrical model with a saw cut discrete source damage (DSD) in the skin 2.5 inches long. The maximum internal pressure for the cyclic loading analysis was 8.6 psi. Damage initiated at 9724 cycles as shown in Figure 4-14. At 10,720 cycles, the crack grew to the second frame (Figure 4-15).

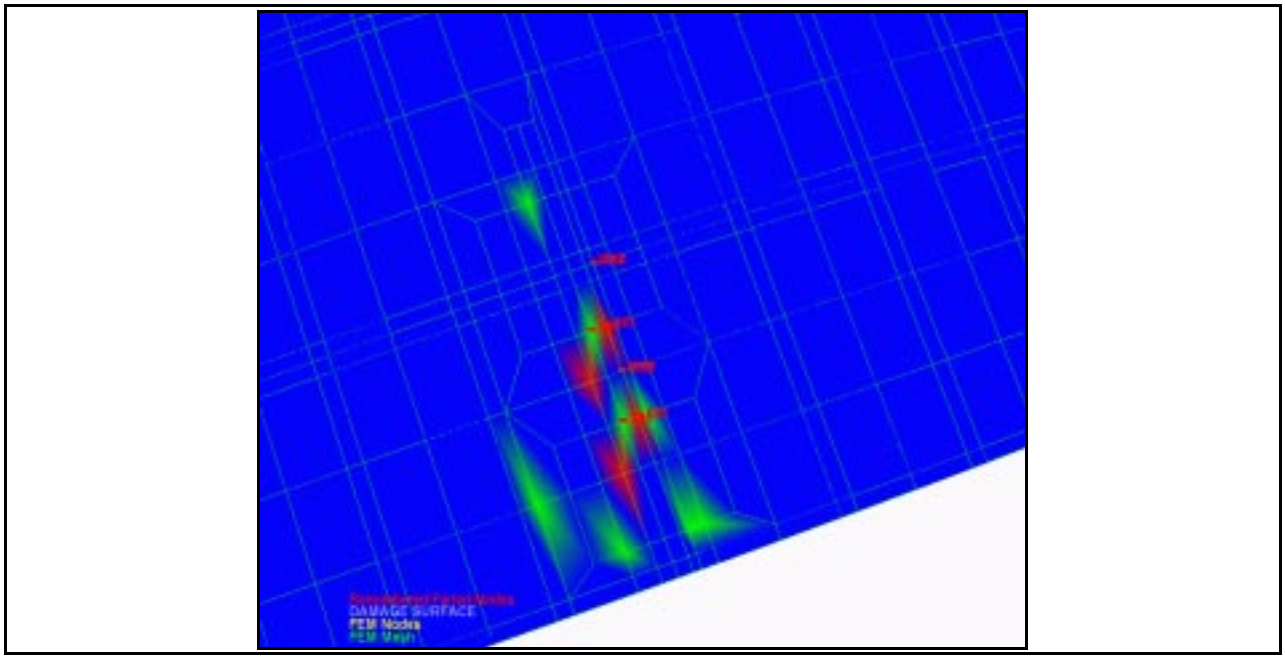

Figure 4-14. Damage Initiation Under Cyclic Loading With Maximum Internal Pressure of 8.6 ksi at 9,724 Cycles.

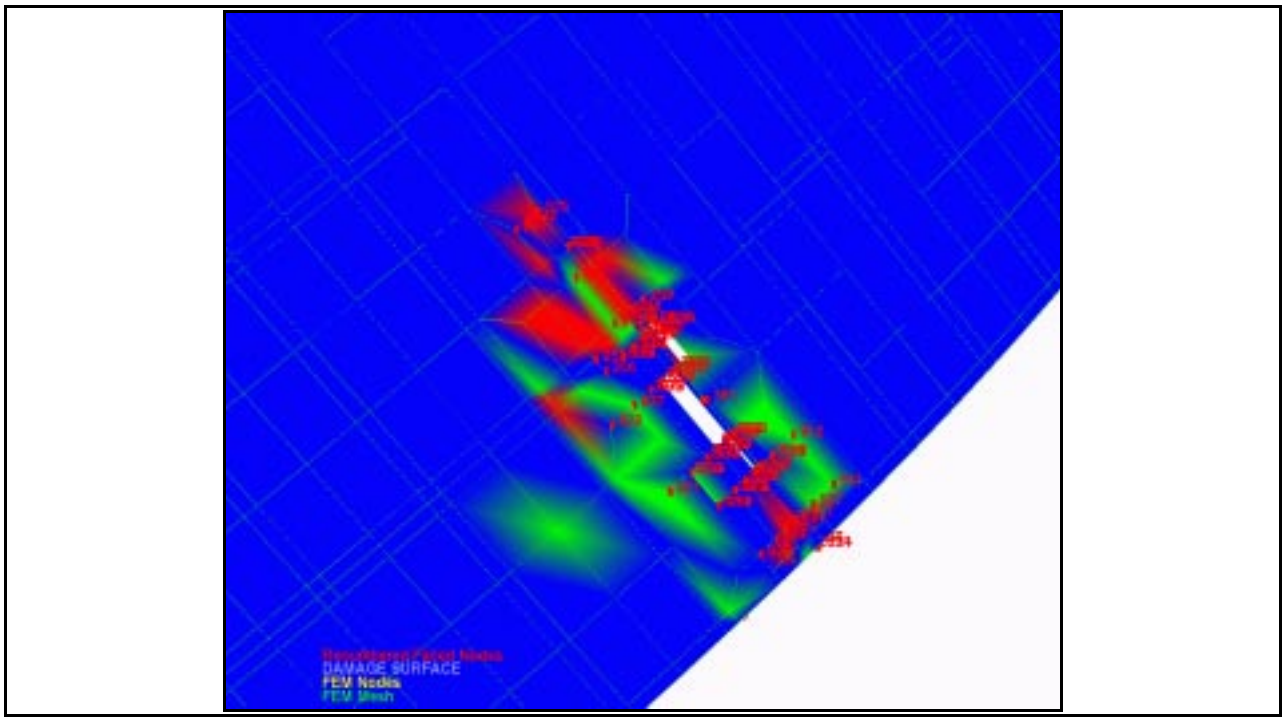

Figure 4-15. Final Fracture Pattern Under Low Cyclic Loading With Maximum Internal Pressure of 15 ksi at 10,720 Cycles.

4.2 High Cycle Fatigue

4.2.1 High Cycle Fatigue Simulation Methodology

Figure 4-16 shows a flow chart for the computational simulation of high cycle fatigue with the modified GENOA-PFA. The computational eigenvalues of vibration modes and frequencies were used in time history analysis of the fluctuating stresses at each time increment

The composite mechanics module is called before and after each finite element time-history analysis. Prior to each finite element analysis, the composite mechanics module computes the composite properties from the fiber and matrix constituent characteristics and the composite layup. The finite element analysis module accepts the composite properties that are computed by the composite mechanics code at each node and performs the global structural analysis at each load increment.

The difference from simulation of low cycle fatigue is the introduction of time history analysis after a finite element analysis. The computed generalized nodal force and moment time histories are supplied to the composite analysis module that evaluates the nature and amount of local damage, if any, in the plies of the composite laminate. The evaluation of local damage due to cyclic loading is based on simplified mathematical models embedded in the composite mechanics module (Murthy and Chamis 1986). The complete details of these models are outlined by Chamis and Ginty (1987). The fundamental assumptions in the development of these models are the following: (1) Fatigue degrades all ply strengths at approximately the same rate (Chamis and Sinclair, 1982). (2) All types of fatigue degrade laminate strength linearly on a semilog plot including: (a) mechanical (tension, compression, shear, and bending); (b) thermal (elevated to cryogenic temperature); hygral (moisture); and combinations (mechanical, thermal, hygral, and reverse-tension compression). (3) Laminated composites generally exhibit linear

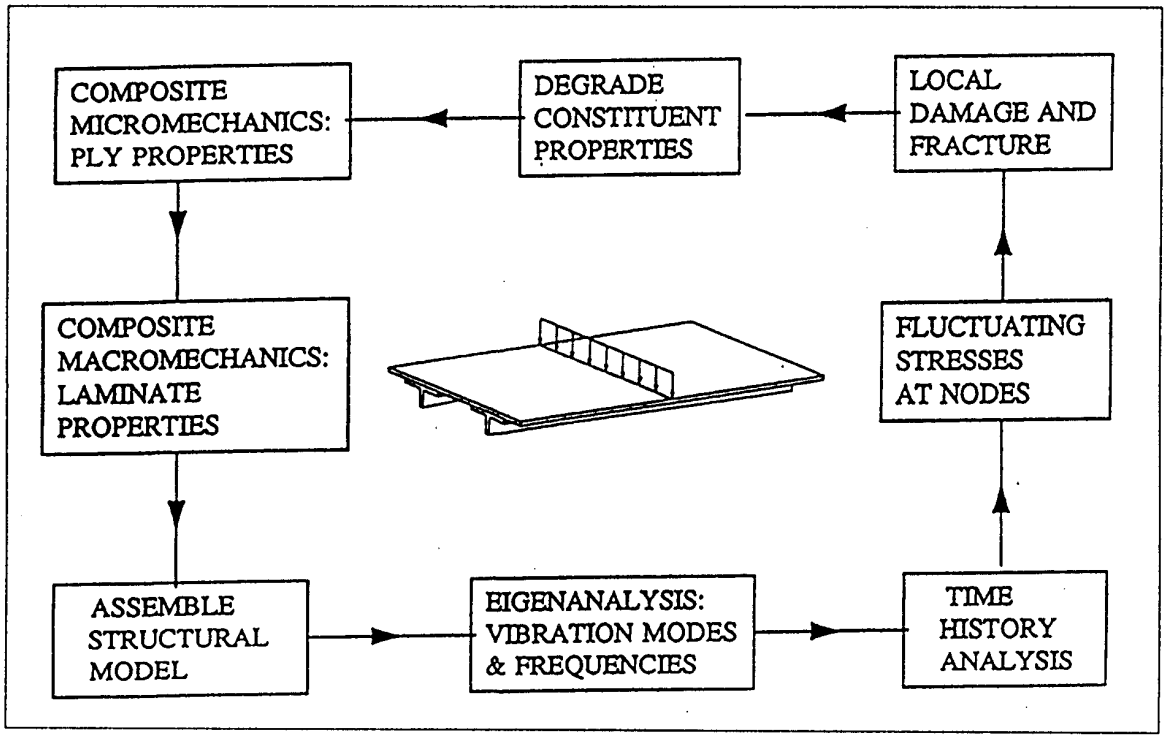

Figure 4-16. Progressive Fracture Flow Diagram For High Cycle Fatigue

behavior to initial damage under uniaxial and combined loading. (4) All ply stresses (mechanical, thermal, and hygral) are predictable by using linear laminate theory.

Individual ply failure modes are assessed by using margins of safety computed by the composite mechanics module via superposition of the six cyclic load ratios. The cyclic loads that are considered are the Nx, Ny, Nxy in-plane loads and Mx, My, Mxy flexural moments. The lower and upper limits of the cyclic loads, the number of cycles, and the cyclic degradation coefficient beta are supplied to the composite mechanics module at each node for the computation of a complete failure analysis based on the maximum stress criteria. The cyclic degradation coefficient beta has been determined to be in the range of 0.01 to 0.02 for graphite/epoxy composites.

Time-history dynamic analysis of composite structures subjected to cyclic excitation is conducted using the modal basis. Computed nodal stress resultant time-histories are used to assess the maximum and minimum values of the local load cycles and frequencies at each node. The composite mechanics module with cyclic load analysis capability evaluates the local composite response at each node subjected to fluctuating stress resultants. The number of cycles and the time required to induce local structural damage are evaluated at each node. After damage initiation, composite properties are re-evaluated based on the degraded ply properties. The overall structural response parameters are recomputed. Iterative application of this computational procedure results in the tracking of progressive damage in the composite structure subjected to cyclic load increments. Computational simulation cycles are continued until the composite structure failures. The number of cycles for damage initiation and the number of cycles for structural fracture are identified in each simulation.

After damage initiation, the number of load cycles will reach a critical level, at which damage begins to propagate rapidly in a composite structure. After the critical damage propagation stage is reached, the composite structure experiences excessive damage or fracture rendering it unsafe for continued use. The generalized local stress-strain relationships are revised according to the composite damage evaluated after each finite element time-history analysis. The model is automatically updated with a new finite element mesh having reconstituted properties, and the structure is reanalyzed for further deformation and damage. If there is no further damage after a cyclic load increment, the structure is considered to be in equilibrium and an additional number of cycles are applied possible leading to possibly damage growth, accumulation, or propagation. Simulation under cyclic loading is continued until structural failure.

In general, overall structural damage may include individual ply damage and through-the-thickness fracture of a composite laminate. The computational simulation procedure uses an accuracy criterion based on the allowable maximum number of damaged and fractured nodes within a simulation cycle. If too many nodes are damaged or fractured in the simulation cycle, the number of cycles are reduced and analysis is restarted from the previous equilibrium state. Otherwise, if there is an acceptable amount of incremental damage, the number of cycles is kept constant but the constitutive properties are updated to account for damage from the last simulation cycle.

4.2.2 GENOA-PFA Modification For Cyclic Fatigue Simulation

The cyclic loading simulation was implemented for harmonic loads using additional subroutines that take over the analysis for the cyclic progressive fracture assessment under dynamic loading. Prior to a time history dynamic analysis, a subroutine PRECYC prepares an MHOST input file for conduction of a free vibration eigenvalue analysis. The computed natural frequencies are supplied to subroutine HSTCYC which prepares an input file to MHOST to perform a time history dynamic analysis over a representative time duration. To determine a representative time duration a comparison is made of the fundamental vibration and harmonic load period. The greater of the two periods is selected as this representative period and the time history dynamic response is taken over one and a half times the representative period as subdivided into 30 time increments.

After the time history dynamic analysis is conducted by MHOST, subroutine INFCYC is called to read the MHOST postprocessing file (unit 19). Subroutine INFCYC reads the time history of generalized stress resultants (Nx, Ny, Nxy, Mx, My, Mxy) for each node and for each of the 30 time increments from fort.19 file. At each node, the maximum and minimum values are determined for each specific stress resultant. The time difference between consecutive maximum and minimum values of a stress resultant is considered to be half the cyclic loading period for that specific stress component. Subroutine INFCYC writes all information to unit 93 (SCRA93).

Next, subroutine ICNCYC is called to prepare ICAN input data for cyclic durability analysis for a given time duration. The time duration of cyclic loading is simply the number of total load cycles times the harmonic load period. For each node, subroutine ICNCYC writes the ply data, checks and degrades material properties according to damage, and writes the maximum and minimum, loads, the number of cycles, and the cyclic degradation coefficient, beta, for each stress resultant. The number of cycles is computed for each stress resultant as the ratio of the cyclic load time duration to the period of loading cycle for the stress resultant computed in subroutine INFCYC. Subroutine ICNCYC calls ICAN for each node to compute the cyclic loading margins with the STRES2 function in ICAN. The results are written to unit 94 (SCRA94).

Subroutine PFMCYC reads the cyclic loading margins from SCRA94. For each ply at each node, fiber failure is checked based on upper and lower ply longitudinal stress, SIGMA11, margins. If a cyclic load margin is negative, then a damage index is established recording the damage mode. Margins associated with upper and lower ply transverse stress, and in-plane shear stress are associated with matrix failures only. The damage index for each failure mode is stored in an array that is used to degrade the fiber and/or matrix stiffnesses in subsequent analyses. When there is additional damage, the cyclic fatigue analysis is repeated over the same time duration. After a cyclic fatigue analysis step, if there is no additional damage the time duration is incremented. This procedure is repeated until the composite structure fails. Changes in structural response parameters such as natural frequencies and ply damage are monitored.

4.2.3 Simulation of PMC Panel Under Cyclic LOAD

The first specimen examined was a stiffened composite panel, (Figures 4-17) subjected to a transverse line load. The boundary conditions were simple supports at the two ends. The composite material is made of AS-4 graphite fibers in a high-modulus, high strength (HMHS) epoxy matrix. The fiber and matrix properties were obtained from a databank of composite constituent material properties (Murthy and Chamis 1986).

The HMHS matrix properties are representative of the 3501-6 resin. The fiber volume ratio is 0.60 and the void volume ratio is 0.01. The laminate ply configuration is [0/45/90] for both the skin and the stringer-stiffeners. The 0º plies are oriented in the longitudinal direction and the 90º plies are oriented in the transverse direction of the stiffeners.

The two T5 stringers were stitched to the skin panel prior to curing. The finite element model used thick shell elements with duplicate nodes to represent the attachment of the T5 flanges to the skin by stitching. Durability of the stiffened panel was evaluated under a transverse line load applied at mid-span.

The panel was simulated under cyclic fatigue loading. The first three natural frequencies of the cantilevered plate are computed by the finite element module as ω_1=245.4 Hz, ω_2=246.5 Hz, and ω_3=342.9 Hz. The stiffened panel was subjected to a fluctuating cyclic line load with full load reversal. Harmonic load excitations at 50 Hz frequency was applied to the center of the panel in simulations with three different cyclic pressure amplitudes. Damage progression was computationally simulated as the number of cycles was increased (Figure 4-18). The percent damage volume in the composite structure is plotted as a function of the number of cycles at pressure amplitudes of 3.56, 7.83, and 16.37 kN (0.80, 1.76, and 3.68 k). For all three cases damage initiation occurs by transverse tensile fracture of 90, 45, and

0 degree plies in the center of the panel at the free edge of the stiffeners. For the higher load amplitudes damage initiation occurs at fewer number of cycles. After damage initiation, damage growth continued by ply transverse tensile fractures. The rate of damage growth depended on the load amplitude. The higher load amplitude caused a more rapid growth of internal damage in the plies of the laminate. For the majority of the fatigue life transverse tensile fractures occurred gradually in plies. Near the very end the fatigue life the 0 degree plies at the edge of the blade laminate fractured in longitudinal tension. The location of this critical longitudinal ply fracture is at the same node as that of the damage initiation. After this stage, fracture rapidly propagates across the laminate thickness, develops into a structural fracture and breaks the specimen into two pieces. Figure 4-19 shows the degradation of the first natural frequency as a function of the number of cycles endured. The degradations of the second and third natural frequencies are very similar as shown in Figures 4-20 and 4-21. The damage initiation and progression stages did not affect the fundamental structural response significantly. Only when the ultimate structural fracture stage was entered due to ply longitudinal fractures was the natural frequency of the specimen is reduced significantly. At the ultimate structural failure the degradation of structural response was very rapid and consistent with a brittle fracture mode.

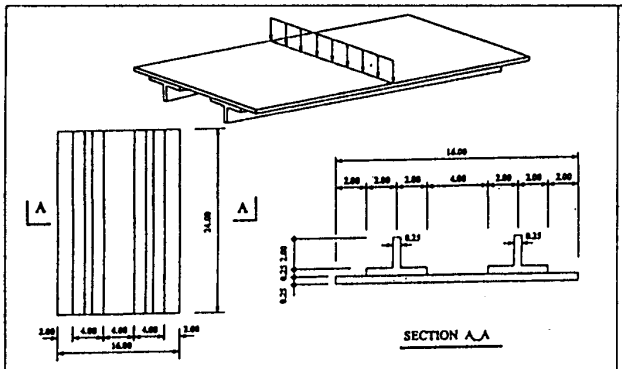

Figure 4-17. Stiffened Composite Panel and Loading AS-4/HMHS: 48 Plies [0/45/90]s6

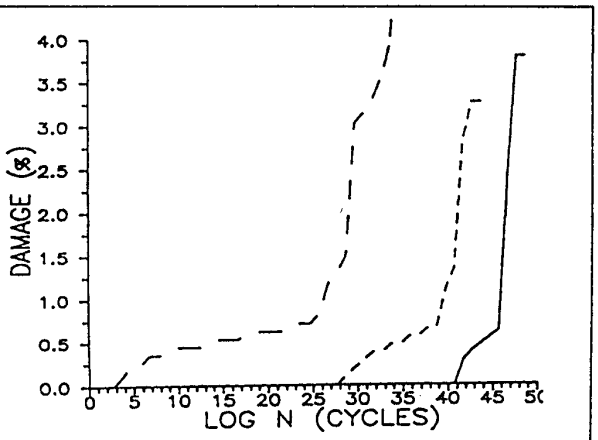

Figure 4-18. Damage Progression under Cyclic Loading AS-4/HMHS: 48 Plies [0/45/90]{s6, Loaded at 50 Hz Solid line: cyclic load amplitude of 3.56 kN (0.80 k) Short dashed line: cyclic load amplitude of 7.83 kN (1.76 k) Long dashed line: cyclic load amplitude of 16.37 kN (3.68 k)

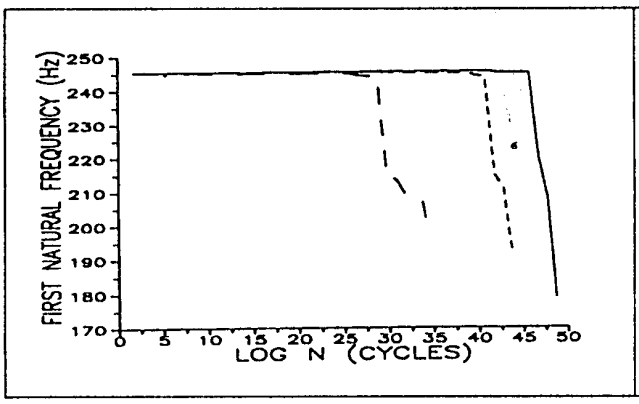

Figure 4-19. First Natural Frequency Degradation under Cyclic Loading AS-4/HMHS: 48 Plies [0/45/90]$_{s6$, Loaded at 50 Hz, Solid line: cyclic load amplitude of 3.56 kN (0.80 k) Short dashed line: cyclic load amplitude of 7.83 kN (1.76 k) Long dashed line: cyclic load amplitude of 16.37 kN (3.68 k)

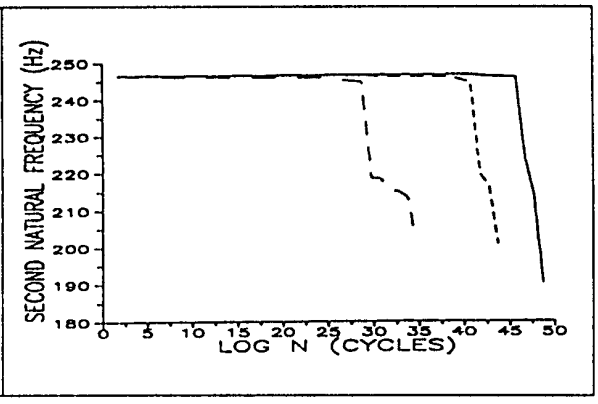

Figure 4-20. Second Natural Frequency Degradation under Cyclic Loading AS-4/HMHS: 48 Plies [0/45/90]s6, Loaded at 50 Hz, Solid line: cyclic load amplitude of 3.56 kN (0.80 k) Short dashed line: cyclic load amplitude of 7.83 kN (1.76 k) Long dashed line: cyclic load amplitude of 16.37 kN (3.68 k)

4.2.4 Simulation Of Composite Plate Under Cyclic Loading

A graphite/epoxy laminated rectangular cantilever plate was simulated to demonstrate high cycle fatigue capability. The plate was 102 mm (4.0 in) long and 51 mm (2.0 in) wide and consisted of four plies configured as $\pm 45^{o}$ with a total thickness of 3.73 mm (0.147 in). The finite element model of the plate contains 8 elements and 15 nodes Figure 4-22.

The composite was made of AS-4 graphite fibers in a high-modulus, high strength (HMHS) epoxy matrix. The fiber and matrix properties were obtained from a databank of composite constituent material properties (Murthy and Chamis 1986). The HMHS matrix properties are representative of the 3501-6 resin. The fiber volume ratio was 0.555 and the void volume was assumed to be zero.

The first three natural frequencies of the cantilevered plate were computed by the GENOA-PFAs finite element module as ω_1=217 Hz, ω_2=1,418 Hz, and ω_3=1,576 Hz. The plate was investigated subjected to a fluctuating surface pressure with load reversal. A harmonic pressure excitation of 50 Hz frequency was applied to the entire surface of the plate. Simulations with three different cyclic pressure amplitudes are conducted. Damage progression was computationally simulated as the number of cycles was increased.

Figure 4-23 shows the damage progression with increasing time duration for the three different cyclic pressure amplitudes. The percent damage volume developed in the composite structure is plotted as a function of time for pressure amplitudes of 110, 138, and 165 MPa (16, 20, and 24 psi). For all three pressure amplitudes damage initiation occurs by transverse tensile fracture of ply 1 at node 5 (Figure 4-22) during the first cycle of loading. However, the evolution of damage growth and ultimate fracture depend on the pressure amplitude. For the lowest pressure amplitude of 110 MPa, damage that was initiated during the first load cycle remains stable for a long time duration as shown in Figure 4-23. For the intermediate pressure amplitude of 138 MPa, damage grows by the transverse tensile fracture of ply 1 at node 6 (Figure 4-22) after a short duration of cyclic loading. For the highest pressure amplitude of 165 MPa the transverse tensile fractures immediately progress within the first ply to nodes 4, 5, 6, 7, 11, 13, and 14. For the two higher pressure amplitudes of 138 and 165 MPa the damage volume was exactly the same for a considerable portion of the fatigue life. However, damage progression for the 165 MPa pressure amplitude was more localized, therefore the ultimate structural fracture stage occurs more suddenly. For all pressure amplitudes at the ultimate fracture stage damage progresses through the

laminate thickness at nodes 8, 9, 11, 15 after structural fracture was initiated by the formation of a through-the-thickness crack at node 11. Simulations indicated that node 6 was damaged in plies 1, 3, and 4 by shear failures as well as experiencing damage due to transverse tensile failure in ply 1 and longitudinal tensile failure in ply 4. Node 7 experienced transverse tensile fracture in plies 1 and 4 and longitudinal tensile fracture in ply 3. The remaining nodes experienced transverse tensile fractures in ply 1 prior to structural fracture of the plate.

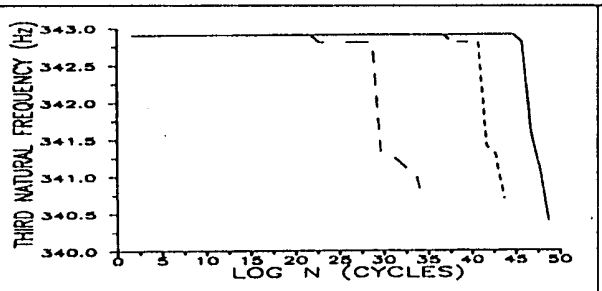

Figure 4-21. Third Natural Frequency Degradation under Cyclic Loading AS-4/HMHS: 48 Plies [0/45/90]s6, Loaded at 50 Hz Solid line: cyclic load amplitude of 3.56 kN (0.80 k) Short dashed line: cyclic load amplitude of 7.83 kN (1.76 k) Long dashed line: cyclic load amplitude of 16.37 kN (3.68 k)

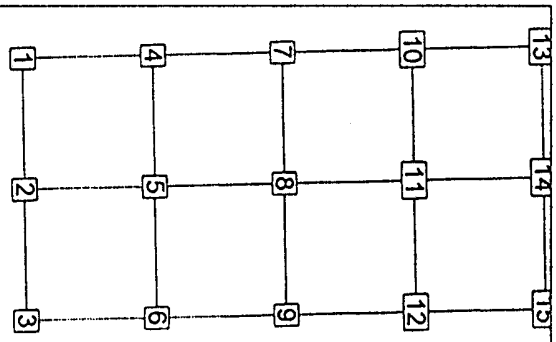

Figure 4-20. Composite Plate Finite Element Model

Figure 4-23 indicates that at higher pressures the ultimate fracture response is more brittle. Results also indicate that logarithm of the time required for structural fracture varies linearly with the pressure amplitude as shown in Figure 4-24.

Figure 4-25 shows the degradation of the first natural frequency as a function of the time duration of the fatigue loading. It is clear that the damage initiation stage affects the fundamental structural response significantly. On the other hand, the damage growth stages do not influence the first natural frequency as much. Figure 4-26 shows the second natural frequency that is somewhat more influenced by the damage growth stages compared to the first natural frequency. Figure 4-27 shows the variation of the third natural frequency with exposure to fatigue loading. Comparison of results depicted in Figures 4-25, 4-26, and 4-27 indicate that during the later stages of fatigue life higher frequency vibration modes are more sensitive to the evolution of composite damage compared to the lower frequency modes. The main reason is that localization of damage that occurs prior to fracture has a greater influence on the high frequency vibration modes. Therefore, structural health monitoring based on response measurements must identify the appropriate high frequency vibration modes that need be tracked to assess impending structural fracture.

For this composite plate subjected to harmonic cyclic loading, the simulation results may be summarized as follows:

1. Damage initiation by transverse tensile fractures of the first +45 ply occurs at node 5 for all three pressure amplitudes considered.

2. Damage initiation begins during the first cycle of loading for all three pressure amplitudes. However, the extent of damage growth immediately after damage initiation depends on the cyclic pressure amplitude.

3. For the example angleplied composite structure considered, the logarithm of the number of cycles endured prior to structural fracture is inversely proportional to the applied cyclic pressure amplitude.

4. The amount of fundamental natural frequency reduction after damage initiation depends on the cyclic pressure amplitude. The higher the pressure amplitude, the larger the reduction in the natural frequency. However, the natural frequencies immediately prior to structural fracture are independent of the pressure amplitude for the plate simulated.

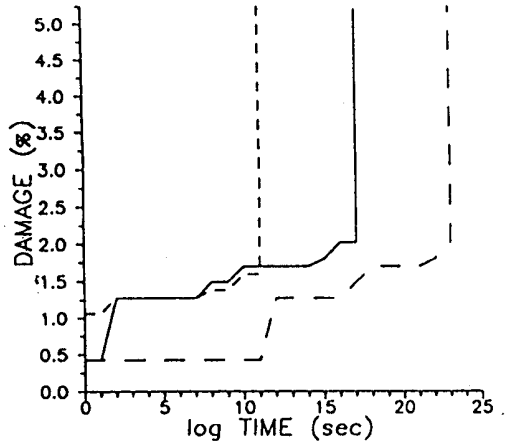

Figure 4-23. Damage Progression under Cyclic Pressure Loading AS-4/HMHS: 4 Plies [±45]s, Pressurization frequency = 50 Hz Long dashed line: cyclic pressure amplitude = 16 psi Solid line: cyclic pressure amplitude = 20 psi Short dashed line: cyclic pressure amplitude = 24 psi

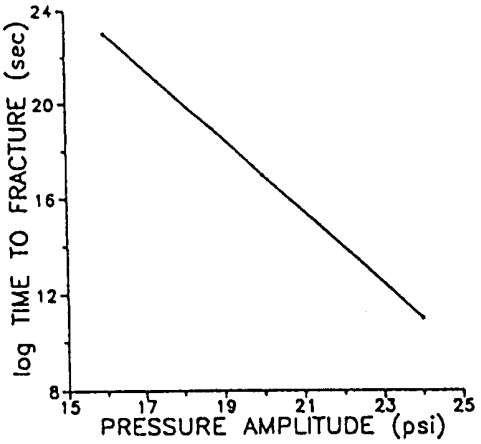

Figure 4-24. Time of Fracture with Pressure Amplitude AS-4/HMHS: 4 Plies [±45]s, Pressurization frequency = 50 Hz

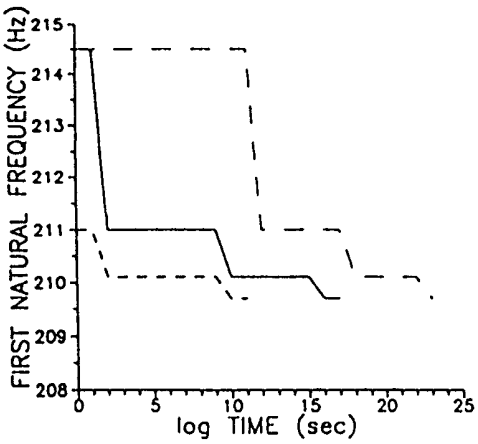

Figure 4-25. First Natural Frequency Degradation with Fatigue Loading AS-4/HMHS: 4 Plies [±45]s, Pressurization frequency = 50 Hz Long dashed line: cyclic pressure amplitude = 16 psi Solid line: cyclic pressure amplitude = 20 psi Short dashed line: cyclic pressure amplitude = 24 psi

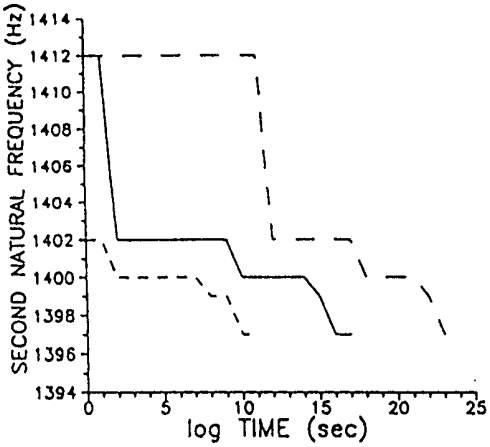

Figure 4-26. Second Natural Frequency Degradation with Fatigue Loading AS-4/HMHS: 4 Plies [±45]s, Pressurization frequency = 50 Hz Long dashed line: cyclic pressure amplitude = 16 psi Solid line: cyclic pressure amplitude = 20 psi Short dashed line: cyclic pressure amplitude = 24 psi

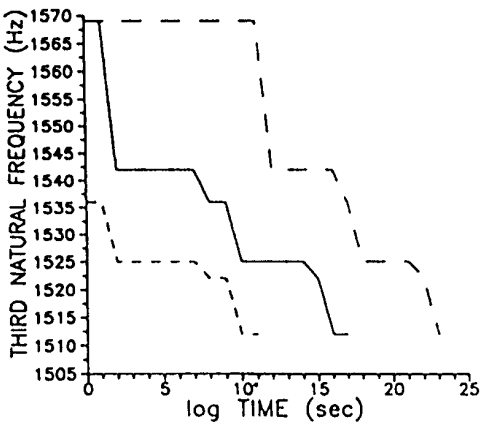

Figure 4-27. Third Natural Frequency Degradation with Fatigue Loading AS-4/HMHS: 4 Plies [±45]s, Pressurization frequency = 50 Hz Long dashed line: cyclic pressure amplitude = 16 psi Solid line: cyclic pressure amplitude = 20 psi Short dashed line: cyclic pressure amplitude = 24 psi

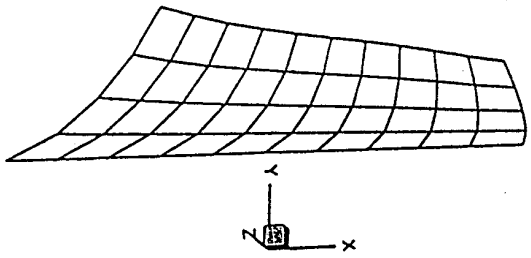

Figure 4-28. Composite Airfoil Finite Element Model

4.2.5 Simulation Of Composite Airfoil Under High Cyclic Loading

A graphite/epoxy laminated cantilever airfoil was used as another example to demonstrate the cyclic fatigue simulation of composite structures. The airfoil has an average length of 371 mm (14.6 in) and the width varies from 73.4 mm (2.89 in) at the tip to 131 mm (5.14 in) at the base. The laminate consists of 16 plies that are configured as [45/0/90$_{4}$45/90/0] with a total thickness of 2.54 mm (0.10 in). The finite element model of the airfoil contains 40 elements and 55 nodes as shown in Figure 4-28.

The composite system is made of AS-4 graphite fibers in a high-modulus, high strength (HMHS) epoxy matrix. The fiber and matrix properties are obtained from the databank of composite constituent material properties (Murthy and Chamis 1986). The fiber and matrix properties corresponding to this case are given in Tables 1 and 2, respectively. The HMHS matrix properties are representative of the 3501-6 resin. The fiber volume ratio is 0.55 and the void volume is assumed to be zero.

The first three natural frequencies of the cantilevered plate are computed by the finite element module as ω_1=50.03 Hz, ω_2=190.1 Hz, and ω_3=263.6 Hz. The airfoil is investigated subjected to a fluctuating lateral force with load reversal. The specimen is loaded by applying a harmonic loading of 50 Hz frequency applied to all nodes of the airfoil. Simulations with four different cyclic amplitudes are conducted. Damage progression is computationally simulated as the number of cycles is increased.

Figure 4-29 shows the damage progression with increasing time duration for the four different cyclic pressure amplitudes. The percent damage volume developed in the composite structure is plotted as a function of time for load amplitudes of 11.83, 13.52, 15.21, and 16.90 N (2.66, 3.04, 3.42, and 3.8 lbs). The loading was applied parallel to the z axis that was oriented transverse to the airfoil. The loading was distributed to all free nodes such that the edge nodes were loaded by half of the load magnitude applied to interior nodes. Corner nodes were applied quarter of the magnitude compared to the interior node loads. For all four load amplitudes damage initiation occurs by transverse tensile fracture of ply 15 at node 46 that is the edge node immediately adjacent to the support along the longer edge of the airfoil. However, the number of cycles required for damage initiation depends on the load amplitude. For the 11.83 N load amplitude damage initiation occurred after 50 x 10^{10} cycles. When the load amplitude was increased to 13.52 N damage initiation required only 50 x 10^{4} cycles. For the load amplitude of 15.21 N damage initiation occurred within the first 50 cycles. For the highest load amplitude of 16.90 N damage initiation occurred immediately as the cyclic load was applied and it was followed by damage growth in the

longitudinal tensile fracture mode of ply 1 at node 46. For all four load amplitudes considered, structural fracture propagated due to the growth of initial ply damage to a through-the-thickness laminate fracture at node 46.

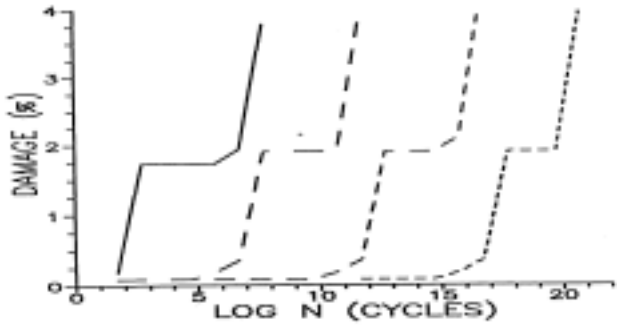

Figure 4-29. Damage Progression under Cyclic Loading AS-4/HMHS: 16 Plies [+45/0/90/-45/90/0]s, Loading frequency = 50 Hz Short dashed line: cyclic load amplitude = 11.83 N Medium dashed line: cyclic load amplitude = 13.52 N Long dashed line: cyclic load amplitude = 15.21 N Solid line: cyclic load amplitude = 16.90 N

Figure 4-29 indicates that for the first three lowest load amplitudes the composite structure endures a significant number of cycles after damage initiation without additional damage. On the other hand, for the highest load amplitude damage growth and accumulation immediately follow the damage initiation stage. The level of damage at the structural fracture stage is approximately independent of the load amplitude. Results also indicate that the logarithm of the number of cycles required for structural fracture varies approximately linearly with the pressure amplitude as shown in Figure 4-30.

Figure 4-31 shows the degradation of the first natural frequency as a function of the number of cycles of the fatigue loading. It is clear that the first damage growth stage affects the fundamental structural response significantly. On the other hand, the damage propagation stages immediately prior to structural fracture do not influence the first natural frequency as much. Figure 4-32 shows the second natural frequency that is somewhat more influenced by the ultimate damage propagation stage as well as by the damage growth stages compared to the first natural frequency. Figure 4-33 shows the variation of the third natural frequency with exposure to fatigue loading. Comparison of results depicted in Figures 4-31, 4-32, and 4-33 indicate that during the later stages of fatigue life higher frequency vibration modes are more sensitive to the evolution of composite damage compared to the lower frequency modes. Again, the main reason is that localization of damage that occurs prior to fracture has a greater influence on the high frequency vibration modes. Therefore, structural health monitoring based on response measurements should identify the appropriate high frequency vibration modes be tracked to assess impending structural fracture.

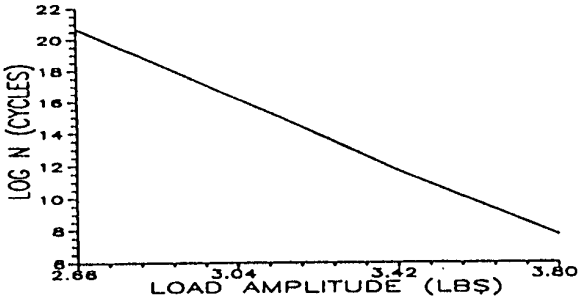

Figure 4-30. Number of Cycles to Fracture with Load Amplitude AS-4/HMHS: 16 Plies [+45/0/90/-45/90/0]s, Loading frequency = 50 Hz

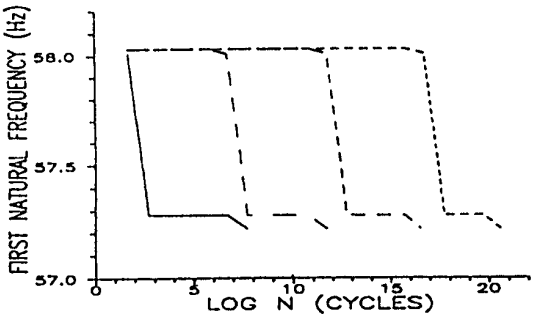

Figure 4-31. First Natural Frequency Degradation with Fatigue Loading AS-4/HMHS: 16 Plies [+45/0/90/ -45/90/0]s, Loading frequency = 50 Hz Short dashed line: cyclic load amplitude = 11.83 N Medium dashed line: cyclic load amplitude = 13.52 N Long dashed line: cyclic load amplitude = 15.21 N Solid line: cyclic load amplitude = 16.90 N

The simulation results for this composite airfoil subjected to harmonic cyclic loading, the simulation results may be summarized as follows:

1. Damage initiation by transverse tensile fractures of a -45 ply occurs at node 46 for all four pressure amplitudes considered.
2. The number of cycles endured prior to damage initiation depends on the cyclic load amplitude.
3. Damage stability after damage initiation also depends on the cyclic load amplitude.

For the airfoil specimen the amount of fundamental natural frequency reduction after damage initiation is independent of the cyclic load amplitude. The natural frequencies immediately prior to structural fracture are also independent of the load amplitude for the composite airfoil simulated.

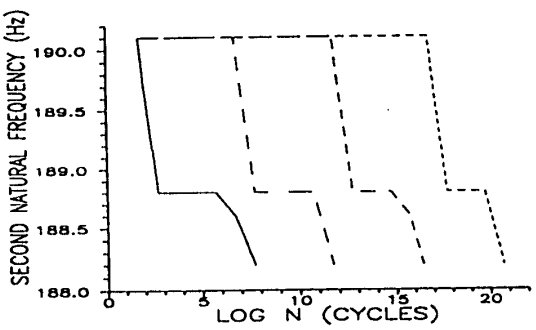

Figure 4-32. Second Natural Frequency Degradation with Fatigue Loading AS-4/HMHS: 16 Plies [+45/0/90/-45/90/0]s, Loading frequency = 50 Hz Short dashed line: cyclic load amplitude = 11.83 N Medium dashed line: cyclic load amplitude = 13.52 N Long dashed line: cyclic load amplitude = 15.21 N Solid line: cyclic load amplitude = 16.90 N

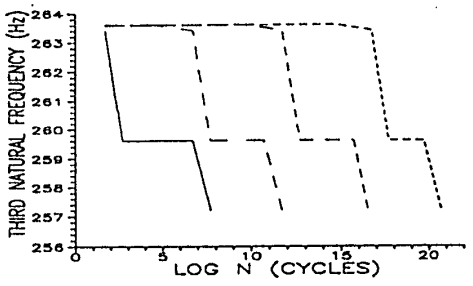

Figure 4-33. Third Natural Frequency Degradation with Fatigue Loading AS-4/HMHS: 16 Plies [+45/0/90/ mp-45/90/0]$_{s$, Loading frequency = 50 Hz Short dashed line: cyclic load amplitude = 11.83 N Medium dashed line: cyclic load amplitude = 13.52 N Long dashed line: cyclic load amplitude = 15.21 N Solid line: cyclic load amplitude = 16.90 N

4.3 CYCLIC LOADING OF BUILT-UP COMPOSITE STRUCTURE

Durability of a built up composite structure under cyclic fatigue is often quite different than that of a coupon level specimen. The main advantage of computational simulation is that structure level physical parameters are included in the analysis. Therefore, once the material properties and the degradation parameter are ascertained/calibrated with a coupon level specimen, the results can be applied to the simulation of structural components and built-up structures. Figure 4-34 shows the cross section and plan of a discontinuously stiffened composite panel that is made of the same materials and laminate structure as the simulated coupon level specimen. Figure 4-35 shows the finite element model for the stiffened panel with 626 nodes and 504 elements. The first three natural frequencies of the stiffened panel are computed by the finite element module as ω_1=181.3 Hz, ω_2=200.0 Hz, and ω_3=388.5 Hz. Alternating surface pressure loads are applied to the flat underside face of the finite element model.

A 23.29 kPa (3.378 psi) alternating surface pressure amplitude is applied at both 50 hz and 70 hz frequencies. An additional simulation is carried out at 50 hz with a pressure amplitude of 11.64 kPa (1.689 psi). Figure 4-36 shows the damage progression for the three cases simulated. Damage progression characteristics are similar for all the three cases. For the pressure amplitude of 23.29 kPa the 70 Hz loading frequency causes more internal damage in the composite structure compared to that caused by the 50 Hz loading frequency. Nevertheless, the number of cycles required for damage initiation and for structural fracture are not affected by the change in the frequency of excitation. However, the number of cycles required for damage initiation and for structural fracture depend on the load amplitude.

Damage initiation occurs by transverse tensile fracture of the 0 degree outer surface ply of the stiffener web at the joint with the stiffener flange and the skin. Damage initiation occurs approximately at the center of the stiffened panel. Initial damage remains stable for a considerable number of cycles then it progresses and spreads up into the web of the stiffener, moving toward the line of symmetry from the center of the finite element model. A second stage of damage stability is followed by the transverse tensile failures progressing to the cap of the stiffener. Followed by damage growth by the in-plane shear failures of the 45-degree plies and the longitudinal tensile failures of the 90 degree plies in the web of the stiffener. Structural fracture occurs due to a laminate fracture in the web of the stiffener.

Figure 4-37 shows the degradation of the first natural frequency as a function of the number of cycles endured. The degradations of the second and third natural frequencies are also very similar. The damage initiation and progression stages do not affect the fundamental structural response significantly. Only when the ultimate structural fracture stage is entered due to a stiffener web laminate fracture the natural frequency of the specimen is reduced. At the ultimate structural fracture stage the degradation of structural response is very sudden and consistent with a brittle fracture mode. None of the three cases simulated shows additional number of cycles endured after the degradation of structural response. Therefore, for this composite structure there will be no warning signs in the form of response degradation as a warning prior to fracture.

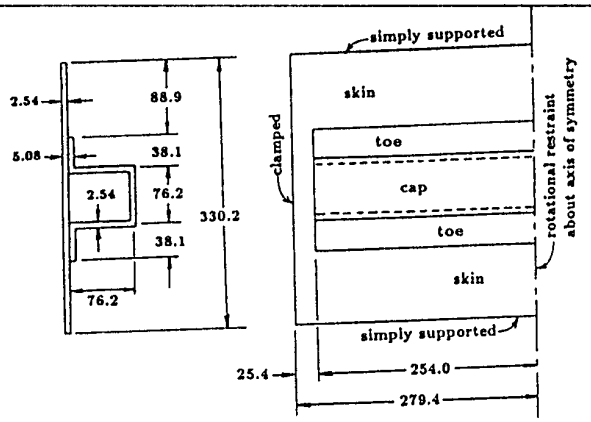

Figure 4-34. Stiffened Composite Panel Cross-section and Plan AS-4/HMHS: 16 Plies [0/45/90]s2 (all dimensions are in mm)

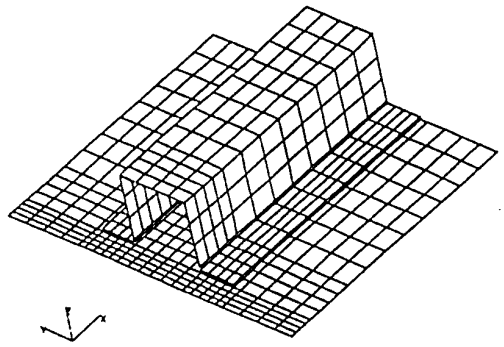

Figure 4-35. Stiffened Composite Panel Finite Element Model AS-4/HMHS: 16 Plies [0/45/90]s2

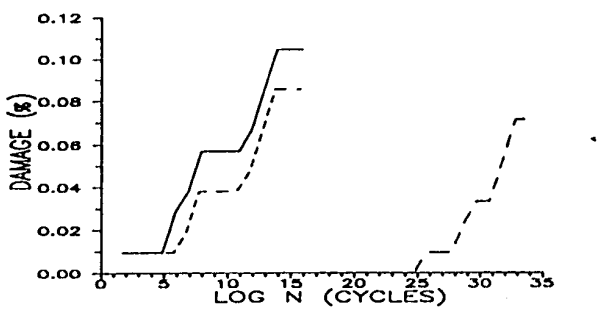

Figure 4-36. Stiffened Composite Panel Damage Progression under Cyclic Loading, AS-4/HMHS: 16 Plies [0/45/90]s2 Long dashed line: cyclic pressure amplitude of 11.64 kPa at 50 Hz Short dashed line: cyclic pressure amplitude of 23.29 kPa at 50 Hz Solid line: cyclic pressure amplitude of 23.29 kPa at 70 Hz

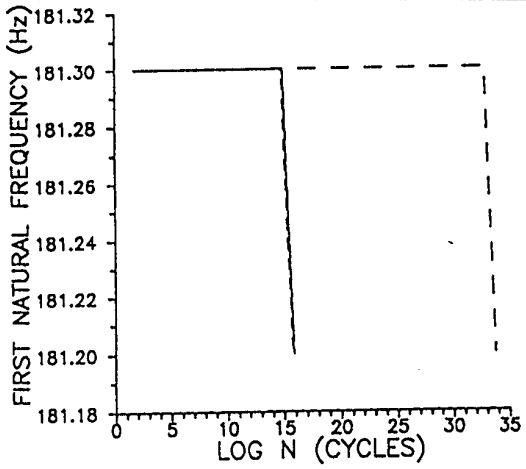

Figure 4-37. Stiffened Composite Panel First Natural Frequency Degradation with Fatigue Loading AS-4/HMHS: 16 Plies [0/45/90]s2 Long dashed line: cyclic pressure amplitude of 11.64 kPa at 50 Hz Short dashed line: cyclic pressure amplitude of 23.29 kPa at 50 Hz Solid line: cyclic pressure amplitude of 23.29 kPa at 70 Hz

4.3.1 Summary Of Results

A summary of insights gained by the development of the present simulation methodology as applicable to graphite/epoxy laminated composite structures is as follows:

1. Damage initiation by transverse tensile fractures of the surface plies occurred for all cases considered.

2. For the coupon level simulation, damage progression with the number of cycles endured was not sensitive to the changes in the cyclic load frequency. Also at the coupon level the damage progression characteristics were not significantly different for the considered pressure amplitudes.

3. The amount of fundamental natural frequency reduction during damage initiation and progression was negligible for all cases, including coupon level and structural level simulations.

4. For the structure level simulation the cyclic load amplitude was the most significant parameter affecting fatigue life.

5. For all cases simulated ultimate structural fracture was immediately preceeded by ply longitudinal tensile failures that initiated the laminate fracture.

6. Damage initiation by transverse tensile fractures of the blade stiffener edge plies occurred for all cases considered.

7. In general, ultimate structural fracture was immediately preceeded by ply longitudinal tensile failures that initiated the laminate fracture.

4.3.2 Generalization Of Procedure

The present computational simulation method is suitable for the design and continued in-service evaluation of composite structures subjected to cyclic loading. Composite structures with different constituents and ply layups can be evaluated under cyclic pressures and base excitation. The cyclic load amplitude may be varied during the simulated fatigue life. Static and dynamic load combinations may also be applied in addition to cyclic loading. Structural health monitoring is based on damage tolerance requirements defined via the computational simulation method. A cyclic fatigue damage tolerance parameter is described as the state of damage after the application of a given number of loading cycles, normalized with respect to the damage state corresponding to ultimate fracture. Identification of damage progression mechanisms and the sequence of progressive fracture modes convey useful information to evaluate structural safety. Computational simulation results can be formulated for health monitoring criteria, increasing the reliability of composite structures. The simulated failure modes and the type of failure provide the necessary quantitative and qualitative information to design an effective health monitoring system. Computed local damage energy release rates are correlated with the magnitudes of acoustic emission signals and other damage monitoring means such as piezoelectric stress sensors and strain gages that are an integral part of a composite structure. Fiber optics data networks embedded in the composite structure can be used to transmit detected local damage information to an expert system that provides feedback and reduces power to delay failure.

The basic procedure is to simulate a computational model of the composite structure subjected to the expected loading environments. Various fabrication defects and accidental damage may be represented at the ply and constituent levels, as well as at the laminate level. Computational simulation may be used to address various design and health monitoring questions as follows:

Evaluation of damage tolerance: Computational simulation will predict the damage that would be caused due to cyclic fatigue damage or overloading of a structure. Also, a fabrication defect or accidental damage produced by inadvertent loading that is not an expected service load can be included in the initial computational model. Once the composite damage is defined, damage tolerance can be evaluated by monitoring damage growth and progression from the damaged state to ultimate fracture. Significant parameters that quantify damage stability and fracture progression characteristics are the rate of damage increase with incremental loading, and the changes in the structural response characteristics with loading. Identification of damage initiation/progression mechanisms and the sequence of progressive fracture modes convey serviceable information to help with critical decisions in the structural design and health monitoring process. Determination of design allowables based on damage tolerance requirements is an inherent use of the computational simulation results. Simulation of progressive fracture from defects allows setting of quality acceptance criteria for composite structures as appropriate for each functional requirement. Detailed information on specific damage tolerance characteristics help establish criteria for the retirement of a composite structure from service for due cause.

Determination of sensitive parameters affecting structural fracture: Computational simulation indicates the damage initiation, growth, and progression modes in terms of a damage index that is printed out for the degraded plies at each damaged node. In turn, the damage index points out the fundamental physical parameters that characterize the composite degradation. For instance, if the damage index shows ply transverse tensile failure, the fundamental physical parameters are matrix tensile strength, fiber volume ratio, matrix modulus, and fiber transverse modulus; of which the most significant parameter is the matrix tensile strength (Murthy and Chamis, 1986). In addition to the significant parameters pointed out by the ply damage index, sensitivity to hygrothermal parameters may be obtained by simulating the composite structure at different temperatures and moisture contents. Similarly, sensitivity to residual stresses may be assessed by simulating the composite structure fabricated at different cure temperatures. Identification of the important parameters that significantly affect structural performance for each design case allows optimization of the composite for best structural performance. Sensitive parameters may be constituent strength, stiffness, laminate configuration, fabrication process, and environmental factors.

Interpretation of experimental results for design decisions: Computational simulation allows interactive experimental-numerical assessment of composite structural performance. Simulation can be used prior to testing to identify locations and modes of composite damage that need be monitored by proper instrumentation and inspection of the composite structure. Interpretation of experimental data can be significantly facilitated by detailed information from computational simulation. Subscale experimental results may be extended to full prototype structures without concern for scale effects since computational simulation does not presume any global parameters but is based on constituent level damage tracking.

4.3.3 Conclusions

On the basis of the results obtained from the investigated composite plate and stiffened panel examples and from the general perspective of the available computational simulation method, the following conclusions are drawn:

1. Computational simulation can be used to track the details of damage initiation, growth, and subsequent propagation to fracture for composite structures subjected to cyclic fatigue.

2. For the considered composite structure, structural response characteristics are not affected by the initiation and progression of composite damage due to cyclic fatigue.

3. Computational simulation, with the use of established composite mechanics and finite element modules, can be used to predict the influence of composite geometry as well as loading and material properties on the durability of composite structures.

4. The demonstrated procedure is flexible and applicable to all types of constituent materials, structural geometry, and loading. Hybrid composites and homogeneous materials, as well as laminated, stitched, woven, and braided composites can be simulated.

5. A new general methodology has been demonstrated to investigate damage propagation and progressive fracture of composite structures due to cyclic fatigue.

4.4 REFERENCES

1. Chamis, C. C., and Ginty, C. A. (1987)``Fiber Composite Structural Durability and Damage Tolerance: Simplified Predictive Methods," NASA TM-100179.

2. Chamis, C. C., Murthy, P. L. N., and Minnetyan, L. (1996)``Progressive Fracture of Polymer Matrix Composite Structures," Theoretical and Applied Fracture Mechanics, Vol. 25, 1996, pp. 1-15.

3. Chamis, C. C., and Sinclair, J. H. (1982) Durability/Life of Fiber Composites in Hygrothermomechanical Environments, Composite Materials, Testing and Design, I. M. Daniel, Ed., ASTM STP-787, ASTM, Philadelphia, pp. 498-512.

4. Gotsis, P. K., Chamis, C. C., and Minnetyan, L. (1997)``Prediction of Composite Laminate Fracture: Micromechanics and Progressive Fracture," Composites Science and Technology, Vol. 57.

5. Minnetyan, L., and Chamis, C. C. (1997) ``Progressive Fracture of Composite Cylindrical Shells Subjected to External Pressure," ASTM Journal of Composite Technology and Research, Vol. 19, No. 2, pp. 65-71.

6. Minnetyan L., Chamis C. C., and Murthy P. L. N. (1992-2) ``Structural Behavior of Composites with Progressive Fracture," Journal of Reinforced Plastics and Composites, Vol. 11, No. 4, pp. 413-442.

7. Minnetyan, L., Chamis, C. C., and Murthy, P. L. N. (1992-3) ``Structural Durability of a Composite Pressure Vessel," Journal of Reinforced Plastics and Composites, Vol. 11, No. 11, pp. 1251-1269.

8. Minnetyan L., Murthy P. L. N., and Chamis C. C. (1990) ``Composite Structure Global Fracture Toughness via Computational Simulation," Computers & Structures, Vol. 37, No. 2, pp.175-180.

9. Minnetyan L., Murthy P. L. N., and Chamis C. C. (1992-1)``Progressive Fracture in Composites Subjected to Hygrothermal Environment," International Journal of Damage Mechanics, Vol. 1, No. 1, pp. 60-79.

10. Minnetyan, L., Rivers, J. M., Chamis, C. C., and Murthy, P. L. N. (1995) ``Discontinuously Stiffened Composite Panel under Compressive Loading," Journal of Reinforced Plastics and Composites, Vol. 14, No. 1, pp. 85-98.

11. Murthy P.L.N. and Chamis C.C. (1986) Integrated Composite Analyzer (ICAN): Users and Programmers Manual, NASA Technical Paper 2515.

12. Murthy P.L.N., Ginty, C.A., and Sanfeliz, J.G. (1993) Second Generation Integrated Composite Analyzer (ICAN) Computer Code, NASA Technical Paper 3290.

13. Nakazawa S., Dias J.B., and Spiegel M.S. (1987) MHOST Users' Manual, Prepared for NASA Lewis Research Center by MARC Analysis Research Corp.

APPENDIX For Chapter 4.0

Table I: AS-4 Fiber Properties:

Number of fibers per end = 10000
Fiber diameter = 0.00762 mm (0.300E-3 in)
Fiber Density = 4.04E-7 Kg/m^3 (0.063 lb/in^3)
Longitudinal normal modulus = 200 GPa (29.0E+6 psi)
Transverse normal modulus = 13.7 GPa (1.99E+6 psi)
Poisson's ratio (ν_{12}) = 0.20
Poisson's ratio (ν_{23}) = 0.25
Shear modulus (G_{12}) = 13.8 GPa (2.00E+6 psi)
Shear modulus (G_{23}) = 6.90 GPa (1.00E+6 psi)
Longitudinal thermal expansion coefficient = -1.0E-6/°C (-0.55E-6/°F)
Transverse thermal expansion coefficient = 1.0E-5/°C (0.56E-5/°F)
Longitudinal heat conductivity = 301 kJ-m/hr/m^2/°C (4.03 BTU-in/hr/in^2/°F)
Transverse heat conductivity = 30.1 kJ-m/hr/m^2/°C (.403 BTU-in/hr/in^2/°F)
Heat capacity = 0.712 kJ/kg/°C (0.17 BTU/lb/°F)
Tensile strength = 3.09 GPa (448 ksi)
Compressive strength = 3.09 GPa (448 ksi)

Table II: HMHS Matrix Properties:

Matrix density = 3.40E-7 Kg/m^3 (0.0457 lb/in^3)
Normal modulus = 4.14 GPa (600 ksi)
Poisson's ratio = 0.34
Coefficient of thermal expansion = 0.72E-4/°C (0.40E-4/°F)
Heat conductivity = 0.648 kJ-m/hr/m^2/°C (0.868E-2 BTU-in/hr/in^2/°F)
Heat capacity = 1.047 KJ/Kg/°C (0.25 BTU/lb/°F)
Tensile strength = 71.0 MPa (10.3 ksi)
Compressive strength = 423 MPa (61.3 ksi)
Shear strength = 161 MPa (23.4 ksi)
Allowable tensile strain = 0.02
Allowable compressive strain = 0.05
Allowable shear strain = 0.04
Allowable torsional strain = 0.04
Void conductivity = 16.8 J-m/hr/m^2/°C (0.225 BTU-in/hr/in^2/°F)
Glass transition temperature = 216 °C (420 °F)

Table III: Composite Ply Properties; 60.0/ 40.0 AS-4/HMHS

Longitudinal modulus = 120.4 GPa (0.1746E+08 psi)
Transverse modulus = 8.963 GPa (0.1300E+07 psi)
Shear modulus G_{12} = 4.892 GPa (0.7095E+06 psi)
Shear modulus G_{23} = 2.864 GPa (0.4154E+06 psi)
Poisson's ratio ν_{12} = 0.2568E+00

Poisson's ratio ν_{23} = 0.4037E+00
Therm. exp. coef. α_{11} = -0.5243E-7/°C (-0.2913E-07/°F)
Therm. exp. coef. α_{22} = 0.3497E-04/°C (0.1943E-04/°F)
Density = 4.09E-7 Kg/m^3 (0.05507 lbs/in^3)
Heat capacity = 820 J/Kg/°C (0.1956E+00 BTU/lb/°F)
Longitudinal heat conductivity, κ_{11} = 181 kJ-m/hr/m^2/°C (2.421 BTU-in/hr/in^2/°F)
Transverse heat conductivity, κ_{22} = 2.241 kJ-m/hr/m^2/°C (0.030 BTU-in/hr/in^2/°F)
Longitudinal tensile strength = 1.835 GPa (0.2661E+06 psi)
Longitudinal compressive strength = 1.266 GPa (0.1836E+06 psi)
Transverse tensile strength = 51.3 MPa (0.7430E+04 psi)
Transverse compressive strength = 304.9 MPa (0.4422E+05 psi)
In-plane shear strength σ_{12} = 112.0 MPa (0.1624E+05 psi)
Out-of-plane shear strength σ_{23} = 98.8 MPa (0.1433E+05 psi)

Table IV: Through the Thickness Laminate Properties

Laminate thickness = 2.54 mm (0.100 in)
Elastic modulus E_{xx} or E_{yy} = 47.1 GPa (0.6832E+07 psi)
Elastic modulus E_{zz} = 10.34 GPa (0.1499E+07 psi)
Shear modulus G_{xy} = 18.12 GPa (0.2628E+07 psi)
Shear modulus G_{xz} or G_{yz} = 3.878 GPa (0.5624E+06 psi)
Poisson's ratio ν_{xy} = 0.300
Thermal exp. coeff. α = 0.2893E-05/°C (0.1607E-05/°F)

5.0 Simulating Manufacturing Process of Composite Textile Preform Reshaping

5.1 INTRODUCTION

A novel cost effective approach is being explored by GE, for reducing fiber preform processing costs by reshaping a simple, commercially available, low cost, cylindrical, tubular braided textile fiber preform. An important aspect of this approach is the use of GENOA software to predict changes in local fiber orientation, fiber volume fraction, and the extent to which a textile tube might be reshaped without fiber lock-up.

Since the reshaping operation can significantly change fiber orientations, it becomes critical to evaluate the extent of this change, its effect on composite performance, and the extent to which the changes can be negated by adjusting the braid angles of the tubular textile preform. In implementing the proposed reshaping process costly and time consuming trial and error experimental evaluations can be avoided by use of the GENOA computational simulation tool. This software allows attainment of the best preform net fit to a desired shape without occurrences of buckling and fiber wrinkling/crimping by: 1) an iterative FEM analysis utilizing resin matrix composite micromechanics; 2) prediction of the effects of changes of braid/weave angle on resin matrix composite micromechanical properties; and 3) use of an iterative contact algorithm for analysis of sock conformance to a shaped tool. The proposed simulation tool has been developed by AlphaSTAR in support of NASA funded AST GE project and verified against experimental results of GE tests of reshaping preforms for conical bent and elliptical components.

The proposed process of generating shaped fiber preforms for composites involves three steps: 1) braiding a simple, commingled fiber tubular preform, 2) reshaping the preform over a mandrel of a desired shape (Figure 5-1), and 3) processing (heating) the reshaped preform to flow the resin matrix material around the high strength fibers.

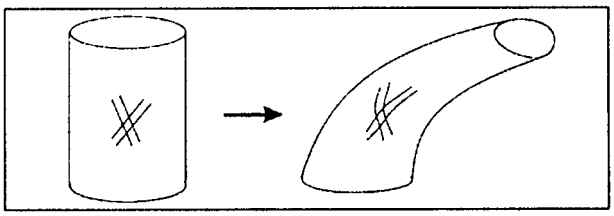

Figure 5-1. Initial and Reshaped Textile Preform

5.1.1 State of Software Simulation

During the design stage it is highly desirable to simulate the mechanical behavior of a proposed composite structure in order to facilitate design optimization and cost reduction. These simulations can be cost effectively accomplished with GENOA, a computer code written specifically for this purpose. However, its use requires an accurate description of the structural material involved. In the case of a reshaped tubular textile preform, the determination of angular relationships of the fibers (or tows) is needed to describe the reshaped geometry. Currently, reshaped preforms have to be empirically evaluated in order to assess fiber orientation angles. This makes rendering a shape-optimization process difficult, time consuming, and very costly. A computational solution rather than empirical means of evaluation is needed such as can be achieved with GENOA.

The GENOA code has provided the needed capabilities for the fiber preform reshaping process used in large, complex, PMC components (e.g, GE90 Turbine blade) made with ply drop-offs to accommodate aero-elastic tailoring, Figure 5-2 (a-d) by: 1) simulating use of multiple reshaped preforms of different sizes with commingled fibers, 2) simulating ply drop-offs, 3) supporting aero-elastic tailoring, and 4) transferring of fiber orientation data directly to design and manufacturing process software. The proposed effort will benefit significantly from the verified GENOA software previously developed to simulate reshaping of tubular fiber textile preforms in a cooperative exploratory effort with GE.

5.0 Simulating Manufacturing Process of Composite Textile Preform Reshaping

Tubular fiber textile preforms can be prepared using a variety of fabric configurations as shown in Figure 5-3. The proposed effort will be directed to simulate braided preforms recognizing that adaptation to any fabric configuration (woven or stitched) is readily feasible. Under a pending patent GENOA can simulate 2D/3D braided/ woven/stitched composite such as satin weaves of Figure 5-4 (or any type of woven textile fabric).

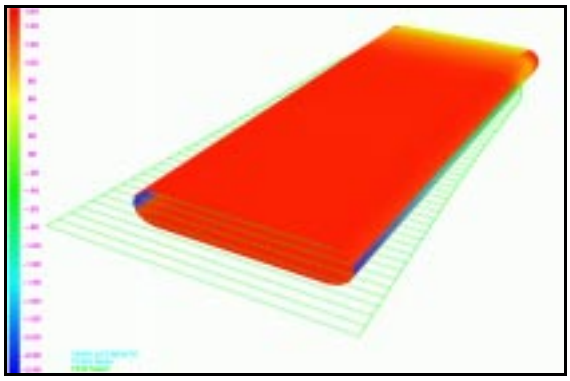

Figure 5-2(a) Step 1: As received Preform Sock of ±45 orientation to be fitted on a flat mandrel

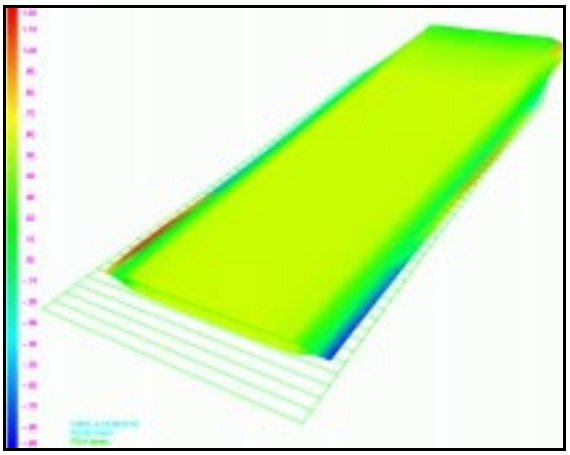

Figure 5-2 (b) Step 2 : Preform Sock of ±45 Orientation Fitted On A Flat Mandrel

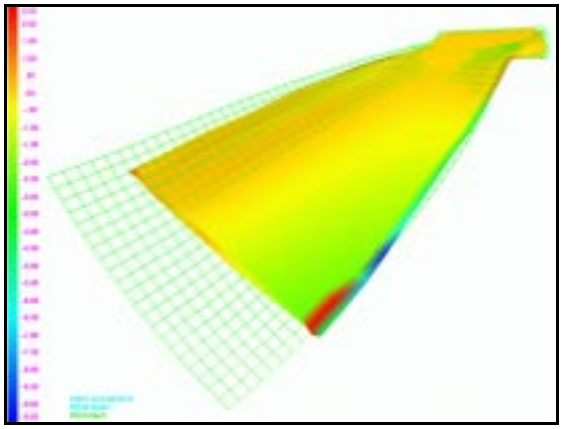

Figure 5-2 (c) Step 3: Preliminary fit of Step 2 Achieved Orientation To Be Fitted On A Curved Mandrel

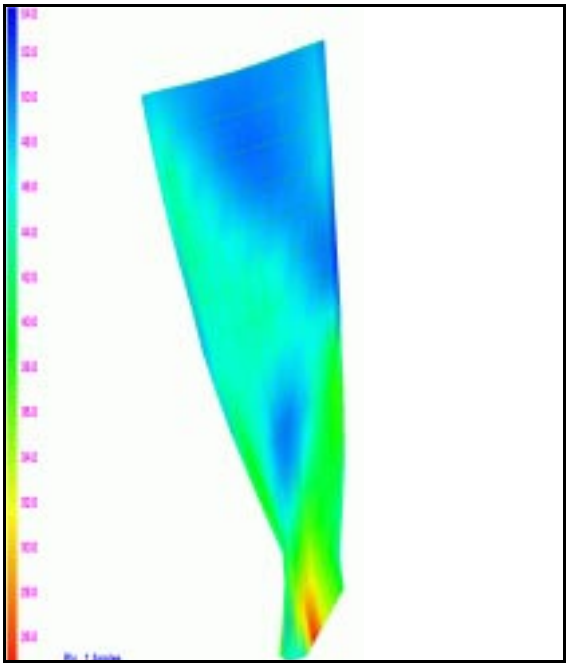

Figure 5-2(d) Step 4:Best Fit Orientation Was Achieved And Fitted On A BoeingGE90 Mandrel

5.0 Simulating Manufacturing Process of Composite Textile Preform Reshaping

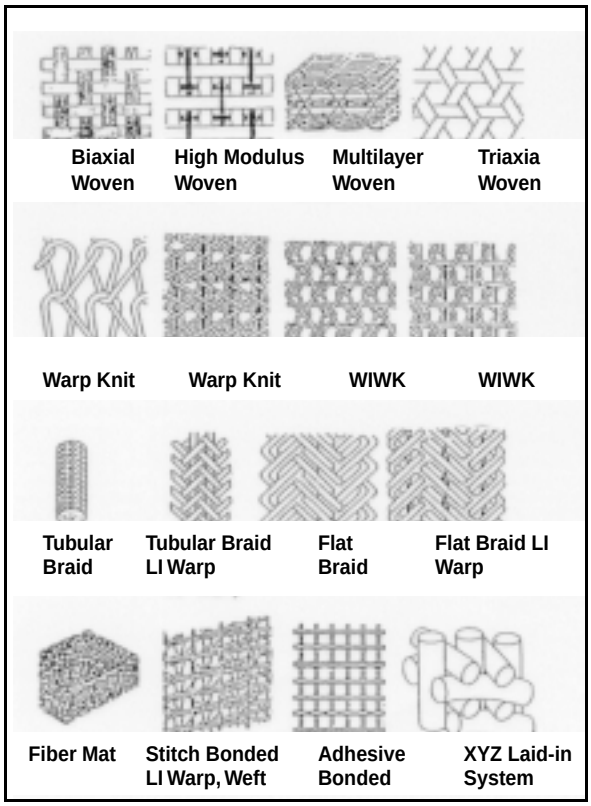

Figure 5-3. Variety of Fabric Structure Such as Woven, Knitted, Braided, & Non-woven Will be Considered for Best Trade Selection

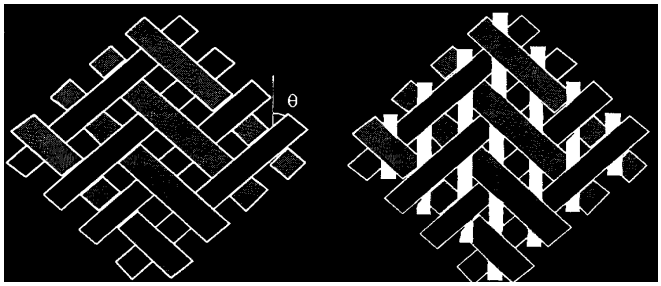

Figure 5-4. Current Weave Status of GENOA to Simulate 2D/3D Braided Fiber Architecture to Perform Ply Drop-offs

Aspects of fiber architecture that GENOA can simulate are: 1) waviness based on wave length, wave amplitude, and fiber/matrix stiffness; 2) tow pinching by using different zonal specifications at pinched tow locations; 3) fiber curvature at cross over locations; 4) float length dependent shear strength in satin weave preforms 5) fiber volume fraction, 6) uneven spreading of compression tows especially when draped over double axis surfaces, and 7) all types of irregularities.

5.1.2 State of Software Development and Concept Verifications

Figures 5-5 through 5-8 shows the current capability of the GENOA software to conform a preform sock FEM model to a FEM model of a bent and tapered circular mandrel. The degree of conformance is indicated by the color coding. Dark blue shows negative distance meaning preform (sock) FEM is has entered the mandrel FEM. Figure 5-6 shows the simulation of a tubular sock preform expanding to conform to an exterior conical die. Figure 5-7 shows the fiber angles after final reshaping of the preform. The fiber orientation angles, presented in a color coded format, range from 44 to 57 degrees with the majority being within 44 to 46 degrees

Based on experience with the prototype code and empirical GE data, the following enhancements of GENOA have been made and are discussed in the following paragraphs.

Mesh-Fitting Algorithm Improved. This improvement was accomplished by: 1) dividing mandrel mesh into slices normal to the center line for easy straightening and progressive bending of the mandrel; or 2).defining the mandrel mesh by sections, with either the same number of nodes for each section or an index to the number of nodes for each sections. The step remaining is to define the type of finite element meshes to be used for describing the mandrel and adapting the mesh-fitting algorithm to take these external meshes into account

Boundary Conditions Established for the Base. The first step of the mesh-fitting process is generally to merge the bases of the tubular sock and the mandrel by imposing displacements on the sock. Unfortunately imposed displacements do not allow for the redistribution of the stresses in the structure, sometimes giving incorrect results. This may induce parasite effects in a non-cylindrical mandrel. Less constrained boundary conditions need to be applied, depending on the shape of the mandrel. This effect explains the scatter between experimental data and simulations in the elliptical cases. In the case of the bent elliptical cylinder, the boundary conditions of the base were ill adjusted for the merging of the sock and the tooling bases creating parasitic stresses that caused incorrect angle computations.

Jamming Angle Computation Introduced. The jamming is a result of the scissoring action illustrated in Figure 5-8. Jamming angles are currently not taken into account. The GENOA micro-mechanics code was enhanced by incorporating GE's empirical equation for estimating jamming angles in order to evaluate if a particular braid can be used to manufacture a specific component. GE's jamming equation expresses the braid angle as a function of braid diameter in the jammed state, the number of carrier yarns, the width of the fiber yarn, and a compaction factor.

Algorithm to Calculate Forces Applied to Reshape a Sock- Computing the reaction forces on the base gives a loading level on a structure. Load vs. time profiles can be obtained for use by manufacturing in reshaping tubular preforms. This approach has been proven accurate by simulation results that are in good accord with the experimental results.

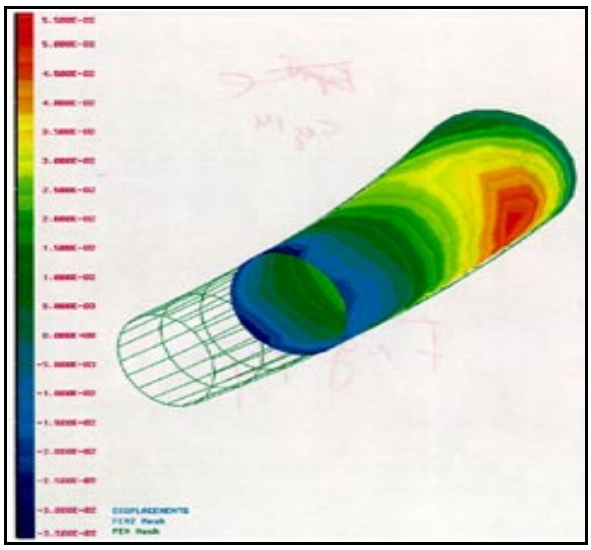

Figure 5-5. The simulated state conformance of a preform FEM to a interior of a bent mandrel

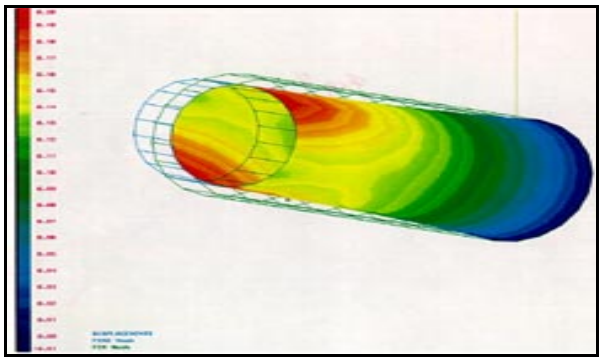

Figure 5-6. The Simulated State Of Conformance Of A Sock FEM to a Exterior of a Mandrel

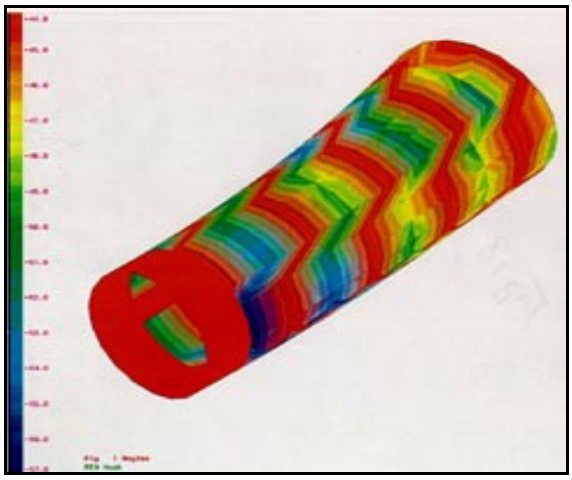

Figure 5-7. Simulated Fiber Orientation Angles in Ply No. 1 After Reshaping

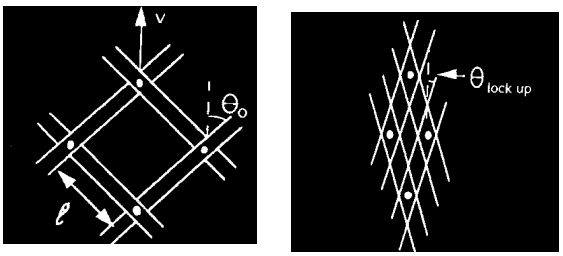

Figure 5-8. GENOA Current Status to Simulate 2D/3D Braided Fiber Architecture

5.2 TECHNICAL APPROACH

In order to predict the fiber configuration of a reshaped preform, the whole reshaping process from the original shape of the braided fiber preform to the final configuration must be simulated. Woven/braided fiber preforms are modeled as composites with very soft-matrices. For these tubular fiber preforms GENOA can evaluate changes in fiber orientations and dynamically change boundary conditions as a tubular fiber preform conformed to a tool.

A typical preform shaping computational cycle is defined in Figure 5-9 [7]. The current geometry is compared to the shape of the mandrel and imposed loads or displacements are computed to conform the preform to a tool shape. Next, the mechanical properties at the mesh nodes are determined by the composite mechanics module starting with the ply properties (based on an elastic constitutive law). The laminate properties are then determined. Displacement analysis under a load increment is made by the finite

element module. Using the computed deformation of the structure, a new fiber orientation FEM mesh is established.

Application of Loads to Reshape Preforms. The mesh fitting algorithm either use loads in order to push the sock towards the mandrel (Figure 5-10), or to pull the sock to stretch it around the mandrel (Figure 5-11).

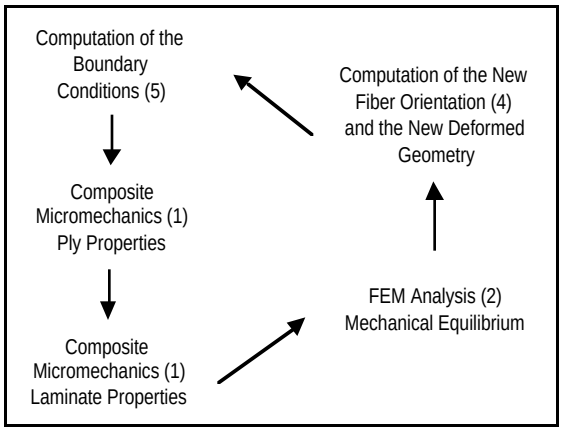

Figure 5-9. Computational Simulation Cycle

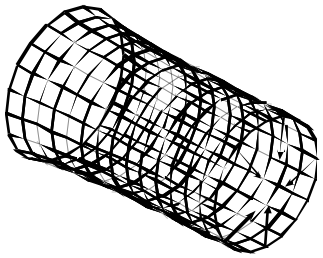

Figure 5-10. Pushing Loads

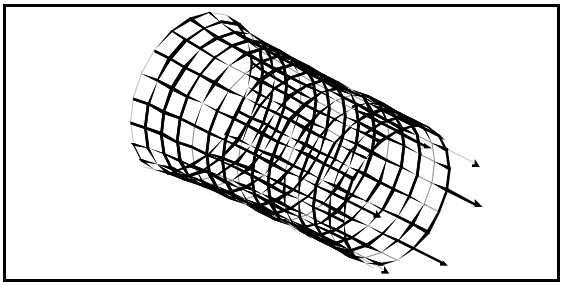

Figure 5-11. Tensile Pulling Loads

Reshaping by Pressure Loading. The process of reshaping a textile fiber preform is simulated using finite element models of a tubular textile preform and the shaped die or mandrel tool to which it is to be fit. The simulation of the reshaping process is accomplished by evaluation of incremental changes of fiber orientations in a preform. Pushing loads are computed normal to the tubular sock preform in the direction of the mandrel.

Reshaping by Applying Tension Loading. The tensile pulling loads are imposed at an absolute level. They can be either in a direction in the global system or in the direction of the sock.

A tubular preform loaded under tension at one end is shown in Figures 5-11. A decrease in a fiber angle upon an incremental increase in loading will result in increased stiffness of the composite at that location. Preform elongation will tend toward a limit controlled by the essentially fixed lengths of the fibers. The necessity of fiber angle adjustment is shown by comparison of the curves in Figure 5-12. The nonlinearity of the curve generated without angle adjustment is due to the large effect of fiber displacement and the updated Lagrangian scheme used in GENOA.

Globally, large strains are governed by the preform Poisson ratio. This ratio is computed very accurately by the composite mechanics module, based on a small strain code, whose validity can be

extended to large strains using the updated Lagrangian scheme for preforms approximated as very soft matrix fiber reinforced composites. As shown in Figure 5-13, changes in the Poisson ratio of a preform in tension become increasingly large for incremental changes in length at high elongations. This necessitates reducing the size of a load increment during a simulation as the preform elongation increases.

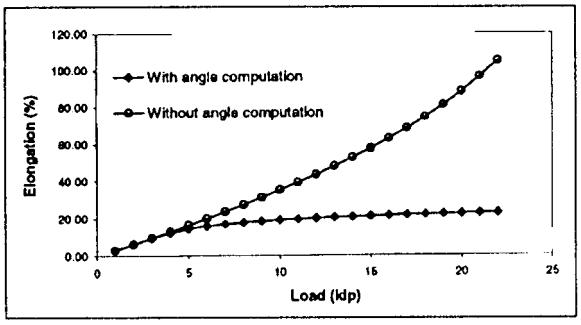

Figure 5-12. Elongation vs. Load With & Without Angle Computation

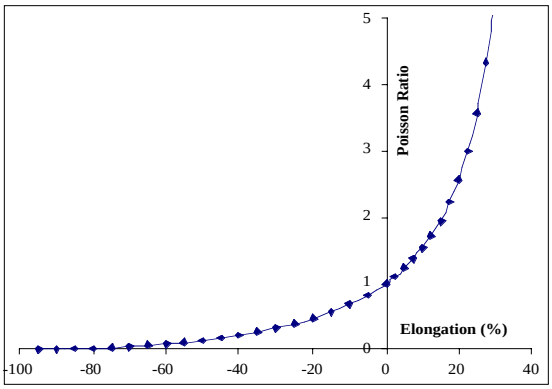

Figure 5-13. Poisson's Ratio at Different Elongations For A Rectangular Plane Panel

Fiber Angle Computation Assumptions. Mechanical properties of a fiber textile are assumed to remain constant during small incremental fiber angle changes permitting uncoupling fiber orientation changes, mechanical property calculations and finite element solutions in the computation cycle further assuming that:

1. Fibers in a textile preform are symmetrically placed with respect to a coordinate axis system.

2. Fiber elongation is negligible because of high stiffness

Computing the Change of Fiber Orientation. The configuration of the fibers in a preform is initially subjected to small loads directed to make the preform conform to the shape of a mandrel or die. The simulation is conducted with very small load increments during which the properties of the preform are assumed constant since the changes in the fiber orientations will be small. After each load increment, the computed strain is used to determine new orientations of braid fibers.

A FEM mesh is generated based on the symmetry of the fiber orientation. After each load increment, strains are recomputed. as total strains; i.e., summations of the strain increments of the incremental steps. Using previous values, new fiber orientations are computed at each node. A new input file is then generated to provide the new orientations for the next load increment calculations.

Boundary Conditions. Two methods are available to describe contact conditions. The first method defines an explicit contact condition. When a finite element node of a braided preform comes in contact with a tooling surface, a displacement boundary condition is applied to the node such that it stays on the tooling surface. The boundary condition is represented by a roller support that disables the displacement of the node in a direction normal to the tooling surface as shown in Figure 5-14. The contacting node remains free to move in any direction tangential to the mandrel surface but is constrained not to leave it. The complexity of this imposed displacement constraint depends on the shape of the tooling. The more complex the surface, the more difficult it will be to program, and the more non-linear the resulting resolution.

The second method is to impose a boundary condition based on a load condition (Figure 5-15). A load is exerted on a node depending on its distance from the tooling surface. This load must allow the finite element mesh to come near the tooling surface but should not be sufficient to allow the nodes to enter the mandrel.

This second solution is easier to program, because the only computational requirement is a distance between a point and a surface (represented by a repulsive load) and a normal vector to this surface (the direction of the repulsive load).

Contact Algorithm for the sock and the mandrel. The distance between sock points and the tooling can be found by averaging the surface normals of the sock element group that the sock point is a member of to get the true surface normal which can then be used to contact each element of the tooling surface within an error band (Figure 5-16). Near the beginning stage of conformance the distance of sock to tool is shown in Figure 5-16 by color coding. The closest contact point might thus be inside the tooling to the slight extent allowed by the error band (Figure 5-17).

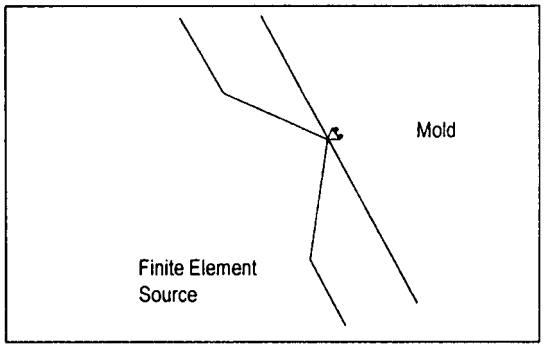

Figure 5-14. Contact Condition

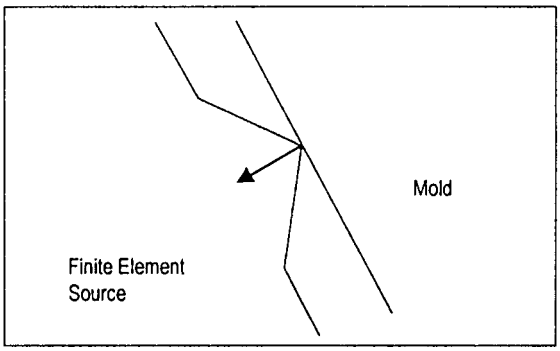

Figure 5-15. Load Condition

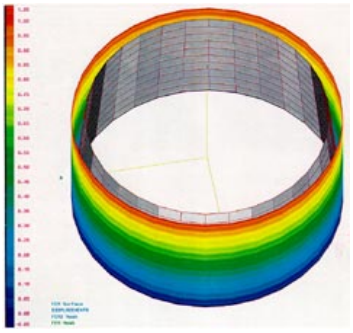

Figure 5-16. Example of FEM Model of Sock FEM Model Conforming to Mandrel (Grey) FEM Model

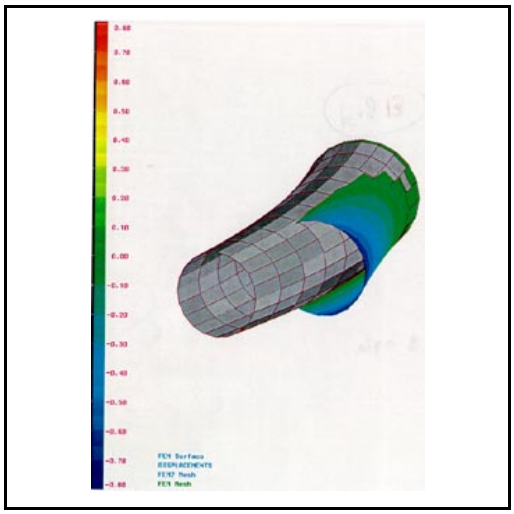

Figure 5-17. Example of FEM Model of Sock Entering FEM Model of Mandrel (Grey) Because of the Lack of a Sufficient Preventive Scheme.

5.0 Simulating Manufacturing Process of Composite Textile Preform Reshaping

Assumptions. A tooling surface can be represented by four sided QUAD elements. The four nodes of the elements are sequenced in the element definition in a counter clockwise direction looking from the positive side of the surface. The element density is high enough to allow the element surfaces to be approximated as a planar surface. The sock is the secondary surface and is defined with the same constraints as the tooling surface. Both surfaces are similar in size and shape (Figure 5-18).

Method. For each element on the tooling and sock surfaces, the surface normal is calculated by taking the cross-product of the diagonal vectors. The vector from node 1 to node 3 is crossed into the vector from Node 2 to node 4. The cross-product vector is then normalized.

Mesh Fitting Strategies. A convenient way to fit a preform FEM mesh to a tool is to first merge it with the base of the tool to give the numerical simulation stability. The preform mesh is then pushed towards the tooling surface using the boundary conditions previously described. This procedure works very well for a cone shaped tool where displacement with free movement in the tangent plane from normal or tensile loads gives the exact same results.

During the physical fitting of the tubular sock preform to a tool, buckling of the fibers may occur. In numerical simulation this can result in instabilities in the computer code. The effect of buckling can be considered for the bent cone example of Figure 5-18.

Automation Process. An automated process to reshape preform must employ a method to push the sock towards the tooling surface without having the bucking occurring and taking into account the following:

Fitting of straight mandrels is very easy and the process is very stable, whether displacements or loads are used.

Severe buckling occurs when the mandrel is bent for more than a few degrees,

When the sock and the tooling surface are distant, extensive user intervention is now required to supervise the mesh-fitting process.

The simulation of a simple automation process starts with a strait mandrel and we bent it progressively using small enough steps to maintain stability. Therefore, no user intervention is required (apart from fixing the step-sizes). The boundary conditions between two steps are equivalent, whether normal loads or normal displacements are used. This process has been evaluated using experimental results provided by GE.

Comparison Between Simulations And Experiments. Favorable comparisons of GENOA simulation results with General Electric experimental results on seven fiber preform reshaping tests (Figure 5-19) have strongly encouraged GE to pursue further development of the proposed preform reshaping technology as a promising cost effective fabrication method for complex PMC components.

Durability Analysis of Manufactured Tube. A typical manufacturing case has been simulated (Figure 5-19). A straight fiber weave cylinder has been shaped over bent cylinder of the same diameter. The damage progression is shown in Figure 5-20. The simulation is the stopped; local laminate fracture occurs in the tube (i.e., when a crack appears). According to this figure the manufactured tube can sustain a larger pressure.

5.0 Simulating Manufacturing Process of Composite Textile Preform Reshaping

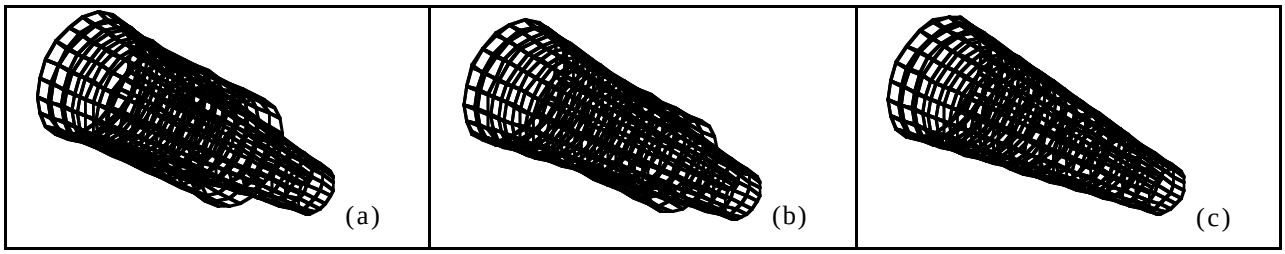

Figure 5-18. Fitting of the cylindrical mesh over a cone. (a) Merged bases, (b) Intermediate step, (c) Final mesh.

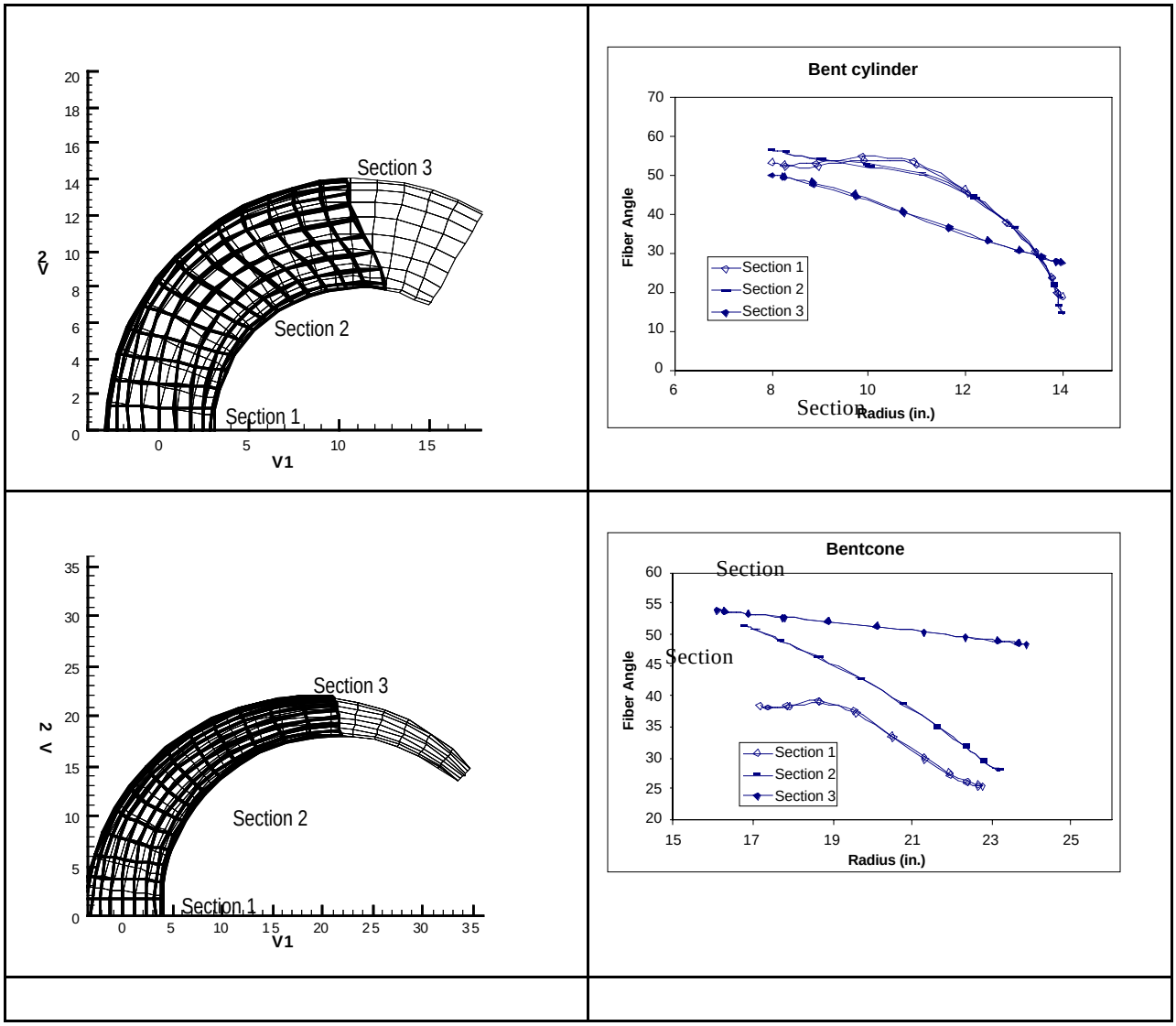

Figure 5-19. Favorable comparisons of GENOA Simulation results with General Electric. Experimental Results On Fiber Preform Reshaping Tests

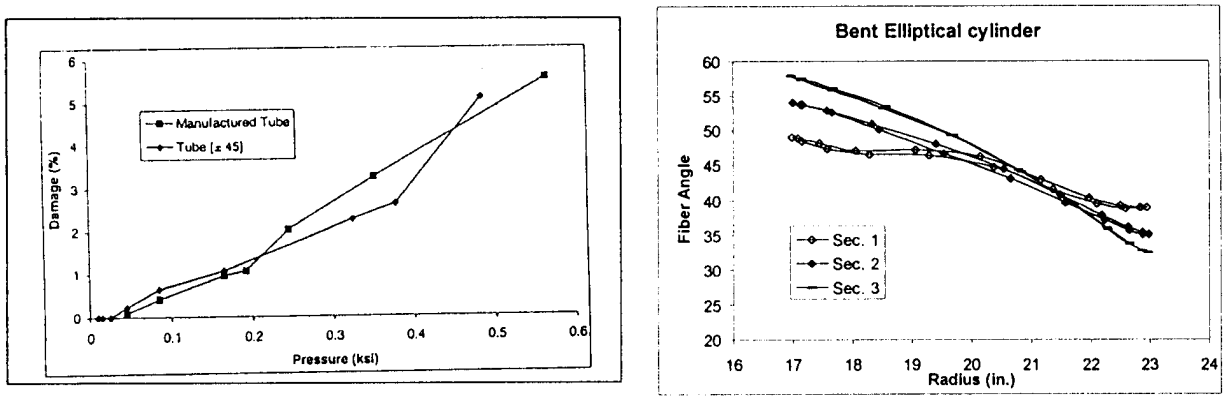

Figure 5-20. Damage Progression In Manufactured and [±45] Tubes

5.3 COMPUTATIONAL SIMULATION CYCLE

CODSTRAN is an integrated and open-ended code developed for the simulation of structural response of fiber composite structures [1]. It consists of three modules: (1) composite mechanics, (2) finite element analysis and (3) damage progression modeling. The composite mechanics module [2] conducts micro-mechanics, macro-mechanics and laminate analysis. The finite element module [3] uses anisotropic thick shell and three-dimensional solid elements as appropriate. We have added the ability to evaluate the change in fiber orientation and to change dynamically the boundary conditions of the structure to fit the preform. A typical computational cycle is defined in Figure 5-21

- First, the distance between the mold and the fiber weave is assessed. A mesh fitting algorithm dynamically generates some pressures and imposed displacements to fit the fiber weave over the mold. An extensive description of this algorithm is provided in paragraph. It should be mentioned that it respects the redistribution of stresses in the fiber weave, and it is compatible with the assumptions made in the code.
- The mechanical properties of the mesh are then computed in the composite mechanics module, first the ply properties (based on an elastic constitutive law) then the laminate properties. Since the code require the presence of matrix, a very soft matrix is used (several order of magnitude softer than the fibers)
- The structural analysis under a load increment is carried out in the finite element module.
- Using the computed deformation of the structure, the new local fiber orientation and the new deformed geometry is determined.

The basic premise of the computational method is that, during one simulation step, the deformations are small. Therefore, although the fiber angles change, this change is small enough to assume that the properties of the material remain constant. This allows for the uncoupling between the fiber orientation change, the property computation and the finite element solution in the computation cycle.

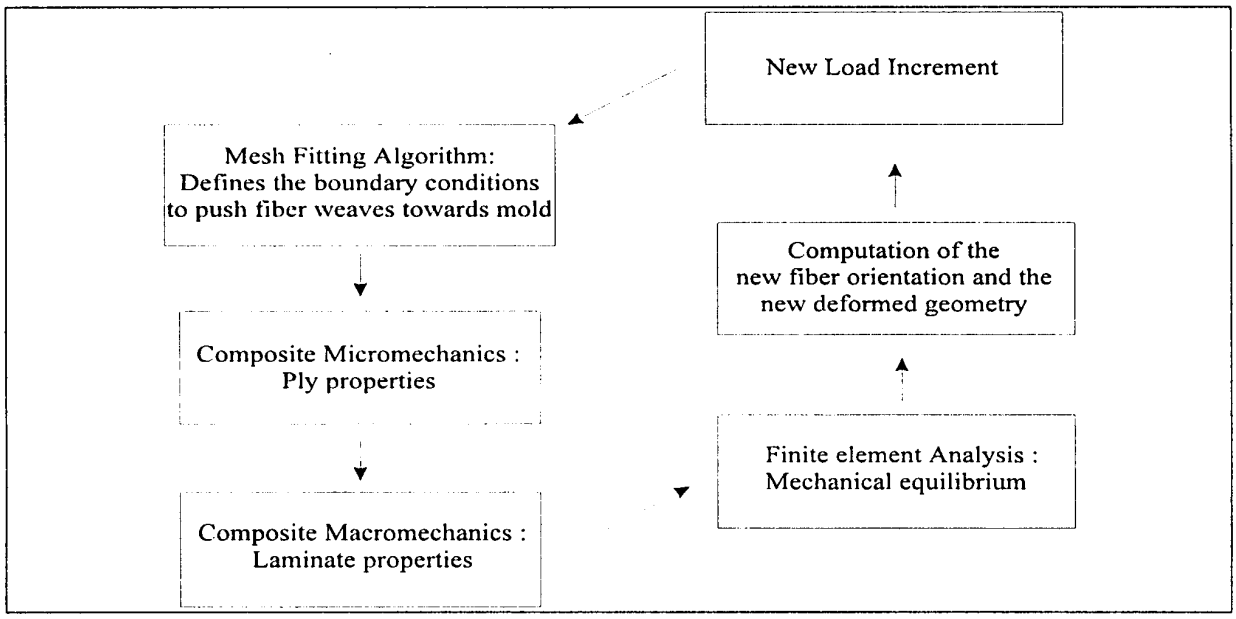

Figure 5-21. Computational Simulation Cycle

5.4 FIBER ANGLE CHANGE

Modeling the change of fiber orientation is based on the assumption of symmetrically woven fibers. The fibers have a very high stiffness so their elongation is negligible. Accordingly, a box with fibers as its diagonals will deform into a box with a different aspect ratio (Figure 5-22).

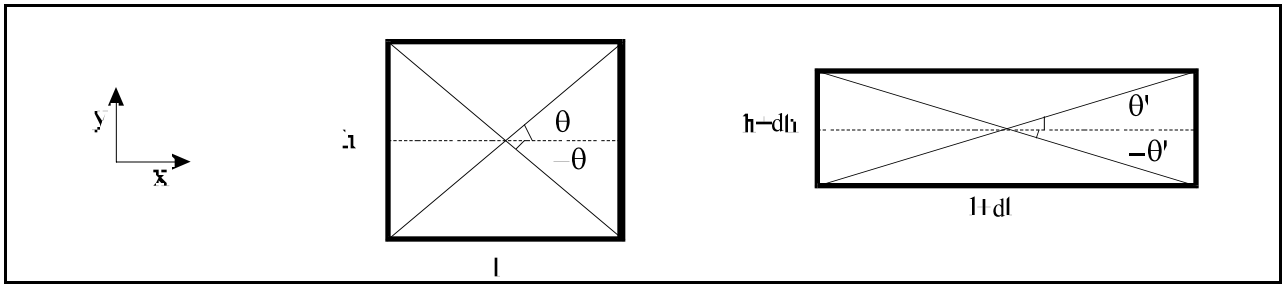

Figure 5-22. Deformation of an Elementary Box

The angle θ‘ is such that

$$\tan\theta' = \frac{h+dh}{l+dl} = \frac{(1+\varepsilon_{yy})h}{(1+\varepsilon_{xx})l} = \frac{1+\varepsilon_{yy}}{1+\varepsilon_{xx}}\tan\theta$$

The new angle is computed with respect to the incremental strain during a finite-element step. Thus the angle computation is coherent with the updated Lagrangian resolution scheme.

5.4.1 Validity of the Large Strain Approach

Assuming that the fibers cannot be elongated leads to the following analytical relationship

$$h = \sqrt{2 - l^2} \qquad \tan\theta = \frac{h}{l}$$

These analytical relationships were used to compute elongations and strains plotted in Figure 5-23 for comparison with similar results from computational simulation relying in updated lagrangian small strain anistropic elastic constitutive law.

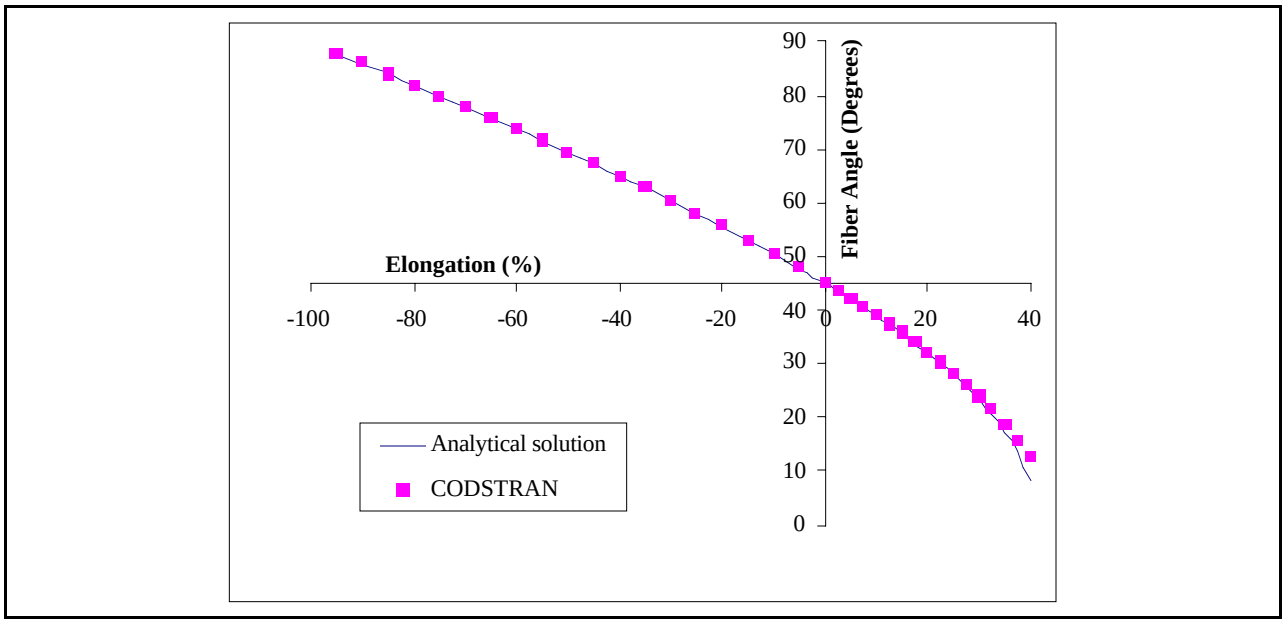

Figure 5-23. Fiber Angles For Different Elongation Of A Rectangular Plane Panel.

The results of the analytical model and of the computational simulation are in very good agreement, which gives credit to the composite mechanics module (where the physical properties of the structure are computed). As we can expect, the angle tends to 0 for an elongation of 41%, which correspond to the point where the fibers are all stretched out.

There appears a slight difference (of about 5 degrees in the fiber angles) when the panel is completely extended by more than 35%. This can be explained with a closer look the deformation.

For soft matrix composites, the mechanisms of deformation do not depend on the properties of the matrix (very low stiffness compared to the fibers, therefore there is very small effect on the global properties) and those of the fibers (which cannot be elongated). The behavior is only driven by the Poisson ratio.

The theoretical Poisson ratio v of the deformation described in this Figure can be computed if we remark that

$$\varepsilon_{xx} = \frac{dl}{l} \qquad \varepsilon_{yy} = \frac{dh}{h} \qquad \nu = -\frac{\varepsilon_{yy}}{\varepsilon_{xx}} = -\frac{l}{h}\frac{dh}{dl}$$

The fiber cannot be elongated, so

(1) $$l^2 + h^2 = (h + dh)^2 + (l + dl)^2 = (1 - \nu\varepsilon_{xx})^2 h^2 + (1 + \varepsilon_{xx})^2 l^2$$

At the first order in ε_{xx}, this equation becomes

(2) $$\nu = \frac{l^2}{h^2} = \frac{1}{\tan^2\theta}$$

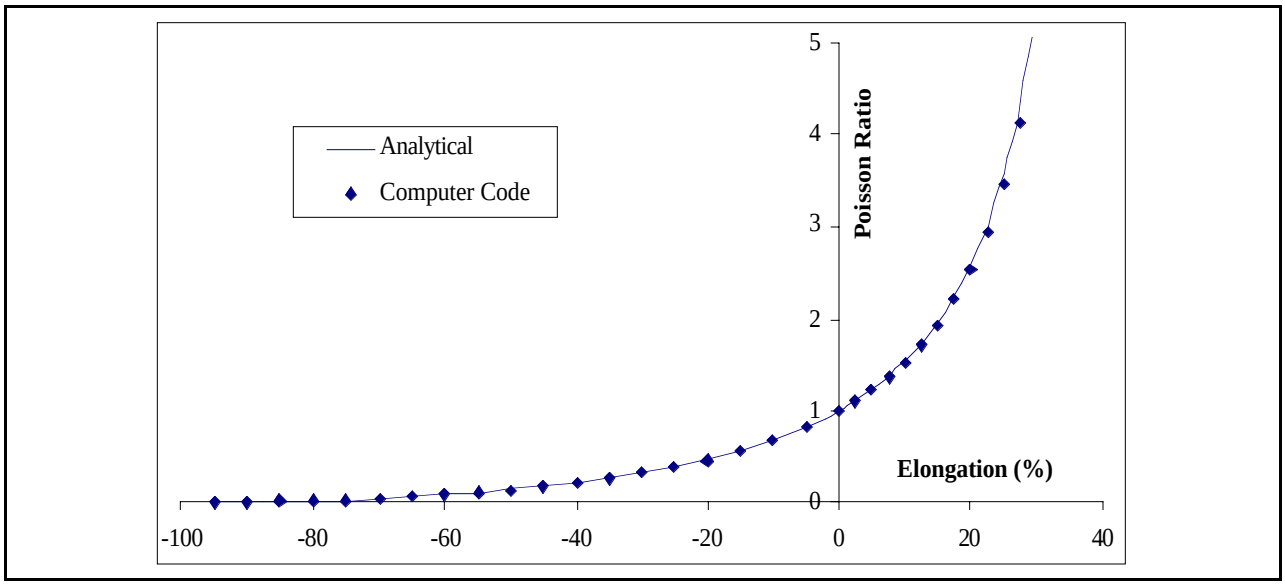

Figure 5-24. Poisson's Ratio at Different Elongation For A Rectangular Plane Panel

When the elongation goes over 30%, the Poisson ratio increases at a very steep rate. At this moment, the assumption that the properties are constant during a step is no longer valid. The Poison ratio is then underestimated, leading to a lesser decrease in the fiber angle. This explains why the fiber angles values computed by the computational simulation are slightly higher than the analytical ones at extreme elongation. The smaller the fiber angles (or the longer the elongations), smaller increment are required in simulations.

Also, when the fibers are very elongated, the load required to deform the structure increases. This leads to possible stretching of the fibers. This effect is taken into account in the computer code and not in the analytical model, which also explains part of the difference at high elongation levels.

Globally, though, this approach gives very good results. Large strains involves by the Poisson ratio that is accounted for very accurately by the composite mechanics module. Therefore, although the computational simulation is based on a small strain code, its validity can be extended to large strains in the case of specific materials such as very soft matrix fiber reinforced composites or fiber weaves.

5.4.2 Possible areas of Improvements

Fiber stress Monitoring

The main area of improvement, for the fiber angle computation, is that of fiber stress monitoring. In some cases, it is possible that the overall constraints applied to a mesh will create fiber elongation and/or unreasonable stress on the fibers. For instance, imposed displacements might create shear stresses in the structure.

It appears to be easy to add a fiber stress monitoring subroutine. At each step, CODSTRAN computes the damage initiation in the composite and since there is no matrix, the program detects matrix damage even for very small loads. Consequently, damage treatment has been disabled by modifying subroutine PFM. The "fiber tension failure" damage mode could be monitored to ensure the mechanical resistance of the fiber preform.

A way to monitor the fiber stress would be to recover the actual value of the fiber stress from ICAN.

A question arises as to what should be done in case of fiber fracture. Some options are:

- Do nothing (current status).
- Change the loading conditions. For instance, the imposed-displacements/contact conditions may create unreasonable loading of the structure. This case, reverting to load instead of displacement controlled deformations gives more control over the stress level attained by the structure. E.g. the loads defined by the program can be restricted to a given maximal value at each step.
- Change the boundary conditions. The biggest stresses are more likely to appear at the more rigid parts of the structure, where the fibers require more load to reach a displacement. This may be due to ill-defined boundary conditions.

Non elastic Fiber Constitutive law

These fibers have plasticity. Let us assume that a constitutive law that allows for plastic elongation of fibers is used in simulations.

In that case, the assumption that the fibers do not elongate is no more valid. A different way to compute the fiber angle must be found.

In the case of large arbitrary displacements, each individual fibers must be followed. The fiber angles will no longer be symmetrical. A method to determine the fiber angle changes, is as follows:

- Define the vector V representing the fiber direction before the deformation step,
- Perform the deformation step,
- Define the gradient tensor F

$$F = \begin{vmatrix} 1+\frac{\partial u_x}{\partial X} & \frac{\partial v_x}{\partial X} & \frac{\partial w_x}{\partial X} \\ \frac{\partial u_x}{\partial Y} & 1+\frac{\partial v_x}{\partial Y} & \frac{\partial w_x}{\partial Y} \\ \frac{\partial u_x}{\partial Z} & \frac{\partial v_x}{\partial Z} & 1+\frac{\partial w_x}{\partial Z} \end{vmatrix}$$

where U is the displacement and XYZ are the axes.

- Find the new direction vector v for the fiber, $v = F.V$
- Using this new direction, find the fiber angle with respect to the new configuration and to the new element coordinates.

Note that, in this method, any constitutive law can be used, since we follow each individual fiber. This method will also allow for more that 2 fibers.

5.5 FAN BLADE MESH FITTING SIMULATION

According to the use of the previous algorithm (the one used for the tube cases), the edges were difficult to model. In particular, they were not accurately and reliably 'seen' by the geometrical algorithm. For instance, in Figure 5-6, the sock goes inside the fan blade and its edges rest over one side of the fan.

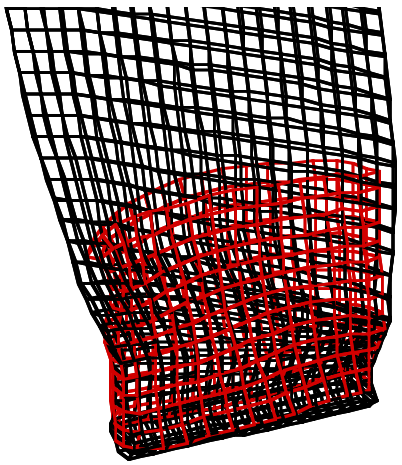

Figure 5-25. Sock over fan blade, initial geometrical algorithm

Some methods were proposed for further evaluation:

- Use the same kind of resolution as in the tube cases: Start with a straight blade which is progressively curved using small steps. This process is easier and can be fine tuned to respect the edges.
- Use a different geometrical algorithm: The load/displacements are currently driven by the position of the sock with respect to the mandrel. This logic can be reversed.
- Use a different representation of the sock to give more importance to the edges, in particular using spline functions for smoother geometry.

5.5.1 Evaluation of the different methods

The following conclusions have been reached:

- Spline functions can be used to describe the edges or the whole mandrel and will allow easy flattening or bending of the surface. In the case of the edges, this leads to making a specific algorithm to take into account the edge, which is of little interest since we can use a specific algorithm for the finite-element edge.

- Use of a mandrel-driven geometrical algorithm leads to the same problems encountered with the sock driven algorithm.

- An algorithm is needed that is able to differentiate the sides/edges of the sock and the mandrel.

We are currently developing a method based on separating the edges and the sides of the surface. The principles are:

- Account for the two sides and the two edges of the mandrel. Divide the sock with the same kind of geometrical consideration, *i.e.* make the distinction between sides and edges.

- The algorithm is to be modified to fit one side/edge of the sock over its corresponding side/edge of the mandrel. Note that a specific fitting-algorithm needs to be developed to ensure the edges are fitted with enough freedom of the mesh.

- To respect the redistribution of the stresses, some points of the edge of the sock must be able to move over to one side and be replaces by points of the sides becoming on the edges. This ensures that the edges are covered at all times. Note that this process will require a mesh refined enough around the edges so that these points are near each other.

For the sake of the stability of the fitting algorithm and to prevent buckling, we use a two-step process for the simulation. This is used to solve the two problems which are (1) elongation/reduction of diameter of the sock (where buckling appears) and (2) fitting of the mesh over multiple curvatures. The process is as follows:

- First, the sock is fitted over a straight mandrel which has the same diameter and same average thickness around the edges as the fan Blade. There is no curvature in the plane of the sock, so the points of the edges of the sock should stay on the edges. At the end of this process, we have a sock with the good diameter Figure 5-26).

- Use this sock and fit it over the fan blade. Depending on the stability of this resolution, the first step might be abandoned and all the resolution be done at once.

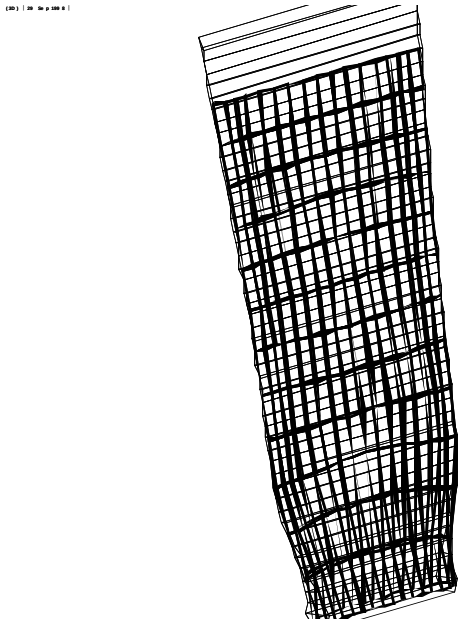

Figure 5-26. Sock over straight mandrel

At this time (September 29th) the project is at the point:

- A straight mandrel is generated according to the fan blade mesh.
- A fan blade where the edges and sides are sorted is available. This required building an index for each element.
- The sock has been added an index to sort the sides and edges as well.

Remains to be done are some programming and debugging of the modified fitting-algorithm which should be done soon, and the evaluation of the need and the consequences of allowing the points of the edges of the sock to move to the side and be replaced by points of the side.

5.5.2 Modifications to the code

Modifications are:

- The MANDREL file format has been updated to distinguish (via elements) between the sides and edges of the mandrel.
- The sock needs distinction. This is stored in the file SCRA grid which should be generated by the mesh generator as well as the CODINP file. The distinction for the sock is node based (to define weather a node should go on a side or on the edge)
- The distance and update boundary subroutines have been heavily modified to include a side specific and edge specific algorithm. Basically, the algorithm is:

  1. Find the displacements to fit one side of the sock to the equivalent side of the mandrel. Do the same for the other side.
  2. Find the displacement to pull the edge of the sock towards the corresponding edge of the mandrel.

3. Transform these displacements in contact conditions,

4. Write the contact conditions in the Finite Element file for processing

Note that no algorithm has been developed to allow one point of the edge of the sock to slide to the side of the Mandrel. According to the geometry of the blade, this should have very little effect on the results.

A fitting algorithm and to prevent buckling, uses a two-step process to determine (1) elongation/reduction of diameter of the sock (where buckling appears) and (2) fitting of the mesh over multiple curvatures. The process is as follows:

- First, the sock is over a strait mandrel which has the same diameter and same average thickness around the edges as the fan Blade. There is no curvature in the plane of the sock, so the points of the edges of the sock should stay on the edges.

- Fit this sock it over the fan blade.

According to the first evaluations of the code, this two step process cannot be avoided. The results are shown in Figures 5-27 to 5-29.

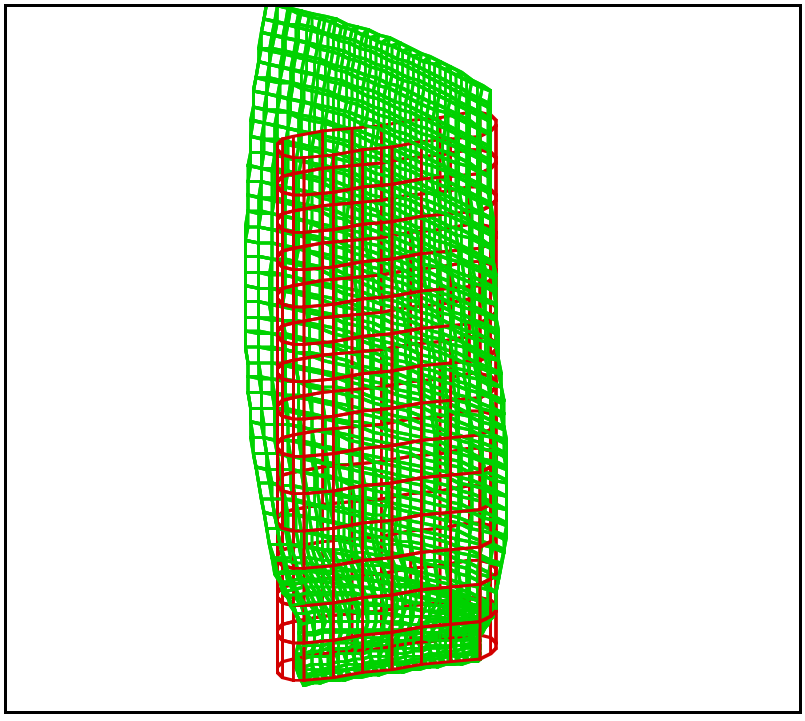

Figure 5-27. Initial Sock and Fan Blade

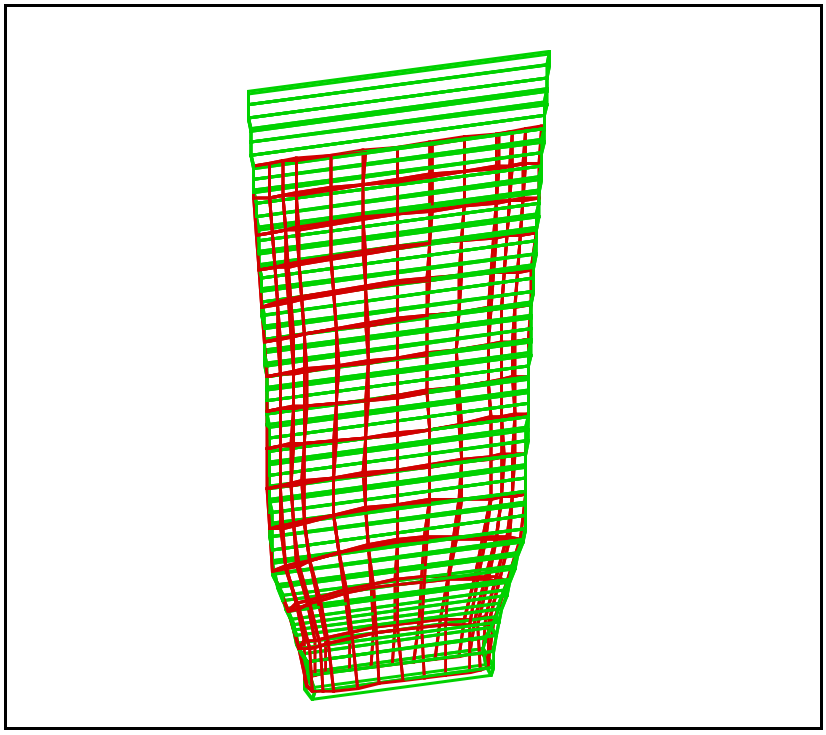

Figure 5-28. Step1: Fitting the Sock Over A Straight Mandrel

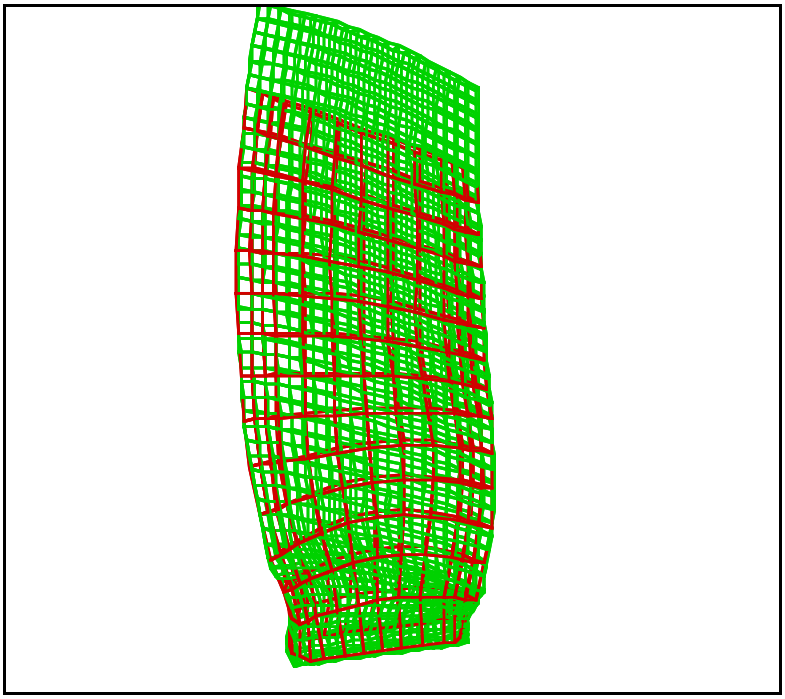

Figure 5-29. Step 2: Fitting the Previous Sock Over The Fan Blade.

6.0 Probabilistic Failure Analysis

Methods and corresponding computer codes are discussed relative to evaluation of progressive damage and fracture in stitched and unstitched composite laminates. A computer code utilized for the simulation of composite structural damage and fracture assesses. Structural response during degradation probabilistically. The effects of design variable uncertainties on structural damage progression are quantified. The Fast Probability Integrator is used to assess the scatter in response of the composite structure at damage initiation. Sensitivity of the damage response to design variables is computed. Methods are general-purpose in nature and are applicable to fracture processes stitched and unstitched composites in all types of structures undergoing damage initiation and unstable crack propagation up to global structural collapse. Results of the methods are demonstrated for polymer matrix composite panels under edge loads indicate that composite constituent properties and fabrication parameters have a significant effect on structural durability. Design implications with regard to damage progression and damage tolerance of composite structures are examined.

Graphite/epoxy composite structures are used in the design of various structural components such as aircraft wing and fuselage structures, jet engine cowls, pressure vessels, containment structures, and rocket motor cases. In these applications it is important to achieve low weight, high strength, stiffness, and safety. For a rational design it is necessary to quantify the damage tolerance of a candidate structure. The assessment of damage tolerance requires a capability to simulate the progressive damage and fracture characteristics of composite structures under loading. Damage tolerance of a structure is quantified by the residual strength, that is the additional load carrying ability after damage. Composite structures are well suited for design with emphasis on damage tolerance as continuous fiber composites have the ability to arrest cracks and prevent self-similar crack propagation. For most fiber reinforcement configurations, cracks and other stress concentrators do not have as important an influence in composites as they do for homogeneous materials. Another important aspect is the multiplicity of design options for composites. The ability of designing composites with numerous possible fiber orientation patterns, stitching, braiding, choices of constituent material combinations, ply drops and hybridizations, render a large number of possible design parameters that may be varied for an optimal design.

Flawed structures, metallic or composites, fail when flaws grow or coalesce to a critical dimension such that (1) the structure cannot safely perform as designed and qualified or (2) catastrophic global fracture is imminent. However, fibrous composites exhibit multiple fracture modes that initiate local flaws compared to only a few for traditional materials. Hence, simulation of structural fracture in fibrous composites must include: (1) all possible fracture modes, (2) the types of flaws they initiate, and (3) the coalescing and propagation of these flaws to critical dimensions for imminent structural fracture. The comprehensive simulation of progressive fracture presented herein is independent of stress intensity factors and fracture toughness. Concepts governing the structural fracture simulation are described in reference [1]. Based on these concepts, a computational simulation procedure has been developed for (1) simulating damage initiation, progressive fracture, and collapse of composite structures and (2) evaluating probability of structural fracture in terms of global quantities which are indicators of structural integrity.

It has been recognized in the structure community that uncertainties in the structural parameters as well as in the service environments need to be considered in the evaluation of structural integrity/reliability. Alpha STAR has developed GENPAM (Figure 6-1), computer software that integrates probabilistic methods, finite element methods, and composite mechanics for probabilistic composite structural analysis. The available probabilistic methods for GENPAM include 1) Monte Carlo Simulation (MCS), 2) advanced reliability algorithms and 3) importance sampling methods. MCS, traditionally used for reliability assessment, is deemed too computationally expensive for large structures or structures with complex behaviors. Consequently, over a period of ten years of probabilistic structural analysis research funded by NASA, advanced reliability algorithms and importance sampling methods were incorporated in the GENPAM program. It is well documented that these algorithm methods are thousands of times faster than Monte Carlo simulation thus significantly reducing computational time for probabilistic analysis of large structures or structures with complex behaviors. The GENPAM software has been integrated into the GENOA suite of codes.

6.0 Probabilistic Failure Analysis

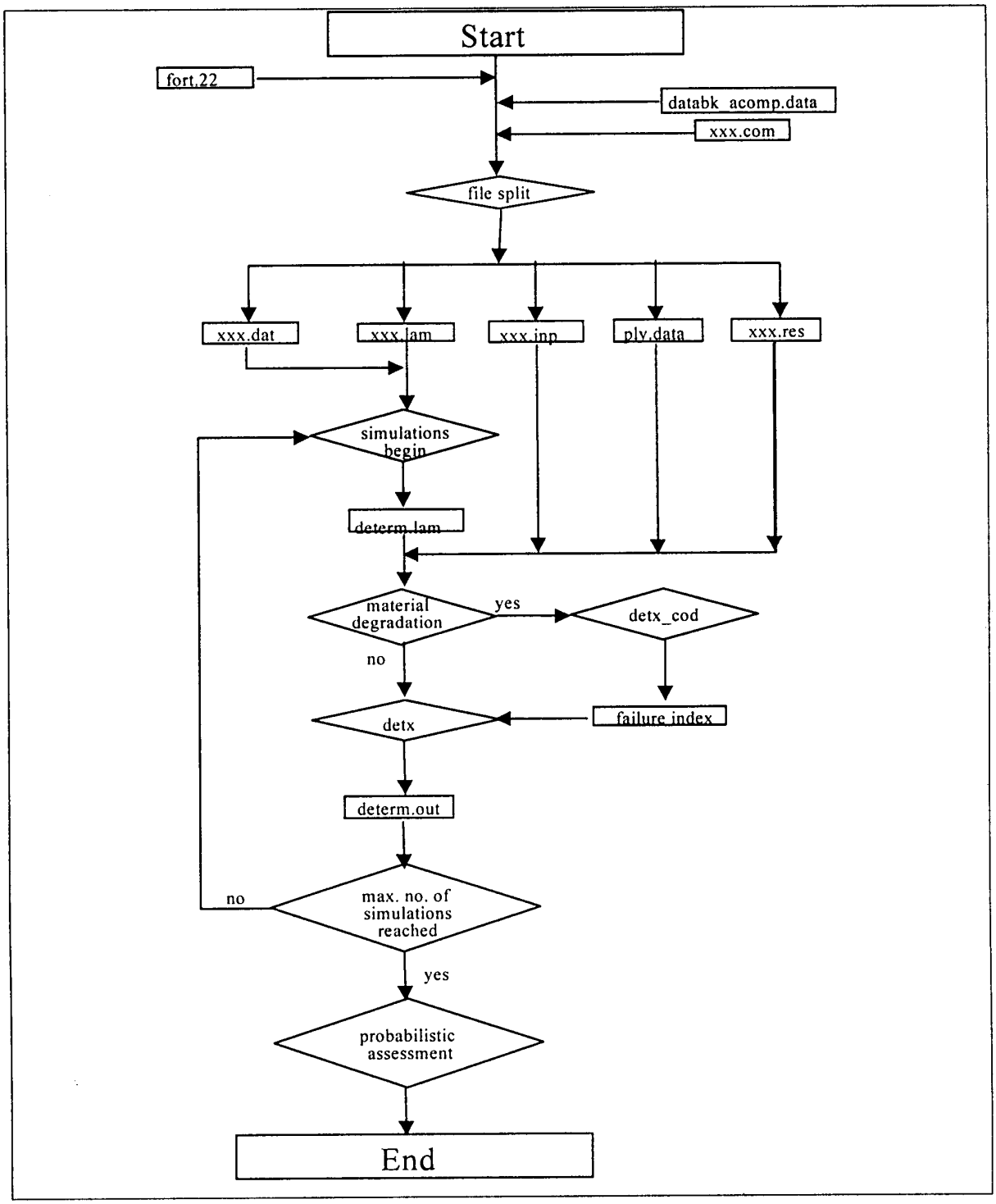

Figure 6-1(a): GENPAM Probabilistic Software Flow Chart

6.0 Probabilistic Failure Analysis

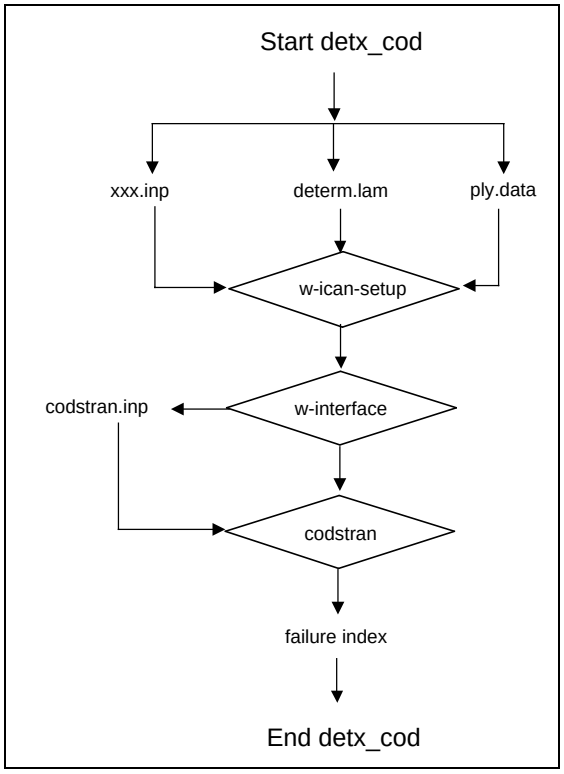

Figure 6-1b. GENPAM Probabilistic Software Flow Chart

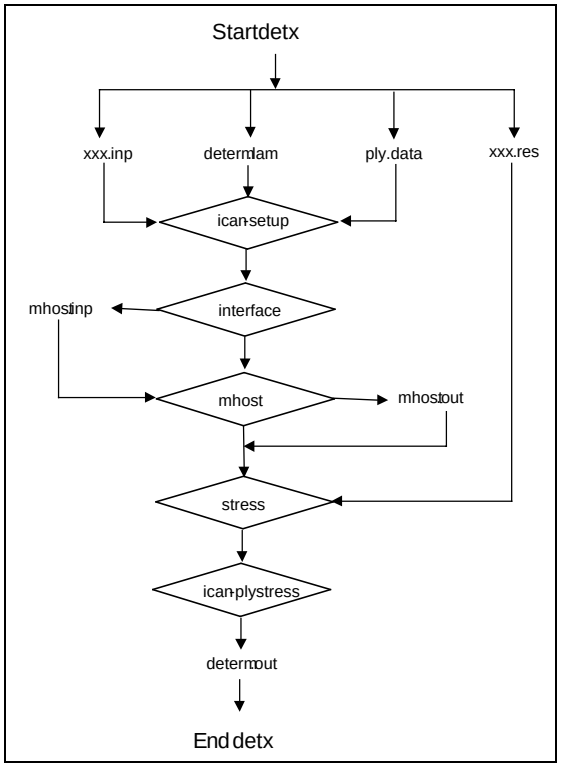

Figure 6-1c. GENPAM Probabilistic Software Flow Chart

GENPAM code is constructed in such a way that any real value in the input file of the deterministic analysis can be selected as a random variable. An interface module can interfaces with any deterministic code as long as the uncertainties are real values shown on the original deterministic input file. Integration with many commercial or in-house computer codes is greatly simplified.

Composite mechanics is embedded in the GENOA-PMC3 module that is an Integrated Composite Analyzer. GENOA-PMC3 will provide ply and laminate properties based on input of fiber, matrix, and fabrication properties. Isotropic material can be modeled by setting the fiber volume fraction to a negligible value and using the isotropic material properties as matrix properties. GENOA-PMC3 also determines ply stress, ply strain and ply strength for failure consideration. Random variables can be any fiber matrix property, ply thickness or orientation, fiber or void volume ratio, temperature, moisture or 3D-braid configuration.

Various responses can be selected to be analyzed probabilistically, such as the cumulative distribution function (CDF), the probability distribution function (PDF), and sensitivities to design random variables. Displacement responses can be specified with node numbers and the three transition degrees-of-freedom. Material response can be specified with node number, layer number, and as selection from a menu of 20 choices as follows:

1. Longitudinal strain
2. In plane shear strain
3. Transverse stress
4. Longitudinal tensile strength
5. Transverse tensile strength
6. In plane shear strength
7. Hoffman's failure criterion
8. Fiber crushing criterion (compressive strength)
9. Fiber microbuckling criterion (compressive strength)
10. Transverse normal shear stress
11. Transverse strain
12. Longitudinal stress
13. In plane shear stress
14. Longitudinal compressive strength
15. Transverse compressive strength
16. MDE failure criterion
17. Interply delamination failure criterion
18. Delamination criterion (compressive strength)
19. Longitudinal normal shear stress
20. Transverse normal shear strength

6.1 CONCEPTUAL MODEL AND MESH MAPPING

Probabilistic structural analyses are inherently computational intensive due to the large number of deterministic analyses required to accurately simulate the effect of uncertainties on the desired structural response (stress, displacement, ultimate load etc.) for structural reliability assessment. Probabilistic structural analysis using finite element models can be economically performed when relatively coarse mesh is employed. However, finite element analyses using coarse mesh not only raise questions regarding the convergence on the deterministic values but also significantly alter the true probability distribution of the structural response. It is important, therefore, to evaluate the influence of mesh refinement on the accuracy of the probabilistic structural response and reliability.

The accuracy of the probabilistic structural response is most affected by two factors. The first is the accuracy of the probability distribution of the random variables involved in the analysis. The second is the coarseness of the finite element model. The random variables are independent of the finite element model and are assumed to be accurately described by the users. Therefore, error in the probabilistic structural response for a given finite element mesh is directly caused by the FEM mesh. A mapping method was developed for coarse finite element mesh use that would give simulation results matching those obtained with fine finite element mesh use within 10 to 20% effectiveness

6.2 COMPUTATIONAL SIMULATION PROCEDURE

The progressive fracture of stitched and unstitched composite laminates is simulated via an innovative approach independent of stress intensity factors and fracture toughness parameters. Computational simulation is able to evaluate damage initiation, damage growth, and fracture in composites under various loading and environmental conditions. It has been applied to the investigation of the effects of composite degradation on structural response [1], effect of hygrothermal environment on durability [2], damage progression in composite shells subjected to internal pressure [3], the durability of stiffened composite shell panels under combined loading [4], and damage progression in stiffened composite structural components [5]. The purpose of this paper is to describe combination of computational simulation with probabilistic methods to identify the salient material and structural parameters for design with damage tolerance considerations.

Computational simulation is carried out by an integrated and open-ended computer code consisting of three modules: composite mechanics, finite element analysis, and damage progression modeling. The overall evaluation of composite structural durability is carried out in the damage progression module [6] that keeps track of composite degradation for the entire structure. The damage progression module relies on composite mechanics [7] for composite micromechanics, macromechanics and laminate analysis, and calls a finite element analysis module that uses anisotropic thick shell elements to model laminated composites [8]. The composite mechanics module is called before and after each finite element analysis. Prior to each finite element analysis, the composite mechanics module computes the composite properties from the fiber and matrix constituent characteristics and the composite layup. The finite element analysis module accepts the composite properties that are computed by the composite mechanics module at each node and performs the analysis at each load increment. After an incremental finite element analysis, the computed generalized nodal force resultants and deformations are supplied to the composite mechanics module that evaluates the nature and amount of local damage, if any, in the plies of the composite laminate. Individual ply failure modes are assessed by the composite mechanics module using failure criteria associated with the negative and positive limits of the six ply-stress components in the material directions. In addition to the failure criteria based on stress limits, interply delamination due to relative rotation of the plies, and a modified distortion energy (MDE) failure criterion that takes into account combined stresses is considered [7]. Depending on the dominant term in the MDE failure criterion, fiber failure or matrix failure is assigned. The generalized stress-strain relationships are revised locally according to the composite damage evaluated after each finite element analysis. The model is

automatically updated with a new finite element mesh having reconstituted properties, and the structure is reanalyzed for further deformation and damage.

If there is no damage after a load increment, the structure is considered to be in equilibrium and an additional load increment is applied leading to possible damage growth, accumulation, or propagation. Simulation is continued until global structural fracture.

The phenomenon of fracture in composite structures is further compounded due to inherent uncertainties in the multitude of material properties, structural geometry, loading, and service environments. The effect of all types of uncertainties must be designed-in for satisfactory, reliable, and affordable structures. The various uncertainties are traditionally accounted for via knockdown (safety) factors with generally unknown reliability. An alternate approach to quantify those uncertainties on structural fracture is to use probabilistic methods as described herein.

Probabilistic evaluation of damage and fracture progression, an integrated probabilistic analysis code [9] is used in conjunction with progressive damage simulation. The probabilistic analysis code considers the uncertainties in material properties as well as in the composite fabrication process and global structural parameters. The effects on the fracture of the structure of uncertainties in all the relevant design variables are quantified. The composite mechanics, finite element structural simulation, and Fast Probability Integrator (FPI) ave been integrated into the probabilistic analysis code. FPI, contrary to the traditional Monte Carlo Simulation, makes it possible to achieve rders-of-magnitude computational efficiencies which are acceptable for practical applications. Therefore, a probabilistic composite assessment becomes feasible which can not be done traditionally, especially for composite materials/structures which have a large number of uncertain variables. Probabilistic analysis starts with defining uncertainties in material properties at the most fundamental composite scale, i.e., fiber/matrix constituents. The uncertainties are progressively propagated to those at higher composite scales subply, ply, laminate, and structural. The uncertainties in fabrication variables are carried through the same hierarchy. The damaged/ fractured structure and ranges of uncertainties in design variables, such as material behavior, structure geometry, supports, and loading are input to the probabilistic analysis module. Consequently, probability density functions (PDF) and cumulative distribution functions (CDF) can be obtained at the various composite scales for the structure response. Sensitivities of various design variables to structure response are also obtained. Input data for probabilistic analysis is generated from the degraded composite model available as progressive damage and fracture stages are monitored.

6.3 SIMULATION OF COMPOSITE PANELS

Rectangular panels of stitched and unstitched graphite/epoxy laminate are considered. The laminate consists of 48 plies that are configured as [0/45/90]s6 with a total thickness of 0.25 in (6.35 mm). Stitching is done using 1200 denier Kevlar thread using a spacing of 0.25 inch and a pitch of 0.1 in. The direction of stitching is along the 0-degree plies. The specimen has a width of 4.0 in (102 mm) and a length of 8.0 in (406 mm). The 0-degree plies are oriented along the 8.0 inches. direction and the 90 degree plies are oriented transverse to the 8.0 in. direction. The finite element model contains 260 nodes and 184 elements. The composite system is made of AS-4 graphite fibers in a high-modulus, high strength (HMHS) epoxy matrix. The graphite fiber volume ratio is 0.55 and the void volume ratio is one percent. The composite is manufactured by resin transfer molding (RTM) of the stitched preform. It has been cured at a temperature of 350F (177C). The use temperature is 70F (21C).

Each panel is subjected to gradually increasing loading. The specimens are loaded by restraining one end and applying uniformly displaced tensile, compressive, in-plane shear, and out of plane transverse loads at the other end. Damage progression is computationally simulated as the loading is increased. The rate of increase in the overall damage during composite degradation is used as a measure of structural propensity for fracture. Figure 6-2 shows the simulated damage progression with increasing tensile and compressive loading on the stitched and unstitched panels. There is no difference in the

damage initiation loads for stitched and unstitched panels. Damage initiation under tension occurs at a lower load compared to compression. Also, due to the large extent of ply transverse tensile failures, composite structural damage reaches a much larger magnitude under tension compared to compression. After the completion of a well defined damage growth stage, the state of damage remains constant until the ultimate load is reached. For tensile loading of the stitched panel damage at the ultimate load is lower than that of the unstitched panel. However, for compressive loading of the stitched panel damage at ultimate load is higher than that of the unstitched panel. Also, the unstitched panel is able to carry a larger compressive load at the ultimate fracture stage.

Figure 6-3 shows the damage progression for in-plane shear and out-of-plane flexural loads. For the ultimate fracture stage of the in-plane shear loading the magnitude of damage is greater for the unstitched panel. On the other hand, for the out-of-plane flexural loading, the stitched panel reaches a much higher damage level compared to the unstitched panel.

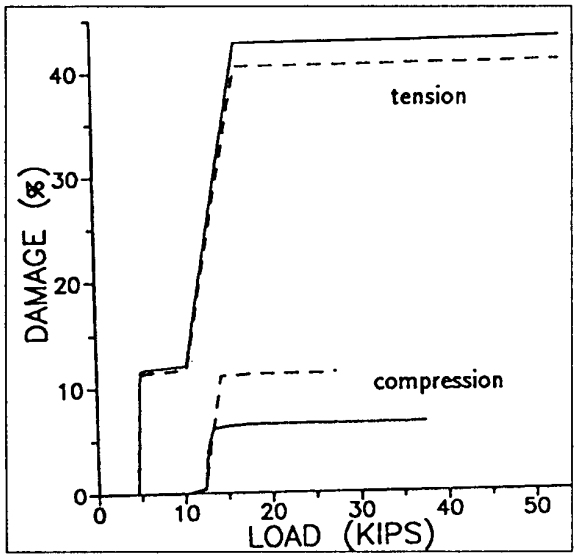

Figure 6-2. Damage Progression under Tension and Compression; Graphite/Epoxy: 48 Plies [0/45/90]s6, Solid lines = Unstitched Composite, Dashed Lines = Stitched Composite

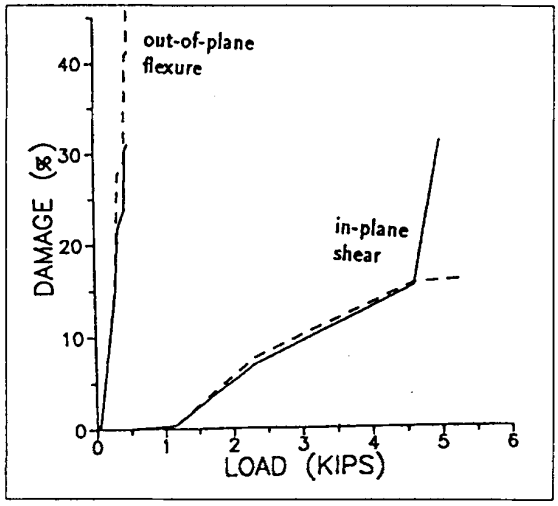

Figure 6-3. Damage Progression Under In-Plane Shear And Out-Of-Plane Flexure; Graphite/Epoxy: 48 Plies [0/45/90]S6; Solid Lines = Unstitched Composite; Dashed Lines = Stitched Composite

The probabilistic analysis code was used to characterize the damage initiation stage for the composite panels. For the out-of-plane flexural loading, the damage initiation stage that occurred at a lateral load of 182 N (41 lbs) was controlled by the modified distortion energy (MDE) failure criterion according to the progressive damage simulation. Therefore, the effects of constituent material uncertainties on the MDE failure criterion as well as the end displacement were computed to assess probabilistic failure at the damage initiation stage. The Cumulative Distribution Function (CDF) of the MDE failure criterion and the end displacement was evaluated. Figure 6-4 shows the CDF for the MDE failure criterion and Figure 6-5 shows the CDF for the panel end displacement at the damage initiation stage. The average value of the MDE criterion is 0.9973 and the standard deviation is $0.3944E\ 10^{-3}$. The average value of the end displacement is 4.78 mm (0.188 in) and the standard deviation is 0.01888 mm (0.743310^{-3}.in).

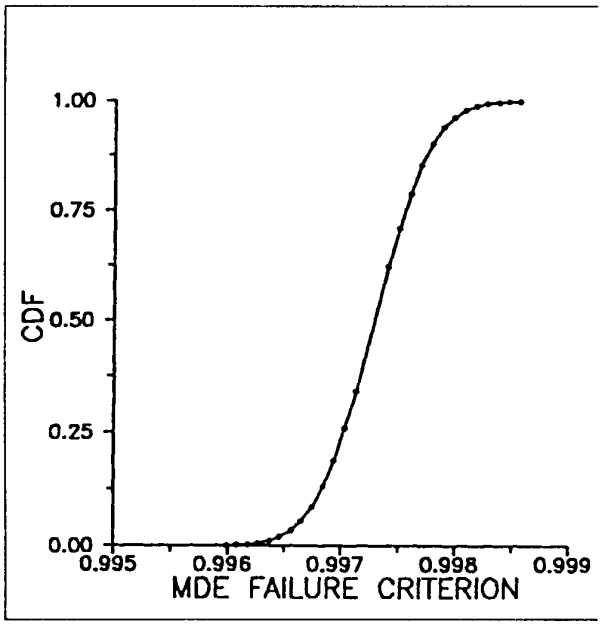

Figure 6-4. Cumulative Distribution Function of MDE Failure Criterion for Out-of-plane Flexure of Panels; Graphite/Epoxy: 48 Plies [0/45/90]s6

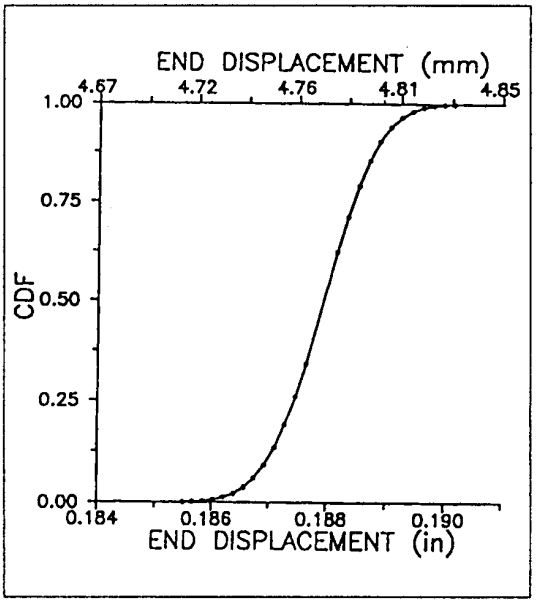

Figure 6-5. Cumulative Distribution Function of End Displacement for Out-of-plane Flexure of Composite Panels; Graphite/Epoxy: 48 Plies [0/45/90]s6

The sensitivity of the 0.001 and 0.999 cumulative probability for the MDE criterion and the panel end displacement to uncertainties in design variables were evaluated. The design variables were (1) Fiber transverse modulus, (2) Matrix tensile strength, (3) Fiber volume ratio, (4) Void volume ratio, (5) Fiber misalignment and (6) Ply thickness. Figure 6-6 shows the sensitivity of the design variables to MDE failure criterion. The fiber volume ratio was the most significant design variable affecting the MDE failure criterion and it had the highest influence at the 0.001 probability level. The ply thickness, fiber transverse modulus, matrix tensile strength, and the void volume ratio had also significant influences. However, their influences were maximum at the 0.999 probability level. Ply misalignment did not have a significant influence on the MDE failure criterion. These results indicate that: (1) the damage initiation is strongly dependent on uncertainties in the indicated five design variables and (2) damage initiation can be most effectively reduced by controlling the fiber volume ratio and the ply thickness.

Sensitivity of the panel end displacement to the design variables was also probabilistically assessed. Figure 6-7 shows the sensitivity of design variables to end displacement due to out-of-plane flexural loading. The fiber misalignment and the ply thickness were the most significant design variables that affected the end displacement. The influence of fiber misalignment was maximum at 0.001 probability and the influence of ply thickness was maximum at 0.999 probability. The fiber volume ratio had a somewhat lower but significant influence on the end displacement. Additionally, the sensitivities of the end displacement to fiber transverse modulus, matrix tensile strength, and void volume ratio were very small. These results establish that (1) the fiber volume ratio, ply thickness, fiber transverse modulus, tensile strength of the matrix, and the void volume ratio are the most significant design variables at damage initiation, and (2) panel end displacement may be controlled by adjusting the fiber misalignments and the ply thickness.

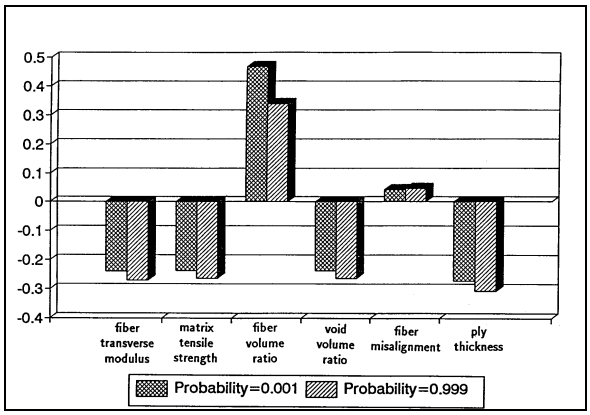

Figure 6-6. Sensitivities of Uncertainties in Design Variables to Composite MDE Failure Criterion; Graphite/Epoxy: 48 Plies [0/45/90]s6

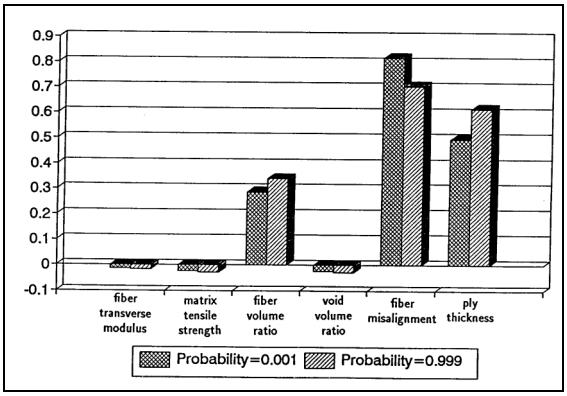

Figure 6-7. Sensitivities of Uncertainties in Design Variables to Composite Panel End Displacement; Graphite/Epoxy: 48 Plies [0/5/90]s6

6.4 CDF AND SENSITIVITY ANALYSIS OF ARA MODEL WITH LAP JOINT

The IAS ARA panel was simulated under static loading to determine the damage initiation load. At the pressure of 29.24 psi, fracture damage initiated at the some rivet location. After fracture initiation the panel arrived at an equilibrium. Probabilistic analysis was conducted at this damaged equilibrium stage. The random variables selected were the thickness of skin in the lap joint area, specifically thickness location of 0.06 inches, of 0.17 inches, and thickness of the frame. The coefficients of variation for all the design variables were taken as five percent. All random variables were assumed to have normal distributions. The response variables for probabilistic analysis were the circumferential stress and shear stress.

Figures 6-8 and 6-9 show cumulative distribution function of the circumferential and shear stresses respectively. The sensitivity of the stresses to the three design parameters varies as a function of the probability level. Figures 6-10 and 6-11 show the sensitivity of the stress response to the design variables at the 0.999 probability level.

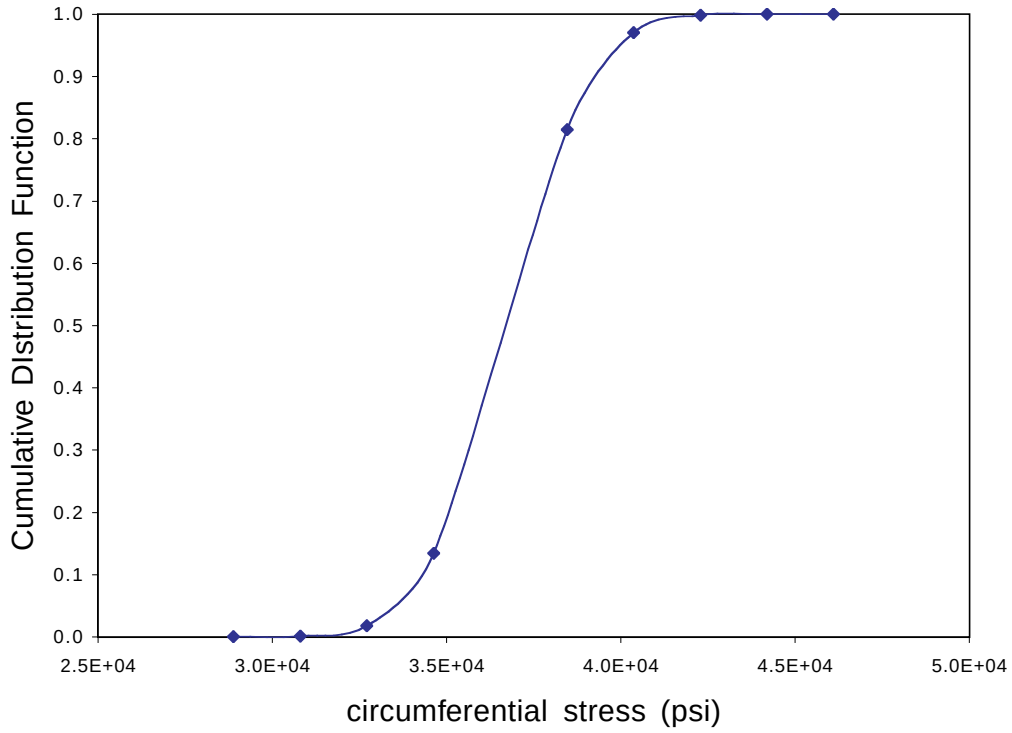

Figure 6-8. Cumulative Distribution Function Of Circumferential Stress At The Rivet On Which Damage Initiated

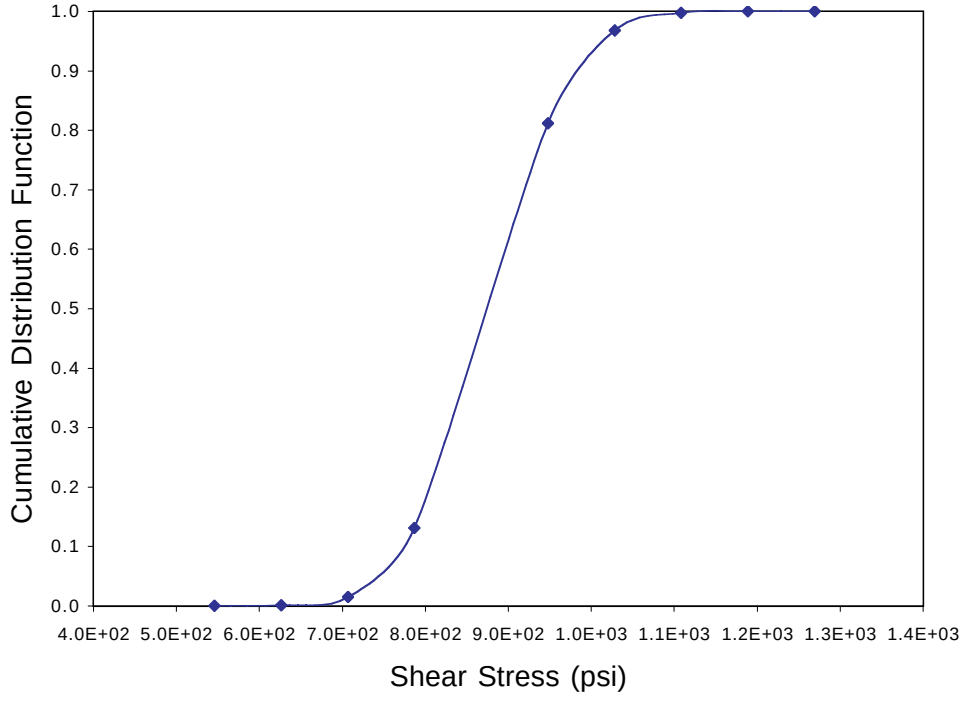

Figure 6-9. Cumulative Distribution Function Of Shear Stress At The Rivet On Which Damage Initiated

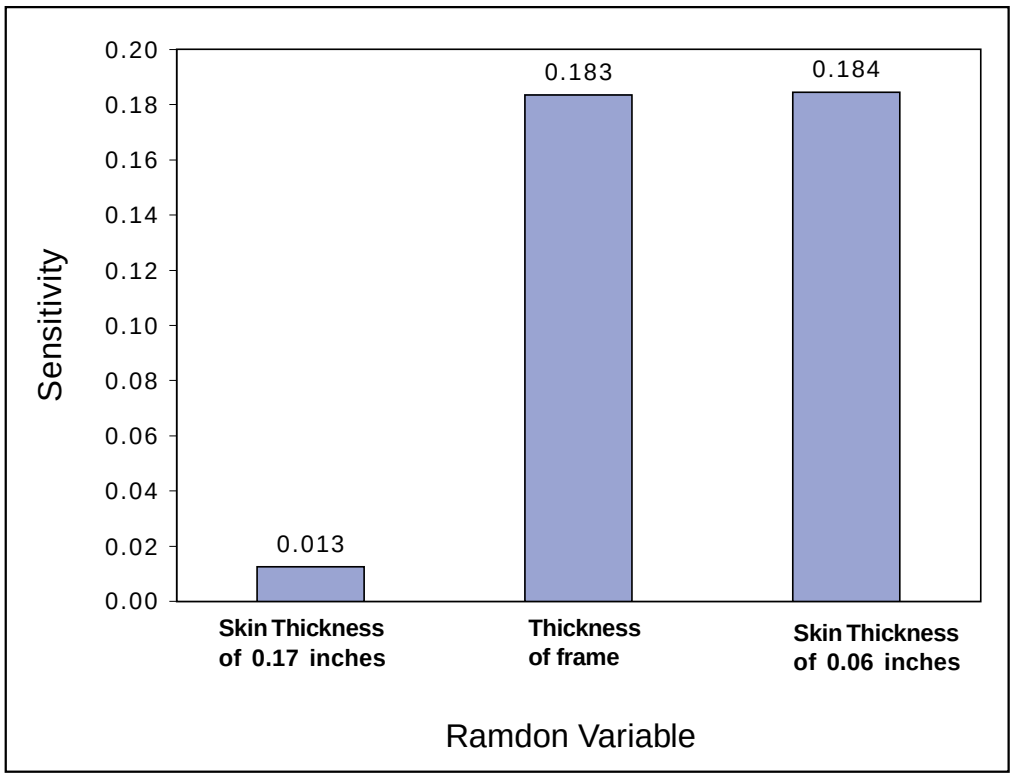

Figure 6-10. Sensitivity Circumferential Stress Skin And Frame Thicknesses

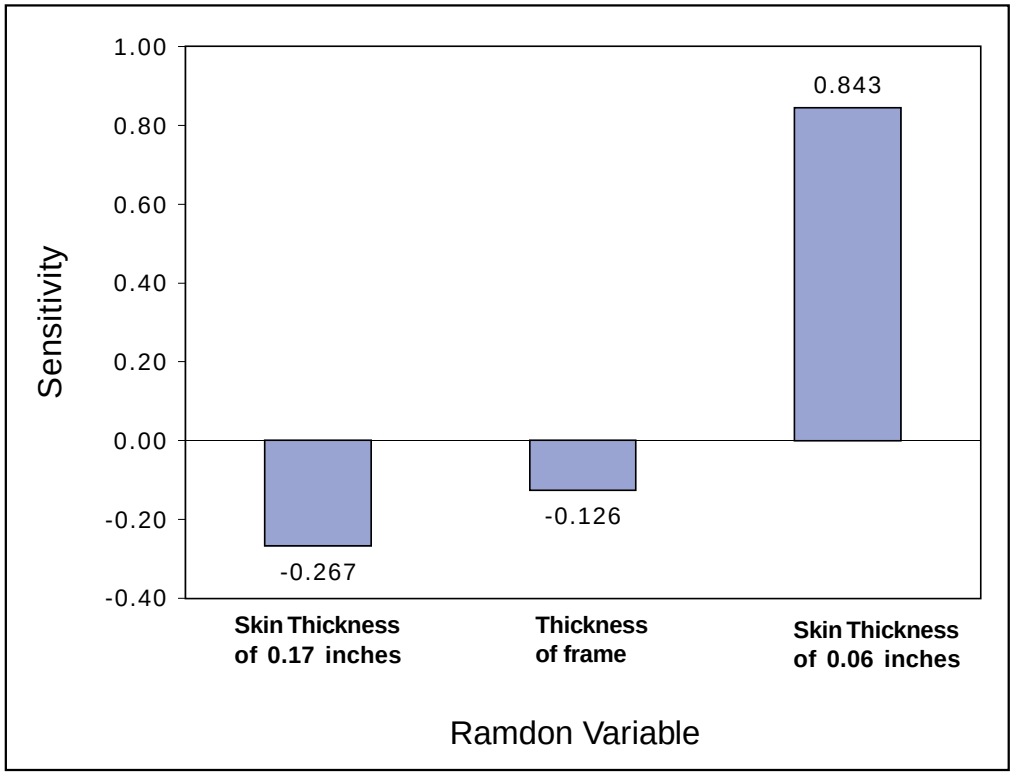

Figure 6-11. Sensitivity Shear Stress Skin and Frame Thicknesses

6.5 CDF AND SENSITIVITY ANALYSIS OF CROWN PANEL WITH 38-INCH SAW CUT

Probabilistic analysis was also performed on crown panels with a 38-inch saw cut. Deterministic analysis was used to determine the damage initiation load. At a pressure of 8.5 psi, damage initiated that grew into fracture at the crack tip. Probabilistic analysis was conducted at the equilibrium stage after fracture initiation. The thicknesses of skin, frame flange, frame blade, and stringer were selected as random variables. The coefficients of variation for all the design variables were taken as five percent. All random variables were assumed to have normal distributions. The response variables for probabilistic analysis were the circumferential stress in the direction of frame, stress in the direction of stringers, and shear stress at the crack tip where the fracture initiated.

Figures 6-12 to 6-14 show cumulative distribution function of stress at the crack tip. The sensitivity of the stresses to the four design parameters varies as a function of the probability level. Figures 6-15 to 6-17 show the sensitivity of the stresses response to the design variables at the 0.999 probability level.

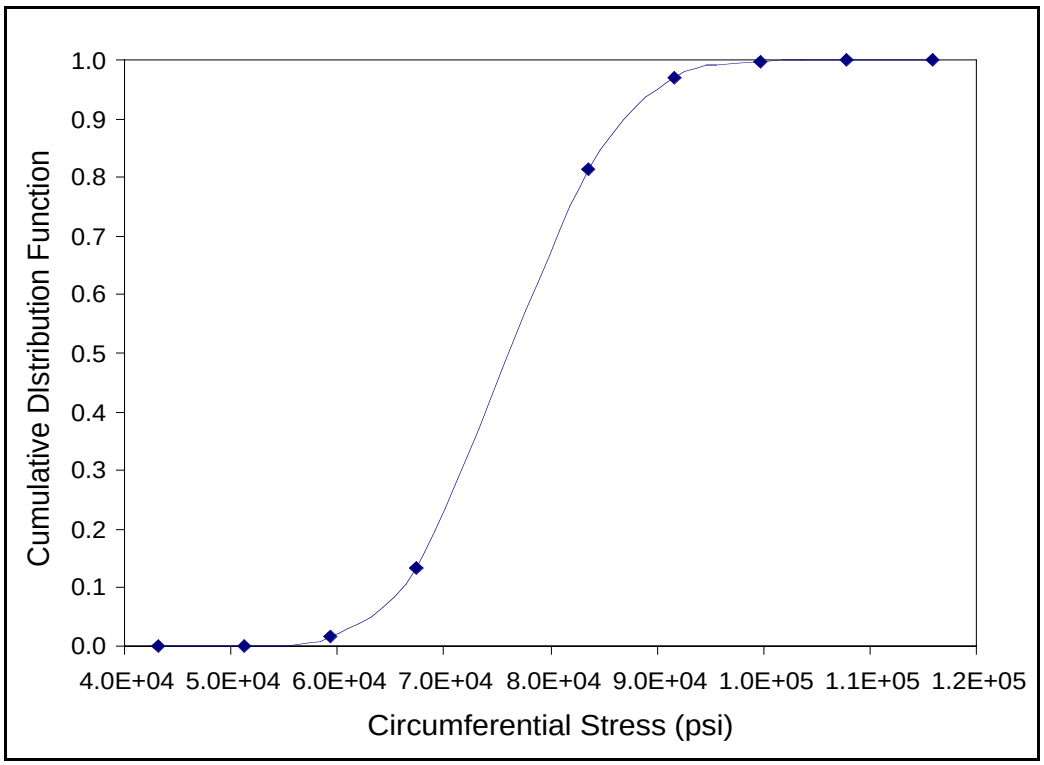

Figure 6-12. Cumulative Distribution Function Of Circumferential Stress At the Crack Tip Where Damage Initiated

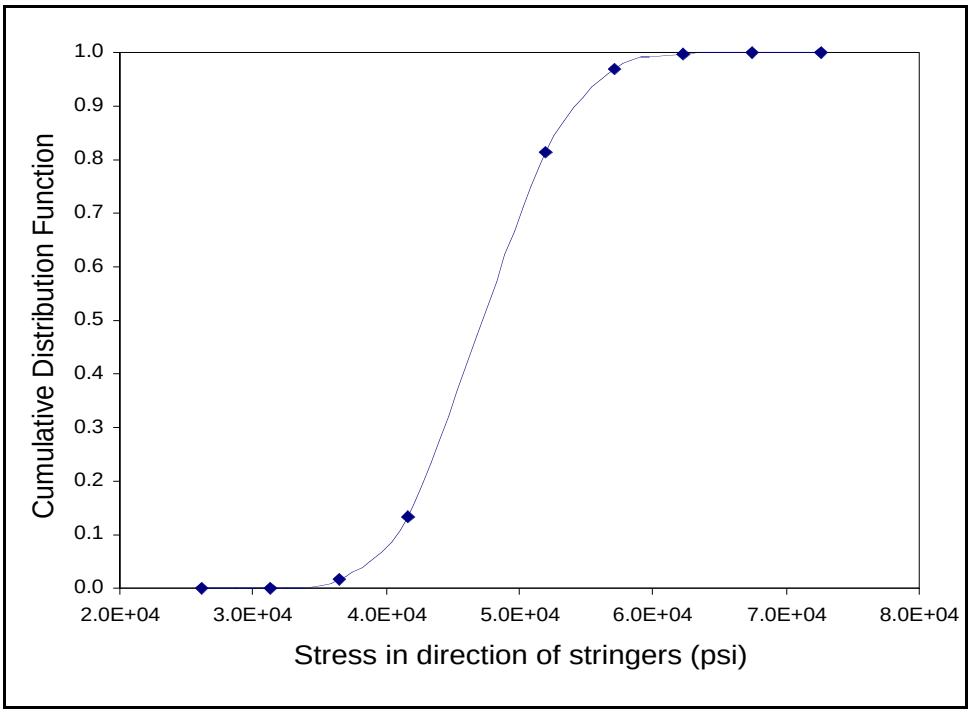

Figure 6-13. Cumulative Distribution Function Of Stress In The Direction Of Stringers At Crack Tip Where Damage Initiated

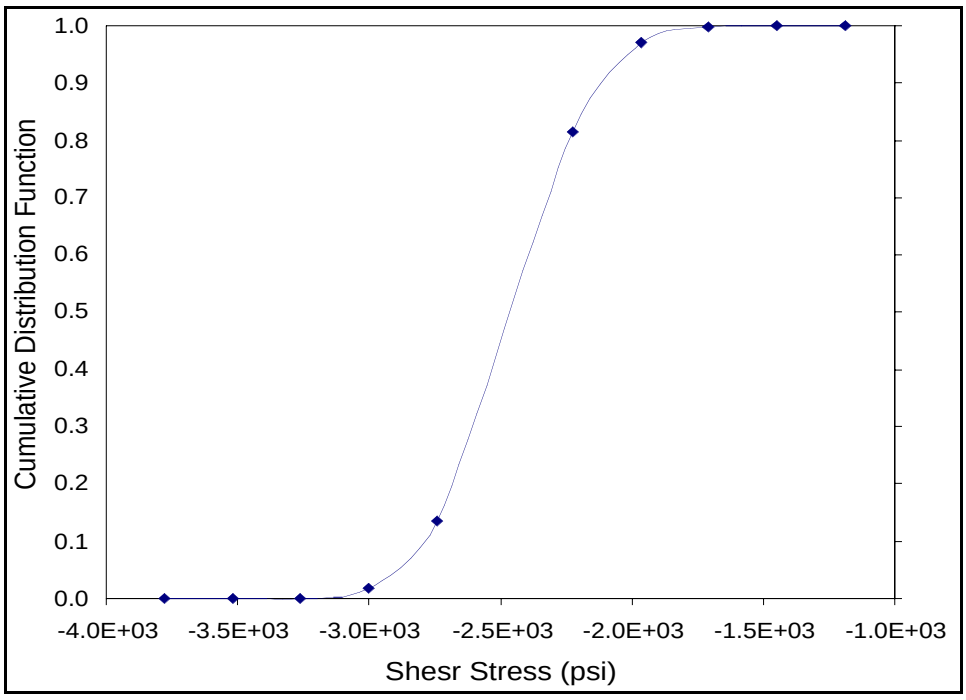

Figure 6-14. Cumulative Distribution Function Of Shear Stress At Crack Tip Where Damage Initiated

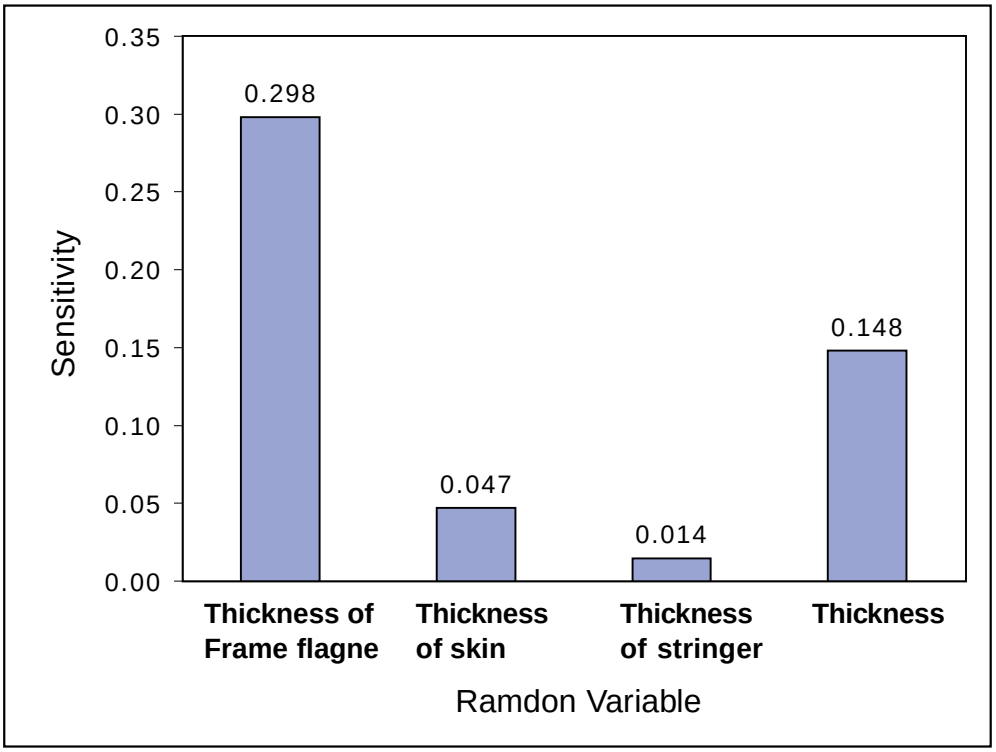

Figure 6-15. Sensitivity of Circumferential Stress Skin, Stringer And Frame Thicknesses

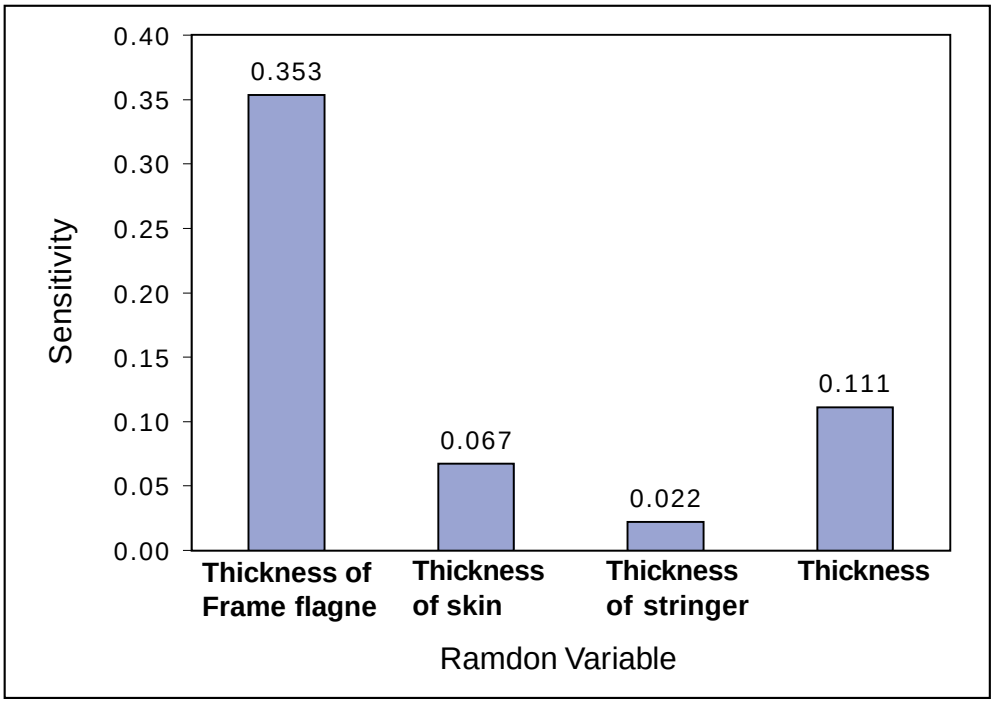

Figure 6-16. Sensitivity of Stress In The Stringer Direction Skin, Stringer And Frame Thicknesses

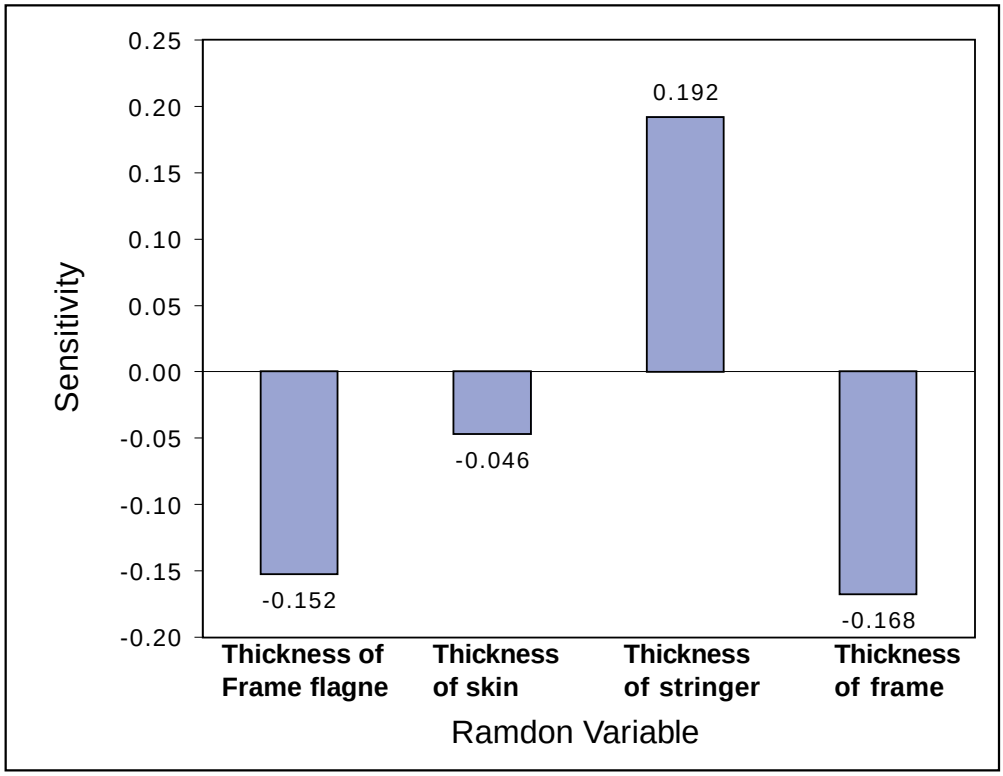

Figure 6-17. Sensitivity of Shear Stress To Skin, Stringer And Frame Thicknesses

Results have demonstrated that the probabilistic evaluation of a damaged composite structure can determine responses, which take into account the uncertainties of the design random variables. Further, the sensitivities of the responses to the design random variables quantified to help with design optimization decisions.

6-6 References

1. L. Minnetyan, C. C. Chamis, and P. L. N. Murthy, "Structural Behavior of Composites with Progressive Fracture," {Journal of Reinforced Plastics and Composites}, Vol. 11, No. 4, April 1992, pp. 413-442}

2. L. Minnetyan, P. L. N. Murthy, and C. C. Chamis, "Progressive Fracture in Composites Subjected to Hygrothermal Environment," International Journal of Damage Mechanics}, Vol. 1, No. 1, January 1992, pp. 60-79}

3. L. Minnetyan, C. C. Chamis, and P. L. N. Murthy, "Damage and Fracture in Composite Thin Shells," NASA TM--105289, November 1991}

4. L. Minnetyan, J. M. Rivers, P. L. N. Murthy, and C. C. Chamis, "Structural Durability of Stiffened Composite Shells," Proceedings of the 33rd SDM Conference, Dallas, Texas, April 13-15, 1992, Vol. 5, pp. 2879-2886}

5. P. K. Gotsis, C. C. Chamis, and L. Minnetyan, "Effect of Combined Loads on the Durability of a Stiffened Adhesively Bonded Composite Structure," Proceedings of the 36th SDM Conference, April 10-14, 1995, New Orleans, Louisiana, Paper No. 95-1283, pp. 1083-1092}

6. L. Minnetyan, P. L. N. Murthy, and C. C. Chamis, "Composite Structure Global Fracture Toughness via Computational Simulation," {Computers Structures}, Vol. 37, No. 2, pp.175-180, 1990}

7. P. L. N. Murthy and C. C. Chamis, {Integrated Composite Analyzer (ICAN): Users and Programmers Manual}, NASA Technical Paper 2515, March 1986.}

8. S. Nakazawa, J. B. Dias, and M. S. Spiegel, {MHOST Users' Manual}, Prepared for NASA Lewis Research Center by MARC Analysis Research Corp., April 1987.}

9. C. C. Chamis and M. C. Shiao, "IPACS -- Integrated Probabilistic Assessment of Composite Structures: Code Development and Application." Third NASA Advanced Composites Technology Conference, Long Beach, CA, June, 1992.}

7.0 Mechanics Of 3-D Woven, Braided And Stitched Composites

Because of the numerous possibilities with material combinations, laminate structure, braid yarn configurations, and loading conditions, it is essential to have an integrated computational capability to predict the behavior of three-dimensionally reinforced composite structures for any loading, geometry, composite material combinations, and boundary conditions. GENOA-PFA provides this computational capability with regard to progressive fracture tracking and assessment of failure modes using failure criteria associated with the negative and positive limits of the six local stress components in the material directions. Also, elastic orthotropic ply properties and stress limits of three-dimensionally reinforced fiber composites can be evaluated and the effects of fiber orientations in weave and braid textiles defined with reference to composite structural coordinates.

The stress limits in the three principal normal material directions are computed separately for tension and compression by the micromechanics equations in ICAN based on constituent stiffness, constituent strength, and fabrication process parameters [Ref 1-Murthy and Chamis, 1986]. Similarly, stress limits are computed for the three shear stress components in the material directions. The equations used for ply stress limits are given in the ICAN Users and Programmers Manual [Ref 2-Murthy and Chamis, 1986]. In the evaluation of 3D braided composite properties, the ICAN composite mechanics equations are used to compute stress limits in the principal material directions for each braid/weave.

Three-dimensional composites are reinforced with three dimensional textile preforms, which are fully integrated continuous-fiber assemblies with multi-axial in-plane and out-of-plane fiber orientations. These composites exhibit several distinct advantages, which are not realized in traditional laminates. First, because of the out-of-plane orientation of some fibers, three-dimensional composites provide enhanced stiffness and strength in the thickness direction. Second, the fully integrated nature of fiber arrangement in three-dimensional preforms reduces or eliminates the inter-laminar surfaces characteristic of laminated composites. Third, the technology of textile preforming provides the unique opportunity of near-net-shape design and manufacturing of composite components and, hence, minimizes the need for cutting and joining the of parts. The potential of reducing manufacturing costs for special applications is high.

Three-dimensional textile preforms can be categorized according to the manufacturing technique. These include braiding, weaving, knitting and stitching. Braiding preforms are formed with three basic techniques, namely two-step, four-step and multi-step braiding. In the case of two step braiding (Florentine 1992), the axial yarns are stationary and the braider yarns move among the axial yarns. In four-step braiding, all yarn carriers change their positions in the braiding process and do not maintain a straight configuration. Multi-step braiding (Kostar and Chou 1994) is an extension to the four-step braiding. By allowing for both individual controls of a given track/column and the insertion of axial yarns, the range of attainable braid architecture is greatly broadened in multi-step braiding.

In woven preforms, there are two major categories. The first is the angle-interlock multi-layer weaving technique which requires interlacing the yarns in three dimensions. The warp yarn in this three-dimensional construction penetrates several weft layers in the thickness direction, and therefore the preform structure is highly integrated. The second is the orthogonal wovens, for which the yarns assume three mutually perpendicular orientations in either a Cartesian coordinate system or a cylindrical coordinate system. The yarns in the Cartesian weave are not wavy, and as a result, matrix rich regions often appear in these composites.

The process of stitching is mainly based upon an existing technology for converting two-dimensional preforms to three-dimensional ones. This process is relatively simple. The basic needs include a sewing machine, needle and stitching thread. Major concerns of the stitching operation include depth of penetration of the stitching yarns and, hence, the thickness of two-dimensional preforms that can be stitch-bonded, as well as the degree of sacrifice of the in-plane properties due to the damage to in-plane yarns.

Three-dimensional knitted fabrics can be produced by either a weft knitting or warp knitting process. The technique of knitting is particularly desirable for producing preforms with complex shapes because the variability of the geometric forms is almost unlimited. The large extensibility and conformability of the

preforms enable them to be designed and manufactured for reinforcing composites subject to complex loading conditions. The versatility of knitted preforms offers a new dimension in textile structural composite technology.

Even though three-dimensional (3-D) composites have attracted much interest due to their unique mechanical properties, such as enhanced transverse moduli and strength, and improved shear resistance and impact damage tolerance, the actual use of the 3-D composite material in engineering design poses many problems. The main problem comes from the complex geometry of 3-D composites. The fiber geometry is so complex that the geometric modeling itself is very difficult, much less accurate stress distributions. For example, in plain weave textile composites, there are many fiber tows (warp and fill) interlacing each other. There can be nesting of the fiber tows of one layer in adjacent layers. The existence of matrix pockets adds to the complexity of the geometry. In fact, many research papers have been devoted just to modeling the geometry of 3-D composites (Pierce 1987, Pastore and Ko 1990, Du and Chou 1991).

The inherent geometric complexity of 3-D composites makes a detailed stress analysis very formidable. Most analytical and numerical techniques are merely used to predict the stiffness properties of 3-D composites. There are few models that have been developed for detailed stress analysis (Woo and Whitcomb 1994, Yoshino et al 1981, Kriz 1989, Pastore et al 1993) and the strength prediction of textile composites. To date, there is no information in the existing literature on simulating the entire procedure of damage propagation of 3-D composites. Some of the earlier works for predicting elastic constants, damage propagation, and strength of woven and braided composites are highlighted.

7.1 METHODOLOGY FOR ANALYTICAL SIMULATION OF 3D COMPOSITES

The standard ICAN code was enhanced to compute the elastic properties and stress limits of general 3D composites. The enhanced ICAN uses micromechanics modules to evaluate intraply hybrid composite properties which are computed separately for each fiber orientation present in a 3D braided/woven composite.

The 3D braided composite properties are obtained from stress-strain relations after using tensor transformations to rotate the local coordinate axes of the braids to the structural coordinate system of the 3D composite.. The local coordinate axes of a braid is taken with the x axis along the fiber direction of the braid. For each braid orientation, the ICAN input file is modified to define the direction of the braid x axis by inputting the angles made by the braid axis with the three global composite structural coordinates. Unless the local x axis is in the global z direction, the local y axis of the braid is determined in the direction of the cross product of the global z axis and the local x axis. If the local x axis is in the global z direction, the local y axis is taken to be in the direction of the cross product of the local x axis by the global x axis. The local z axis is determined by taking the cross product of local x and local y directions. Components of the unit vectors of braid local coordinates written with respect to the composite structural coordinates define the coefficients of the braid orientation matrix:

$$[\ell] = \begin{bmatrix} \ell_{11}\ell_{12}\ell_{13} \\ \ell_{21}\ell_{22}\ell_{23} \\ \ell_{31}\ell_{32}\ell_{33} \end{bmatrix} \tag{7-1}$$

The coefficients in the first row represent components of the unit vector along the braid fiber direction, defined with respect to the composite global x, y, z coordinates. The second and third rows respectively represent components of the unit vectors along the braid transverse local y and z directions with respect to the composite x, y, z coordinates. The elastic properties rotation matrix is defined in terms of the orientation matrix lij coefficients according to the following relations [Ref 3-Lekhnitskii 1977]:

$$[\Re] = \begin{bmatrix} \ell_{11}^2 & \ell_{12}^2 & \ell_{13}^2 & \ell_{12}\ell_{13} & \ell_{13}\ell_{11} & \ell_{12}\ell_{11} \\ \ell_{21}^2 & \ell_{22}^2 & \ell_{23}^2 & \ell_{23}\ell_{22} & \ell_{23}\ell_{11} & \ell_{12}\ell_{11} \\ \ell_{31}^2 & \ell_{32}^2 & \ell_{33}^2 & \ell_{33}\ell_{32} & \ell_{33}\ell_{31} & \ell_{33}\ell_{31} \\ 2\ell_{31}\ell_{21} & 2\ell_{32}\ell_{22} & 2\ell_{32}\ell_{22} & 2\ell_{33}\ell_{22} + 2\ell_{32}\ell_{23} & 2\ell_{33}\ell_{21} + 2\ell_{31}\ell_{23} & 2\ell_{31}\ell_{22} + 2\ell_{32}\ell_{21} \\ 2\ell_{31}\ell_{11} & 2\ell_{32}\ell_{12} & 2\ell_{33}\ell_{13} & 2\ell_{33}\ell_{12} + 2\ell_{32}\ell_{13} & 2\ell_{33}\ell_{11} + 2\ell_{31}\ell_{13} & 2\ell_{31}\ell_{12} + 2\ell_{32}\ell_{11} \\ 2\ell_{21}\ell_{11} & 2\ell_{12}\ell_{22} & 2\ell_{13}\ell_{23} & 2\ell_{13}\ell_{22} + 2\ell_{12}\ell_{23} & 2\ell_{13}\ell_{21} + 2\ell_{11}\ell_{23} & 2\ell_{11}\ell_{22} + 2\ell_{12}\ell_{21} \end{bmatrix} \quad (7\text{-}2)$$

The properties of each braid are transformed to the structural directions, multiplied by the ratio of fibers in that braid to the total composite fibers, and superimposed onto the 3D composite properties. When the contribution of each braid is added, composite structural properties are obtained. The 3D elastic, thermal, and hygral properties are represented by the following equations:

$$[E_c] = \sum_{j=1}^{Nw} f_{wj} \left[R_{wj}\right]^T \left[E_{wj}\right] \left[R_{wj}\right] \quad (7\text{-}3)$$

$$\{\alpha_c\} = [E_c] = \sum_{j=1}^{Nw} f_{wj} \left[R_{wj}\right]^T \left[E_{wj}\right] \left[\alpha_{wj}\right] \quad (7\text{-}4)$$

$$\{\beta_c\} = [E_c] = \sum_{j=1}^{Nw} f_{wj} \left[R_{wj}\right]^T \left[E_{wj}\right] \left[\beta_{wj}\right] \quad (7\text{-}5)$$

where N_w indicates the number of weave ply directions, $[R_{wj}]$ is the coordinate transformation matrix for the jth weave, f_{wj} is the jth weave or braid ply volume fraction, (viz. $\sum_{j=1}^{Nw} f_{wj} = 1$), and E_{wj} is the stiffness matrix in the local coordinate system of the jth weave ply.

7.0 Mechanics Of 3-D Woven, Braided And Stitched Composites

The structural properties may be supplied to a 3-D finite element module for global structural analysis. Similarly, the generalized force-deformation and moment-curvature relations for laminate analysis are represented by the equations:

$$\begin{Bmatrix} \{N_{Cx}\} \\ \{M_{Cx}\} \end{Bmatrix} = \begin{bmatrix} [A_{CX}] & [C_{Cx}] \\ [C_{Cx}] & [D_{Cx}] \end{bmatrix} \begin{Bmatrix} \{E_{Csx}\} \\ \{W_{Cb}\} \end{Bmatrix} - \begin{Bmatrix} \{N_{CT\ell X}\} \\ \{M_{CT\ell X}\} \end{Bmatrix} - \begin{Bmatrix} \{N_{CM\ell X}\} \\ \{M_{CM\ell X}\} \end{Bmatrix} \tag{7-6}$$

Where $\{N_{cx}\}$ represents the applied in-plane forces, $\{M_{cx}\}$ represents the bending moments, $\{E_{csx}\}$ represents the in-plane strains, $\{W_{cb}\}$ represents the out-of-plane curvatures, $\{N_{CTlX}\}$ represents the thermal forces, $\{M_{CTlX}\}$ represents the thermal moments, $\{N_{CMlX}\}$ represents the hygral forces, and $\{M_{CMlX}\}$ represents the hygral moments. The laminate equations contain the contribution of weave or braid plies as well as the contribution of the in-plane plies as follows:

$$[A_{cx}] = \frac{1}{2} \sum_{i=1}^{Ni} \left(Z_{l\,i+1} - Z_{l\,i+1} \right) \left[\sum_{j=1}^{Nw} f_{wj} \left[R_{wj} \right]^T \left[E_{wij} \right] \left[R_{wj} \right] \right] \tag{7-7}$$

$$[C_{cx}] = \frac{1}{2} \sum_{i=1}^{Ni} \left(Z_{l^2{}_{i+1}} - Z_{l^2{}_{i+1}} \right) \left[\sum_{j=1}^{Nw} f_{wj} \left[R_{wj} \right]^T \left[E_{wij} \right] \left[R_{wj} \right] \right] \tag{7-8}$$

$$[D_{cx}] = \frac{1}{3} \sum_{i=1}^{Ni} \left(Z_{l^3{}_{i+1}} - Z_{l^3{}_{i+1}} \right) \left[\sum_{j=1}^{Nw} f_{wj} \left[R_{wj} \right]^T \left[E_{wij} \right] \left[R_{wj} \right] \right] \tag{7-9}$$

$$[N_{CT\ell X}] = \sum_{i=1}^{Ni} \Delta T_{l_i} \left(Z_{l_{i+1}} - Z_{l_{i+1}} \right) \left[\sum_{j=1}^{Nw} f_{wj} \left[R_{wj} \right]^T \left[E_{wij} \right] \left[R_{wj} \right] \right] \tag{7-10}$$

$$[N_{CM\ell X}] = \sum_{i=1}^{Ni} M_{l_i} \left(Z_{l_{i+1}} - Z_{l_i} \right) \left[\sum_{j=1}^{Nw} f_{wj} \left[R_{wj} \right]^T \left[E_{wij} \right] \left[R_{wj} \right] \right] \tag{7-11}$$

$$[M_{CT\ell X}] = \frac{1}{2} \sum_{i=1}^{Ni} \Delta T_{l_i} \left(Z_{l^2{}_{i+1}} - Z_{l^2{}_{i+1}} \right) \left[\sum_{j=1}^{Nw} f_{wj} \left[R_{wj} \right]^T \left[E_{wij} \right] \left[\alpha_{wj} \right] \right] \tag{7-12}$$

$$[M_{CM\ell X}] = \sum_{i=1}^{Ni} M_{l_i} \left(Z_{l^2{}_{i+1}} - Z_{l^2{}_{i+1}} \right) \left[\sum_{j=1}^{Nw} f_{wj} \left[R_{wj} \right]^T \left[E_{wij} \right] \left[\beta_{wj} \right] \right] \tag{7-13}$$

The through-the-thickness composite properties given by Eq. (6) may be supplied to a structural analysis module that uses shell finite elements. After a finite element analysis, the computed generalized nodal force/moment resultants and deformations can be supplied to the modified ICAN module that then evaluates the nature and amount of local damage, if any, in the plies of the composite laminate. Individual ply/braid/weave failure modes are assessed by via failure criteria associated with the negative and positive limits of the six ply-stress components in the material directions,and a modified distortion energy (MDE) combined stress failure criterion [Ref 4-Murthy and Chamis, 1986].

Fiber volume ratios may be different for each braid orientation as specified by material inputs to ICAN. Also, different fibers may be selected for different braids and laminae. Results indicate the implemented method is consistent with published results [5,6]. but there remain some differences between the computed elastic properties and experimental data. These differences may be due to the effects of fiber waviness and residual stresses introduced by the curing process.

The fundamental distinction of the present method is that the augmented ICAN code is also able to compute the 3D composite stress limits by accumulating the contribution of each braid/weave/ply to each composite strength component via tensor transformations of local strengths in the absolute value. The stress limits in the composite structural coordinates corresponding to first ply failure (FPF) are written in general as:

$$\{S_{a\pm}\} = \sum_{j=1}^{Nw} f_{wj}\left[Abs\left(R_{wj}\right)\right]^{T}\{S_{wi\pm}\} \tag{7-14}$$

Where $S_{c\pm}$ represents the positive or negative stress limits in the composite structural coordinate directions;
$S_{c\pm}$ represents the stress limits in the local coordinate system of each braid or ply; and $[Abs(R_{wj}]$ is the property rotation matrix taken in the absolute value. In composite strength computations, the fiber and matrix contributions are considered separately to enable the representation of matrix damage that degrades the composite properties prior to fracture.

Each of the three composite normal stress limits are computed in both tension and compression. At the stage of matrix damage initiation, tensile stress limits are determined by the stress contributions from all components excepting the fiber tensile strength. In computing the composite tensile fracture strengths, only the contributions of fiber strengths are considered. Compressive normal stress limits are also computed with reference to matrix crushing and fiber fracture. Similarly, shear strengths are obtained with reference to the three global structural axes by the accumulation of absolute tensor transformations of braid shear strengths and the relevant normal strength contributions. The appropriate normal strength components for the computation of shear strengths are the compressive strength in the braid longitudinal direction and tensile strengths in the braid transverse direction..

The computed elastic properties and the composite stress limits for each of eleven specimens are given in Tables 7-1 and 7-2. The computed components of strength (with names ending with the letter “f”) correspond to the stress limits for fiber fracture in the absence of matrix degradation in the composite. Strength components (with names ending with the letter “m”) indicate the matrix damage initiation stresses. Any general 3D composite structure with arbitrary fiber orientations can be analyzed for stress limits as well as composite elastic properties.]

7.0 Mechanics Of 3-D Woven, Braided And Stitched Composites

The following woven composite examples assume that the x axis is taken in the direction of the stuffer fibers, the y axis is taken in the direction of the filler fibers, and the z axis is taken in the normal direction. Warp fibers are in various directions depending on the specimen.

7.1.1 Stiffness Properties of Three Dimensional Composites

The stiffness averaging method which was developed by Kregers et al (1978, 1979) is widely used to predict the deformation characteristics of a composite with three-dimensional reinforcement from the known mechanical properties of its components. The basic idea behind stiffness averaging method is to treat the fibers and matrix as a set of composite rods having various spatial orientations. The local stiffness tensor for each of these rods is calculated and rotated in space to fit the global composite axes. The global stiffness tensors of all the composite rods are then superimposed with respect to their relative volume fraction to form the composite stiffness tensor. This approach is also called the Fabric Geometry Model (Pastore and Gowayed, 1994) or Orientation Averaging Method. The stiffness of the individual directions of reinforcement are averaged in accordance with the following expressions:

$$A_{jklm} = \frac{1}{V}\sum_{i=1}^{N} V_i A_{jklm}^{(i)}$$
$$V = \sum_{i=1}^{N} V_i \qquad (7\text{-}15)$$

Where A_{jklm} are the components of the stiffness tensor of the three-dimensionally reinforced composite: V_i is the calculated volume of the *i-th* direction of reinforcement; N is the number of discrete directions of reinforcement, $N \geq 1$.

Ko (1986) presented a geometric model for three-dimensional braid composite using the concept of average cosine to evaluate the tensile strength and modulus of a three-dimensional braid composite. The three-dimensional braid composite was divided into a series of unit cells and the yarn segment was idealized as straight in a unit cell as shown in Figure 7-1.

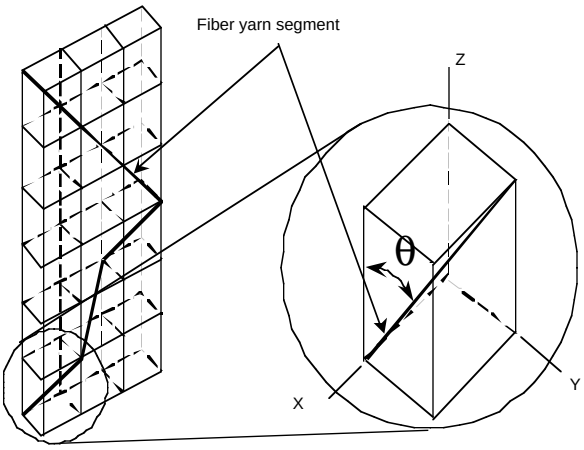

Figure 7-1. Idealized Fiber Yarn Segment in Unit Cell of 3D Braid Composites

To obtain an average representation of yarn orientation, the average cosine of yarn angles was used:

$$\cos\bar{\theta} = ND_y / D_f \qquad (7\text{-}16)$$

Where N = number of yarns in the fabric, D_y = yarn linear density, D_f = fabric linear density. The predicted composite tensile strength and modulus in the longitudinal direction based on the average angle of yarn, in general, were within 20 percent of the experimental results.

The concept of unit cell structure have been used by many investigators to facilitate the description of complex geometry of 3-D composites. A unit cell is a representative volume element small enough to reflect the structural details, yet large enough to represent the overall response of the composite. When unit cells are repeated, they will reconstruct the entire structural geometry.

7.0 Mechanics Of 3-D Woven, Braided And Stitched Composites

Yang et al. (1986) presented a "Fiber Inclination Model" to predict the elastic properties of 3-D textile structural composites. The unit cell of a composite was treated as an assemblage of inclined unidirectional laminate. The orientation of the yarns, for a 3-D braided composite, in the braided preform is controlled by the three orthogonal motions. Therefore, the resultant preform is a continuous interwoven structure composed of yarns oriented in various directions. An idealized unit cell structure is constructed based upon the fiber bundles oriented in four body diagonal direction in a rectangular parallelepiped which is shown schematically in Figure 7-2, the unit cell is considered as an assemblage of four inclined unidirectional laminae, and each unidirectional laminae is characterized by a unique fiber orientation and all the laminae have the same thickness and fiber volume fraction of each lamina is assumed to be the same as that of the composite. The laminate approximation of the unit cell structure is shown schematically in Figure 7-3. The properties of each lamina can be obtained from the classical laminated plate theory, the composite properties can be obtained from these lamina properties based on the stiffness averaging approach.

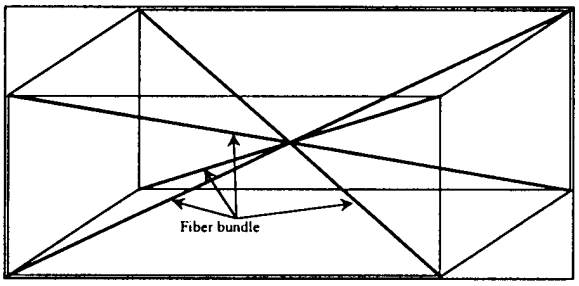

Figure 7-2. The Unit Cell Structure of a 3-D Braided Structural Composites With Yarns Moving in Three Orthogonal Directions

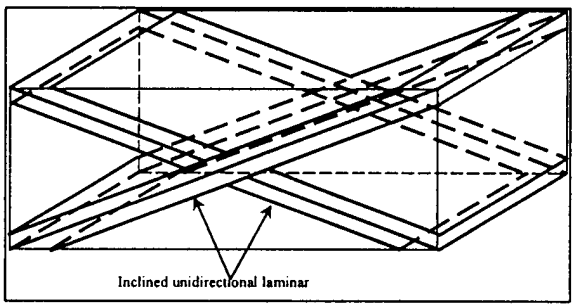

Figure 7-3. The Unit Cell of the "Fiber Inclination Model" Composed of Four Unidirectional Laminae

Whitney et al. (1989) extended the Fiber Inclination Model to predict the in-plane elastic properties of 3-D angle-interlock textile structural composites. In the case of angle-interlock geometry, the unit cell is inherently more complex. Since there are no repeatable units in the thickness direction, the unit cell essentially occupied the entire preform thickness. Also, the yarns can occupy any number of positions within the unit cell. Yarns in warp and weft directions may occupy positions which are horizontal or inclined in the thickness direction. To account for varying bundle positions, the authors divided the unit cell into micro-cells that are repeated to reconstruct the entire unit cell, and the calculations are made on a generic unit cell with micro-cells. Crimping of fibers at the corners of the cell and the intersection of fibers at the unit cell center are ignored.

Stiffness averaging method was also used to predict elastic constants of two-step braided composites by Byun et al. (1991). The architecture of this material was investigated by identifying the geometric and braiding process parameters which include the linear density ratio between axial and braider yarns, the aspect ratio of axial yarn and the aspect ratio of braider yarn. The predicted results of axial tensile modulus shows reasonably good agreements with test results, however, shear moduli show a lack of agreement between prediction and measurement.

All the aforementioned models are based on the concept of averaging stiffness. Ma et al. (1990) developed another methodology based on an energy approach to evaluate elastic stiffness of 3-D braided textile structural composites. Three types of elastic strain energies in the composite rods were taken into account. These included the strain energies due to bending, extension, and compression over the region of fiber contact. Closed form expressions for axial elastic moduli and Poisson's ratio were derived as functions of fiber volume fraction and fiber orientations. Numerical results show that the axial elastic moduli are sensitive to the geometrical braiding pattern. The moduli increase as the yarn orientation angle decreases, that is, the fiber becomes more aligned with the tensile axis.

Fiber bundle orientations are the essential geometrical properties for determining mechanical behavior. For the sake of simplicity, the geometry of 3-D composites have been represented by idealization rather than reality by most researchers. Most models have dealt with perfectly regular structures. The fibers are assumed to be straight inside a unit cell. However, real composites are highly irregular, and waviness of fibers is unavoidable. The angles between axial tows and braiders change in an irregular way. In order to take account of these irregularities, Cox and Dadkhah (1995) promoted a more practical approach to characterize the geometrical inconsistencies of typical triaxially braided composites. Out-of-plane misalignments were taken into account by introducing a cumulative probability distribution (CPD) for the misalignment angle ξ. Typical CPDs can be fit quite well by a symmetric normal distribution $F_\xi(\xi)$ with corresponding density function $f_\xi(\xi) = dF_\xi / d\xi$ given by

$$f_\xi(\xi) = \frac{1}{\sigma_\xi \sqrt{2\pi}} \exp\left(-\xi^2 / 2\sigma_\xi^2\right). \tag{7-17}$$

The standard deviation σ_ξ can be determined experimentally. The Young's modulus E_x can be determined by

$$< E_x > = \left\{ \int_{-\infty}^{\infty} \frac{f_\xi(\xi) d\xi}{\overline{E}_x} \right\}^{-1} \tag{7-18}$$

Where $E_x(\xi)$ is Young's modulus for a unidirectional composite under a load oriented at angle ξ to the fiber direction X. $\overline{E}_x(\xi)$ can be expressed by

$$\frac{1}{\overline{E}_x(\xi)} = \frac{\cos^4 \xi}{E_x} + \cos^2 \xi \sin^2 \xi \left(\frac{1}{G_{xy}} - \frac{2\upsilon_{xy}}{E_x} \right) + \frac{\sin^4 \xi}{E_y} \tag{7-19}$$

7.1.2 Stress and Strength Analysis of Three Dimensional Composites

Strength of 3-D composites is more difficult to predict than stiffness. This section summarizes work done on predicting the strength, fracture, and damage tolerance behavior of 3-D composites.

7.0 Mechanics Of 3-D Woven, Braided And Stitched Composites

Ishikawa and Chou (1983)developed a 2-D fiber undulation model based on classical lamination theory which considered the undulation in the fill yarn direction but neglected the undulation in the warp yarns of woven composites. They modeled nonlinear shear response of both the fill yarns and the interstitial matrix along with the effects of transverse cracking of the warp yarns to predict the knee in the stress-strain response of woven composites. Kriz (1985) used a generalized plane strain finite element model which assumed a linear undulation path for the fill and warp yarns to study the effect of transverse cracking on the stiffness and internal stresses of a glass/epoxy plain weave composite.

Stanton and Kipp (1985) developed a nonlinear constitutive model for plain weave carbon-carbon composites which accounted for the differences in tension and compression response, warp-fill crossover damage and multiaxial stress interactions using a simple interaction formula along with experimental stress-strain data for all six components under tension and compression loading. Jortner (1986) developed a 2-D mechanistic model which modeled the undulations of the fill yarns but neglected the undulations of warp yarns. He used a stress-averaging scheme which accounted for the nonlinear shear response of the fill yarns and the transverse cracking of the warp yarns to analyze plain weave carbon-carbon composites.

Ko and Pastore (1985)used a fabric geometry model to define the yarn orientations in a three-dimensional braided composite. They used the yarn orientations to first estimate the strength of the fabric preform and then compute composite strength using a simple rule of mixtures. Ko (1989)also used the fabric geometry model together with a maximum strain energy criterion to predict yarn failures and ultimate strength of a 3-D braided composite.

Dow and Ramnath (1987) modeled woven fabric composites using a simple geometry model that assumed a linear undulation path for the fill and warp yarns. They computed constituent fiber and matrix stresses from local yarn stresses which were calculated using an iso-strain assumption and predicted failure based on the average stresses in the fiber and the matrix along with a maximum stress criterion. Dow and Ramnath (1987) used the fabric geometry model together with a simple linear yarn bending model and an iso-strain assumption to compute average fiber and matrix stresses which were used to predict local yarn failure and strength for 2-D triaxial braided composites.

Naik (1994 & 1995) developed a micromechanics analysis technique for the prediction of failure initiation, damage progression, and strength of 2-D woven and braided composite materials. The yarn architecture was discretely modeled using sinusoidal undulations at yarn crossovers. Overall thermal and mechanical properties were calculated based on an iso-strain assumption. This analysis technique included the effects of nonlinear shear response and nonlinear material response due to the accumulation of damage in the yarns and the interstitial matrix and also the effects of yarn bending and the geometrically nonlinear effects of yarn straightening/wrinkling during axial tension/compression loading. Parametric studies were also performed on the woven and braided architectures to investigate the effects of yarn size, yarn spacing, yarn crimp, braid angle, and overall fiber volume fraction on the strength properties of the textile composite.

Three-dimensional finite element models (FEM) have also been used for the prediction of nonlinear material properties (Bhandarker et al 1991) and the modeling of damage (Blackketter 1993) of plain weave composites. The 3-D FEMs are highly computer intensive and also require considerable time and effort for model generation. Foye (1993) developed homogenized replacement finite elements and analyzed sub-cells within the repeating unit cell to overcome these limitations. However, he had to manually calculate the orientations of the different yarn directions, yarn interfacial planes and volume fractions, for each element in the 3-D model. FEM is, therefore, not well suited for performing parametric studies to investigate the sensitivity of composite strength properties to fabric architecture parameters.

Compared with the regular finite element analysis, a global/local finite element method which was developed by Sun and Mao (1988 and 1990) is more efficient to analyze textile composites. The global/local finite element method was based on the regular finite element method in conjunction with three basic steps, i.e. the global analysis, the local analysis and the refined global analysis. In the first two steps, a coarse finite element mesh was used to analyze the entire structure to obtain the nodal displacements which were subsequently used as displacement boundary conditions for local regions of interest. These local regions with the prescribed boundary conditions were then analyzed with refined meshes to obtain more accurate stresses. In the third step, a new global displacement distribution based on the results of the previous two steps was assumed for the analysis, from which, such improved solutions for both stresses and displacements were produced.

Woo and Whitcomb (1994 and 1996) utilized global/local finite elements to analyze textile composites. A relatively crude global mesh was used to obtain the overall response of the structure and refined local meshes were used in the region of interest where rapid stress change may occur. The homogenized engineering properties could be used in the crude global mesh away from the free boundary and transitional regions. In the local meshes, the details of the coarse microstructure of textile composites (e.g., the individual tows and matrix pockets) could be modeled discretely. In the transitional range of microstructure, however, discrete modeling may not be practical even with supercomputers due to the huge computer memory and CPU requirements. Use of homogenized material properties is also usually inappropriate. In this range, special macro finite elements can be used. The macro-elements employ a number of subdomains or subelements to account for the micro-structural details inside individual elements. Whitcomb et al. (1994) discussed two types of macro-elements. The elements described in these references are based on single or multiple assumed displacement fields.

The global/local method with local refinement assumes that the region, which, requires further mesh refinement can be localized. If the solution behavior is complicated everywhere, the correction by the global/local iteration does not necessarily reflect the nature of the true solution accurately. For example, if the solution behavior is complicated everywhere and only some portion of the global domain is refined in the local mesh, the global/local iteration may do more harm than good in solving the problem. A solution to this problem is using an engineering global/local analysis. In this procedure, the initial coarse global solution is assumed to be close enough for the purpose at hand. That is, no global/local iteration is employed. The local problem is solved only once with boundary displacements from the coarse global solution.

7.1.3 Woven Patterns

Xu et al. (1994) provided complete statements of the rather complex sequencing of through-the-thickness yarns. Figure 7-4 shows the three typical types of weave in woven composites, namely, (a) layer to layer, (b) through the thickness angle interlock, (c) orthogonal interlock weaves.

In woven composites, the stuffers and fillers alternate in layers through thickness. The stuffers and fillers form a coarse 0°/90° array shown in Figure 7-4 for most woven composites. Nevertheless, the proposed method allows the arbitrary orientation of stuffers and fillers in the X-Y plane. The through the thickness reinforcement, or warp weavers, may be oriented in any direction with reference to the 3D composite coordinate axes. Stitched composites may be modeled by weaver or stitch fibers that are oriented perpendicular to the X-Y plane and parallel to the Z-axis of the composite.

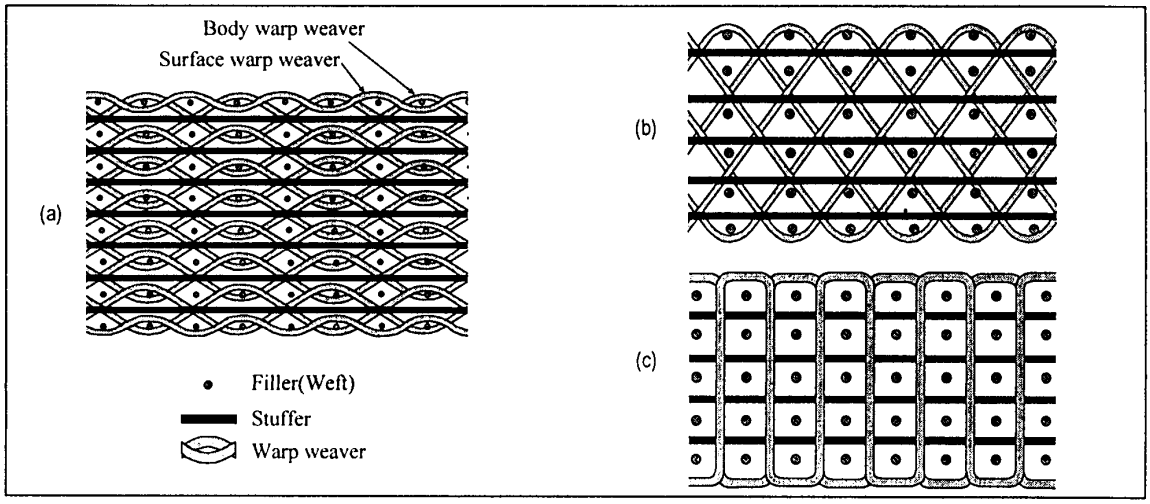

Figure 7-4. Schematics of (A) Layer-to-layer Angle Interlock, (B) Through-the- Thickness Angle Interlock, and (C) Orthogonal Interlock Weaves.

7.1.4 Fiber Arrangement

Complete understanding of arrangement of fibers, including stuffer, filler, and warp weaver fibers, is essential to predict the engineering properties accurately. Woven composites are typically composed of n_s layers of stuffers and n_s+1 layers of fillers through the thickness as shown in Figure 7-5.

In order to estimate the elastic properties of 3-D woven composites, an approach based on modified laminate theory and orientation average is used. First of all, composites are divided into plies so that every ply contains either stuffer or filler fibers as shown in Figure 7-6. Since the weaver fibers go through the entire thickness, each ply must contain some weaver fibers for woven composites.

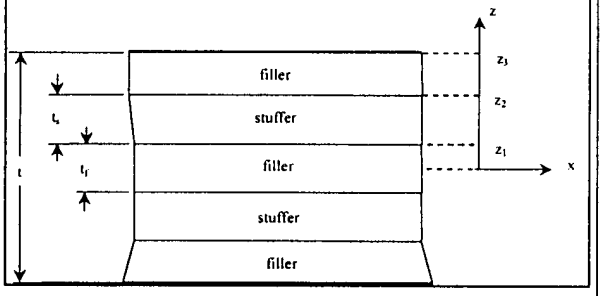

Figure 7-5. Representative Layer Sequence of Fillers and Stuffers Through the Thickness, With the Layer Thickness T_f and T_s Defined. For the Case Shown n_s = 2

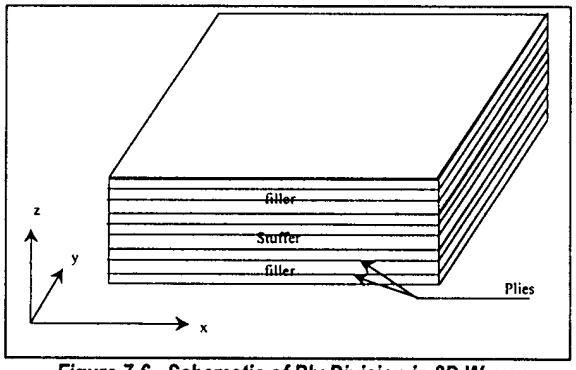

Figure 7-6. Schematic of Ply Division in 3D Woven Composites

For orientation averaging, a three-dimensional fiber arrangement can be considered as composed of two types of structures, the baseline structure formed by fibers in X-Y plane direction, such as stuffer fibers and filler fibers, and the interwoven or braided structure composed of warp weaver fibers which penetrate the thickness of composites. Therefore each ply contains two types of domains, the primary domains which consist of baseline fibers, and the weaver domains which consist of weaver fibers, the occupying volume fractions of these domains are denoted by f_p and f_w respectively. Each domain is

characterized by an orientation along which the fibers within it are presumed to lie. All of the fibers in the primary domains are assumed to be parallel to X-Y plane and each ply can consist of the primary fibers in the same direction. Warp weaver fibers are always assumed to be piecewise straight and their orientations are defined by the directional angles to the X,Y,Z axes.

Let $[E^{(\alpha)}]$ denotes the stiffness matrix for domain α . Basing on orientation averaging method, the composite stiffness matrix $[E_C]$ of 3-D woven composite can be predicted by the following equation:

$$\left[E_C\right] = \sum_{\alpha} f_{\alpha}\left[\tilde{E}^{(\alpha)}\right] \tag{7-20}$$

Where $[\tilde{E}^{(a)}]$ denotes $[E^{(\alpha)}]$ transformed from domain α material coordinate system into the composite coordinate system and f_{α} denotes volume fraction of domain α.

7.1.5 Three Dimensional Hygrothermoelastic Properties

The first step in the computation of composite properties for any fiber configuration is the evaluation of the local orthotropic properties of a unidirectional composite ply. From composite mechanics (Jones, 1975), the compliance (inverse stiffness) matrix in material axes for each orthotropic ply written in terms of the engineering constants is

$$\left[\overline{E}_{\alpha}\right]^{-1} = \begin{bmatrix} \frac{1}{E_{11}} & -\frac{\upsilon_{21}}{E_{22}} & -\frac{\upsilon_{31}}{E_{33}} & 0 & 0 & 0 \\ -\frac{\upsilon_{12}}{E_{11}} & \frac{1}{E_{22}} & -\frac{\upsilon_{32}}{E_{33}} & 0 & 0 & 0 \\ -\frac{\upsilon_{13}}{E_{11}} & -\frac{\upsilon_{23}}{E_{22}} & \frac{1}{E_{33}} & 0 & 0 & 0 \\ 0 & 0 & 0 & \frac{1}{G_{23}} & 0 & 0 \\ 0 & 0 & 0 & 0 & \frac{1}{G_{31}} & 0 \\ 0 & 0 & 0 & 0 & 0 & \frac{1}{G_{12}} \end{bmatrix} \tag{7-21}$$

Total ply stiffness properties of a composite layer containing one primary in-plane fiber orientation and N_w weaver orientations can be obtained from combination of the primary domain and weaver domain properties according to their volume fractions. Note that it is possible for a ply to have multiple weaver domains, but only one primary domain is considered. Therefore the stiffness matrix for the *ith* layer containing the primary and weaver domains may be written as:

$$\left[\overline{E}_i\right] = f_p\left[\overline{R}_i^p\right]^T\left[\overline{E}_i^p\right]\left[\overline{R}_i^p\right] + \sum_{j=1}^{N_w} f_{w_j}\left[\overline{R}_i^{w_j}\right]^T\left[\overline{E}_i^{w_j}\right]\left[\overline{R}_i^{w_j}\right] \tag{7-22}$$

where

$\overline{E}_i$ is the three dimensional lamina stiffness matrix of *ith* ply.

R_i^p is the three dimensional coordinate transformation matrix from primary domains material axes to composite structural axes. If the angle between material axes and structural axes is θ, R_i^p can be expressed by

$$\overline{R}_i^p = \begin{bmatrix} \cos^2\theta & \sin^2\theta & 0 & 0 & 0 & 2\cos\theta\sin\theta \\ \sin^2\theta & \cos^2\theta & 0 & 0 & 0 & -2\cos\theta\sin\theta \\ 0 & 0 & 1 & 0 & 0 & 0 \\ 0 & 0 & 0 & \cos\theta & -\sin\theta & 0 \\ 0 & 0 & 0 & \sin\theta & \cos\theta & 0 \\ -\cos\theta\sin\theta & \cos\theta\sin\theta & 0 & 0 & 0 & \cos^2\theta - \sin^2\theta \end{bmatrix} \quad (7\text{-}23)$$

f_p is the primary domain volume fraction

N_w is the number of weaver domains, each weaver domain consists of weaver fibers in the same direction. If weavers contain fibers in different direction, they should be grouped into different weaver domains.

$\overline{R}_i^{w_j}$ is the three dimensional coordinate transformation matrix from *jth* weaver domains material axes to composite structural axes. Since directions of weavers are arbitrary, there dimensional coordinate transformation matrix is used here. If the direction cosines between the weaver local axes and structural axes are $l_1, m_1, \ldots, n_3$, $\overline{R}_i^{w_j}$ can be written as (Lekhnitskii 1977),

$$\overline{R}_i^{w_j} = \begin{bmatrix} l_1^2 & m_1^2 & n_1^2 & l_1m_1 & m_1n_1 & n_1l_1 \\ l_2^2 & m_2^2 & n_2^2 & l_2m_2 & m_2n_2 & n_2l_2 \\ l_3^2 & m_3^2 & n_3^2 & l_3m_3 & m_3n_3 & n_3l_3 \\ 2l_1l_2 & 2m_1m_2 & 2n_1n_2 & (l_1m_2 + l_2m_1) & (m_1n_2 + m_2n_1) & (n_1l_2 + n_2l_1) \\ 2l_2l_3 & 2m_2m_3 & 2n_2n_3 & (l_2m_3 + l_3m_2) & (m_2n_3 + m_3n_2) & (n_2l_3 + n_3l_2) \\ 2l_3l_1 & 2m_3m_1 & 2n_3n_1 & (l_3m_1 + l_1m_3) & (m_3n_1 + m_1n_3) & (n_3l_1 + n_1l_3) \end{bmatrix} \quad (7\text{-}24)$$

f_{w_j} is the *jth* weaver domain volume fraction

Note: $f_p + \sum_{j=1}^{N_w} f_{w_j} = 1$

$\overline{E}_i^{w_j}$ is the Stiffness matrix in the local coordinate system of *jth* weaver in *ith* ply. Before damage occurs, $\overline{E}_i^{w_j}$ should be same for each *i* since we assume every layer to have the same weaver arrangement. But after damage, every layer may have its own property degradation which could be different between layers, therefore degraded $\overline{E}_i^{w_j}$ could be different for different *i*.

7.0 Mechanics Of 3-D Woven, Braided And Stitched Composites

In order to differentiate three dimensional properties from two dimensional properties which are discussed in the next section, an overbar is added to three dimensional stiffness matrices and coordinate transformation matrices, such as $\left[\overline{E}_i\right]$ and $\left[\overline{R}_i\right]$.

The averaged properties of the entire composite laminate can be obtained by summing up all the layer properties and the properties due to interply distortion energy (Murthy, P.L.N., Chamis 1986). The interply distortion energy terms represent the stiffening effects of changes in the primary fiber orientation angles between adjacent layers. Therefore the composite laminate stiffness matrix is written as:

$$\left[\overline{E}_C\right] = \frac{1}{t_C}\left[\sum_{i=1}^{N_l}\left(z_{i+1}-z_i\right)\left[\overline{E}_i\right] + \sum_{j=1}^{N_l-1} H_j\left[\overline{S}_j\right]\right] \tag{7-25}$$

where

$\overline{E}_C$ is the three dimensional stiffness matrix of entire composite.

t_C is the thickness of the entire composite.

N_l is the number of plies of the entire composite.

z_i is the distance from reference plane to the bottom of *ith* ply.

H_j is the interply layer distortion energy coefficient.

$\overline{S}_j$ is the can be generated from following equation [Murthy and Chamis, 1986]:

$$\left[\overline{S}_j\right] = \begin{bmatrix} A^2 & -A^2 & 0 & 0 & 0 & -AB \\ -A^2 & A^2 & 0 & 0 & 0 & AB \\ 0 & 0 & 0 & 0 & 0 & 0 \\ 0 & 0 & 0 & 0 & 0 & 0 \\ 0 & 0 & 0 & 0 & 0 & 0 \\ -AB & AB & 0 & 0 & 0 & B^2 \end{bmatrix} \tag{7-26}$$

$$A = \sin 2\theta_{j+1} - \sin 2\theta_j$$

$$B = \cos 2\theta_{j+1} - \cos 2\theta_j$$

θ_j is the fiber angle of *jth* ply from material axes to composite structural axes.

Thermal and hygral coefficients of expansion about the composite structural axes can be obtained from the following equations:

$$\left\{\overline{\alpha}_C\right\} = \frac{1}{t_C}\left[\overline{E}_C\right]^{-1}\sum_{i=1}^{N_l}\left(z_{i+1}-z_i\right)\left[f_p\left[\overline{R}_i^{\,p}\right]^T\left[\overline{E}_i^{\,p}\right]\left[\overline{R}_i^{\,p}\right]\left\{\overline{\alpha}_i^{\,p}\right\} + \sum_{j=1}^{N_w} f_{w_j}\left[\overline{R}_i^{\,w_j}\right]^T\left[\overline{E}_i^{\,w_j}\right]\left[\overline{R}_i^{\,w_j}\right]\left\{\overline{\alpha}_i^{\,w_j}\right\}\right] \tag{7-27}$$

$$\left\{\overline{\beta}_C\right\} = \frac{1}{t_C}\left[\overline{E}_C\right]^{-1}\sum_{i=1}^{N_l}(z_{i+1}-z_i)\left[f_p\left[\overline{R}_i^p\right]^T\left[\overline{E}_i^p\right]\left[\overline{R}_i^p\right]\left\{\overline{\beta}_i^p\right\} + \sum_{j=1}^{N_w} f_{w_j}\left[\overline{R}_i^{w_j}\right]^T\left[\overline{E}_i^{w_j}\right]\left[\overline{R}_i^{w_j}\right]\left\{\overline{\beta}_i^{w_j}\right\}\right] \quad (7\text{-}28)$$

Where $\left\{\overline{\alpha}_C\right\}, \left\{\overline{\beta}_C\right\}$ are thermal and moisture coefficients of expansion about the composite structural axes.

$$\left\{\overline{\alpha}_C\right\} = \left\{\alpha_{C_{11}}, \alpha_{C_{22}}, \alpha_{C_{33}}, \alpha_{C_{23}}, \alpha_{C_{13}}, \alpha_{C_{12}}\right\} \quad (7\text{-}29)$$

$$\left\{\overline{\beta}_C\right\} = \left\{\beta_{C_{11}}, \beta_{C_{22}}, \beta_{C_{33}}, \beta_{C_{23}}, \beta_{C_{13}}, \beta_{C_{12}}\right\} \quad (7\text{-}30)$$

7.1.6 Two Dimensional Hygrothermoelastic Properties

In most cases computational evaluation of composite structures is carried out by using plate and shell finite elements. Therefore, the composite properties need be expressed as two-dimensional plate stiffness with membrane and bending degrees of freedom. The resultant forces and moments in terms of the middle surface extensional strain and curvatures can be expressed as:

$$\begin{Bmatrix}\{N\}\\ \{M\}\end{Bmatrix} = \begin{bmatrix}[A] & [B]\\ [B] & [D]\end{bmatrix}\begin{Bmatrix}\{\varepsilon\}\\ \{\kappa\}\end{Bmatrix} - \begin{Bmatrix}\{N_T\}\\ \{M_T\}\end{Bmatrix} - \begin{Bmatrix}\{N_M\}\\ \{M_M\}\end{Bmatrix} \quad (7\text{-}31)$$

where

$\{N\} = \{N_x, N_y, N_{xy}\}^T$

$\{M\} = \{M_x, M_y, M_{xy}\}^T$

$\{\varepsilon\} = \{\varepsilon_x, \varepsilon_y, \varepsilon_{xy}\}$ is the reference plane membrane strains.

$\{\kappa\} = \{\kappa_x, \kappa_y, \kappa_{xy}\}$ is the reference plane curvatures.

$\{N_T\}$, $\{N_M\}$ is the resultant forces due to temperature and moisture change.

$\{M_T\}, \{M_M\}$ is the resultant moments due to temperature and moisture change.

For a three-dimensionally reinforced laminate containing layers of primary and woven fiber reinforcement domains, the resultant forces due to external load can be obtained from the following equation:

$$\begin{aligned}\{N_\varepsilon\} &= \sum_{i=1}^{N_l}\int_{z_{i-1}}^{z_i}\{\sigma_i\}dz \\ &= \sum_{i=1}^{N_l}\int_{z_{i-1}}^{z_i}[E_i](\{\varepsilon\}+z\{\kappa\})dz \\ &= \sum_{i=1}^{N_l}\int_{z_{i-1}}^{z_i}\left[f_p\left[R_i^p\right]^T\left[E_i^p\right]\left[R_i^p\right]+\sum_{j=1}^{N_w}f_{w_j}\left[\tilde{E}_i^{w_j}\right]\right](\{\varepsilon\}+z\{\kappa\})dz \\ &= [A']\{\varepsilon\}+[B']\{\kappa\}\end{aligned} \tag{7-32}$$

where

$$[E_i] = f_p\left[R_i^p\right]^T\left[E_i^p\right]\left[R_i^p\right]+\sum_{j=1}^{N_w}f_{w_j}\left[\tilde{E}_i^{w_j}\right] \tag{7-33}$$

$$[A'] = \sum_{i=1}^{N_l}(z_i-z_{i-1})\left[f_p\left[R_i^p\right]^T\left[E_i^p\right]\left[R_i^p\right]+\sum_{j=1}^{N_w}f_{w_j}\left[\tilde{E}_i^{w_j}\right]\right]$$

$$[B'] = \frac{1}{2}\sum_{i=1}^{N_l}(z_i^2-z_{i-1}^2)\left[f_p\left[R_i^p\right]^T\left[E_i^p\right]\left[R_i^p\right]+\sum_{j=1}^{N_w}f_{w_j}\left[\tilde{E}_i^{w_j}\right]\right]$$

and E_i is the two dimensional lamina stiffness matrix of *ith* ply.

E_i^p is the two dimensional lamina stiffness of primary domain of *ith* ply in local axes.

$$\left[E_i^p\right] = \begin{bmatrix} \frac{1}{E_{11}} & -\frac{\upsilon_{21}}{E_{22}} & 0 \\ -\frac{\upsilon_{12}}{E_{11}} & \frac{1}{E_{22}} & 0 \\ 0 & 0 & \frac{1}{G_{12}} \end{bmatrix} \tag{7-34}$$

R_i^p is the two dimensional coordinate transformation matrix of primary domain.

$$\left[R_i^p\right] = \begin{bmatrix} \cos^2\theta_i & \sin^2\theta_i & \frac{1}{2}\sin 2\theta_i \\ \sin^2\theta_i & \cos^2\theta_i & -\frac{1}{2}\sin 2\theta_i \\ -\sin 2\theta_i & \sin 2\theta_i & \cos 2\theta_i \end{bmatrix} \tag{7-35}$$

$\tilde{E}_i^{w_j}$ is the two dimensional stiffness of weaver domain in structural axes. It can be obtained by extracting relevant terms, which correspond to σ_{11}, σ_{22}, σ_{12}, from the three dimensional stiffness matrix that can be generated by the following transformation:

$$\left[\overline{R}_i^{w_j}\right]^T\left[\overline{E}_i^{w_j}\right]\left[\overline{R}_i^{w_j}\right] \tag{7-36}$$

Superimposing the stiffness contributions due to interply layer distortion energy:

$$\begin{aligned}[A] &= [A'] + \sum_{j=1}^{N_l-1} H_j\left[S_j\right] \\ &= \sum_{i=1}^{N_l}\left(z_i - z_{i-1}\right)\left[f_p\left[R_i^p\right]^T\left[E_i^p\right]\left[R_i^p\right] + \sum_{j=1}^{N_w} f_{w_j}\left[\tilde{E}_i^{w_j}\right]\right] + \sum_{j=1}^{N_l-1} H_j\left[S_j\right]\end{aligned} \tag{7-37}$$

$$\begin{aligned}[B] &= [B'] + \sum_{j=1}^{N_l-1} z_j' H_j\left[S_j\right] \\ &= \frac{1}{2}\sum_{i=1}^{N_l}\left(z_i^2 - z_{i-1}^2\right)\left[f_p\left[R_i^p\right]^T\left[E_i^p\right]\left[R_i^p\right] + \sum_{j=1}^{N_w} f_{w_j}\left[\tilde{E}_i^{w_j}\right]\right] + \sum_{j=1}^{N_l-1} z_j' H_j\left[S_j\right]\end{aligned} \tag{7-38}$$

where z_j' is the distance from the interply layer to the composite reference plane (mid-thickness). Similarly,

$$\begin{aligned}\left\{M_\varepsilon\right\} &= \sum_{i=1}^{N_l}\int_{z_{i-1}}^{z_i}\left\{\sigma_i\right\} z\, dz \\ &= \sum_{i=1}^{N_l}\int_{z_{i-1}}^{z_i}\left[E_i\right]\left(\left\{\varepsilon\right\} + z\left\{\kappa\right\}\right) z\, dz \\ &= \sum_{i=1}^{N_l}\int_{z_{i-1}}^{z_i}\left[f_p\left[R_i^p\right]^T\left[E_i^p\right]\left[R_i^p\right] + \sum_{j=1}^{N_w} f_{w_j}\left[\tilde{E}_i^{w_j}\right]\right]\left(\left\{\varepsilon\right\} + z\left\{\kappa\right\}\right) z\, dz \\ &= [B']\left\{\varepsilon\right\} + [D']\left\{\kappa\right\}\end{aligned} \tag{7-39}$$

where

$$[D'] = \frac{1}{3}\sum_{i=1}^{N_l}\left(z_i^3 - z_{i-1}^3\right)\left[f_p\left[R_i^p\right]^T\left[E_i^p\right]\left[R_i^p\right] + \sum_{j=1}^{N_w} f_{w_j}\left[\tilde{E}_i^{w_j}\right]\right] \tag{7-40}$$

Superimposing the stiffness due to interply layer distortion:

$$\begin{aligned}[D] &= [D'] + \frac{1}{2}\sum_{j=1}^{N_l-1} z_j'^2 H_j\left[S_j\right] \\ &= \frac{1}{3}\sum_{i=1}^{N_l}\left(z_i^3 - z_{i-1}^3\right)\left[f_p\left[R_i^p\right]^T\left[E_i^p\right]\left[R_i^p\right] + \sum_{j=1}^{N_w} f_{w_j}\left[\tilde{E}_i^{w_j}\right]\right] + \frac{1}{2}\sum_{j=1}^{N_l-1} z_j'^2 H_j\left[S_j\right]\end{aligned} \tag{7-41}$$

For the primary domain, the thermal forces are

$$\left\{N_{T_i}^p\right\} = \int_{z_{i-1}}^{z_i}\left[E_i^p\right]\Delta T\left\{\alpha_i^p\right\} dz = \left(z_i - z_{i-1}\right)\Delta T\left[E_i^p\right]\left\{\alpha_i^p\right\} \tag{7-42}$$

For the *jth* weaver domain, the thermal forces are

$$\left\{N_{T_i}^{w_j}\right\} = \int_{z_{i-1}}^{z_i} \left[E_i^{w_j}\right] \Delta T \left\{\alpha_i^{w_j}\right\} dz = (z_i - z_{i-1}) \Delta T \left[E_i^{w_j}\right] \left\{\alpha_i^{w_j}\right\} \tag{7-43}$$

Transforming $N_{T_i}^{p}$ and $N_{T_i}^{w_j}$ to global axes, and then averaging them in terms of the weight of their volume fraction to get resultant force for *ith* ply in global coordinate system due to temperature change:

$$\begin{aligned} \left\{N_{T_i}\right\} &= f_p \left[R_i^p\right] \left\{N_{T_i}^p\right\} + \sum_{j=1}^{N_w} f_{w_j} \left[R_i^{w_j}\right] \left\{N_{T_i}^{w_j}\right\} \\ &= \Delta T_i \left(z_i - z_{i-1}\right) \left\{ f_p \left[R_i^p\right] \left[E_i^p\right] \left\{\alpha_i^p\right\} + \sum_{j=1}^{N_w} f_{w_j} \left[R_i^{w_j}\right] \left[E_i^{w_j}\right] \left\{\alpha_i^{w_j}\right\} \right\} \end{aligned} \tag{7-44}$$

Summing up the N_{T_i} for all plies to get the resultant thermal force for entire composite structure:

$$\begin{aligned} \left\{N_T\right\} &= \sum_{i=1}^{N_l} \left\{N_{T_i}\right\} \\ &= \sum_{i=1}^{N_l} \left[\Delta T_i \left(z_i - z_{i-1}\right) \left\{ f_p \left[R_i^p\right] \left[E_i^p\right] \left\{\alpha_i^p\right\} + \sum_{j=1}^{N_w} f_{w_j} \left[R_i^{w_j}\right] \left[E_i^{w_j}\right] \left\{\alpha_i^{w_j}\right\} \right\} \right] \end{aligned} \tag{7-45}$$

Similarly, $\left\{N_M\right\}, \left\{M_T\right\}$ and $\left\{M_M\right\}$ can be generated by:

$$\left\{N_M\right\} = \sum_{i=1}^{N_l} \left[\Delta M_i \left(z_i - z_{i-1}\right) \left\{ f_p \left[R_i^p\right] \left[E_i^p\right] \left\{\beta_i^p\right\} + \sum_{j=1}^{N_w} f_{w_j} \left[R_i^{w_j}\right] \left[E_i^{w_j}\right] \left\{\beta_i^{w_j}\right\} \right\} \right] \tag{7-46}$$

$$\left\{M_T\right\} = \frac{1}{2} \sum_{i=1}^{N_l} \left[\Delta T_i \left(z_i^2 - z_{i-1}^2\right) \left\{ f_p \left[R_i^p\right] \left[E_i^p\right] \left\{\alpha_i^p\right\} + \sum_{j=1}^{N_w} f_{w_j} \left[R_i^{w_j}\right] \left[E_i^{w_j}\right] \left\{\alpha_i^{w_j}\right\} \right\} \right] \tag{7-47}$$

$$\left\{M_M\right\} = \frac{1}{2} \sum_{i=1}^{N_l} \left[\Delta M_i \left(z_i^2 - z_{i-1}^2\right) \left\{ f_p \left[R_i^p\right] \left[E_i^p\right] \left\{\beta_i^p\right\} + \sum_{j=1}^{N_w} f_{w_j} \left[R_i^{w_j}\right] \left[E_i^{w_j}\right] \left\{\beta_i^{w_j}\right\} \right\} \right] \tag{7-48}$$

7.1.7 Stresses in the primary domain and in the weaver domain

In order to perform damage propagation simulation, one needs to evaluate the stresses in stuffer, filler, and weaver fibers and matrices. For most composite structures, the first step for stress analysis is the assembly of a finite element model using the stiffness properties given in the previous section. After finite element analysis, the resultant forces and moments are obtained for each node. From equation (7-31), we can write:

$$\begin{Bmatrix} \{\varepsilon\} \\ \{\kappa\} \end{Bmatrix} = \begin{bmatrix} [A] & [B] \\ [B] & [D] \end{bmatrix}^{-1} \left\{ \begin{Bmatrix} \{N\} \\ \{M\} \end{Bmatrix} + \begin{Bmatrix} \{N_T\} \\ \{M_T\} \end{Bmatrix} + \begin{Bmatrix} \{N_M\} \\ \{M_M\} \end{Bmatrix} \right\} \tag{7-49}$$

The strains and stresses in global axes for a specific ply—the *ith* ply can be obtain from following equations:

$$\begin{aligned}\{\varepsilon_i\} &= \{\varepsilon\} - z\{\kappa\} \\ &= [A]^{-1}\left\{\{N\} + \{N_T\} + \{N_M\} - [B]\{\kappa\}\right\} - z\{\kappa\}\end{aligned} \tag{7-50}$$

$$\{\sigma_i\} = [E_i]\left(\{\varepsilon_i\} - \Delta T_i\{\alpha_i\} - \Delta M_i\{\beta_i\}\right) \tag{7-51}$$

where

$$\{\varepsilon_i\} = \left\{\varepsilon_{11}^{(i)}, \varepsilon_{22}^{(i)}, \varepsilon_{12}^{(i)}\right\}$$

$$\{\sigma_i\} = \left\{\sigma_{11}^{(i)}, \sigma_{22}^{(i)}, \sigma_{12}^{(i)}\right\}$$

the other stress components $\sigma_{13}^{(i)}, \sigma_{23}^{(i)}, \sigma_{33}^{(i)}$ can be obtained from the transverse shear resultants Q_{13}, Q_{23} and the transverse pressures P_u, P_l by following equation (Vladimir, 1975):

$$\begin{Bmatrix}\sigma_{13}^{(i)} \\ \sigma_{23}^{(i)} \\ \sigma_{33}^{(i)}\end{Bmatrix} = \begin{Bmatrix} \dfrac{1.5\mathrm{Q}_{13}}{t_c}\left(1 - \dfrac{4z_i^{\,2}}{t_c^2}\right) \\ \dfrac{1.5\mathrm{Q}_{13}}{t_c}\left(1 - \dfrac{4z_i^{\,2}}{t_c^2}\right) \\ \dfrac{P_u + P_l}{2} + 1.5\left(P_u - P_l\right)\left(\dfrac{z_i}{t_c} - \dfrac{16z_i^3}{3t_c^3}\right)\end{Bmatrix} \tag{7-52}$$

Stresses in the primary and weaver domains are computed from the corresponding strains using the appropriate stress-strain relations. Since the primary domain is in same plane as the ply, it has the same strain components as the ply, that is

$$\{\varepsilon_i^p\} = [R_i^p]\{\varepsilon_i\} \tag{7-53}$$

and the primary domain stresses are computed from:

$$\begin{aligned}\left\{\sigma_i^p\right\} = &\left[E_i^p\right]\left[R_i^p\right][A]^{-1}\left(\{N\}+\left\{N_T\right\}+\left\{N_M\right\}-[B]\{\kappa\}\right)\\ &-\left[E_i^p\right]\left(\Delta T_i\left\{\alpha_i^p\right\}+\Delta M_i\left\{\beta_i^p\right\}+z\left[R_i^p\right]\{\kappa\}\right)\end{aligned} \tag{7-54}$$

Since the weaver is not in the same plane as the ply, one needs to transform the three dimensional strain components of the ply to the weaver axes to obtain the weaver strains. Weaver domain stresses can be computed from the weaver strains.

The three dimensional stress-strain-temperature-moisture relationship can be expressed as:

$$\left\{\bar{\sigma}_i\right\} = \left[\bar{E}_i\right]\left(\left\{\bar{\varepsilon}_i\right\} - \Delta T_i\left\{\bar{\alpha}_i\right\} - \Delta M_i\left\{\bar{\beta}_i\right\}\right) \tag{7-55}$$

where

$$\left\{\bar{\sigma}_i\right\} = \left\{\sigma_{11}^{(i)},\sigma_{22}^{(i)},\sigma_{33}^{(i)},\sigma_{23}^{(i)},\sigma_{13}^{(i)},\sigma_{12}^{(i)}\right\}^T$$

$$\left\{\bar{\varepsilon}_i\right\} = \left\{\varepsilon_{11}^{(i)},\varepsilon_{22}^{(i)},\varepsilon_{33}^{(i)},\varepsilon_{23}^{(i)},\varepsilon_{13}^{(i)},\varepsilon_{12}^{(i)}\right\}^T$$

From (7-25) and (7-27), we computed $\varepsilon_{11}^{(i)},\varepsilon_{22}^{(i)},\varepsilon_{12}^{(i)},\sigma_{13}^{(i)},\sigma_{23}^{(i)},\sigma_{33}^{(i)}$. Now, in terms of (7-30), we may find the other three strain components $\varepsilon_{13}^{(i)},\varepsilon_{23}^{(i)},\varepsilon_{33}^{(i)}$. Transferring the strains $\left\{\bar{\varepsilon}_i\right\}$ to weaver axes we obtain the weaver strains in local material coordinates:

$$\left\{\bar{\varepsilon}_i^{w_j}\right\} = \left[\bar{R}_i^{w_j}\right]\left\{\bar{\varepsilon}_i\right\} \tag{7-56}$$

Then the weaver stresses can be expressed as:

$$\left\{\sigma_i^{w_j}\right\} = \left[E_i^{w_j}\right]\left(\left\{\varepsilon_i^{w_j}\right\} - \Delta T_i\left\{\alpha_i^{w_j}\right\} - \Delta M_i\left\{\beta_i^{w_j}\right\}\right) \tag{7-57}$$

7.1.8 The Influence of Fiber Waviness

In woven 3-D composites, nominally straight in-plane yarns, stuffers and fillers, are often much more wavy than those in conventional laminates because of the existence of weaver fibers. The most important effect of tow waviness on elastic properties is to reduce the axial stiffness of a tow. Since the microstructure of a woven composite is highly complex and the waviness of fibers is random rather than possessing a single characteristic wavelength or amplitude, it is not currently practical to model the actual tow geometry. Idealization is mandatory. For simplicity, a composite unit cell with wavy fibers shown in Figure 7-7 is analyzed in this section.

To simulate the fiber configuration, the following form of waviness is assumed,

$$y = \frac{4C}{l^2}\left(lx - x^2\right) \tag{7-58}$$

Where l is the half-wavelength and C is the amplitude of waviness. Therefore, the length of yarn $S(l,C)$ can be expressed by

$$S(l,C)=\int_0^l \sqrt{1+y'^2}\,dx$$

$$=\frac{1}{2}\sqrt{l^2+16C^2}+\frac{1}{16}\frac{L^2}{C}\left[\ln\left(\sqrt{1+\frac{16C^2}{l^2}}+\frac{4C}{l}\right)-\ln\left(\sqrt{1+\frac{16C^2}{l^2}}-\frac{4C}{l}\right)\right] \qquad (7\text{-}59)$$

Supposing that the composite unit sustains axial tensile load σ_1 as shown in Figure 7-7, the extension of the unit in the X direction is caused by two parts: one is due to fiber axial extension under axial tensile load, and the second is due to the reduction of fiber waviness, i.e. the fiber will become more straight under the axial tensile load, and therefore, additional extension will occur to the composite unit. Since the first component has been widely studied in the literature, this section is focused on the second component--the extension due to the reduction of fiber waviness. Fiber axial extension is not taken into account when considering the second component contributing to composite extension. Therefore, it is reasonable to assume that the length of fiber yarn remains unchanged, i.e. $S(l,C)$ is constant when analyzing the second component of extension. When the fiber waviness reduces, the amplitude C decreases and the wavelength increases.

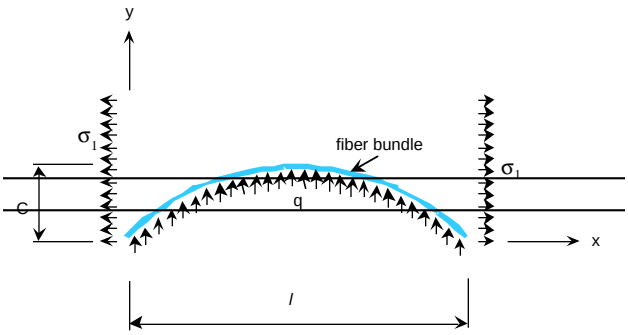

Figure 7-7. Wavy Tow Model for Analyzing the Influence of Fiber Waviness on Longitudinal Stiffness of Unidirectional Composites

Since $S(l,C)$ is constant, one may write

$$S(l,C)=\frac{\partial S}{\partial l}\delta l+\frac{\delta S}{\delta C}\delta C=0$$

Therefore the change in composite length becomes:

$$\delta l=-\left(\frac{\partial S}{\partial C}\Big/\frac{\partial S}{\partial l}\right)\delta C=-F(l,C)\delta C \qquad (7\text{-}60)$$

Where

$$F(l,C)=\frac{\frac{\sqrt{l^2+16C^2}}{2C}+\frac{16C}{\sqrt{l^2+16C^2}}-\frac{l^2}{16C^2}\left[\ln\left(\sqrt{1+\frac{16C^2}{l^2}}+\frac{4C}{l}\right)-\ln\left(\sqrt{1+\frac{16C^2}{C^2}}+\frac{4C}{l}\right)\right]}{\frac{1}{2}\sqrt{1+\frac{16C^2}{l^2}}-\frac{l}{8C+\sqrt{l^2+C^2}}-\frac{4C^2}{l\sqrt{l^2+16C^2}}+\frac{l}{8C}\left[\ln\left(\frac{4C}{l}+\sqrt{1+\frac{16C}{l^2}}\right)-\ln\left(\sqrt{1+\frac{16C^2}{C^2}}-\frac{4C}{l}\right)\right]} \tag{7-61}$$

Assuming the original length of the composite unit is l_0, after the axial load is applied, the length increases to l, then extension of the unit can be expressed by

$$l-l_0=\frac{\sigma_1}{E_{11}^0}l_0+\delta l \tag{7-62}$$

Where E_{11}^0 is the composite longitudinal modulus based on orientation averaging method. $\frac{\sigma_1}{E_{11}^0}l_0$ is the extension due to fiber axial extension, δl is the extension due to reduction of fiber waviness.

When the composite unit cell is subjected to tensile load $T_C=\sigma_1 A_C$, the fiber bundle is subjected a tensile force $T_f=\sigma_f A_f$. Since the fiber bundle is not straight, there must be balancing reaction q as shown in Figure 7-7 to counteract the vertical component of T_f. According to equilibrium equation, q can be written as

$$q=-\sigma_f A_f\frac{d^2y}{d^2x}=\frac{8C}{l^2}\sigma_f A_f \tag{7-63}$$

Where σ_f is the longitudinal stress in the fiber and A_f is the cross section area of the fiber.

The compressive stress in the composite unit cell in Y direction due to q can be expressed by

$$\sigma_2=\frac{q}{T}=E_{22}^0\varepsilon_2=E_{22}^0\frac{\delta y}{y}=-E_{22}^0\frac{\delta C}{C} \tag{7-39}$$

where σ_2 is transverse stress due to q, ε is transverse strain due to q, T is the thickness of the composite, and E_{22}^0 is transverse modulus of the composite.

Substituting q from (7-39) to (7-38), we obtain

$$\frac{8C}{l^2}\sigma_f A_f=-\frac{E_{22}^0 T\delta C}{C} \tag{7-64}$$

and

$$\delta C=-\frac{8C^2\sigma_f A_f}{E_{22}^0 l^2 T} \tag{7-65}$$

Assuming the composite and the fiber bundle have the same strain in the *X* direction,

$$\sigma_f = \frac{E_f}{E_{11}^0}\sigma_0$$

If fiber volume fraction is denoted as V_f , then

$$A_f = A_0 V_f = CTV_f \tag{7-66}$$

Therefore, (7-34) can be rewritten as

$$\delta C = -\frac{8C^3 E_f \sigma_0 V_f}{E_{11}^0 E_{22}^0 l^2} \tag{7-67}$$

Effective strain ε_1 can be expressed as

$$\begin{aligned}\varepsilon_1 &= \frac{l - l_0}{l_0} \\ &= \frac{1}{l}\left(\frac{\sigma_1}{E_{11}^0} l + F(l,C)\delta C\right) \\ &= \frac{1}{l}\left(\frac{\sigma_1}{E_{11}^0} l + \frac{8C^3 E_f \sigma_1 L_0 V_f F(l,C)}{E_{11}^0 E_{22}^0 l^2}\right)\end{aligned} \tag{7-68}$$

Therefore

$$E_{11} = \frac{\sigma_1}{\varepsilon_1} = KE_{11}^0 \tag{7-69}$$

where *K* is a knockdown factor of longitudinal modulus for the composite,

$$K = \frac{1}{1 + \dfrac{8C^3 E_f V_f F(l,C)}{E_{22}^0 l^3}} \tag{7-70}$$

Equation (7-70) can be used to estimate the waviness knockdown factor for misoriented unidirectional composite segments with axially loaded wavy tows. The value of *K* is less than one and depends on the ratios of C/l and E_f / E_{22}^0. The larger the C/l and/or E_f / E_{22}^0, the smaller the *K*.

7.2 RESULTS AND DISCUSSION OF 2D/3D WOVEN COMPOSITES

The developed method was tested by simulating an experimental study on eleven woven composite specimens [Cox and Dadkhah, 1995]. Five of these specimens were lightly compacted with fiber volume ratios of approximately 0.35. The remaining six specimens were heavily compacted with fiber volume ratios of approximately 0.60 (Table 7-1)

7.0 Mechanics Of 3-D Woven, Braided And Stitched Composites

Table 7-1. Designation of Woven Composite Types

Symbol	Description
LL	Lightly compacted layer-to-layer angle interlock
LT	Lightly compacted through-the-thickness angle interlock
LO	Lightly compacted through-the-thickness orthogonal interlock
HL	Heavily compacted layer-to-layer angle interlock
HT	Heavily compacted through-the-thickness angle interlock
HO	Heavily compacted through-the-thickness orthogonal interlock

Table 7-2 shows the fiber volume ratios for the different tows of each specimen. All of the specimens had stuffer and filler fibers made of AS graphite. The LL and LT woven composite specimens consisted of one with warp weaver fibers made of graphite and one with warp weaver fibers made of glass. All fibers were made of graphite for the heavily compacted composites. All heavily compacted composites (HL, HT, and HO) were made with all graphite fibers. Each type of heavily compacted composite material was represented by two specimens with different stuffer/filler/warp weaver fiber ratios.

Table 7-2. Fiber Volume Fraction of Specimens Considered

	Specimen Thickness	Nominal Volume Fraction			Total Fiber Volume Fraction	Fraction by Volume of all Fibers Lying Inc Stuffers Fillers Wrap Weavers		
Composite	(cm) [a]	V_a [b]	V_f [c]	V_w [d]	V	f_s	f_f	f_w
j-1-1	1.26	0.14	0.15	0.07	0.35+0.03	0.385	0.418	0197
l-L-2	1.24	0.14	0.20	0.05	0.370+0.005 [g] 0.066±0.004 [h]	0.347	0.502	0.151
1-T-1	1.02	0.16	0.21	0.05	0.466+0,003	0.381	0.504	0.115
1-T-2	0.97	0.18	0.22	0.04	0.408±0.020 [g] 0.044±0.004 [h]	0.406	0.497	0.097
l-0	0.88	0.18	0.15	0.04	0.483±0.010	0.387	0.524	0.090
h-L-1	0.561	0.38	0.20	0.05	0.620±0.008	0.587	0.340	0.073
h-L-2	0.525	0.33	0.21	0.025	0.557±0.015	0.580	0.375	0.045
h-T-1	0.573	0.37	0.22	0.065	0.613±0.003	0.571	0.331	0.098
h-T-2	0.577	0.36	0.23	0.035	0.592±0.014	0.571	0.369	0.069
h-0-1	0.579	0.37	0.22	0.045	0.619±0.008	0.586	0.340	0.073
h-0-2	0.587	0.35	0.23	0.065	0.593±0.014	0.545	0.353	0.102

[a] in direction normal to wrap and weft directions
[b] V_a = volume fraction of stuffer (straight wrap) tows
[c] V_f = volume fraction of filler (weft) tows
[d] V_w = volume fraction of wrap weaver (3D wrap) tows
[e] measured by acid digestion
[f] determined from weaver's specification
[g] graphite fibers
[h] glass fiber

7.0 Mechanics Of 3-D Woven, Braided And Stitched Composites

The coupon specimens were made with the most common types of PMC weaves:. layer-to-layer, through-the-thickness angle interlock, and orthogonal interlock weaves (Figure 7-8). "Stuffer" and "filler" tows form an orthogonal array suggestive of a course 0/90 laminate, while "wrap weaver" tows provide through-thickness reinforcement. Figure 7-8 also shows that stuffers and fillers are in reality not straight. The irregularity or waviness can be quite dramatic for fillers. It is generally larger for fillers than stuffers because the stuffers, being wrap yarns, are held in tension during weaving, whereas the fillers are non-tensioned weft.

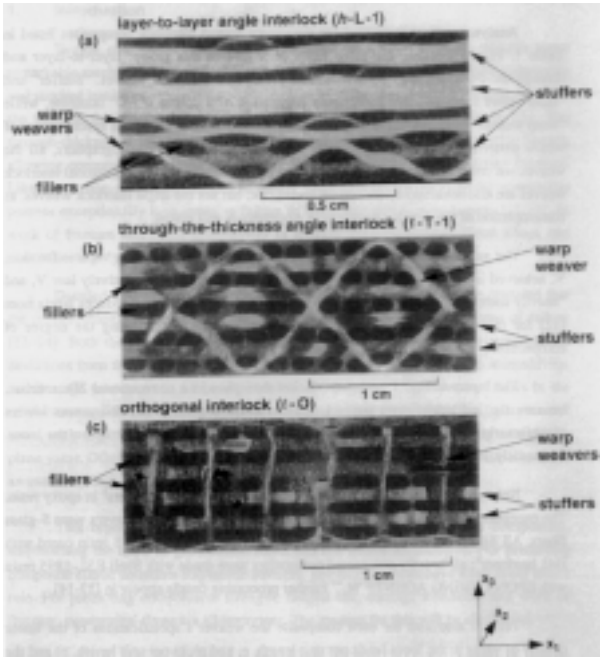

Figure 7-8 Specimen with Three Different Weave Types Stuffers and Wrap Weavers Appear as Light Ribbons while Sections of Fillers Appear as Dark Patches.

The enhance ICAN composite mechanics module was able to predict 3D composite properties and stress limits (Appendix B) consistently for all eleven specimens. Comparisons of these results with those computed by Cox and Dadkhah and those obtained from experiments are presented in Appendix C. In the majority of cases the enhanced ICAN module evaluated the 3D stiffness properties closer to experimental measurements than did the orientation averaging method reported by Cox and Dadkhah. However, in the direction of filler yarns, stiffness computations by the extended ICAN code, as well as those computed by Cox and Dadkhah, were considerably higher than the experimentally measured values. Composite stress limits computed by ICAN based on fiber strength and matrix strength always provided upper and lower bounds bracketing the experimental failure strengths.

GENOA-PFA's 3D composite analysis method enables the assessment of damage tolerances and structural responses of braided and woven composites. However, the developed methods can be further improved by quantifying the effects of tow waviness on composite structural response and stress limits. Additionally, an alternative formulation that preserves the spatial configurations of individual stuffer and filler tows may be more appropriate for composites subjected to bending.

7.2.1 Formulation Of The Effect Of Ply Waviness On Composite Properties.

Simulations carried out on the different types of woven composite specimens indicated that COD6 simulations of lightly compacted specimens that did not take into account fiber misalignment due to waviness significantly over predicted the stiffness and failure load. In order to improve the simulation of general 3D fiber reinforced composites a new method was developed to quantify the effect of fiber

waviness (the ratio W of the wave amplitude C to wavelength L) on composite response The method considers the transverse equilibrium of a fiber bundle that is half a wavelength long. The cambered shape of the fiber is approximated by a quadratic polynomial. The axial force carried by the fiber bundle is assumed to remain constant. The total lateral force is produced by the fiber axial forces due to the curvature of each fiber segment. The change in the wave amplitude due to axial loading depends on the lateral support provided by the transverse stiffness of the composite surrounding the wavy fibers. If the ratio of the fiber modulus to composite transverse modulus increases then the reduction of composite stiffness due to axial loading is greater.

Results indicate that for typical composite fiber modulus to transverse modulus ratios the reduction in composite stiffness may be negligible for very small values of the waviness parameter. However, as the waviness increases, composite stiffness is significantly reduced. The reduction in the stiffness is inversely proportional to the cube of the waviness parameter W plus unity. For example, if the ratio of fiber longitudinal modulus to composite transverse modulus is 70, then a waviness of W=0.06 would reduce the stiffness by only one percent. However, if the waviness parameter increases to W=0.20 then the reduction in composite stiffness becomes 46 percent. Many of the 3D reinforced woven and braided composites contain different levels of waviness in their fiber tows. In those cases an effective value of the waviness parameter s need to be identified for the assessment of composite properties. Additional work is in progress to determine the effect of fiber waviness and other possible factors in 3D composites.

Changes to input data

The node numbers for which ply stresses and micro stresses are to be printed out are specified by the user in the input immediately before the ICAN statement in one line using a (24X,i8) format to give the number of nodes for which ply stresses and micro stresses are to be printed out. Subsequent lines give the specific node numbers using (10i8) format**.**

Another change was made to eliminate unnecessary data lines when simulating 3D reinforced woven or braided composites. The LTYP, PLY, and MATCRD statements are the same as in the previous (COD6) version. However, the STUFFER, FILLER, and WEAVER statements have been eliminated. Instead, for each fiber orientation that has an out-of-plane component a BRAID card is used to specify the braid number, the fiber/matrix constituents, the three directional angles (degrees) of the fiber orientation with respect to the laminate x,y,z coordinates, and the ratio of braid fiber volume to the total fiber volume. The BRAID card uses (a8,i8,2a4,3f8.2,f8.0) format. The last braid parameter (i.e.,. the ratio of braid fiber volume to the total fiber volume) is computed from the weight of stitching thread, ws, and the stitches' pitch and row spacings, ps and rs.

7.3 SIMULATION OF THE WOVEN COMPOSITE

The developed method was first used to evaluate the structural response properties and damage tolerance characteristics of plain-weave and non-woven composite panels subjected to in-plane loads.

The plain weave composites were inside from 16 layers of fabric preforms and non-woven laminates contained 32 plies contained 32 plies arranged in a $[0/90]_{16s}$, cross-ply configuration.

The fiber volume ratio was 0.64 and the panel thickness was 0.20 for all cases. Simulations were conducted using a 2in.x2in. square finite element model with 400 quadrilateral elements and 441 nodes. The panels were restrained along one of their edges and loads were applied along the unrestrained edges to represent biaxial stress states. Five in-plane load combinations were considered. Each load combination contained N_x, forces applied as either tension or compression plus a smaller intensity of N_{xy}, in-plane shear forces. The five load combinations consisted of the following cases: (1) Tension plus shear with a ratio of N_x/ N_{xy}=20; (2) Tension plus shear with a ratio of N_x/ N_{xy} =10; (3) Tension plus shear with ratio of N_x/ N_{xy} =5; (4) Compression plus shear with a ratio of N_x/ N_{xy} =10; and (5) Compression plus shear with a ratio of N_x/ N_{xy} =5. Each load combination was applied to both woven and non-woven composite panels.

Figure 7-9 shows the stress-strain relations for both the plain-weave and non-woven composites subjected to loading case (1) with the tension/shear ratio N_x/ N_{xy}=20. The simulated ultimate tensile stress for the woven composite was 103 ksi, whereas the simulated ultimate tensile stress of the non-woven laminate was 143 ksi. However, the non-woven laminate experienced significant stiffness degradation after the tensile stress exceeded 125 ksi. As the stiffness degradation at 125 ksi was due to fiber fractures in the 0º plies, the practical strength of the non-woven laminated composite may be assumed to be limited to 125 ksi. The stiffness of the plain-weave composite was less than that of the non-woven laminate.

Figure 7-10 shows the damage energy for both woven and non-woven composite. The damage energy for (the non-woven composite surged to a very high level immediately before ultimate fracture. The damage energy of the woven composite was also expected to surge at the ultimate load. However, the damage energy is computed only for equilibrium stages and for the woven composite the last equilibrium point was prior to the beginning of the ultimate surge in the damage energy. Prior to the ultimate load the damage energy levels appeared to be the same for 6otli composites except during the damage growth stage when the woven composite expanded more damage energy.

Figure 7-11 shows the structural damage volume V_d produced in both woven and non-woven composites. Damage initiation, growth, and propagation all occurred sooner in the woven composite subjected to tensile loading with five percent shear.

After simulation of case (1) additional simulations were carried out, under tensile loading with higher values of shear. Figure 7-12 shows the stress-strain relationship) for tensile loading with 10 percent shear, or N_x/ N_{xy} =10. In this case tensile strength of the woven composite was 71 ksi and tensile strength of the non-woven laminate was 123 ksi. The stiffness of the non-woven laminate was greater than that of the woven laminate as in case (1). Figure 7-13 shows the damage energies for woven arid non-woven laminates for case (2). More energy was released by the woven composite during the damage growth stage. In this case, the surge of damage energy at ultimate loading was captured for the woven composite. However, Figure 7-13 shows only as a slight upturn of the damage energy for the last equilibrium point of the non-woven laminate. Figure 7-14 shows the percent increase in the structural damage volume Vd with applied stress. Damage volumes for the damage initiation, growth, and propagation stresses were consistently higher for non-woven composites compared to those of woven composites.

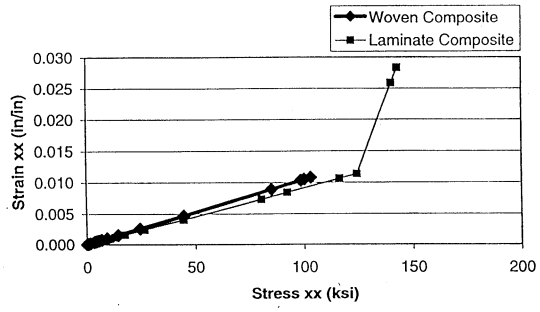

Figure 7-9: Stress-Strain Relations for Graphite/Epoxy Woven and Non-Woven Composite Laminates Subject to Tension and Shear Nx/Nxy = 20.

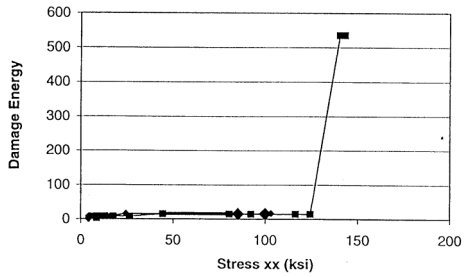

Figure 7-10: Damage Energy with Stress for Graphite/Epoxy Woven and Non-Woven Composite Laminates Subject to Tension and Shear N_x/N_{xy} = 20.

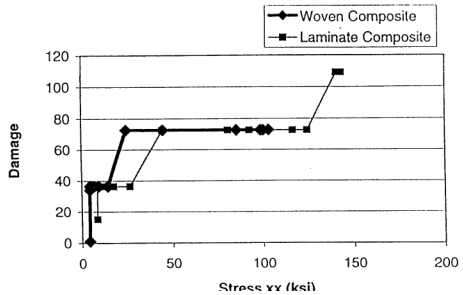

Figure 7-11: Structural Damage with Stress for Graphite/Epoxy Woven and Non-Woven Composite Laminates Subject to Tension and Shear N_x/N_{xy} = 20.

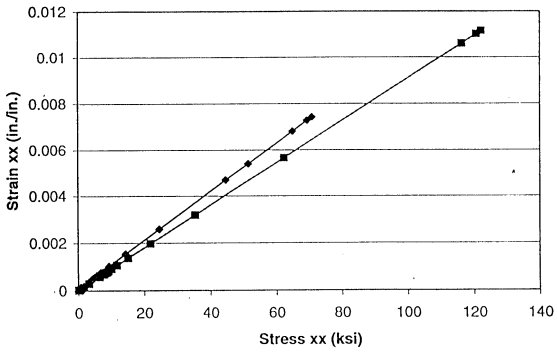

Figure 7-12: Stress-Strain Relations for Graphite/Epoxy Woven and Non-Woven Composite Laminates Subject to Tension and Shear N_x/N_{xy} = 10.

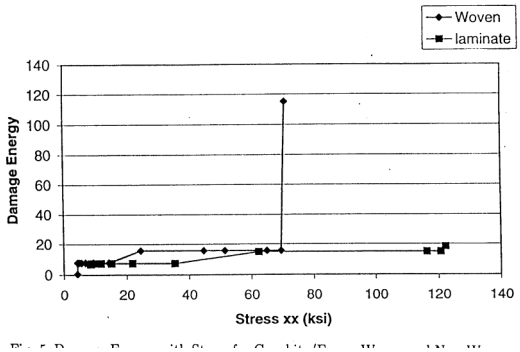

Figure 7-13: Damage Energy with Stress for Graphite/Epoxy Woven and Non-Woven Composite Laminates Subject to Tension and Shear N_x/N_{xy} = 10

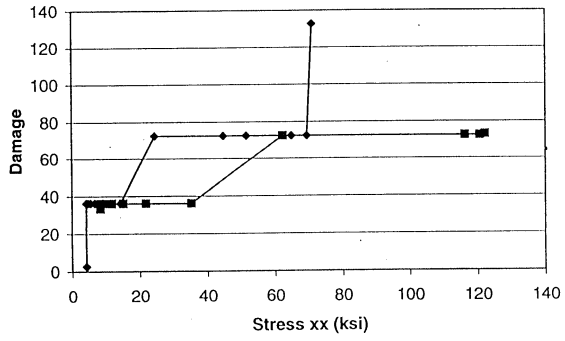

Figure 7-14: Structural Damage with Stress for Graphite/Epoxy Woven and Non-Woven Composite Laminates Subject to Tension and Shear N_x/N_{xy} = 10.

Next, case (3) simulation with 20 percent shear, or N.,/N.,y=5 was carried out on both woven and non-woven composites. 'Figure 7-15 shows the stress-strain relationships for case (3). I,7or this case the ultimate strength of the woven composite was 46 ksi and that of the non-woven composite was 76 ksi.

The stiffness of the non-woven composite was higher than the stiffness of the woven composite as in the previous two cases. Figure 7-16 shows the damage energy released by the woven and non-woven composites. Similar to the previous cases, more energy was released by the woven composite during the damage growth stage. For this case the ultimate surge in the damage energy was captured for both woven and non-woven laminates. Figure 7-17 shows the percent damage volume V_d for case (3). Damage initiation, growth, and propagation stresses shown in Figure 7-17 are lower for the woven composite compared to those of the non-woven laminates as in the previous cases.

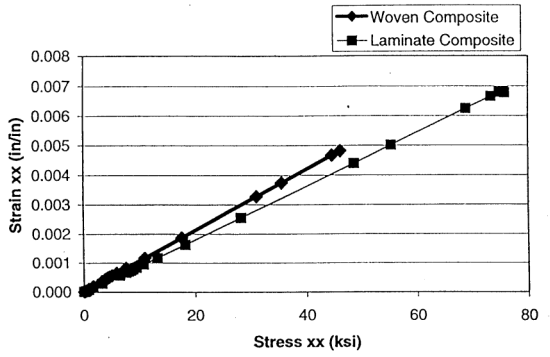

Figure 7-15: Stress-Strain Relations for Graphite/Epoxy Woven and Non-Woven Composite Laminates Subject to Tension and Shear $N_x/N_{xy} = 5$

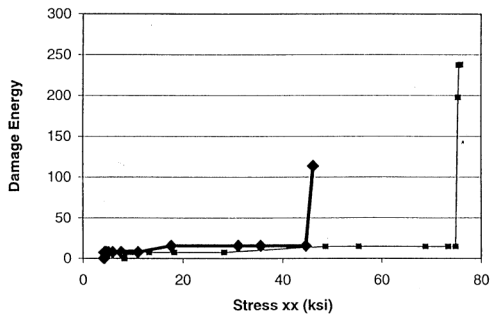

Figure 7-16: Damage Energy with Stress for Graphite/Epoxy Woven and Non-Woven Composite Laminates Subject to Tension and Shear $N_x/N_{xy} = 5$

Figure 7-18 shows the effect of shear, to tensile loading ratio on the tensile strength of woven an non-woven composites. In all cases the tensile strength is degraded with the increased shear component.

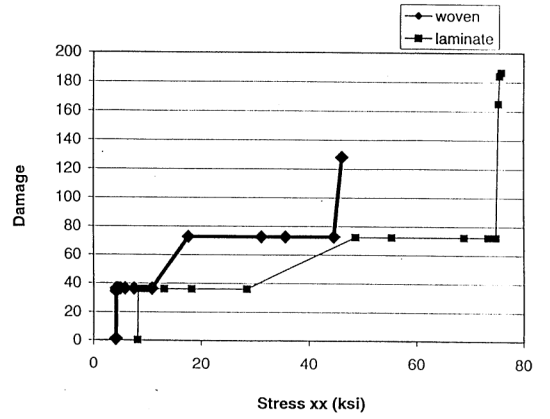

Figure 7-17: Structural Damage with Stress for Graphite/Epoxy Woven and Non-Woven Composite Laminates Subject to Tension and Shear $N_x/N_{xy} = 5$.

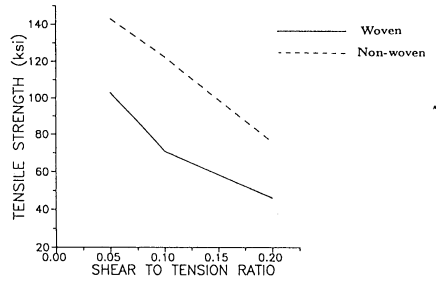

Figure 7-18: Effect of Shear on Ultimate Strength for Graphite/Epoxy Woven and Non-Woven Composite Laminates Subject to Tension and Shear $N_x/N_{xy} = 5$.

After the simulation of tensile loading cases, the previously outlined two cases subject to compressive loading with shear were simulated. Figure 7-19 Shows the stress-strain relations for case (4) woven and non-woven composites subjected to in-plane compression with 10 percent shear, or N./N.,y=10.

Compressive strength of the woven composite was 79 I<sl and the compressive strength of the non-woven laminate was 88 ksi. The stiffness of the non-woven laminate was greater than that of the woven laminate as in tension. Figure 7-20 shows the damage energies for woven and non-woven laminates of case (4). In the case of compression with shear loading a significant amount of damage energy was released during the damage initiation stage. More energy was released by the woven composite.

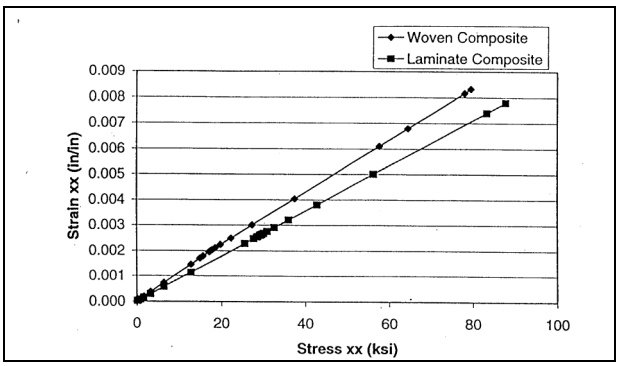

Figure 7-19: Stress-Strain Relations for Graphite/Epoxy Woven and Non-Woven Composite Laminates Subject to Compression and Shear N_x/N_{xy} = 10.

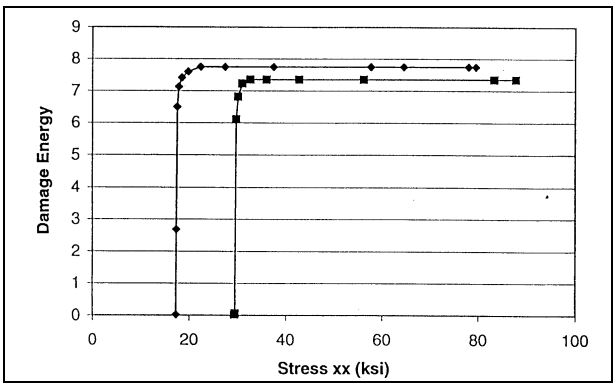

Figure 7-20: Damage Energy with Stress for Graphite/Epoxy Woven and Non-Woven Composite Laminates Subject to Compression and Shear N_x/N_{xy} = 10.

Figure 7-21 shows the increase in the structural damage volume Vd with applied stress. The damage initiation stress was lower for the woven composite. However, the ultimate damage volume was the same for woven and non-woven composites.

Next, case (5) simulation of in-plane compression with 20 percent shear, or N,/N,y=5 was carried out on both woven and non-woven composites. Figure 7-22 shows the stress-shear relationships for case (5). In this case ultimate strength of the woven composite was 39 ksi and that of tile non-woven composite was 61 ksi. The stiffness of the non-woven composite was higher than that of the woven composite as in the previous four cases. Figure 7-23 shows the damage energy released by the woven and non-woven composites. Similar to case (4), more energy was released by the woven composite during the damage initiation stage. Figure 7-24 shows tile percent damage volume Vd for case (5). Damage initiation and propagation stresses shown in Figure 7-24 are lower for the woven composite compared to the non-woven laminate as in case (4) However, in case (5) the total damage volume is slightly higher for the woven composite.

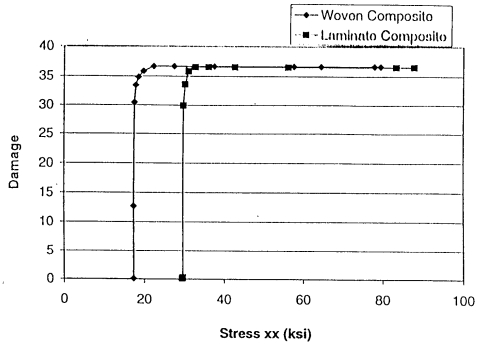

Figure 7-21: Structural Damage with Stress for Graphite/Epoxy Woven and Non-Woven Composite Laminates Subject to Compression and Shear N_x/N_{xy} = 10.

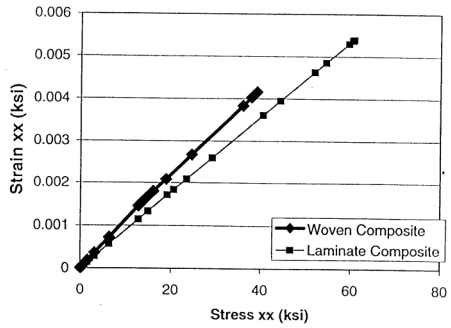

Figure 7-22: Stress-Strain Relations for Graphite/Epoxy Woven and Non-Woven Composite Laminates Subject to Compression and Shear N_x/N_{xy} = 5.

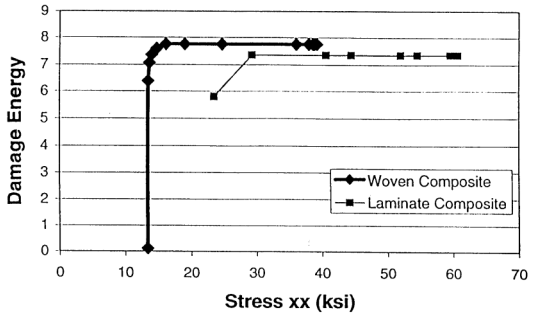

Figure 7-23: Damage Energy with Stress for Graphite/Epoxy Woven and Non-Woven Composite Laminates Subject to Compression and Shear N_x/N_{xy} =5.

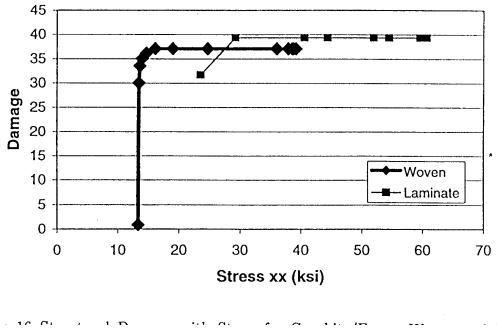

Figure 7-24: Structural Damage for Graphite/Epoxy Woven and Non-Woven Composite Laminates Subject to Compression and Shear N_x/N_{xy} = 5

Structural response of woven in non-woven composite panels subjected to compression and shear may be summarized as follows:

- The average compressive strength of woven composites was 22 percent lower than that of non-woven composites.
- The stiffness of woven composites was 16 percent lower than that of non-woven composites.
- The damage initiation stage occurred at a lower load for woven composites.
- After damage initiation was completed there was no damage growth stage. Structural fracture occurred suddenly with the compressive failure of O' plies for both woven and non-woven composites.

As the shear component of the load was increased the ultimate strength was decreased for both woven and non-woven composites.

- Increasing the shear component of loading increased tile difference. between the strengths of woven and non-woven composites.

Figure 7-25 shows the effect of shear to compressive loading ratio on the compressive strength of woven and non-woven composites. Compressive strength is degraded with increase of the shear component**.**

TRANSVERSE LOADING OF BEAM - Next, tile response of a short, simply supported, and centrally loaded beam as shown in Figure 7-26, with 1.5 in. span, and 1.25 in. width, made of AS4/3501-6 Graphite/Epoxy composite with fiber volume ratio of V_f =0.64 was investigated. Both non-woven and layer-to-layer angle interlock woven composite beams were simulated. In each case the composite thickness was 0.2-inch. The woven specimen had a 3-D angle interlock preform whereas the non-woven composite contained 32 plies arranged with a $[0/90]_{16s}$, layup.

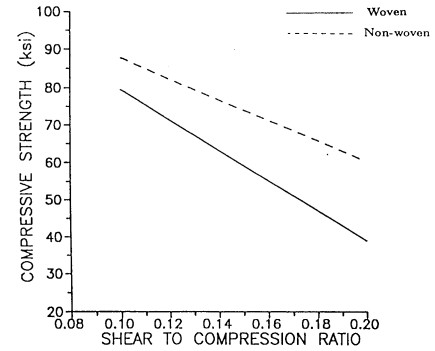

Figure 7-25: Effect of Shear on Ultimate Strength for Graphite/Epoxy Woven and Non-Woven Composite Laminates Subject to Compression with Shear

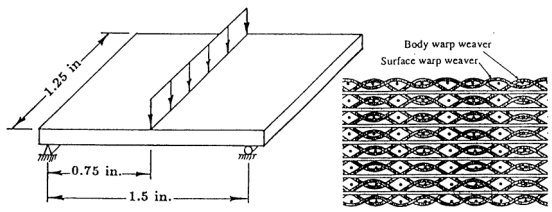

Figure 7-26: Short Beam Flexure Specimen for Graphite/Epoxy Woven and Non-Woven Composite Laminates Subject to Transverse Loading

Figure 7-27 shows the force-displacement relationship for the transversely loaded beam. In this case the ultimate load for the woven composite was 44 kips, whereas the ultimate load for the non-woven laminate was 18 kips. Also, after damage initiation the displacements for the non-woven composite were significantly greater than those of the woven composite. However, the deflections at the ultimate loading were approximately the same for the woven and non-woven specimens. Figure 7-28 shows the damage energies for the transverse loading case. The non-woven composite expanded a much larger damage energy at a lower load level compared to the woven composite. Figure 7-29 shows the percent damage volume V_d for this case. The structural damage volume during the damage initiation stage is approximately the same for woven and non-woven composites. However, the damage growth and propagation stresses shown in Figure 7-29 are lower for the non-woven laminate compared to the woven Composite.

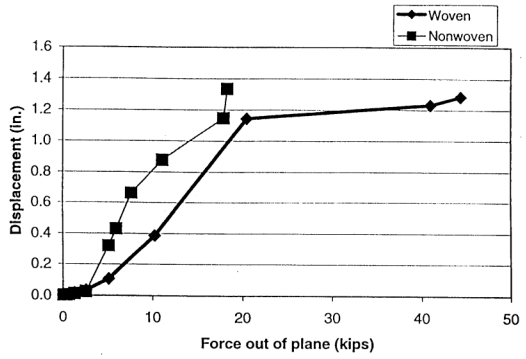

Figure 7-27: Load Displacement Relations for Graphite/Epoxy Woven and Non-Woven Composite Laminates Subject to Short Beam Transverse Loading

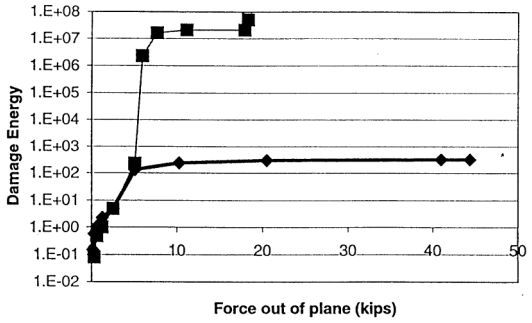

Figure 7-28: Damage Energy With Loading for Graphite/Epoxy Woven and Non-Woven Composite Laminates Subject to Short Beam Transverse Loading

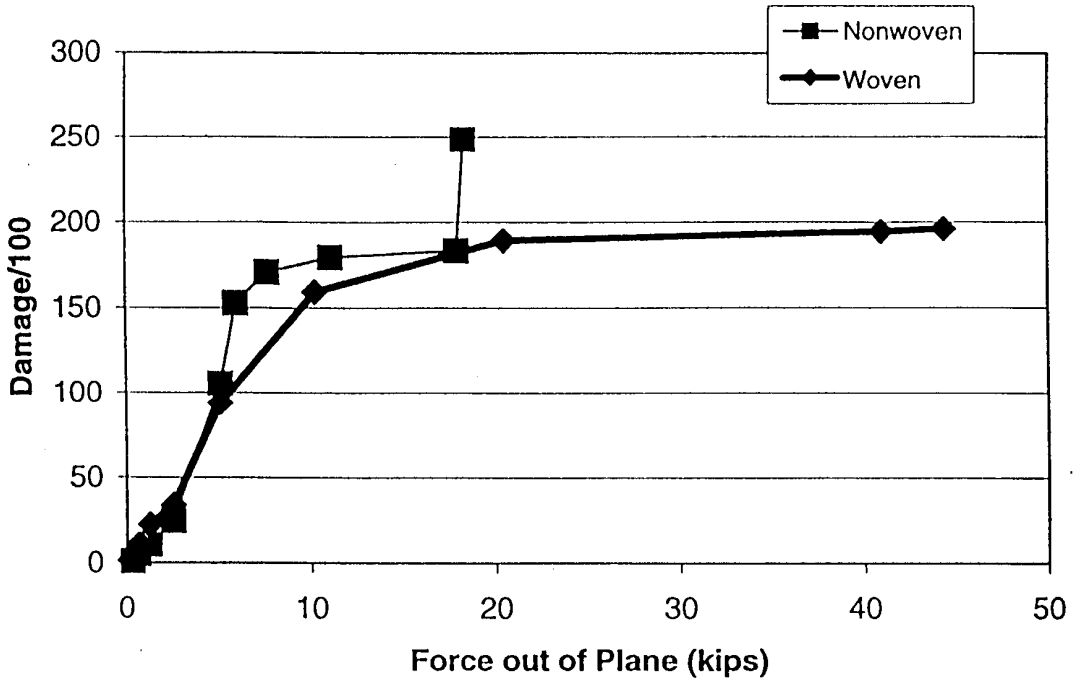

Figure 7-29: Damage Out of Plane Force Relations for Graphite/Epoxy Woven and Non-Woven Composite Laminates Subject to Short Beam Transverse Loading

Structural response of woven an non-woven simply supported composite short beams subjected to transverse loading my be summarized as follows:

- The flexural strength of the woven composite was more than twice the flexural strength of the non-woven composite.

- Both woven and non-woven composites begin (damage initiation by transverse tensile fractures of the 90º plies under the same loading. However, damage growth was more pronounced and abrupt for the non-woven Composite.

- After-damage initiation, the apparent stiffness of the woven composite was significantly higher than the stiffness of the non-woven laminate
- Deflections at failure were approximately the same for both woven and non-woven composites.
- The damage energy increased much more rapidly for the non-woven composite.

7.3.1 Conclusion

- Progressive damage and fracture of woven and non-woven composites has been simulated under tensile and compressive loads with the presence of shear, and also under short beam flexure.
- Non-woven composite panels are stronger than woven composite panels when subjected to in-plane tension or compression with shear.
- Non-woven composite panels are stiffer than woven composite panels when subjected to in-plane tension or compression with shear
- Both woven and non-woven cross-ply composites are sensitive to the presence and magnitude of in-plane shear stresses.
- Under compressive loading, the magnitude of in-plane shear stresses affects the woven composites more significantly compared to the effects on non-woven composites.
- Non-woven composite panels are weaker than 3-D woven composite panels when subjected to short beam flexure.
- Non-woven composite panels are less stiff than 3-D woven composite panels when subjected to short beam flexure.

7.4 STITCHED SIMULATION CAPABILITY

GENOA's verified algorithm for simulating stitched PMC materials was used in the composite mechanics module (PMC3) by ASC to simulate S/RFI materials. The S/RFI composites were divided into a series of unit cells (Figure 7-30) with both the fiber and stitch segments idealized as linear in the unit cells. The modified PMC3 module computes S/RFI stress limits by adding the oriented contribution of each stitch to each strength (longitudinal or transverse tension, compression or shear) component by tensor transformations in the absolute value.

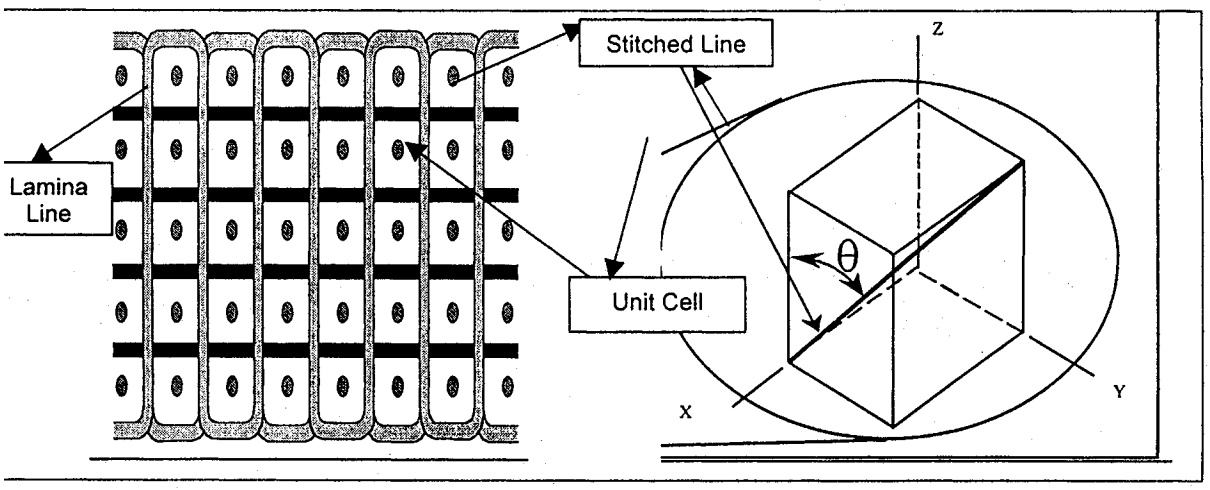

Figure 7-30. Idealized Fiber Stitch Segment in Unit Cell of 3D Braid Composites

7.4.1 Modification of Delamination Criteria Based on Stitching.

Introduction of stitching capability required the delamination criterion to be modified to reflect the effect of the stitching on the longitudinal compressive failure mechanism (Table 7-3) responsible for delamination failure as shown by Equation 7-71. The modification to account for the stitching effect on delamination was verified against coupon tests as shown in Table 7-3.

$$S_{DL11C}^{new} = F \cdot S_{DL11C}^{0ld} \tag{7-71}$$

Where

$$F = 1.0 + 17 V_w Cos^2\theta_w f_1\left(\sigma_1^w\right) f_2\left(\sigma^w, S^w\right)$$

V_W = woven fiber volume fraction

θ_W = Angle between woven fiber and Z axis

$$f_1\left(\sigma_1^w\right) = \begin{cases} 0 & 1f\ \sigma_1^w \le 0 \\ 1 & 1f\ \sigma_1^w \ge 0 \end{cases}$$

$$f_2\left(\sigma^w, S^w\right) = \begin{cases} 0 & 1f\ \text{woven fiber broken}\ \left(\sigma^w \ge S^w\right) \\ 1 & 1f\ \text{woven fiber not broken}\ \left(\sigma^w \le S^w\right) \end{cases}$$

7.5 TEST OF SIMULATING STITCHING EFFECT ON A COMPOSITE PANEL

Rectangular panels made of stitched and unstitched graphite/epoxy composite laminates were simulated to gain confidence in the capability of GENOA to determine the effects of stitching. Experimental test results were not available to verify the simulation results. The simulated laminates consisted of 48 plies configured in [0/+,-45/90]s6 orientation with a total thickness of 0.25 inch. The panels were 8.0 inches long and 4.0 inches wide. Stitching was in the 0º fiber direction and was done with 1200-denier Kevlar thread at a spacing of 0.25 inch and a pitch of 0.1 inch. The composite system was AS-4 graphite fibers in a high-modulus, high strength (HMHS) epoxy matrix. The graphite fiber volume ratio was 0.55 and the void volume ratio was 1%.

Table 7-3. Contribution of Stitched Fibers to Delamination Failure Criteria

Specimen	Simulation With New Delamination Criterion	Simulation With Old Delamination Criterion (GENOA-COD7 COD5)	Test Results
Short Block Compression	28.81 (3.9%)	20.32 (22.58)	30.0
Longitudinal Tension	31.98 (5.0%)	32.23 (33.40)	30.38 31.5 31.5 29.8 29.6 29.6
Transverse Tension	9.90 (2.9%)	(9.85)	10.20 10.3 10.2 10.1
Longitudinal Open Hole Tension	16.41 (9.8%)	(13.1)	18.45 17.6 17.8 29.8
Transverse Open Hole Tension	6.73 (4.2%)	7.02 (7.34)	7.03 6.93 6.95 7.21

Each panel was loaded with one end restrained by applying uniformly displaced tensile, compressive, in-plane shear, and out of plane transverse loads at the other end. Figure 7-31 shows the simulated damage progression with increasing tensile and compressive loading on stitched and unstitched panels. There was no difference in the damage initiation loads for stitched and unstitched panels, although damage initiation under tension occurred at a lower load compared to compression. Also, due to the large extent of ply transverse tensile failures, composite structural damage was much greater under tension than compression. After the completion of a well-defined damage growth stage, the state of damage remained constant until the ultimate load was reached. For tensile loading the stitched panel damage at the ultimate load was lower than that of the unstitched panel. For compressive loading the stitched panel damage at ultimate load is higher than that of the unstitched panel which was able to carry a larger compressive load at the ultimate fracture stage.

Figure 7-32 shows the damage progression for in-plane shear and out-of-plane flexural loads. At the ultimate fracture stage the magnitude of in-plane shear loading damage was greater for the unstitched panel. On the other hand, for the out-of-plane flexural loading, the stitched panel reached a much higher damage level compared to the unstitched panel.

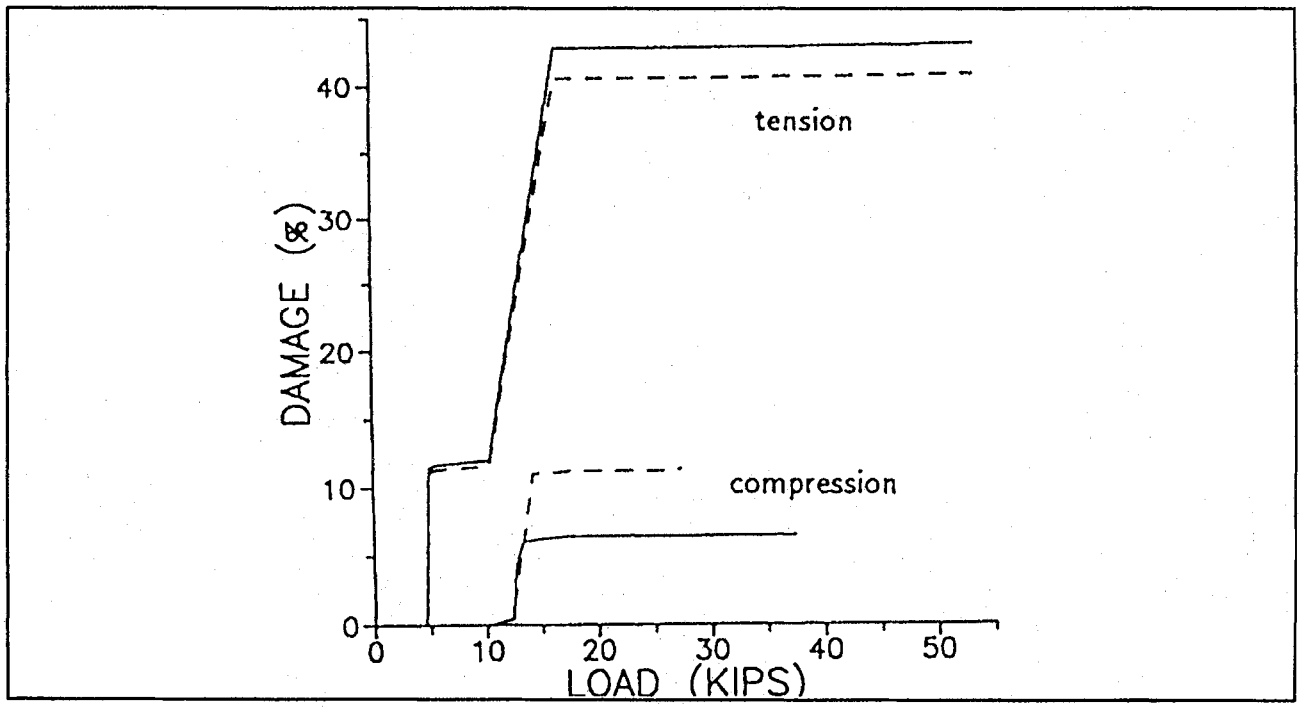

Figure 7-31. Damage Progression Under Tension and Compression; Graphite/Epoxy: 48 Plies [0/+45/-45/90]s6; Solid Lines =unstitched Composite, Dashed lines = Stitched Composite

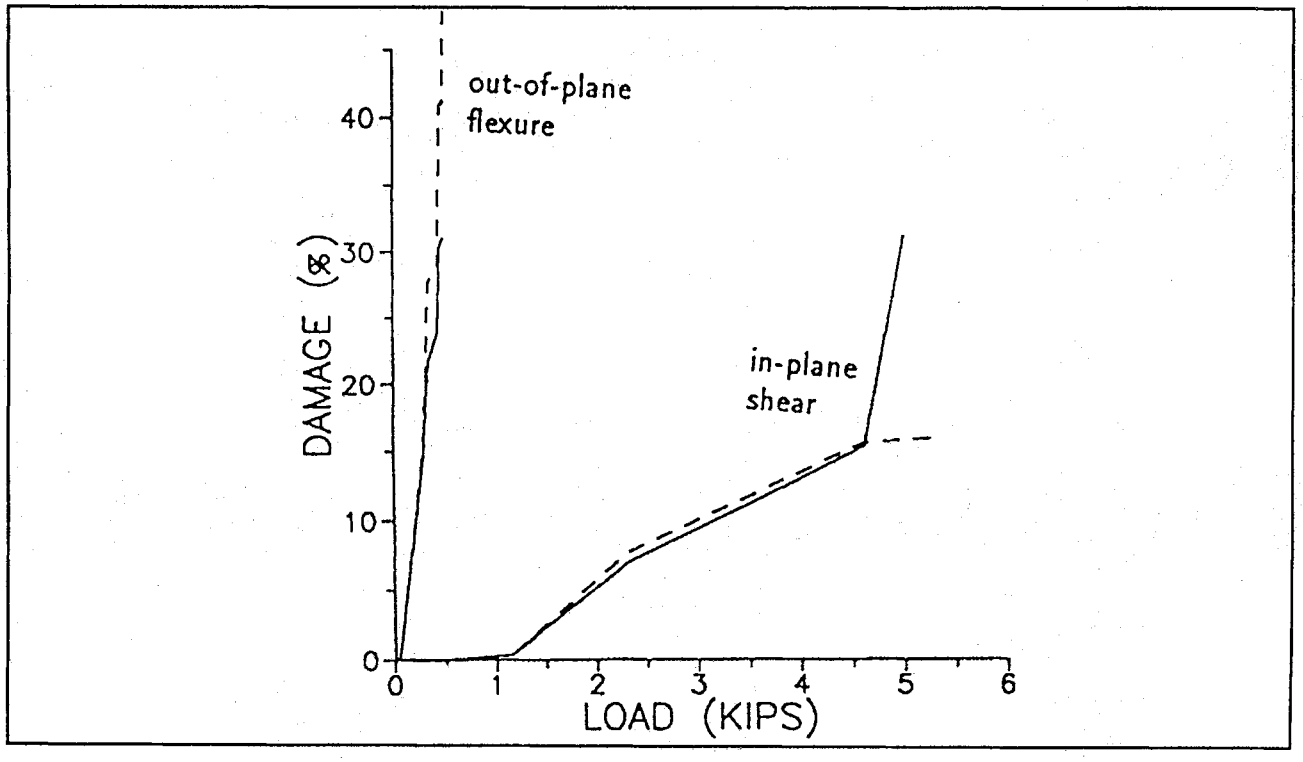

Figure 7-32. Damage Progression Under In-plane Shear and Out-of-plane Flexure; Graphite/Epoxy: 48 Plies [0/+45/-45/90]s6; Solid Lines =Unstitched Composite, Dashed Lines = Stitched Composite

REFERENCES

1. Chamis, C. C., Murthy, P. L. N., and Minnetyan, L. (1996)"Progressive Fracture of Polymer Matrix Composite Structures," Theoretical and Applied Fracture Mechanics, Vol. 25, 1996, pp. 1-15

2. Murthy P.L.N. and Chamis C.C., Integrated Composite Analyzer (ICAN): Users and Programmers Manual}, NASA Technical Paper 2515, March 1986.}

3. Lekhnitskii, S.G., Theory of Elasticity of an Anisotropic Body}, Mir Publishers, Moscow, 1977; English Translation, Mir Publishers, 1981, p. 42.}

4. Minnetyan L., Chamis C.C., and Murthy P.L.N., ``Structural Behavior of Composites with Progressive Fracture," {\em Journal of Reinforced Plastics and Composites}, Vol. 11, No. 4, April 1992, pp. 413-442}

5. Cox, B.N. and Dadkhah, M. S., (1995) "The Macroscopic Elasticity of 3D Woven Composites," Journal *of Composite Materials,* Vol. 29, No. 6, pp. 785-819.

6. Cox, B.N. and Dadkhah, M.S., ``The Macroscopic Elasticity of 3D Woven Composites," Journal of Composite Materials, Vol. 29, No. 6, 1995, pp. 785-819.}

APPENDIX A - CONSTITUENT MATERIAL PROPERTIES

The following properties were used in the ICAN databank to represent the fiber and matrix constituents:

ASW4 Graphite Fiber Properties:

Number of fibers per end = 10000
Fiber diameter = 0.00762 mm (0.300E-3 in)
Fiber Density = 4.04E-7 Kg/m^3 (0.063 lb/in^3)
Longitudinal normal modulus = 235 GPa (34.08E+6 psi)
Transverse normal modulus = 17.0 GPa (2.47E+6 psi)
Poisson's ratio (v_{12}) = 0.25
Poisson's ratio (v_{23}) = 0.27
Shear modulus (G_{12}) = 55.1 GPa (7.98E+6 psi)
Shear modulus (G_{23}) = 6.90 GPa (1.00E+6 psi)
Longitudinal thermal expansion coefficient = -1.0E-6/°C (-0.55E-6 °F)
Transverse thermal expansion coefficient = 1.0E-5/°C (0.56E-5 /°F)
Longitudinal heat conductivity = 0.302 J-m/hr/m^2/°C (4.03 BTU-in/hr/in^2/°F)
Transverse heat conductivity = 0.0302 J-m/hr/ m^2/°C (0.403 BTU-in/hr/ in^2/°F)
Heat capacity = 712 J/Kg/°C (0.17 BTU/lb/°F)
Tensile strength = 3,723 MPa (540 ksi)
Compressive strength = 3,351 MPa (486 ksi)

SGLW Glass Fiber Properties:
Number of fibers per end = 204
Fiber diameter = 0.00914 mm (0.360E-3 in)
Fiber Density = 5.77E-7 Kg/m^3 (0.090 lb/ in^3)
Longitudinal normal modulus = 84.8 GPa (12.3E+6 psi)
Transverse normal modulus = 84.8 GPa (12.3E+6 psi)
Poisson's ratio (v_{12}) = 0.22
Poisson's ratio (v_{23}) = 0.22
Shear modulus (G_{12}) = 34.8 GPa (5.04E+6 psi)
Shear modulus (G_{23}) = 34.8 GPa (5.04E+6 psi)
Longitudinal thermal expansion coefficient = 0.504E-5/°C (0.280E-5 / °F)
Transverse thermal expansion coefficient = 0.504E-5/°C (0.280E-5 / °F)
Longitudinal heat conductivity = 3.90E-3 J-m/hr/m^2/°C (5.208E-2 BTU-in/hr/in^2/°F)
Transverse heat conductivity = 3.90E-3 J-m/hr/ m^2/°C (5.208E-2 BTU-in/hr/in^2/°F)
Heat capacity = 712 J/Kg/°C (0.17 BTU/lb/°F)

Tensile strength = 2,482 MPa (360 ksi)
Compressive strength = 2,069 MPa (300 ksi)

Dow Tactix 138 Epoxy resin with H41 hardener Matrix Properties:
Matrix density = 3.35E-7 Kg/m^3 (0.0450 lb/in^3)
Normal modulus = 2.99 GPa (435 ksi)
Poisson's ratio = 0.300
Coefficient of thermal expansion = 0.72E-4/ °C (0.40E-4 /°F)
Heat conductivity = 8.681E-3 BTU-in/hr/ in^2/°F
Heat capacity = 0.25 BTU/lb/°F
Tensile strength = 85.0 MPa (12.3 ksi)
Compressive strength = 423 MPa (61.3 ksi)
Shear strength = 147 MPa (8.17 ksi)
Allowable tensile strain = 0.02
Allowable compressive strain = 0.05
Allowable shear strain = 0.04
Allowable torsional strain = 0.04
Void conductivity = 16.8 J-m/hr/m^2/°C (0.225 BTU-in/hr/ in^2\ °F)
Glass transition temperature = 216°C (420°F)

APPENDIX B - COMPOSITE ELASTIC PROPERTIES AND STRESS LIMITS COMPUTED BY EXTENDED ICAN.

The following notation is used:

Exx= Elastic modulus in stuffer direction

Eyy= Elastic modulus in filler direction

Ezz= Elastic modulus in normal direction

Gyz= Shear modulus in the filler-normal plane

Gzx= Shear modulus in the stuffer-normal plane

Gxy= Shear modulus in the stuffer-filler plane

NUxy= Poisson's ratio in the stuffer-filler plane

NUyz= Poisson's ratio in the filler-normal plane

NUxz= Poisson's ratio in the stuffer-normal plane

SWxxTf= Tensile strength in the stuffer direction based on fiber stress

SWxxTm= Tensile strength in the stuffer direction based on matrix stress

SWxxCf= Compressive strength in the stuffer direction based on fiber stress

SWxxCm= Compressive strength in the stuffer direction based on matrix stress

SWyyTf= Tensile strength in the filler direction based on fiber stress

SWyyTm= Tensile strength in the filler direction based on matrix stress

SWyyCf= Compressive strength in the filler direction based on fiber stress

SWyyCm= Compressive strength in the filler direction based on matrix stress

SWzzTf= Tensile strength in the normal direction based on fiber stress

SWzzTm= Tensile strength in the normal direction based on matrix stress

SWzzCf= Compressive strength in the normal direction based on fiber stress

SWzzCm= Compressive strength in the normal direction based on matrix stress

SWyzS= Shear strength in the filler-normal plane

SWzxS= Shear strength in the stuffer-normal plane

SWxyS= Shear strength in the stuffer-filler plane

Specimen 1 (LL1) Computed Properties

Exx= 0.45227E+07(psi) 0.31183E+11(Pa)

Eyy= 0.46543E+07(psi) 0.32090E+11(Pa)

Ezz= 0.11917E+07(psi) 0.82166E+10(Pa)

Gyz= 0.31874E+06(psi) 0.21976E+10(Pa)

Gzx= 0.67230E+06(psi) 0.46353E+10(Pa)

Gxy= 0.38089E+06(psi) 0.26261E+10(Pa)

NUxy= 0.46757E-01
NUyz= 0.35303E+00
NUxz= 0.49432E+00
SWxxTf= 0.91530E+05(psi) 0.63108E+09(Pa)
SWxxTm= 0.81016E+04(psi) 0.55858E+08(Pa)
SWxxCf= 0.82377E+05(psi) 0.56797E+09(Pa)
SWxxCm= 0.28341E+05(psi) 0.19541E+09(Pa)
SWyyTf= 0.78840E+05(psi) 0.54358E+09(Pa)
SWyyTm= 0.57421E+04(psi) 0.39590E+08(Pa)
SWyyCf= 0.70956E+05(psi) 0.48922E+09(Pa)
SWyyCm= 0.28617E+05(psi) 0.19731E+09(Pa)
SWzzTf= 0.18630E+05(psi) 0.12845E+09(Pa)
SWzzTm= 0.11901E+05(psi) 0.82058E+08(Pa)
SWzzCf= 0.16767E+05(psi) 0.11560E+09(Pa)
SWzzCm= 0.47279E+05(psi) 0.32598E+09(Pa)
SWyzS= 0.16716E+05(psi) 0.11526E+09(Pa)
SWzxS= 0.30041E+05(psi) 0.20712E+09(Pa)
SWxyS= 0.17531E+05(psi) 0.12087E+09(Pa)

Specimen 2 (LL2) Computed Properties

Exx= 0.47564E+07(psi) 0.32794E+11(Pa)
Eyy= 0.60985E+07(psi) 0.42047E+11(Pa)
Ezz= 0.11685E+07(psi) 0.80567E+10(Pa)
Gyz= 0.35379E+06(psi) 0.24393E+10(Pa)
Gzx= 0.44924E+06(psi) 0.30974E+10(Pa)
Gxy= 0.41936E+06(psi) 0.28914E+10(Pa)
NUxy= 0.40003E-01
NUyz= 0.37639E+00
NUxz= 0.46028E+00
SWxxTf= 0.84600E+05(psi) 0.58330E+09(Pa)
SWxxTm= 0.74442E+04(psi) 0.51326E+08(Pa)
SWxxCf= 0.75540E+05(psi) 0.52083E+09(Pa)
SWxxCm= 0.30148E+05(psi) 0.20786E+09(Pa)
SWyyTf= 0.10800E+06(psi) 0.74463E+09(Pa)
SWyyTm= 0.47825E+04(psi) 0.32974E+08(Pa)
SWyyCf= 0.97200E+05(psi) 0.67017E+09(Pa)
SWyyCm= 0.23835E+05(psi) 0.16434E+09(Pa)

SWzzTf= 0.90000E+04(psi) 0.62053E+08(Pa)
SWzzTm= 0.11007E+05(psi) 0.75888E+08(Pa)
SWzzCf= 0.75000E+04(psi) 0.51711E+08(Pa)
SWzzCm= 0.47902E+05(psi) 0.33027E+09(Pa)
SWyzS= 0.15996E+05(psi) 0.11029E+09(Pa)
SWzxS= 0.21372E+05(psi) 0.14735E+09(Pa)
SWxyS= 0.17107E+05(psi) 0.11795E+09(Pa)

Specimen 3 (LT1) Computed Properties

Exx= 0.61217E+07(psi) 0.42208E+11(Pa)
Eyy= 0.76844E+07(psi) 0.52982E+11(Pa)
Ezz= 0.13440E+07(psi) 0.92668E+10(Pa)
Gyz= 0.40277E+06(psi) 0.27770E+10(Pa)
Gzx= 0.65706E+06(psi) 0.45303E+10(Pa)
Gxy= 0.49072E+06(psi) 0.33834E+10(Pa)
NUxy= 0.32469E-01
NUyz= 0.34154E+00
NUxz= 0.47028E+00
SWxxTf= 0.11034E+06(psi) 0.76080E+09(Pa)
SWxxTm= 0.74093E+04(psi) 0.51085E+08(Pa)
SWxxCf= 0.87420E+05(psi) 0.60274E+09(Pa)
SWxxCm= 0.30012E+05(psi) 0.20692E+09(Pa)
SWyyTf= 0.12683E+06(psi) 0.87444E+09(Pa)
SWyyTm= 0.50119E+04(psi) 0.34556E+08(Pa)
SWyyCf= 0.10048E+06(psi) 0.69277E+09(Pa)
SWyyCm= 0.24978E+05(psi) 0.17222E+09(Pa)
SWzzTf= 0.14469E+05(psi) 0.99762E+08(Pa)
SWzzTm= 0.11259E+05(psi) 0.77629E+08(Pa)
SWzzCf= 0.11463E+05(psi) 0.79036E+08(Pa)
SWzzCm= 0.49199E+05(psi) 0.33921E+09(Pa)
SWyzS= 0.15954E+05(psi) 0.11000E+09(Pa)
SWzxS= 0.25400E+05(psi) 0.17513E+09(Pa)
SWxyS= 0.17520E+05(psi) 0.12080E+09(Pa)

Specimen 4 (LT2) Computed Properties

Exx= 0.61907E+07(psi) 0.42684E+11(Pa)
Eyy= 0.73329E+07(psi) 0.50559E+11(Pa)
Ezz= 0.12385E+07(psi) 0.85393E+10(Pa)
Gyz= 0.38965E+06(psi) 0.26865E+10(Pa)
Gzx= 0.45656E+06(psi) 0.31479E+10(Pa)
Gxy= 0.47943E+06(psi) 0.33055E+10(Pa)
NUxy= 0.36262E-01
NUyz= 0.37852E+00
NUxz= 0.43640E+00
SWxxTf= 0.10699E+06(psi) 0.73766E+09(Pa)
SWxxTm= 0.67638E+04(psi) 0.46635E+08(Pa)
SWxxCf= 0.87205E+05(psi) 0.60126E+09(Pa)
SWxxCm= 0.28568E+05(psi) 0.19697E+09(Pa)
SWyyTf= 0.12131E+06(psi) 0.83639E+09(Pa)
SWyyTm= 0.50269E+04(psi) 0.34659E+08(Pa)
SWyyCf= 0.98700E+05(psi) 0.68051E+09(Pa)
SWyyCm= 0.25053E+05(psi) 0.17273E+09(Pa)
SWzzTf= 0.78919E+04(psi) 0.54413E+08(Pa)
SWzzTm= 0.10851E+05(psi) 0.74816E+08(Pa)
SWzzCf= 0.65766E+04(psi) 0.45344E+08(Pa)
SWzzCm= 0.48938E+05(psi) 0.33742E+09(Pa)
SWyzS= 0.15707E+05(psi) 0.10830E+09(Pa)
SWzxS= 0.20686E+05(psi) 0.14263E+09(Pa)
SWxyS= 0.17224E+05(psi) 0.11875E+09(Pa)

Specimen 5 (LO) Computed Properties

Exx= 0.68661E+07(psi) 0.47340E+11(Pa)
Eyy= 0.83406E+07(psi) 0.57506E+11(Pa)
Ezz= 0.20268E+07(psi) 0.13974E+11(Pa)
Gyz= 0.42243E+06(psi) 0.29126E+10(Pa)
Gzx= 0.39636E+06(psi) 0.27328E+10(Pa)
Gxy= 0.50941E+06(psi) 0.35123E+10(Pa)
NUxy= 0.44636E-01
NUyz= 0.23683E+00
NUxz= 0.24207E+00

SWxxTf= 0.10876E+06(psi) 0.74989E+09(Pa)
SWxxTm= 0.59287E+04(psi) 0.40877E+08(Pa)
SWxxCf= 0.83541E+05(psi) 0.57599E+09(Pa)
SWxxCm= 0.29547E+05(psi) 0.20372E+09(Pa)
SWyyTf= 0.13667E+06(psi) 0.94230E+09(Pa)
SWyyTm= 0.48424E+04(psi) 0.33387E+08(Pa)
SWyyCf= 0.10498E+06(psi) 0.72379E+09(Pa)
SWyyCm= 0.24133E+05(psi) 0.16639E+09(Pa)
SWzzTf= 0.15649E+05(psi) 0.10790E+09(Pa)
SWzzTm= 0.95529E+04(psi) 0.65865E+08(Pa)
SWzzCf= 0.12020E+05(psi) 0.82876E+08(Pa)
SWzzCm= 0.47609E+05(psi) 0.32825E+09(Pa)
SWyzS= 0.15209E+05(psi) 0.10486E+09(Pa)
SWzxS= 0.15096E+05(psi) 0.10409E+09(Pa)
SWxyS= 0.16863E+05(psi) 0.11627E+09(Pa)

Specimen 6 (HL1) Computed Properties

Exx= 0.12664E+08(psi) 0.87313E+11(Pa)
Eyy= 0.78820E+07(psi) 0.54344E+11(Pa)
Ezz= 0.18247E+07(psi) 0.12581E+11(Pa)
Gyz= 0.58689E+06(psi) 0.40465E+10(Pa)
Gzx= 0.97941E+06(psi) 0.67528E+10(Pa)
Gxy= 0.86847E+06(psi) 0.59879E+10(Pa)
NUxy= 0.43653E-01
NUyz= 0.32418E+00
NUxz= 0.42246E+00
SWxxTf= 0.20875E+06(psi) 0.14393E+10(Pa)
SWxxTm= 0.51780E+04(psi) 0.35701E+08(Pa)
SWxxCf= 0.13084E+06(psi) 0.90213E+09(Pa)
SWxxCm= 0.21210E+05(psi) 0.14624E+09(Pa)
SWyyTf= 0.11383E+06(psi) 0.78484E+09(Pa)
SWyyTm= 0.70545E+04(psi) 0.48639E+08(Pa)
SWyyCf= 0.71350E+05(psi) 0.49194E+09(Pa)

SWyyCm= 0.35158E+05(psi) 0.24240E+09(Pa)
SWzzTf= 0.12220E+05(psi) 0.84255E+08(Pa)
SWzzTm= 0.11452E+05(psi) 0.78961E+08(Pa)
SWzzCf= 0.76596E+04(psi) 0.52811E+08(Pa)
SWzzCm= 0.52479E+05(psi) 0.36183E+09(Pa)
SWyzS= 0.16392E+05(psi) 0.11302E+09(Pa)
SWzxS= 0.22701E+05(psi) 0.15652E+09(Pa)
SWxyS= 0.18343E+05(psi) 0.12647E+09(Pa)

Specimen 7 (HL2) Computed Properties

Exx= 0.10925E+08(psi) 0.75324E+11(Pa)
Eyy= 0.74970E+07(psi) 0.51690E+11(Pa)
Ezz= 0.16265E+07(psi) 0.11214E+11(Pa)
Gyz= 0.52363E+06(psi) 0.36103E+10(Pa)
Gzx= 0.76341E+06(psi) 0.52636E+10(Pa)
Gxy= 0.74773E+06(psi) 0.51554E+10(Pa)
NUxy= 0.43899E-01
NUyz= 0.35415E+00
NUxz= 0.41978E+00
SWxxTf= 0.18122E+06(psi) 0.12495E+10(Pa)
SWxxTm= 0.48686E+04(psi) 0.33568E+08(Pa)
SWxxCf= 0.12368E+06(psi) 0.85277E+09(Pa)
SWxxCm= 0.21460E+05(psi) 0.14796E+09(Pa)
SWyyTf= 0.11279E+06(psi) 0.77768E+09(Pa)
SWyyTm= 0.65485E+04(psi) 0.45150E+08(Pa)
SWyyCf= 0.76981E+05(psi) 0.53077E+09(Pa)
SWyyCm= 0.32636E+05(psi) 0.22502E+09(Pa)
SWzzTf= 0.67675E+04(psi) 0.46661E+08(Pa)
SWzzTm= 0.10946E+05(psi) 0.75467E+08(Pa)
SWzzCf= 0.46189E+04(psi) 0.31846E+08(Pa)
SWzzCm= 0.51746E+05(psi) 0.35678E+09(Pa)
SWyzS= 0.15988E+05(psi) 0.11024E+09(Pa)
SWzxS= 0.19790E+05(psi) 0.13645E+09(Pa)
SWxyS= 0.17721E+05(psi) 0.12218E+09(Pa)

Specimen 8 (HT1) Computed Properties

Exx= 0.12217E+08(psi) 0.84235E+11(Pa)

Eyy= 0.76116E+07(psi) 0.52480E+11(Pa)

Ezz= 0.18565E+07(psi) 0.12800E+11(Pa)

Gyz= 0.57941E+06(psi) 0.39949E+10(Pa)

Gzx= 0.10334E+07(psi) 0.71249E+10(Pa)

Gxy= 0.84644E+06(psi) 0.58360E+10(Pa)

NUxy= 0.44398E-01

NUyz= 0.31640E+00

NUxz= 0.43024E+00

SWxxTf= 0.20523E+06(psi) 0.14150E+10(Pa)

SWxxTm= 0.55990E+04(psi) 0.38604E+08(Pa)

SWxxCf= 0.12978E+06(psi) 0.89481E+09(Pa)

SWxxCm= 0.21743E+05(psi) 0.14991E+09(Pa)

SWyyTf= 0.10957E+06(psi) 0.75544E+09(Pa)

SWyyTm= 0.71343E+04(psi) 0.49189E+08(Pa)

SWyyCf= 0.69286E+05(psi) 0.47771E+09(Pa)

SWyyCm= 0.35556E+05(psi) 0.24515E+09(Pa)

SWzzTf= 0.16220E+05(psi) 0.11183E+09(Pa)

SWzzTm= 0.11688E+05(psi) 0.80587E+08(Pa)

SWzzCf= 0.10257E+05(psi) 0.70718E+08(Pa)

SWzzCm= 0.52090E+05(psi) 0.35915E+09(Pa)

SWyzS= 0.16566E+05(psi) 0.11422E+09(Pa)

SWzxS= 0.25014E+05(psi) 0.17247E+09(Pa)

SWxyS= 0.18438E+05(psi) 0.12713E+09(Pa)

Specimen 9 (HT2) Computed Properties

Exx= 0.11641E+08(psi) 0.80263E+11(Pa)

Eyy= 0.79638E+07(psi) 0.54909E+11(Pa)

Ezz= 0.17288E+07(psi) 0.11920E+11(Pa)

Gyz= 0.56226E+06(psi) 0.38766E+10(Pa)

Gzx= 0.86794E+06(psi) 0.59842E+10(Pa)

Gxy= 0.81056E+06(psi) 0.55886E+10(Pa)

NUxy= 0.42309E-01
NUyz= 0.33746E+00
NUxz= 0.42197E+00
SWxxTf= 0.19197E+06(psi) 0.13236E+10(Pa)
SWxxTm= 0.51484E+04(psi) 0.35497E+08(Pa)
SWxxCf= 0.12476E+06(psi) 0.86021E+09(Pa)
SWxxCm= 0.21964E+05(psi) 0.15143E+09(Pa)
SWyyTf= 0.11796E+06(psi) 0.81332E+09(Pa)
SWyyTm= 0.66731E+04(psi) 0.46009E+08(Pa)
SWyyCf= 0.76666E+05(psi) 0.52859E+09(Pa)
SWyyCm= 0.33257E+05(psi) 0.22930E+09(Pa)
SWzzTf= 0.94306E+04(psi) 0.65021E+08(Pa)
SWzzTm= 0.11197E+05(psi) 0.77198E+08(Pa)
SWzzCf= 0.61291E+04(psi) 0.42259E+08(Pa)
SWzzCm= 0.52106E+05(psi) 0.35926E+09(Pa)
SWyzS= 0.16170E+05(psi) 0.11149E+09(Pa)
SWzxS= 0.21217E+05(psi) 0.14629E+09(Pa)
SWxyS= 0.18034E+05(psi) 0.12434E+09(Pa)

Specimen 10 (HO1) Computed Properties
Exx= 0.12920E+08(psi) 0.89079E+11(Pa)
Eyy= 0.77892E+07(psi) 0.53705E+11(Pa)
Ezz= 0.23411E+07(psi) 0.16142E+11(Pa)
Gyz= 0.49392E+06(psi) 0.34055E+10(Pa)
Gzx= 0.59733E+06(psi) 0.41184E+10(Pa)
Gxy= 0.70879E+06(psi) 0.48869E+10(Pa)
NUxy= 0.53865E-01
NUyz= 0.22979E+00
NUxz= 0.22127E+00
SWxxTf= 0.20390E+06(psi) 0.14058E+10(Pa)
SWxxTm= 0.41234E+04(psi) 0.28430E+08(Pa)
SWxxCf= 0.12786E+06(psi) 0.88154E+09(Pa)
SWxxCm= 0.20550E+05(psi) 0.14169E+09(Pa)
SWyyTf= 0.11365E+06(psi) 0.78358E+09(Pa)
SWyyTm= 0.69853E+04(psi) 0.48162E+08(Pa)
SWyyCf= 0.71264E+05(psi) 0.49135E+09(Pa)

SWyyCm= 0.34813E+05(psi) 0.24003E+09(Pa)
SWzzTf= 0.16379E+05(psi) 0.11293E+09(Pa)
SWzzTm= 0.10070E+05(psi) 0.69430E+08(Pa)
SWzzCf= 0.10270E+05(psi) 0.70812E+08(Pa)
SWzzCm= 0.50186E+05(psi) 0.34602E+09(Pa)
SWyzS= 0.15345E+05(psi) 0.10580E+09(Pa)
SWzxS= 0.15215E+05(psi) 0.10491E+09(Pa)
SWxyS= 0.17737E+05(psi) 0.12229E+09(Pa)

Specimen 11 (HO2) Computed Properties
Exx= 0.11681E+08(psi) 0.80535E+11(Pa)
Eyy= 0.76406E+07(psi) 0.52680E+11(Pa)
Ezz= 0.26057E+07(psi) 0.17966E+11(Pa)
Gyz= 0.47795E+06(psi) 0.32953E+10(Pa)
Gzx= 0.55656E+06(psi) 0.38373E+10(Pa)
Gxy= 0.65578E+06(psi) 0.45215E+10(Pa)
NUxy= 0.55867E-01
NUyz= 0.20306E+00
NUxz= 0.19595E+00
SWxxTf= 0.18509E+06(psi) 0.12761E+10(Pa)
SWxxTm= 0.44334E+04(psi) 0.30567E+08(Pa)
SWxxCf= 0.12002E+06(psi) 0.82753E+09(Pa)
SWxxCm= 0.22095E+05(psi) 0.15234E+09(Pa)
SWyyTf= 0.11304E+06(psi) 0.77937E+09(Pa)
SWyyTm= 0.67972E+04(psi) 0.46865E+08(Pa)
SWyyCf= 0.73301E+05(psi) 0.50539E+09(Pa)
SWyyCm= 0.33875E+05(psi) 0.23356E+09(Pa)
SWzzTf= 0.22095E+05(psi) 0.15234E+09(Pa)
SWzzTm= 0.97808E+04(psi) 0.67436E+08(Pa)
SWzzCf= 0.14328E+05(psi) 0.98788E+08(Pa)
SWzzCm= 0.48745E+05(psi) 0.33608E+09(Pa)
SWyzS= 0.15341E+05(psi) 0.10577E+09(Pa)
SWzxS= 0.15167E+05(psi) 0.10457E+09(Pa)
SWxyS= 0.17516E+05(psi) 0.12077E+09(Pa)

APPENDIX C - COMPARISON OF COMPOSITE PROPERTIES COMPUTED BY THE EXTENDED ICAN WITH COX [COX AND DADKHAH, 1995] AND EXPERIMENTAL DATA.

Specimen 1 (LL1) Woven Composite

Property	ICAN	Cox	Experiment
Exx (GPa)	31.18	36.8	30+/-6
Eyy (GPa)	32.09	38.7	
Ezz (GPa)	8.22	9.0	5.7
Gyz (GPa)	2.2	2.1	
Gzx (GPa)	4.64	6.0	
Gxy (GPa)	2.63	2.3	
NUxy	0.0468	0.023	0.024
NUyz	0.353	0.216	
NUxz	0.494	0.207	0.22

Specimen 2 (LL2) Woven Composite

Property	ICAN	Cox	Experiment
Exx (GPa)	32.79	34.9	28.5
Eyy (GPa)	42.05	47.6	
Ezz (GPa)	8.06	7.0	5.9
Gyz (GPa)	2.44	2.2	
Gzx (GPa)	3.10	3.2	
Gxy (GPa)	2.89	2.4	
NUxy	0.040	0.027	0.11
NUyz	0.376	0.310	
NUxz	0.460	0.457	0.50

Specimen 3(LT1) Woven Composite

Property	ICAN	Cox	Experiment
Exx (GPa)	42.21	47.3	27
Eyy (GPa)	52.98	59.5	
Ezz (GPa)	9.27	9.4	8.0
Gyz (GPa)	2.78	2.7	
Gzx (GPa)	4.53	5.6	
Gxy (GPa)	3.38	3.0	
NUxy	0.0325	0.02	0.048
NUyz	0.342	0.243	
NUxz	0.470	0.541	0.375

Specimen 4(LT2) Woven Composite

Property	ICAN	Cox	Experiment
Exx (GPa)	42.68	43.5	39
Eyy (GPa)	50.56	51.6	
Ezz (GPa)	8.54	7.0	7.9
Gyz (GPa)	2.69	2.4	
Gzx (GPa)	3.15	3.1	
Gxy (GPa)	3.31	2.6	
NUxy	0.036	0.027	0.021
NUyz	0.379	0.325	
NUxz	0.436	0.37	0.37

Specimen 5(L-O) Woven Composite

Property	ICAN	Cox	Experiment
Exx (GPa)	47.34	51.9	30+/-2
Eyy (GPa)	57.50	63.9	45.5+/-1.5
Ezz (GPa)	13.97	13.7	7.0+/-1
Gyz (GPa)	2.91	2.7	
Gzx (GPa)	2.73	2.8	
Gxy (GPa)	3.51	3.1	
NUxy	0.0446	0.034	0.053
NUyz	0.236	0.183	
NUxz	0.242	0.184	0.49

Specimen 6(HL1) Woven Composite

Property	ICAN	Cox	Experiment
Exx (GPa)	87.31	91.5	85+/-8
Eyy (GPa)	54.34	56.2	43.8
Ezz (GPa)	12.58	12.1	16+/-2
Gyz (GPa)	4.47	4.1	
Gzx (GPa)	6.75	7.1	
Gxy (GPa)	5.99	5.4	6.2
NUxy	0.0437	0.034	0.061
NUyz	0.324	0.286	
NUxz	0.422	0.456	

Specimen 7(HL2) Woven Composite

Property	ICAN	Cox	Experiment
Exx (GPa)	75.32	81.2	80
Eyy (GPa)	51.69	55	42.3
Ezz (GPa)	11.21	10.2	14.0
Gyz (GPa)	3.61	3.6	

Gzx (GPa)	5.26	5.3	
Gxy (GPa)	5.16	4.6	5.8
NUxy	0.0439	0.035	0.13
NUyz	0.354	0.298	
NUxz	0.420	0.425	0.45+/-0.05

Specimen 8(HT1) Woven Composite

Property	ICAN	Cox	Experiment
Exx (GPa)	84.24	88.6	79
Eyy (GPa)	52.48	54.4	42.5
Ezz (GPa)	12.80	12.8	13.8
Gyz (GPa)	3.99	4.0	
Gzx (GPa)	7.12	7.8	
Gxy (GPa)	5.84	5.3	5.6
NUxy	0.0444	0.033	0.054
NUyz	0.316	0.248	
NUxz	0.430	0.486	

Specimen 9(HT2) Woven Composite

Property	ICAN	Cox	Experiment
Exx (GPa)	80.26	85.1	72
Eyy (GPa)	54.91	57.6	45.8
Ezz (GPa)	11.92	11.2	13.9
Gyz (GPa)	3.88	3.9	
Gzx (GPa)	5.98	6.2	
Gxy (GPa)	5.59	5.0	5.7
NUxy	0.0423	0.033	0.097
NUyz	0.337	0.280	
NUxz	0.422	0.443	

Specimen 10(HO1) Woven Composite

Property	ICAN	Cox	Experiment
Exx (GPa)	89.08	93.1	88
Eyy (GPa)	53.71	56.4	39.9
Ezz (GPa)	16.14	17.3	15.4
Gyz (GPa)	3.41	4.1	
Gzx (GPa)	4.12	4.7	
Gxy (GPa)	4.89	5.4	5.0
NUxy	0.0539	0.051	0.055
NUyz	0.230	0.192	
NUxz	0.221	0.190	

Specimen 11(HO2) Woven Composite

Property	ICAN	Cox	Experiment
Exx (GPa)	80.54	83.8	69+/-5
Eyy (GPa)	52.68	55.9	41.6
Ezz (GPa)	17.97	20.4	22.3
Gyz (GPa)	3.30	4.0	
Gzx (GPa)	3.84	4.4	
Gxy (GPa)	4.52	4.9	
NUxy	0.0559	0.052	0.07
NUyz	0.203	0.158	
NUxz	0.196	0.157	

8.0 Impact Loading of Woven/Braided/Stitched Composite Structure

Impact loading of woven/braided/stitched composite structure is performed by; 1) modification of PFA to perform Pseudo-dynamic (include inertia, and acceleration) analysis, and 2) post processing of PFA static analysis to generate Pseudo static (excluding inertia, and acceleration) impact.

8.1 MODIFICATION OF CODSTRAN FOR IMPACT SIMULATION INCLUDING INERTIAL EFFECTS OF THE IMPACTED STRUCTURE

Formulation of this implementation is similar to that of the former pseudo-static analysis of a composite cylindrical shell containment structure impacted by an escaped engine blade. However, in the new approach, the inertial forces of the impacted structure are not neglected.

The escaped blade (impacting object) has a mass m and initial contact velocity $\boldsymbol{u_{b0}}$. After contact, the escaped blade loses its velocity due to the impulse of the impact. According to the first law of thermodynamics the reduction of the kinetic energy of the escaped blade is equal to the work done by the impact force, therefore the velocity of the blade may be computed from:

$$\frac{1}{2}m\dot{u}^2{}_{b0} - \frac{1}{2}m\dot{u}_b^2 = W_e \tag{1}$$

If the time history of the impact force $\boldsymbol{F_i}$ and the change in the velocity of the impactor are known, the amount of time elapsed with reference to the initiation of contact between the impactor and the impacted structure may be computed from the impulse-momentum relationship.

$$m\dot{u}_{b0} - m\dot{u}_b = \int_{t0}^{t} F dt \tag{2}$$

where $\boldsymbol{m}$ is the mass of the escaped blade. The equations of dynamic equilibrium are written for the combined containment structure and impacting escaped blade dynamic system from the time of initial contact that starts the impact. The system dynamic equations in matrix form are:

$$[M]\{\ddot{u}\} + [D]\{\dot{u}\} + [K][u\} = [0] \tag{3}$$

where [M] is the mass matrix of combined containment plus blade finite element model, ***[D]*** is the damping matrix, [K] is the stiffness matrix, and {u},{u˙}, and {u¨},are the displacement, velocity, and acceleration vectors of the system. The right hand side of Equation (3) is zero since the impact force is internal to the system. The mass matrix ***[M]*** may be decomposed into the component mass matrices of [M$_c$] and [m] corresponding to the masses of containment structure and blade, respectively. Therefore, the dynamic equations can be written as:

$$[M_c]\{\ddot{u}_c\} + [m]\{\ddot{u}_b\} + [D]\{\dot{u}\}[K]\{u\} = \{0\} \tag{4}$$

Where the $\boldsymbol{[M_c]}$ {u$_c$¨}term represents the vector of inertial forces on the containment and the $\boldsymbol{[m]\{u_b\ddot{}\}}$ term represents the inertial forces on the blade. For pseudo-static analysis without damping, the $\boldsymbol{[M_c]\{u_c\ddot{}\}}$and the $\boldsymbol{[D]\{u\dot{}\}}$ terms may be neglected and the system equations written as:

$$[m]\{\ddot{u}_b\} + [K]\{u\} = \{0\} \tag{5}$$

In which the sum of $\boldsymbol{[M_b]\{u_b\ddot{}\}}$inertial forces represents the negative of the impact force $\boldsymbol{\{F\}_i}$. Therefore the equations of pseudo-static equilibrium are written in the form:

$$[K]\{u\} = \{F\}_i \tag{6}$$

Equation 6 may be solved via computational simulation for displacements and damage as a function of the impact force. The instantaneous velocity $\{uc^{\cdot}\}$ of the impacting blade is obtained from Equation 1 in which the right hand side is evaluated by computing the work done by the impact force

$$W_e = \int_0^{ub} F du \tag{7}$$

where u_b is the current displacement of the impacting blade.

Whether or not the inertial forces of the impacted structure may be neglected depends on the size of the impacted structure and the impact velocity. The larger the size of the impacted structure and the higher the impact velocity the more important are the effects of the inertial forces of the impacted structure. It is not always feasible to make an a priori determination of the importance of inertial forces on the simulation of impact response. Therefore, it is necessary to have the ability to include the effects of inertial forces of the impacted structure. If structural damping is neglected, the dynamic equations can be written as:

$$[M_c]\{\ddot{u}_c\} + [m]\{\ddot{u}_b\} + [K]\{u\} = \{0\} \tag{8}$$

The computational simulation of progressive damage and fracture in the CODSTRAN code is a step by step procedure using a small load increment. The incremental equations of dynamic equilibrium may be written as:

$$[M_c]\Delta\{\ddot{u}_c\} + [m]\Delta\{\ddot{u}_b\} + [K]\Delta\{u\} = \{0\} \tag{9}$$

As before, considering that the impact force exerted on the structure is the equal and opposite of the force exerted on the impacting object, we write:

$$[M_c]\Delta\{\ddot{u}_c\} + [K]\Delta\{u\} = \Delta\{F\}_i \tag{10}$$

Computational simulation of the incremental loading analysis described by Equation 10 is implemented by treating the impact force $\{F\}_i$ as the independent variable. After each incremental loading analysis, the change in the velocity of the impactor is computed from Equation 1 and the time increment is computed from Equation 2. Next, nodal velocities of the impacted structure are computed as the ratio of the incremental displacements to the time increment. Nodal velocities are saved in a scratch file to enable computation of nodal accelerations in the next increment. Nodal accelerations are computed as the ratios of the changes in velocities to the time increment. If nodal accelerations of the impacted structure are multiplied by the nodal masses, the inertial forces $[M_c]\{u_c^{\cdot\cdot}\}$ in Equation 8 would be obtained. However, since computational simulation is carried out in terms of the incremental formulation given by Equation 10, the incremental changes in nodal accerations are required. Therefore, nodal accelerations are saved in a scratch file to compute

the incremental changes in accelerations in the next step. Multiplying the incremental changes in nodal accelerations by the nodal masses gives the inertial load increments $[M_c]\{u_c^{\cdot\cdot}\}$ required in Equation 10. Simulation of the impact response begins with the initiation of contact when the impact force, displacement, velocity, and acceleration of the impacted structure have zero initial conditions.

The analysis of dynamic impact is implemented by modifying the CODSTRAN simulation process to include inertial forces of the impacted structure as follows:

1. Subroutine INITIM is called by CODEXE prior to the start of an impact simulation. It initializes impact variables (force, displacement, work) and the files VELOC.SCRATCH.OLD and ACCEL.SCRATCH.OLD to zero. Each file contains three entries per node as the x, y, and z components of the velocity and acceleration vectors, respectively.

2. Subroutine VELOC is called by CODEXE after each simulation step. It first computes the velocity of the impactor from Equation 1. Next, it computes the time increment from Equation 2. Then it computes the velocity vector at each node as the ratio of incremental displacement to time increment and writes them to a scratch file named VELOC.SCRATCH.NEW. Note that VELOC.SCRATCH.OLD data will need to be reordered when elements are deleted and nodes are renumbered. However, the VELOC.SCRATCH.OLD file from the last equilibrium stage need be saved in VELOC.EQUIL.OLD in case the analysis needs to be restarted from the last equilibrium stage. Alternately, VELOC.SCRATCH.OLD can be saved in the equilibrium database SCRA76.

   Subroutine VELOC also computes nodal accelerations. It computes the accelerations at each node by taking the difference between VELOC.SCRATCH.NEW and VELOC.SCRATCH.OLD data and dividing by the time increment. Accelerations thus computed are written to a scratch file named ACCEL.SCRATCH.NEW.

   Note that ACCEL.SCRATCH.OLD data will need to be reordered when elements are deleted and nodes are renumbered. However, the ACCEL.SCRATCH.OLD file from the last equilibrium stage need be saved in ACCEL.EQUIL.OLD in case the analysis needs to be restarted from the last equilibrium stage. Alternately, ACCEL.SCRATCH.OLD can be saved in the equilibrium database SCRA76.

3. Subroutine INERLD is called by CODEXE before a finite element analysis. It computes the acceleration increments by taking the difference between ACCEL.SCRATCH.NEW and ACCEL.SCRATCH.OLD. The acceleration increments are multiplied by the lumped mass at each node to obtain the inertial load increments. Subroutine INERLD modifies the MHOST input file SCRA55 to write the inertial force increments. Subroutine INERLD also computes the lumped mass value associated with each node. (Units of mass are lbs-sec^2/in.)

At present input data to dynamic impact simulation requires the selection of the first 3 displacements to be tracked as the x, y, z components of displacement for a characteristic node of contact between the impactor and impacted structure. Additionally, the CODINP file requires three additional cards in sequence. The first card of which must start with the IMPACT keyword. The second card contains the impactor total mass (lbs-sec^2/in), the initial velocity (in/sec), and the number of impactor nodes as list directed input. The next card(s) contain the node numbers of the impactor nodes. In the current version numbers of the impactor nodes should come before the node numbers of the impacted structure nodes to prevent changes of node numbers on the impactor if elements on the impacted structure are removed after fractures.

Output is the same as a typical CODSTRAN run except for a new file SCRA24 that contains the impact force, displacement, and velocity of the impactor. The code stops when the impactor penetrates through the impacted structure, the structure breaks into two pieces, or if the impactor velocity is reduced to zero (impacting object is stopped by the impacted structure).

8.2 MODIFICATION OF CODSTRAN FOR IMPACT SIMULATION NOT INCLUDING INERTIAL EFFECTS OF THE IMPACTED STRUCTURE

8.2.1 Summary Of The Governing Equations

Equilibrium Equation:

$$[M]\{\ddot{u}\} + [D]\{\dot{u}\} + [K]\{u\} = \{F(t)\}$$

In the present work:

$$[K]\{u\}_i = \{F(t)\}_i \tag{11}$$

Kinetic energy :

$$\frac{1}{2} m\dot{u}^2_{b0} - \frac{1}{2} m\dot{u}_b^2 = W_e \tag{12}$$

m is the mass of the escape object (blade)
u_{0}'' u_b. is the initial and impact velocity of the blade respectivley

$$W = \{F\}_i^T \{u\}_i$$

Impulse Law:

$$m\dot{u}_{b0} - m\dot{u}_b = \int_{t0}^{t} F dt \tag{13}$$

8.3 RESULTS AND DISCUSSION

Pseudo tatic, and Pseudo dynamic analysis was tested using An Escaping blade impacted a composite cylinder. The impacted blade had an initial velocity of 1400 ft/sec. The cylinder (length = 96. In, R-= 36.1 inch, thickness = 0.25 in.) used graphite/epoxy (FVR = 60%, VVR =1 %) , with (0/45/90/0-45/45/90/3s of 48 uniform plies. Figure 8-1 shows the location of the damaged nodes and Pattern of Failure during the initial impact. Figure 8-2:shows the simulated Photo-Elastic Isocromatic Pattern at Failure. Figure: 8-3. Shows Stress in X direction Critical Impact Event Before Failure, and Figure 8-4 shows the zoomed stress in X direction near the damaged zone. Figure 8-5 shows the Final Failure pattern, Figure 8-6 identifies the Most Contributing Failure as the Transverse Tensile). Figure 8-7 shows the Comparison of Force Vs. Time for fully dynamic and static of PMC Cylinder impacted by blade. Figure 8-8 Comparison of Displacement Vs. Time for fully dynamic and static of PMC cylinder impacted by blade. Figure 8-9 Comparison of Velocity

Vs. Time for Pseudo static and fully dynamic. Figure 8-10: Comparison of Damage Vs. Time for Pseudo. Figure 8-11: Comparison of DERR Vs. Time for Pseudo dynamic and static of PMC cylinder impacted by blade. Figure 8-12: Comparison of TDERR Vs. Time for fully dynamic and static of PMC cylinder

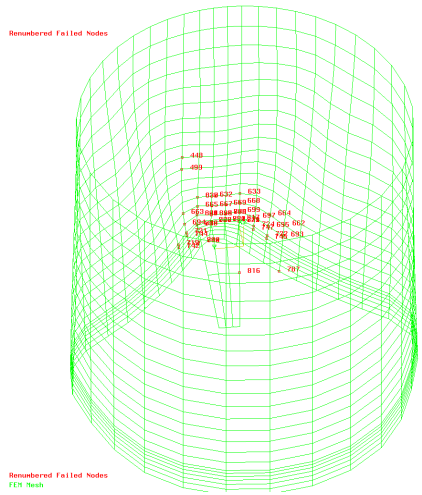

Figure 8-1: Damaged Node Pattern during Failure

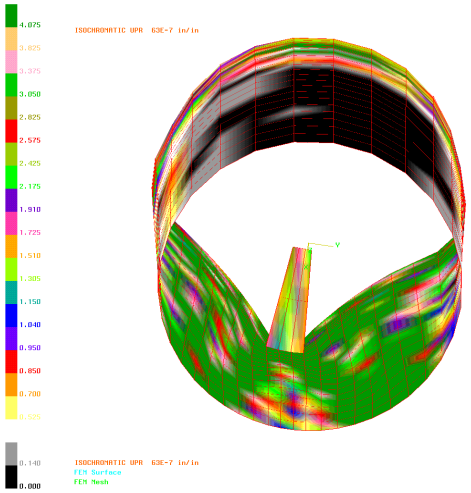

Figure 8-2: Photo-Elastic Isocromatic Pattern at Failure

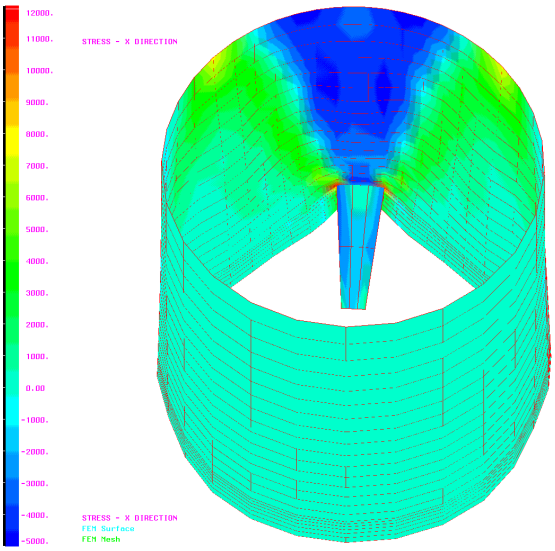

Figure: 8-3. Stress X at Critical Impact Event Before Failure

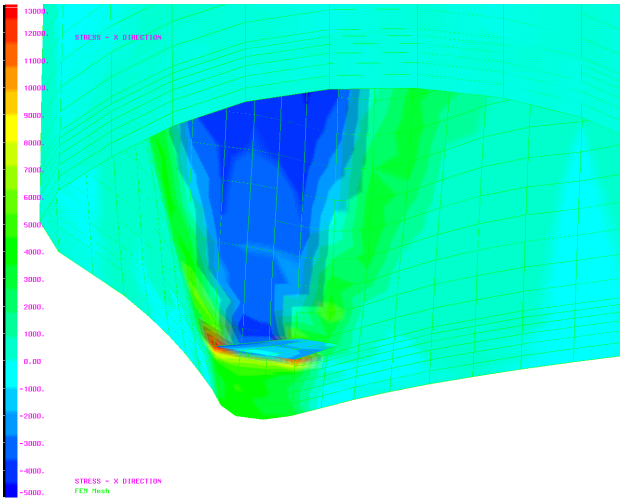

Figure: 8-4. Stress X at Critical Impact Event Before Failure

8.0 Impact Loading of Woven/Braided/Stitched Composite Structure

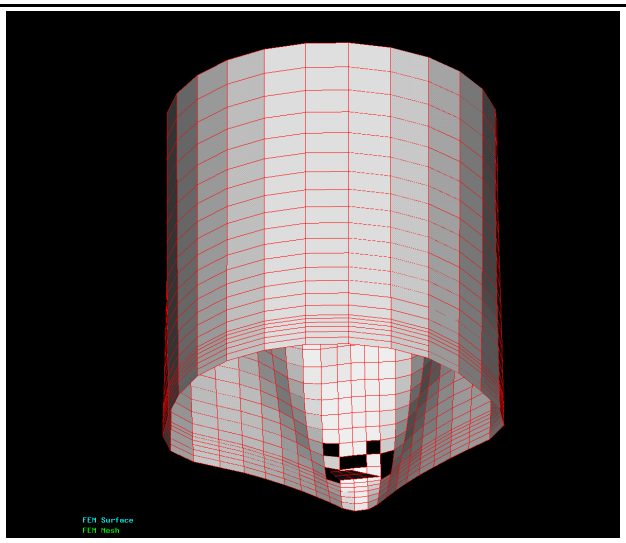

Figure 8-5 Final Failure

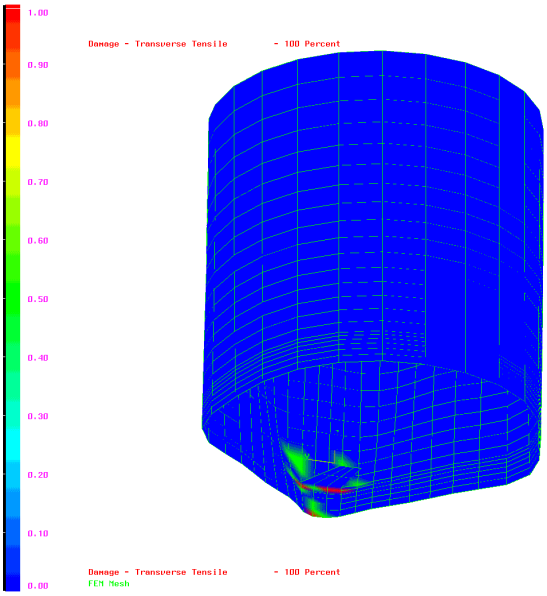

Figure 8-6: Most Contributing Failure (Transverse Tensile)

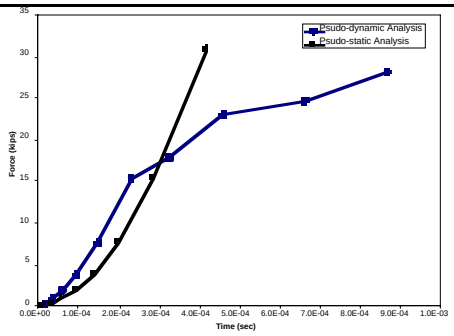

Figure 8-7: Comparison of Force Vs. Time for Pseudeo dynamic and static of PMC Cylinder impacted by blade

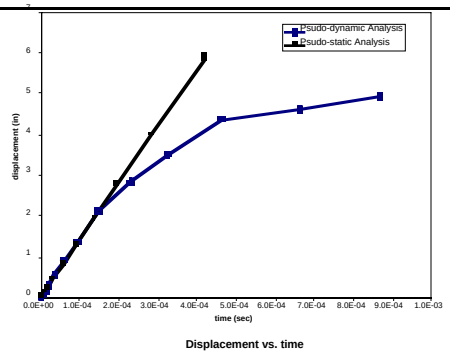

Figure 8-8: Comparison of Displacement Vs. Time for Pseudeo dynamic and static of PMC cylinder impacted by blade

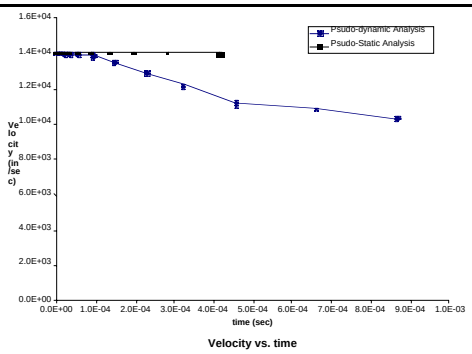

Figure 8-9: Comparison of Velocity Vs. Time for Pseudeo dynamic and static of PMC cylinder impacted by blade

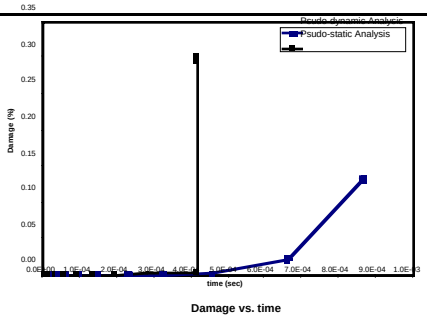

Figure 8-10: Comparison of Damage Vs. Time for Pseudeo dynamic and static of PMC cylinder impacted by blade

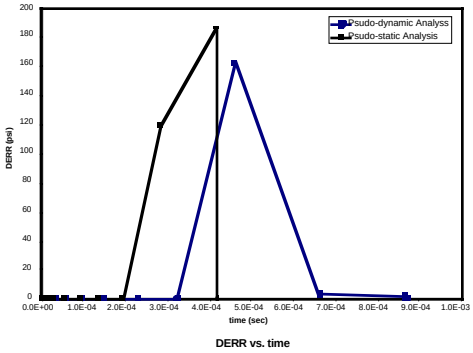

Figure 8-11: Comparison of DERR Vs. Time for Pseudeo dynamic and static of PMC cylinder impacted by blade

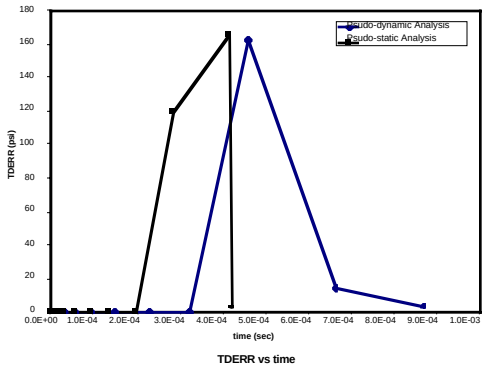

Figure 8-12: Comparison of TDERR Vs. Time for Pseudeo dynamic and static of PMC cylinder

9.0 Graphics User Interface in GENOA

GENOA Graphics User Inetrface (GUI) can be utilized to execute all other GUI's such as GENEX, Post Cycle, 3D Plot, Xgenoa2D. (Figure 9-1). Figure 9-2 shows the GUI post cycle tool bar used to extract the desired file for post analysis viewing. Figure 9-3 Shows 3D Plot GUI with visualization ICONS.

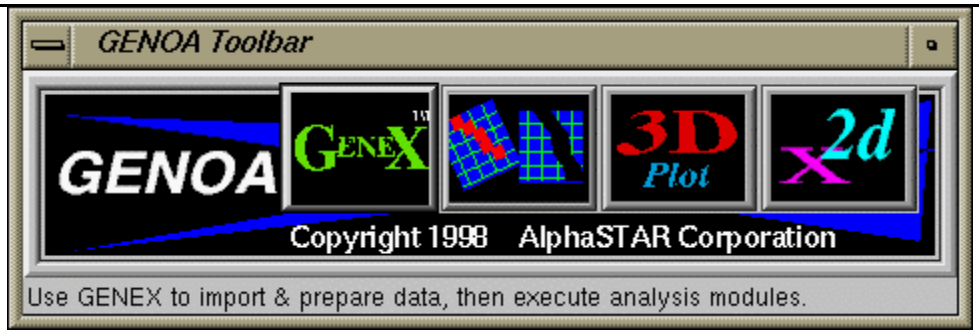

9-1. GENOA Graphics User Interface : GENEX, Post Cycle, 3D Plot, Xgenoa2D

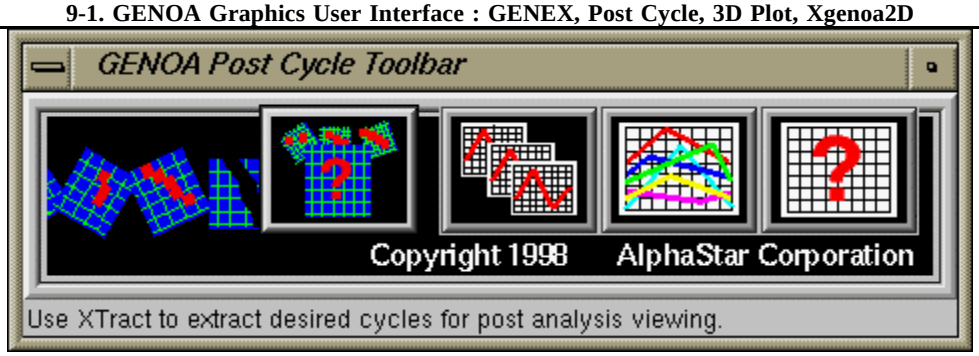

9-2. GENOA Post Cycle Tool Bar

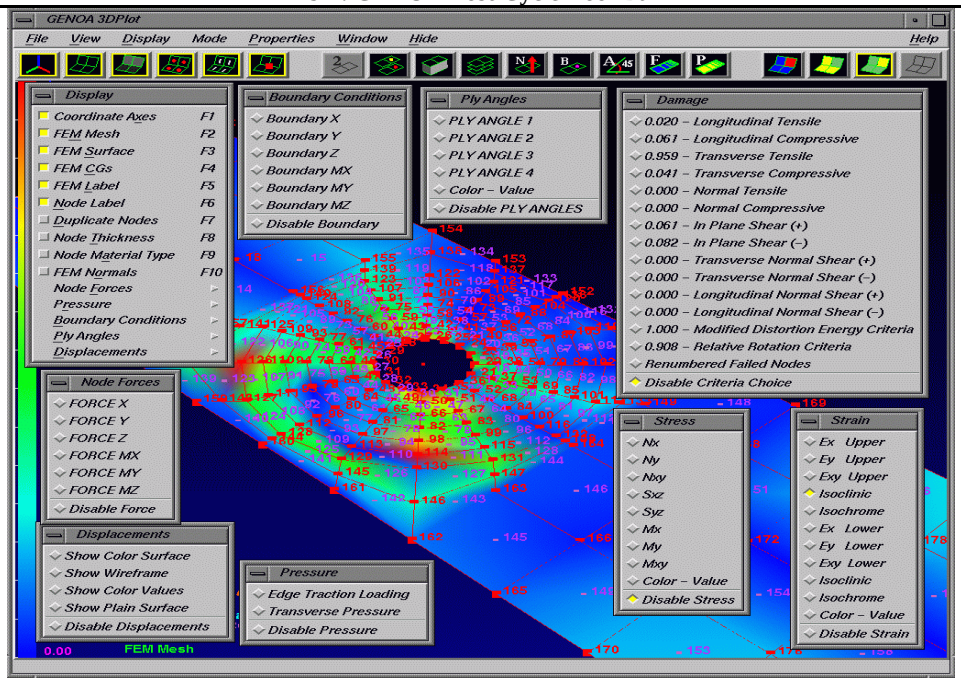

Figure 9-3. An Up-Close View of Default Display Properties Initiated from a Pull-Down Menu

9.1 Display of Stress, Strain, EIgenValue and Damage

The graphical presentation feature of GENOA-PFA is designed to generate 3D plots for visualization of: 1) PFA input file data, and 2) stress, strain, and damage results.

PFA Input File Visualization

The menu to specify the PFA input file visuaization is shown in Table 9-1. The entry "CODINP" in Table 4.7-1 is an example of a typical GENOA-PFA input file name. The GUI can plot the PFA input file data relative to: 1) global coordinate axes, 2) FEM mesh, 3) FEM surface, 4) FEM cg, 5) FEM element label, (6) Node label, 7) master/slave (duplicate) nodes, 8) node thickness, 9) node layer types, 10) FEM normalas (clockwise or counter clockwise), 11) Node Forces, 12) nodal Boundary conditionss, and 13) Ply angles.

Table 9-1 Visualization of PFA STRESS, STRAIN, DAMAGE DATA

PLOT -------PLOT PFA STRESS, STRAIN, DAMAGE DATA -------- PLOT		
(L)	(A)	POLYMER PFA
Filename	**SET A ON LINES 1 Through 4**	
1)	CODINP	GENOA-PFA Input data
2)		
3)		
4)		
5)		
OUTPUT	**SET A ON LINE 7**	
1	NONE	POST CQUAD FILE
COMMANDS: HE - HELP, RE - REFRESH, BA - BACK, / - EXPRESS BACK PRESS ENTER TO CREATE THE POST FILE - / TO RETURN TO PFA		

PFA Stress, Strain, Eigen modes, Damage, and Original FEM Visualization

The menu to specify which GENOA-PFA stress, strain, and damage result files are to be generated by the POST program for use in subsequent graphical presentations is shown in Table 9-.2. _The user can plot any state of stress, strain, damage, and eigen modes occuring at any iteration in the simulation by inputing the selected iteration number and the associated file name (e.g. FEM018;.pat=FEM of PATRAN neutral file, at iteration number 018, STR018.nes= stress file at iteration number 018, EPS018.nes=strain field at iteartion number 018; DAM018.nes=state of danmage at iteration number 018, and FEM019.pat=PATRAN data number 019). The first entry (e.g., FEM018.pat) must be made in all cases. The other entries are optional. The user can also visualize the original FEM and compare the displacement vector from the current visualized iteration.

Table 9-2. Visualization of PFA STRESS, STRAIN, DAMAGE DATA

PLOT -------PLOT PFA STRESS, STRAIN, DAMAGE DATA -------- PLOT		
(L)	(A)	POLYMER PFA
Filename	**SET A ON LINES 1 Through 4**	
1)	FEM018.pat	PATRAN DATA
2)	STR018.nes	STRESS DATA
3)	EPS018.nes	STRAIN DATA
4)	DAM018.nes	DAMAGE DATA
5)	EIGEN018.nes	EIGEN VALUE DATA
5)	FEM019.pat	PATRAN DATA Number 019
OUTPUT	**SET A ON LINE 7**	
1	NONE	POST CQUAD FILE
COMMANDS: HE - HELP, RE - REFRESH, BA - BACK, / - EXPRESS BACK PRESS ENTER TO CREATE THE POST FILE - / TO RETURN TO PFA		

The user can "click on" a damage icon and a list will be presented giving the percent of damage that occurred in each of 14 damage modes. Clicking on a damage mode in this list will produce a graphical plot showing the distribution of damage in that damage mode. This manner of presentation is a powerful feature by which GENOA-PFA presents results in a clear and very accessible manner.

There are several sub-menu s are available in XGENOA. These are as follow:

- isolate FEM Nodes: picks user selected FEM nodes.
- zoom of certain area of the model
- change the color of outlined or filled polygons, or the background color.
- project in either the orthotropic or perspective mode.
- optionally stand and View in -y, +y, -x, +x, -z, +z, or default view.
- capture the screen and save in the RGB format

Examples of the GENOA-PFA post-processing graphical outputs are shown in the Figures 9-4 through 9-10.

9-2 PFA/FEM Attributes Visualization

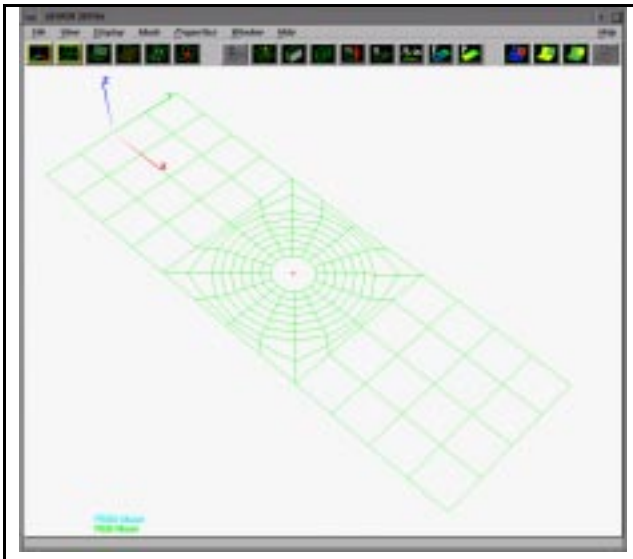

Figure 9-4 (a). The Starting View of an Open Hole Tension FEM Mesh of a Model

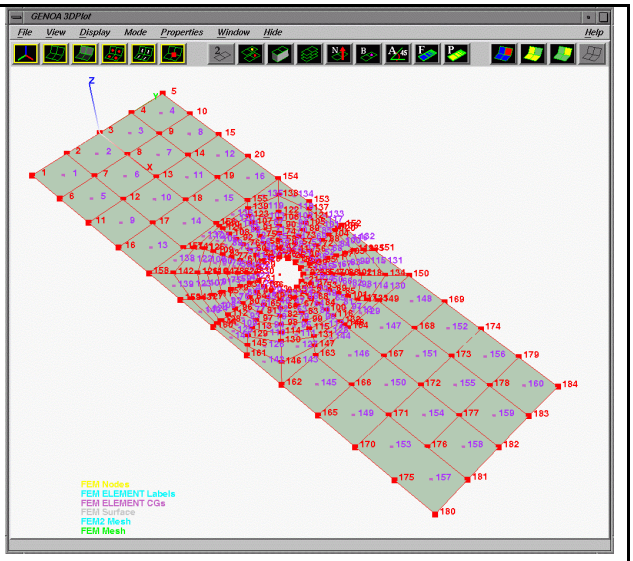

Figure 9-4 (b). FEM Mesh Display After Activating All Display Attributes

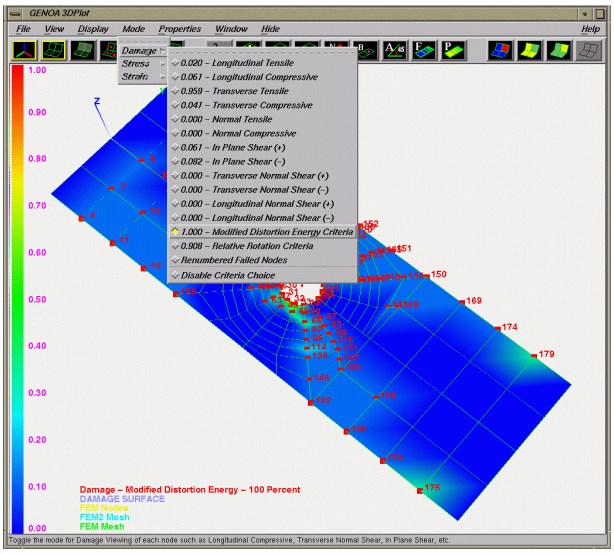

Figure 9-4 (c).. Distribution of Modified Distortion Energy Damage

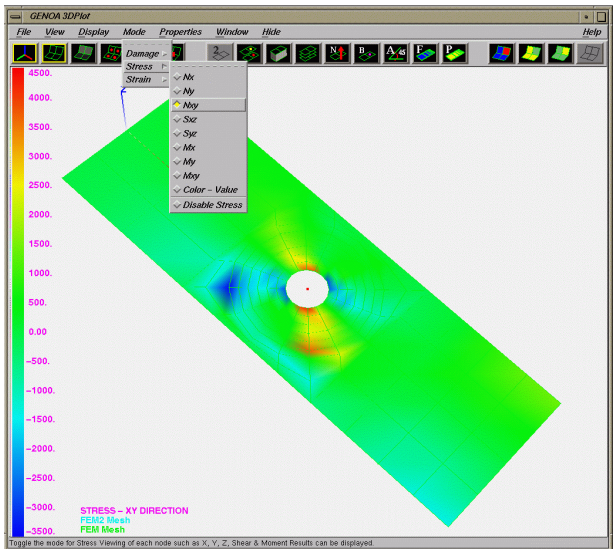

Figure 9-4 (d). Distribution of Y-Moment Generated Stress Mode

9.0 Graphics User Interface in GENOA

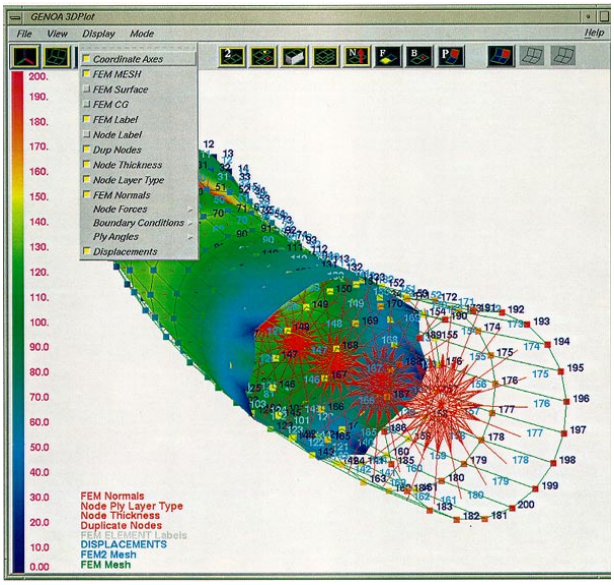

Figure 9-4 (e). Simultaneous Display of Multiple Properties And Modes on an FEM Mesh

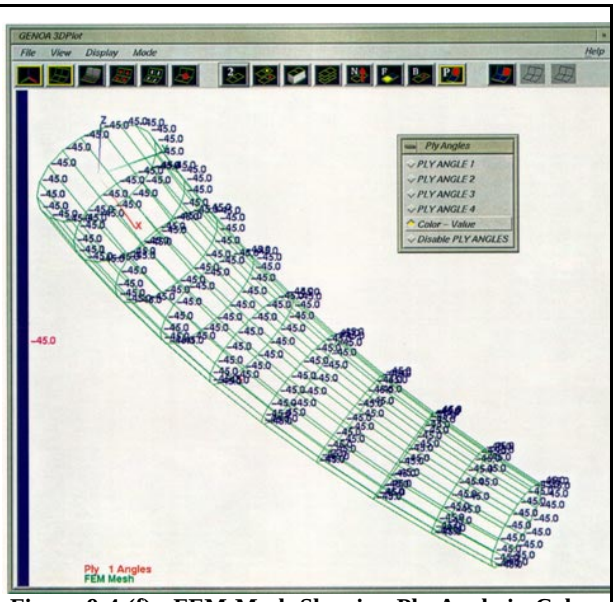

Figure 9-4 (f). FEM Mesh Showing Ply Angle in Color Value Mode with Angle Values Labeled on Mesh

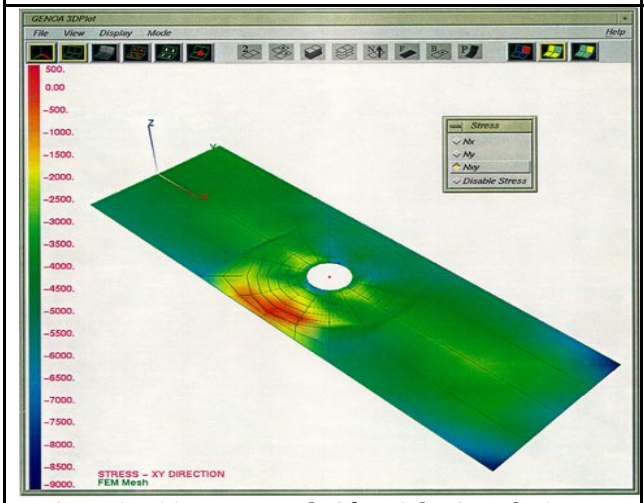

Figure 9-4 (g). FEM Mesh After Selecting Ply Stress Distribution Option

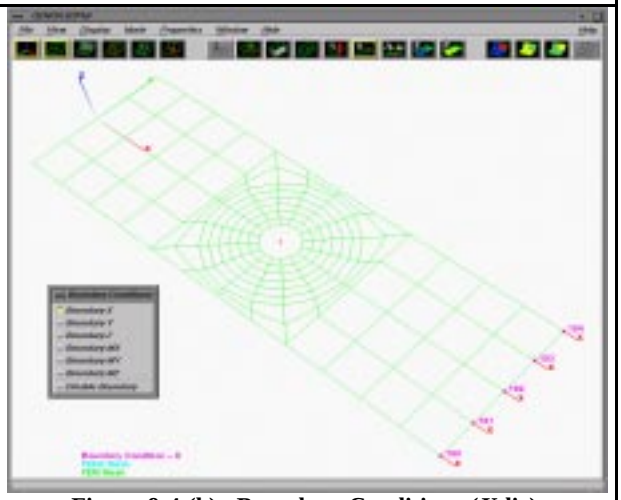

Figure 9-4 (h). Boundary Conditions (Xdir)

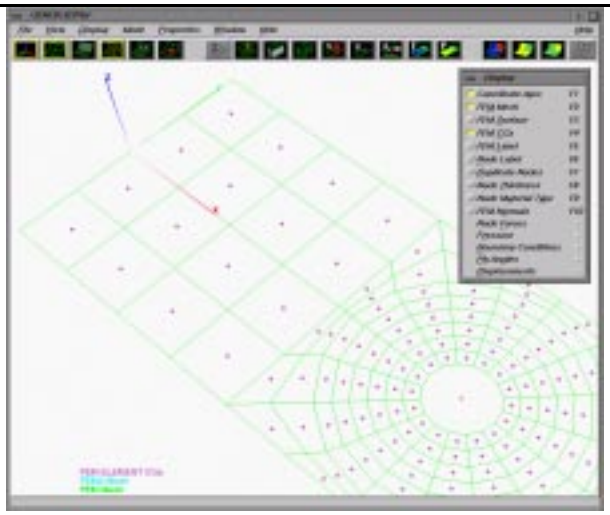

Figure 9-4 (i). Center Of Gravity (Cg) For Each Element

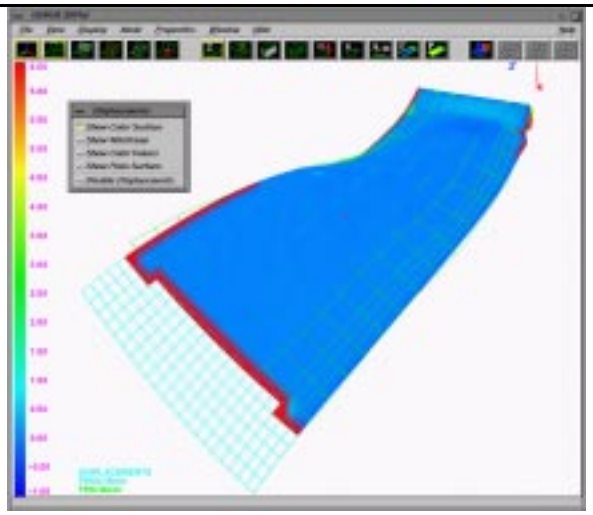

Figure 9-4 (j). Normal FEM Mesh And A Comparison With The Second Displacement FEM

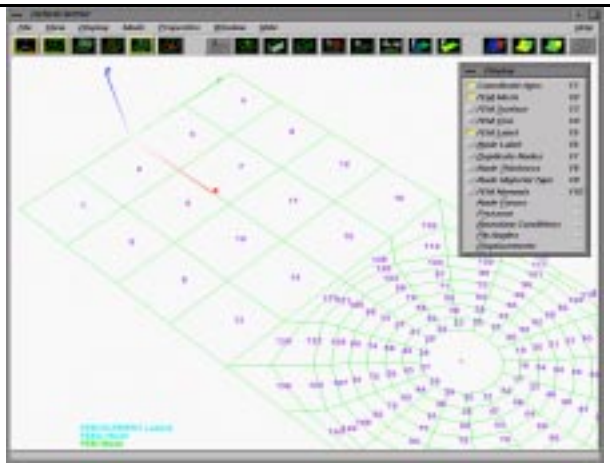

Figure 9-4 (k). FEM Element Number

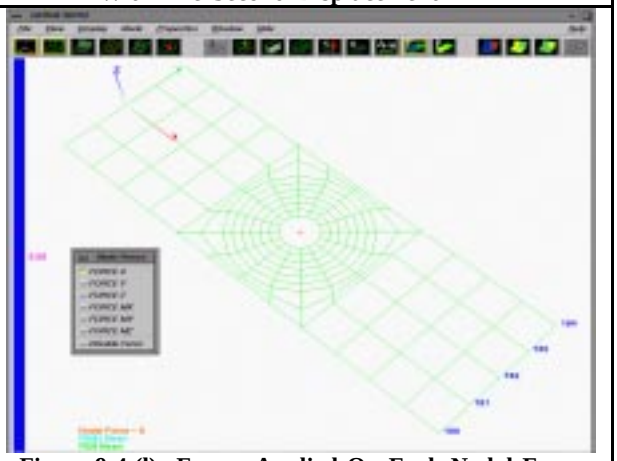

Figure 9-4 (l). Forces Applied On Each Nodal Force Distribution

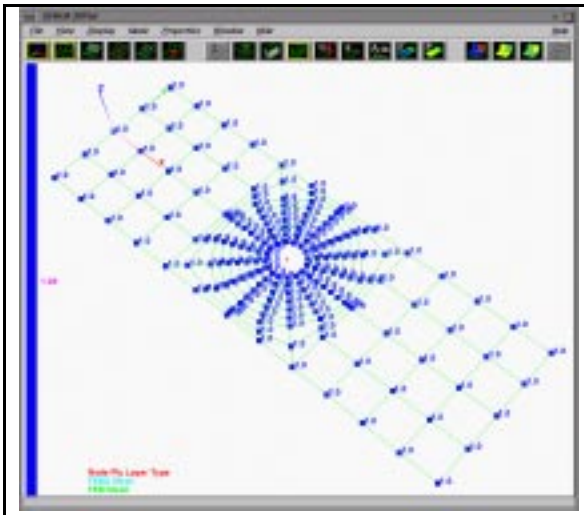

Figure 9-4 (m). FEM Nodes Material Identification (Layer Type)

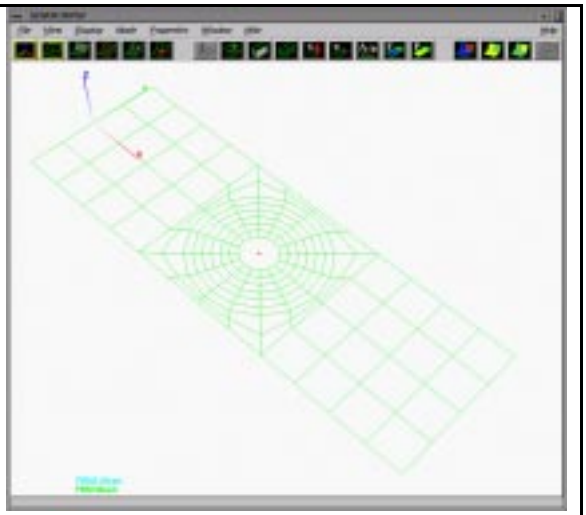

Figure 9-4 (n). FEM Mesh And Global Coordinate System

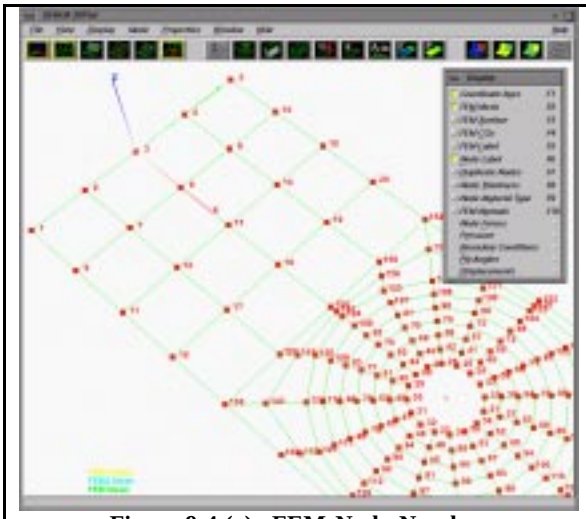

Figure 9-4 (o). FEM Node Number

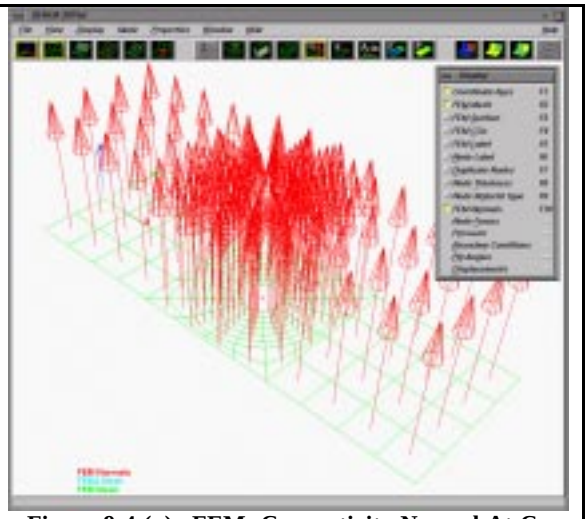

Figure 9-4 (p). FEM Connectivity Normal At Cg

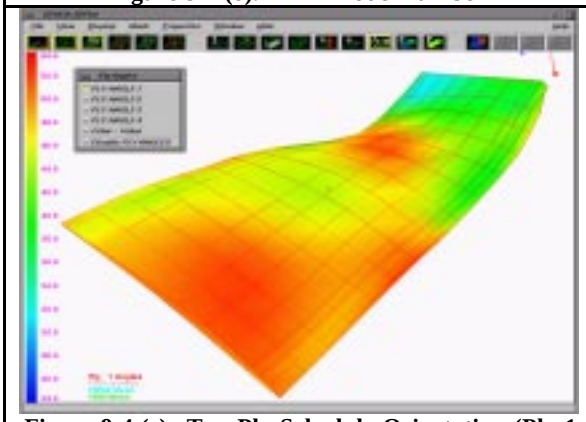

Figure 9-4 (r). Top Ply Schedule Orientation (Ply 1 Angle)

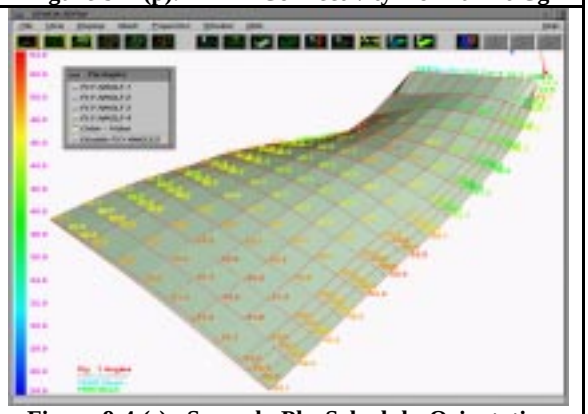

Figure 9-4 (s). Second Ply Schedule Orientation (Ply 2 Angle)

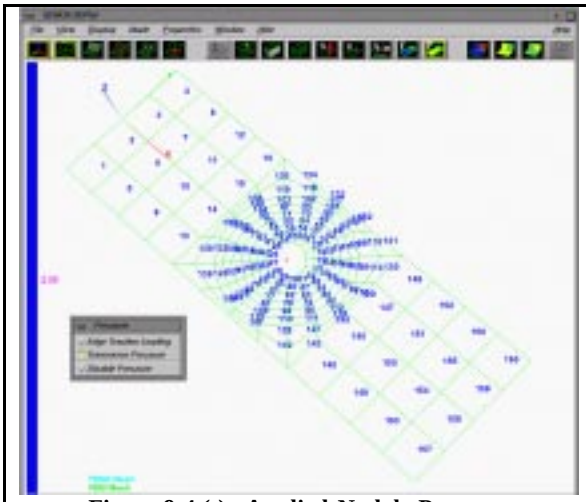

Figure 9-4 (t). Applied Nodal Pressure

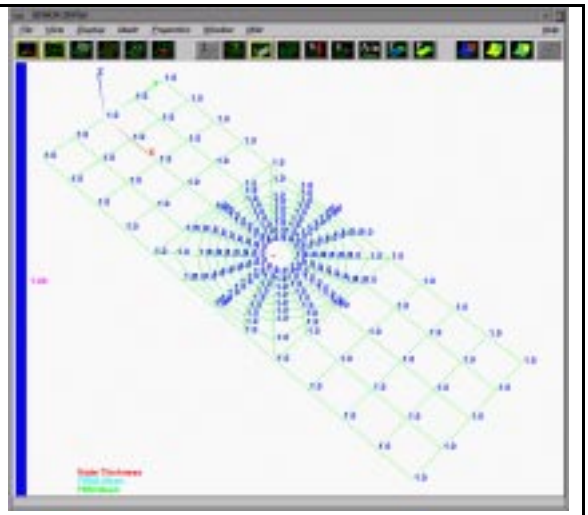

Figure 9-4 (u). FEM Mesh With Node Thicknesses Given

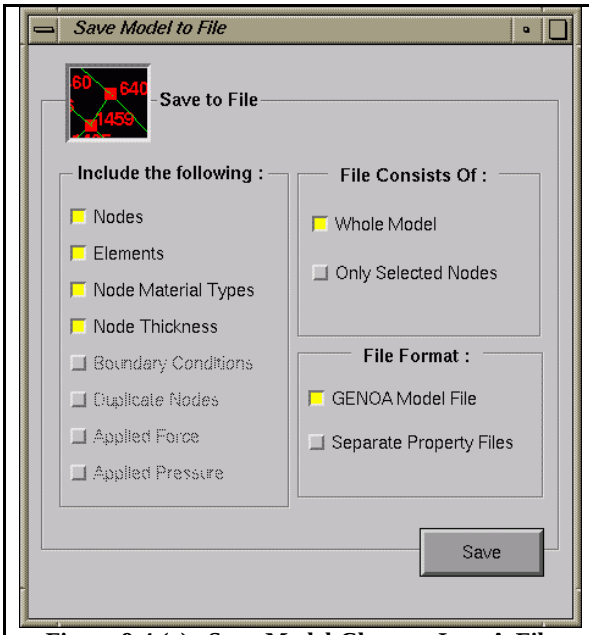

Figure 9-4 (v). Save Model Changes Into A File

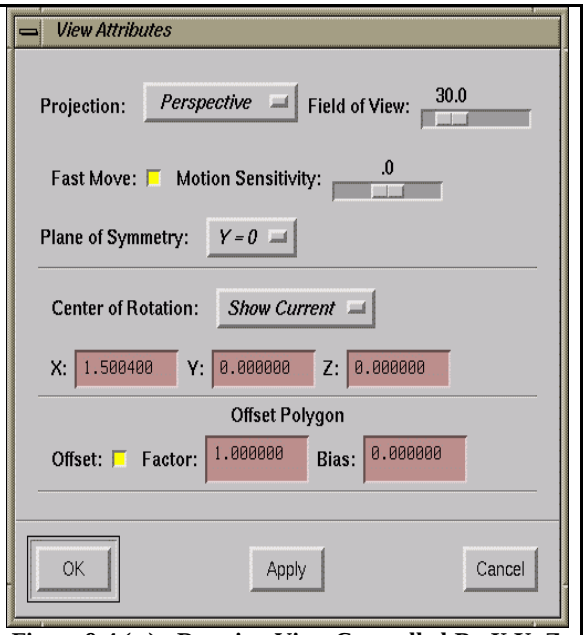

Figure 9-4 (w). Rotation View Controlled By X,Y, Z Coordinates

9.3 MENU VISUALIZATION

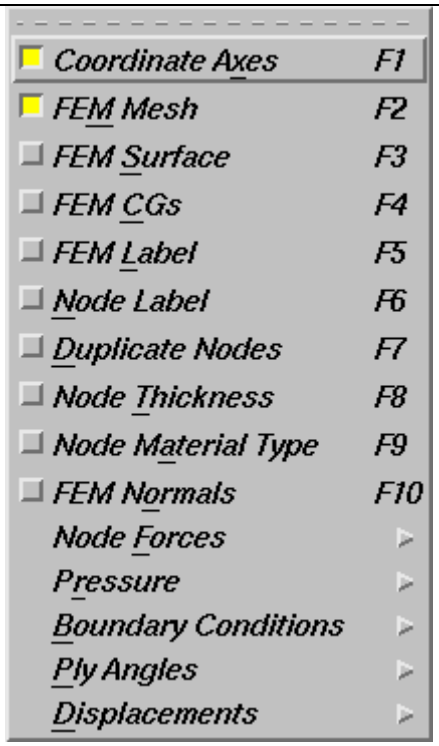

Figure 9-5 (a). display Menu

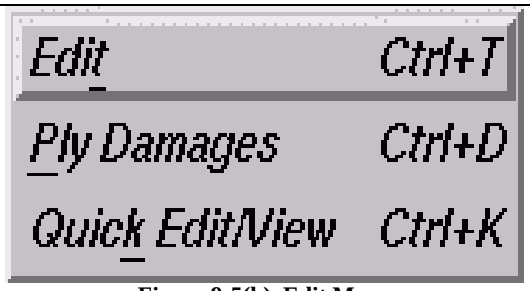

Figure 9-5(b). Edit Menu

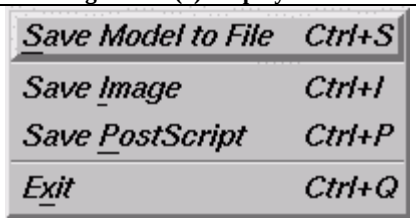

Figure 9-5 (c) Field Menu

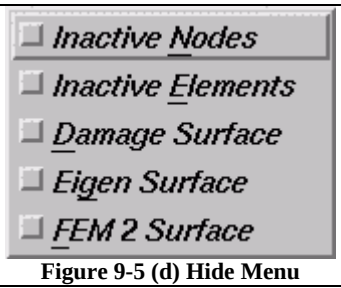

Figure 9-5 (d) Hide Menu

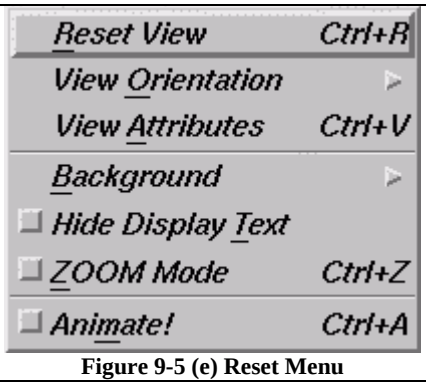

Figure 9-5 (e) Reset Menu

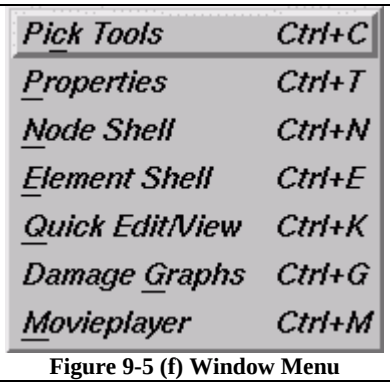

Figure 9-5 (f) Window Menu

9.4 MODE OF FAILURE VISUALIZATION

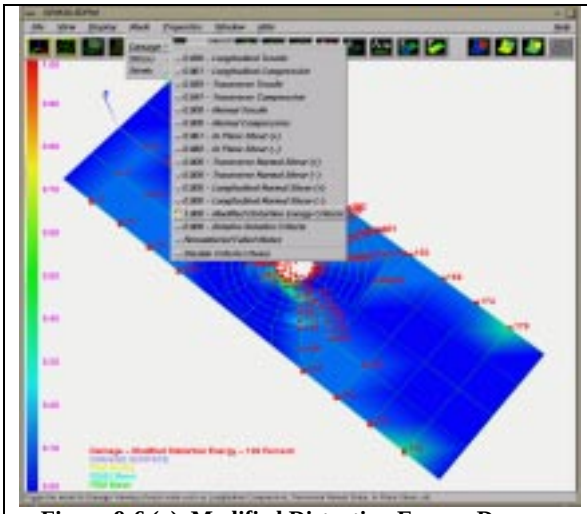

Figure 9-6 (a). Modified Distortion Energy Damage Index

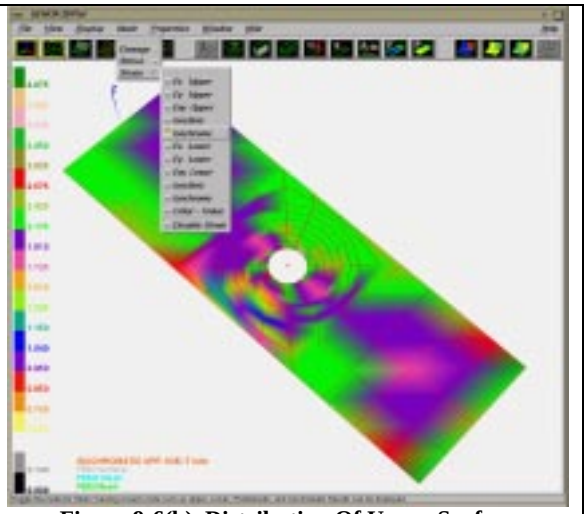

Figure 9-6(b). Distribution Of Upper Surface Isochromatic Photo-Elastic Fringe Pattern

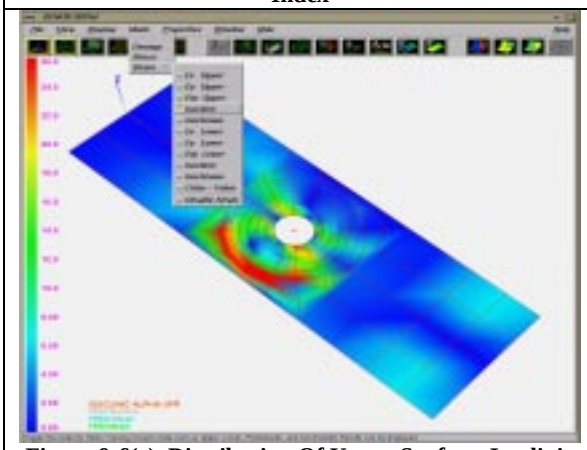

Figure 9-6(c). Distribution Of Upper Surface Isoclinic Photo-Elastic Fringe

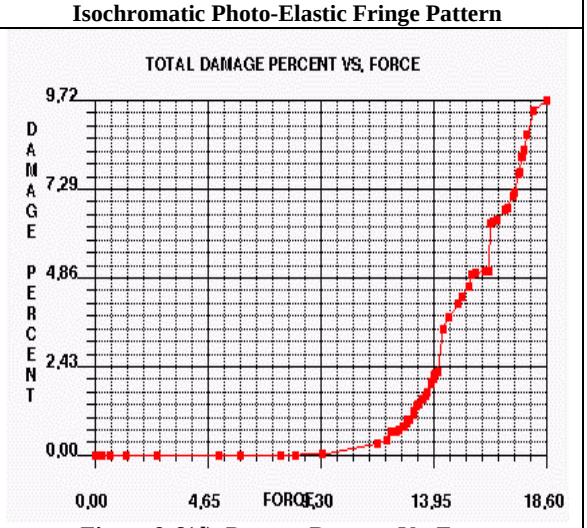

Figure 9-6(d). Percent Damage Vs. Force

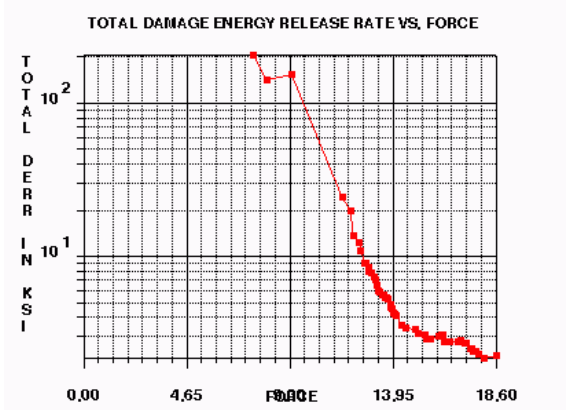

Figure 9-6(e). Total Damage Energy Release Rate Vs. Load

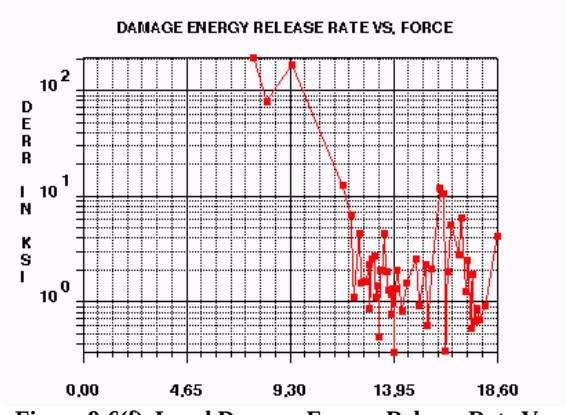

Figure 9-6(f). Local Damage Energy Release Rate Vs. Load

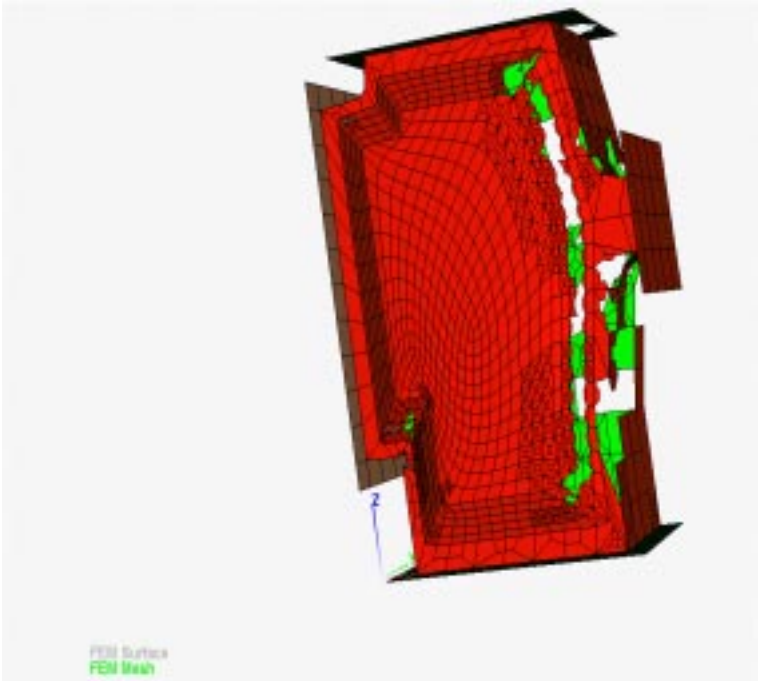

Figure 9-6(g). Collapsed Fem Model With Adaptive Meshing

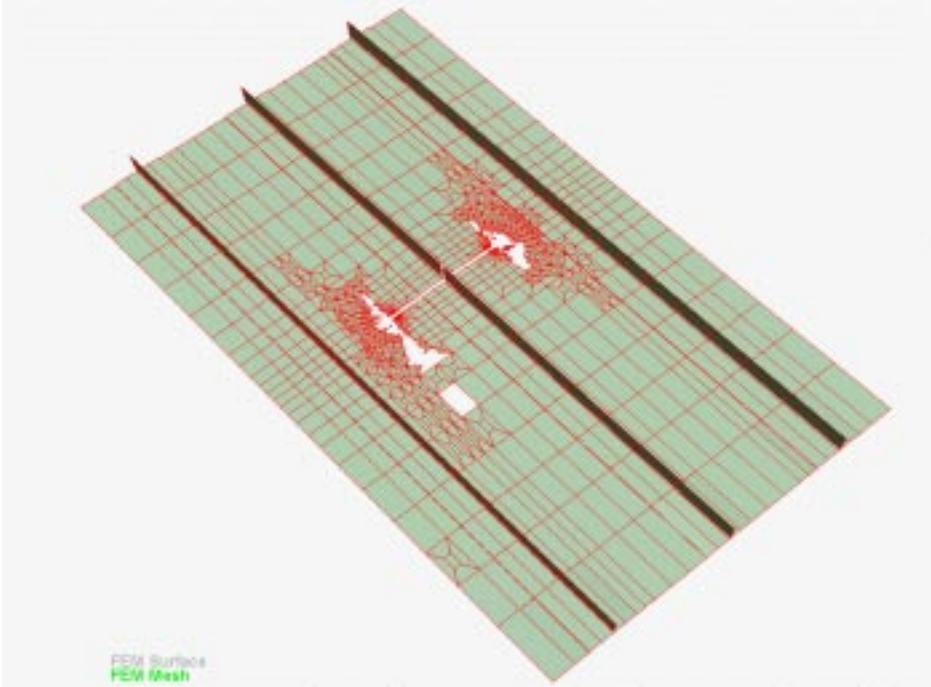

Figure 9-6(h). Fracture Path And Damage Progression With Adaptive Meshing (2148 Nodes, 1707 Elements)

9.5 Region Picking

The pick command allows the user to select FEM attributes (nodes) for further parameter editing options as shown in Figures 9-7(a-l), 9-8, and 9-9.

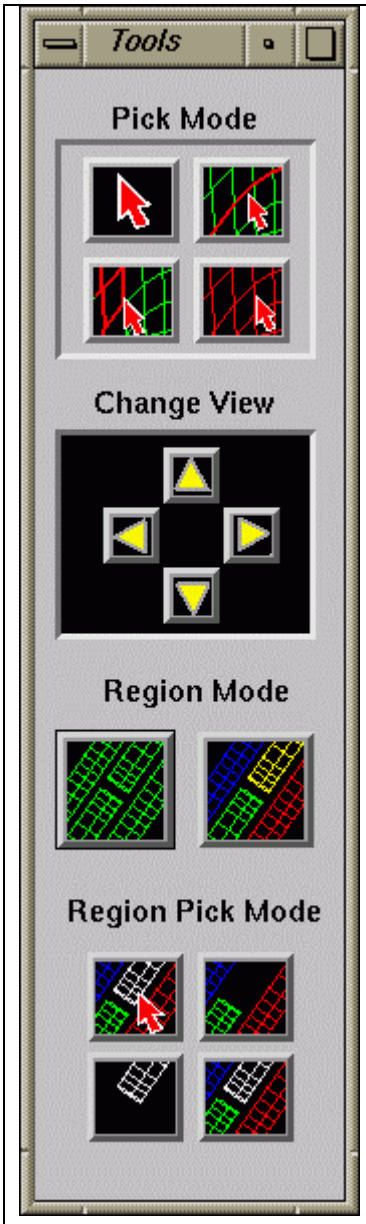

Window - Region Picking

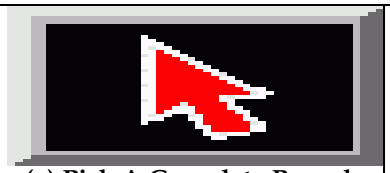

(a) Pick A Complete Bound Line Through Nodes Using Elements For Search Normal Default Picking Mode

(b) Pick A Complete Bound Line Through Nodes Using Elements For Search

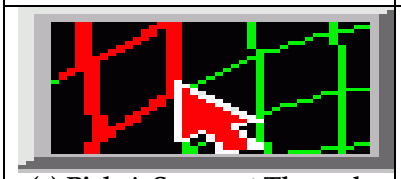

(c) Pick A Segment Through Nodes Using Polar Angles

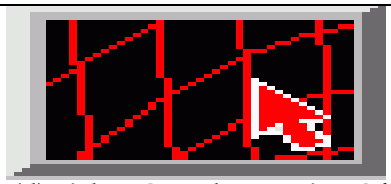

(d) Pick A Complete Region Of Nodes

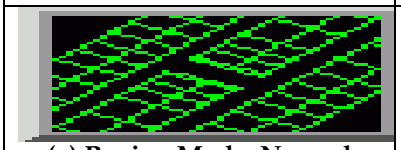

(e) Region Mode: Normal Default

(f) Region Mode: Enable Search For Region Picking

(g) Region Pick: Mode 1 Picks A Region

(h) Region Pick: Mode 2 Hides The Selected Region

(k) Region Pick: Mode 3 Swaps Hidden Regions

(l) Region Pick: Mode 4 Restores All Regions

Figure 9-7(a-l). The pick command allows the user to select FEM attributes (nodes) for further parameter editing

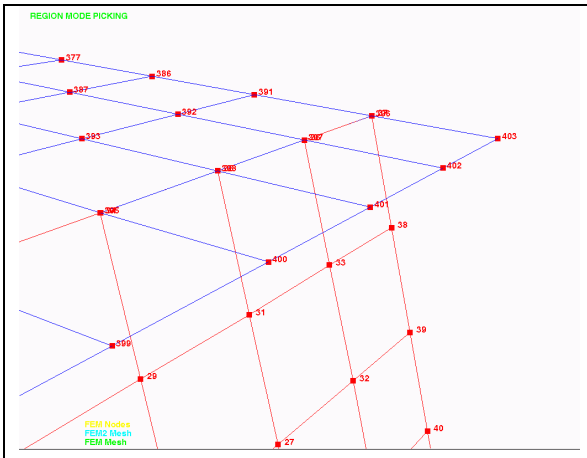

Figure 9-8(a). Duplicate Nodes 1

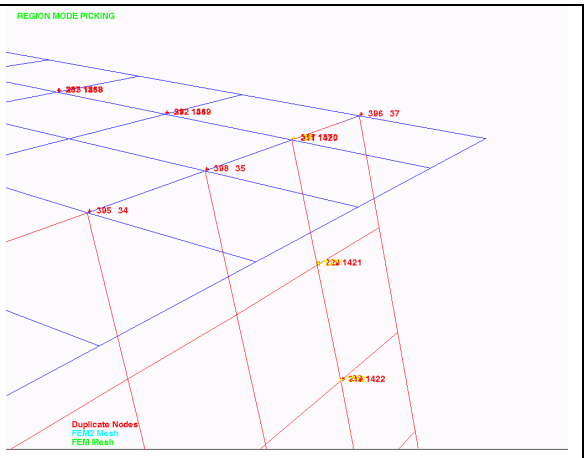

Figure 9-8(b). Duplicate Nodes 2

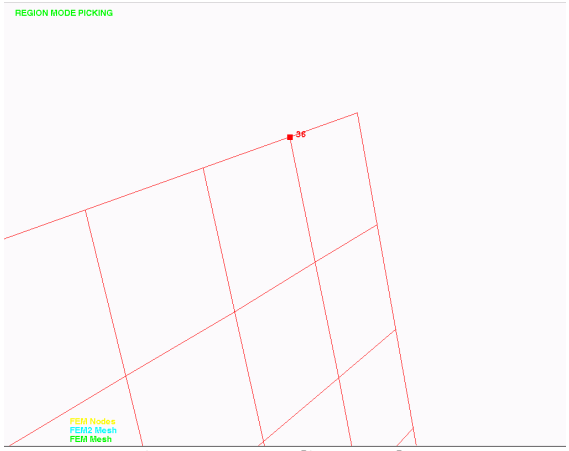

Figure 9-8© Duplicate Nodes 4

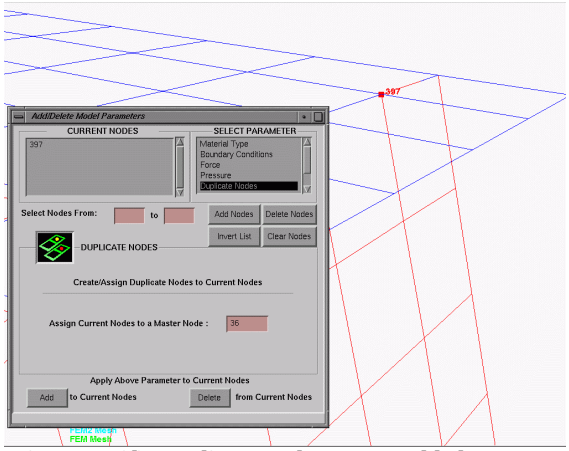

Figure 9-8(d). Duplicate Nodes 6 Was Added To FEM

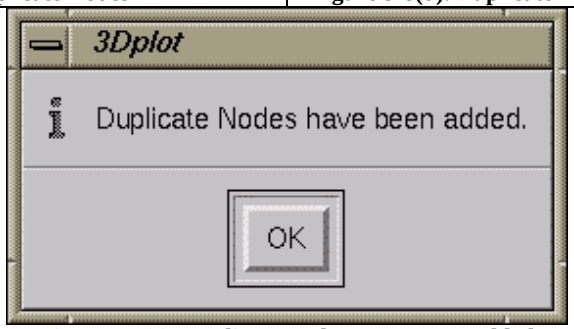

Figure 9-8(e). Duplicate Nodes Have Been Added

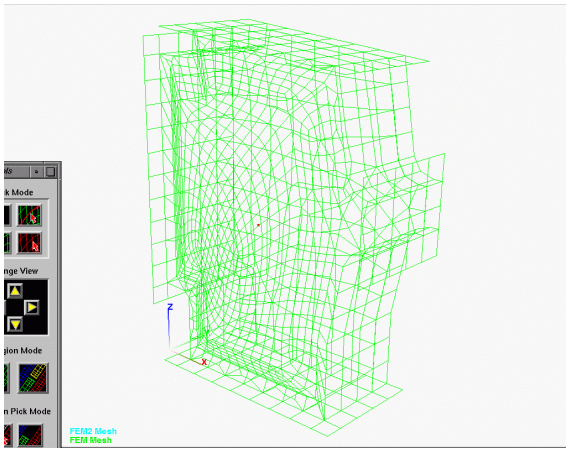

Figure 9-9(a). Normal Default Mode

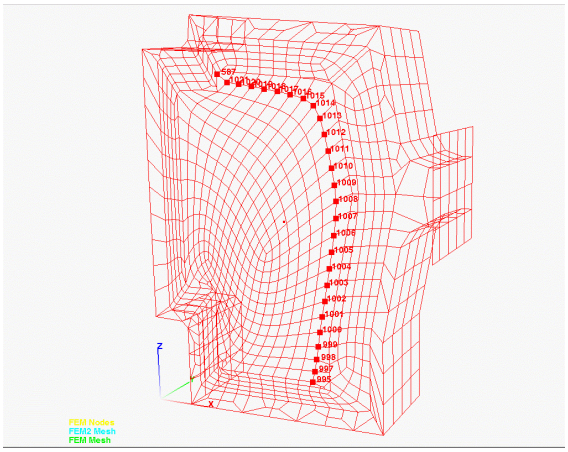

Figure 9-9(b). From (B) Pick A Complete Bound Of Line

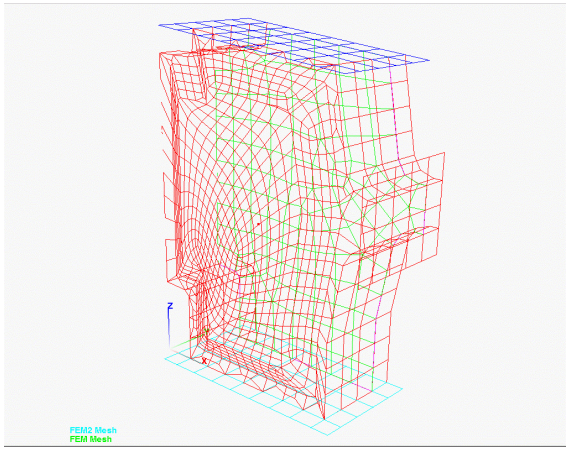

Figure 9-9(c). Activated Region Mode

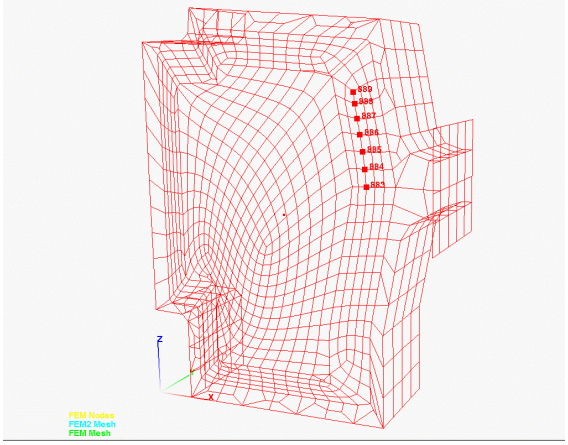

Figure 9-9(d). Pick A Segment Through Nodes Using Polar Angles

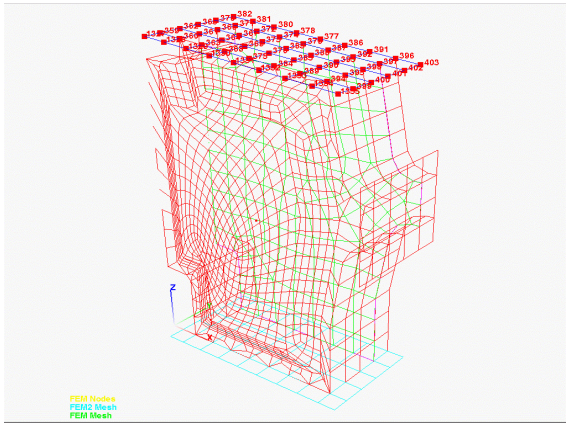

Figure 9-9(e). Pick A Complete Region Of Nodes

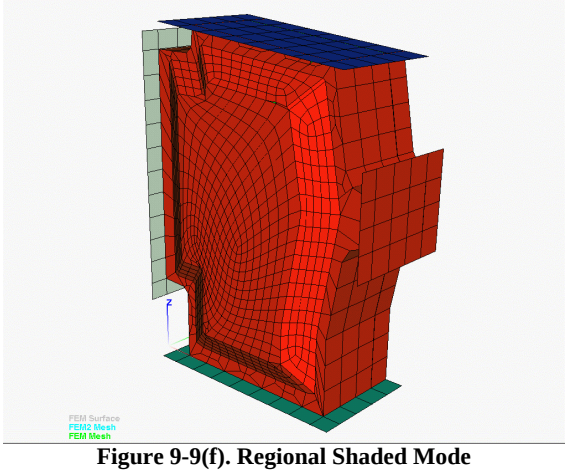

Figure 9-9(f). Regional Shaded Mode

9.6 Movie Of Failure Events

The movie player allows the user to animate the entire PFA simulation. The user can animate the desired files generated by post: at each equilibrium, or the entire loading session. The data can be loaded into memory or directly processes as batch files. The movie player allows the user to play fast forward (FF) or Rewind (RW) to slowly animate each sequence of failure. Figure 9-10 (a) will add to the simulation the damage energy release rate, and percent damage history as a function of loading.

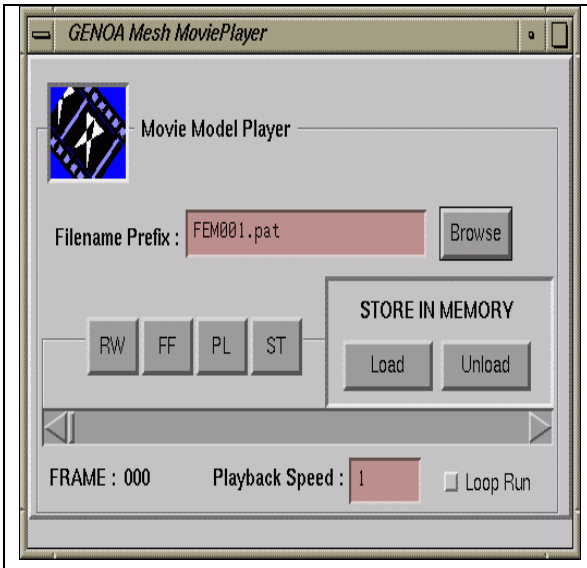

Figure 9-10(a). Movie Player

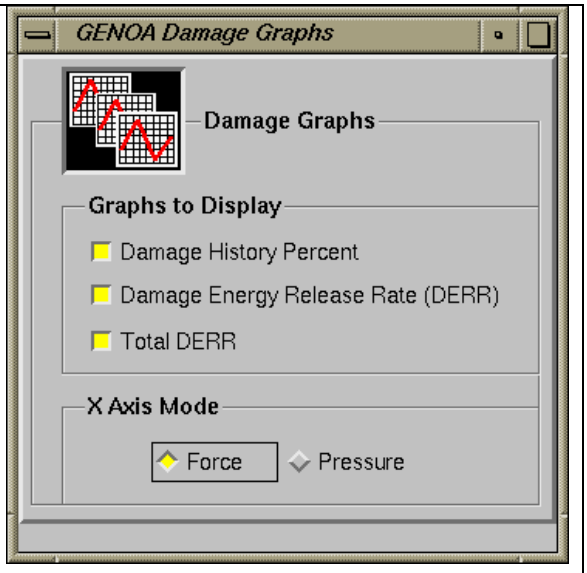

Figure 9-10(b). Damage Window

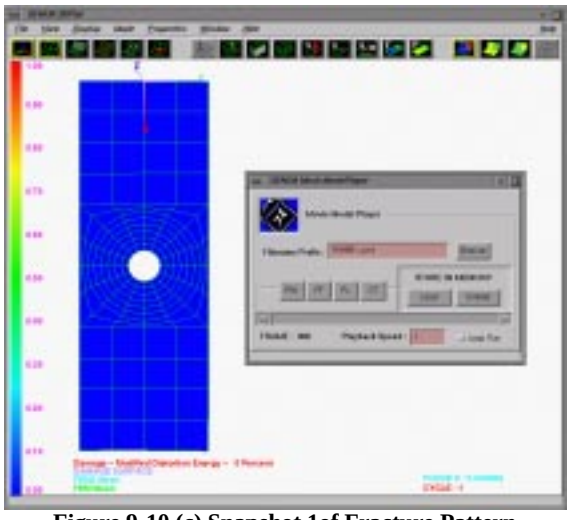

Figure 9-10 (c) Snapshot 1of Fracture Pattern

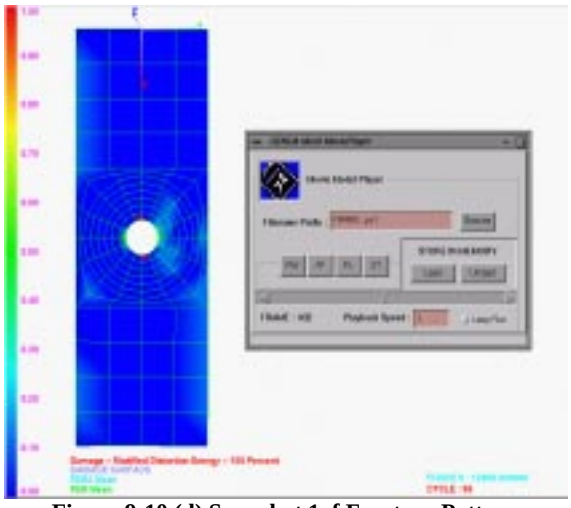

Figure 9-10 (d) Snapshot 1of Fracture Pattern

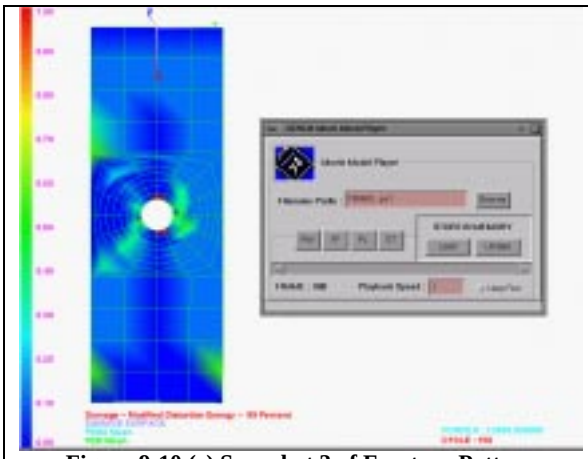

Figure 9-10 (e) Snapshot 3 of Fracture Pattern

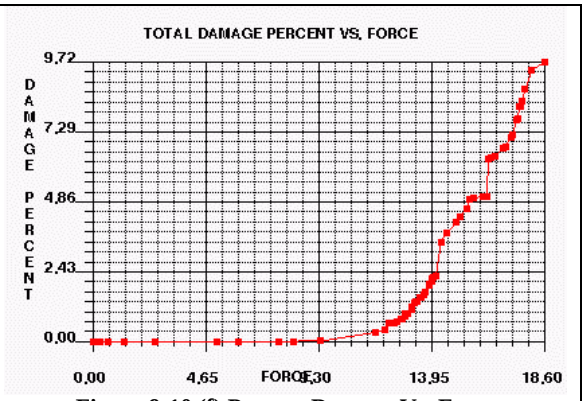

Figure 9-10 (f) Percent Damage Vs. Force

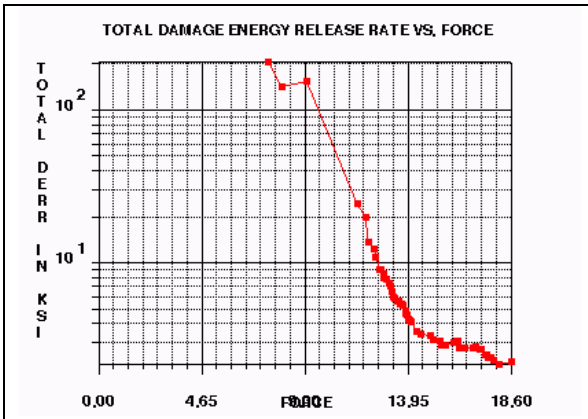

Figure 9-10 (g) Total Damage Energy Release Rate Vs. Load

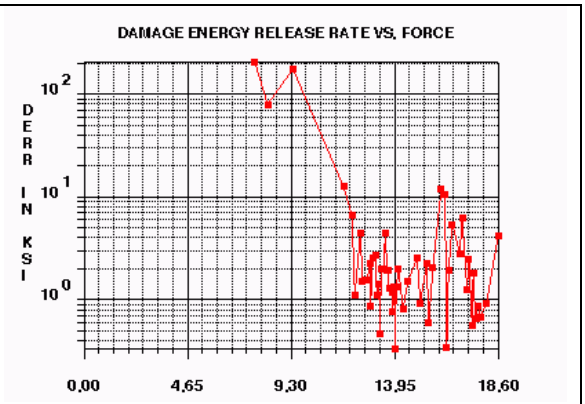

Figure 9-10 (i) Local Damage Energy Release Rate Vs. Load

REPORT DOCUMENTATION PAGE

Form Approved
OMB No. 0704-0188

1. AGENCY USE ONLY (*Leave blank*)	2. REPORT DATE	3. REPORT TYPE AND DATES COVERED
	December 1999	Final Contractor Report

4. TITLE AND SUBTITLE

Development of GENOA Progressive Failure Parallel Processing Software Systems

5. FUNDING NUMBERS

WU–523–22–13–00
NAS3–97041 SBIR

6. AUTHOR(S)

Frank Abdi and Levon Minnetyan

7. PERFORMING ORGANIZATION NAME(S) AND ADDRESS(ES)

Alpha STAR Corporation
5150 E. Pacific Coast Hwy, Suite 500
Long Beach, California 90804

8. PERFORMING ORGANIZATION REPORT NUMBER

E–11929

9. SPONSORING/MONITORING AGENCY NAME(S) AND ADDRESS(ES)

National Aeronautics and Space Administration
John H. Glenn Research Center at Lewis Field
Cleveland, Ohio 44135–3191

10. SPONSORING/MONITORING AGENCY REPORT NUMBER

NASA CR—1999-209404

11. SUPPLEMENTARY NOTES

Project Manager, C.C. Chamis, Research and Technology Directorate, NASA Glenn Research Center, organization code 5000, (216) 433–3252.

12a. DISTRIBUTION/AVAILABILITY STATEMENT

Unclassified - Unlimited
Released as Publicly Available August 1999 Distribution: Nonstandard
Subject Category: 39

This publication is available from the NASA Center for AeroSpace Information, (301) 621–0390.

12b. DISTRIBUTION CODE

13. ABSTRACT ***(Maximum 200 words)***

A capability consisting of software development and experimental techniques has been developed and is described. The capability is integrated into GENOA-PFA to model polymer matrix composite (PMC) structures. The capability considers the physics and mechanics of composite materials and structure by integration of a hierarchical multilevel macro-scale (lamina, laminate, and structure) and micro scale (fiber, matrix, and interface) simulation analyses. The modeling involves (1) ply layering methodology utilizing FEM elements with through-the-thickness representation, (2) simulation of effects of material defects and conditions (e.g., voids, fiber waviness, and residual stress) on global static and cyclic fatigue strengths, (3) including material nonlinearities (by updating properties periodically) and geometrical nonlinearities (by Lanrangian updating), (4) simulating crack initiation, and growth to failure under static, cyclic, creep, and impact loads, (5) progressive fracture analysis to determine durability and damage tolerance, (6) identifying the percent contribution of various possible composite failure modes involved in critical damage events, and (7) determining sensitivities of failure modes to design parameters (e.g., fiber volume fraction, ply thickness, fiber orientation, and adhesive-bond thickness). GENOA-PFA progressive failure analysis is now ready for use to investigate the effects on structural responses to PMC material degradation from damage induced by static, cyclic (fatigue), creep, and impact loading in 2D/3D PMC structures subjected to hygrothermal environments. Its use will significantly facilitate targeting design parameter changes that will be most effective in reducing the probability of a given failure mode occurring.

14. SUBJECT TERMS

Composites; Woven; Fabric; Preform; 3-D; Failure mechanisms; Material components; Strucutres; Fracture; Testing; Data fabrication variables

15. NUMBER OF PAGES

241

16. PRICE CODE

A11

17. SECURITY CLASSIFICATION OF REPORT	18. SECURITY CLASSIFICATION OF THIS PAGE	19. SECURITY CLASSIFICATION OF ABSTRACT	20. LIMITATION OF ABSTRACT
Unclassified	Unclassified	Unclassified	